DEVELOPMENT OF OFFSHORE STRUCTURES (MOORING/RISER) PERFORMANCE ASSESSMENT AND MONITORING USING COMPUTER SIMULATIONS AND NUMERICAL SENSORS

A Dissertation

by

WOO CHUL CHUNG

Submitted to the Office of Graduate and Professional Studies of
Texas A&M University
in partial fulfillment of the requirements for the degree of

DOCTOR OF PHILOSOPHY

Chair of Committee,	Moo-Hyun Kim
Co-Chair of Committee	Robert Randall
Committee Members,	Hamn-Ching Chen
	Steven DiMarco
Head of Department,	Sharath Girimaji

May 2021

Major Subject: Ocean Engineering

ABSTRACT

In this research, five subjects which are related to offshore structure (mooring lines and risers) performance assessment and monitoring will discuss mainly such as chain mooring OPB-induced failure and riser structure health monitoring with numerical sensors.

First, a multi-scale approach concept is introduced to estimate OPB (out of plane bending)-induced failure considering time-varying interlink bending stiffness by using both high-fidelity nonlinear-FEM (finite element method)-based local structural analysis and low-fidelity global-system-simulation program so that they can mutually be interfaced during the time-stepping procedure.

Second, the effects of underwater-chain-stopper (UCS) bearing friction at fairlead connection and time-varying interlink EI (bending stiffness) at the UCS exit on the OPB-fatigue-induced chain failure are investigated. To demonstrate their effects through numerical simulations, three different approaches, such as only considering time-varying EI, considering both time-varying EI and fairlead bearing friction, and neither considered, are modeled and the results are systematically compared.

Third, a new algorithm for the real-time structural health monitoring of TLP (tension-leg platform) tendons is presented. The algorithm is based on bi-axial sensors installed along the tendon and top tension-meter. Then, the tension and bending moment along the tendon can be estimated by using the developed algorithm. For bending moment, a generalized-

coordinate-based FEA (Finite Element Analysis) formulas with cubic interpolation are derived. For tension, analytical formulas with small angle assumption are derived.

Fourth, the methodology for the real-time tracing of riser profile and bending moment by multiple inclinometers along the riser is presented with the assumption that its top (by GPS; global positioning system) and bottom (anchoring) points are known. For riser x-y-z displacement and bending-moment tracing, quadratic and cubic interpolation functions for each line element between two neighboring bi-axial inclinometers are employed with respect to the global and generalized coordinate systems to derive analytical solutions.

Lastly, the monitoring methodology with minimum top sensors using digital twin with assumption that there is a significantly wave excitation loads reduction below certain water depth (last sensor attached) is presented. Also, multivariate regression can be applied to predict current profile at the remaining water depth.

ACKNOWLEDGEMENTS

First, I would like to express my gratitude to chair Prof. Moo-Hyun Kim for his continuous warm encouragement and generous support to finalize this dissertation and guidance to academia. Second, I want to extend my deep appreciation to co-chair Prof. Randall for his insightful comments and precious advice for this research. Additionally, I would like to thank my committee members Prof. Chen and Prof. DiMarco for sharing valuable knowledge and experience.

Also, my sincere gratitude goes to my colleagues and staff in the Department of Ocean Engineering at Texas A&M University for making an excellent experience.

Lastly, I would like to give special thanks to my lovely family, Boyoung Choi (my wife), Chloe Chung (my daughter), and Jaden Chung (my son) for their support and love during my study.

CONTRIBUTERS AND FUNDING SOURCES

Contributors

This work was supported by a dissertation committee consisting of Professor Moo-Hyun Kim [advisor] and Professor Robert Randall [co-advisor]. All work conducted for the dissertation was completed by the student independently.

Funding Sources

Portions of this research were conducted with the advanced computing resources provided by Texas A&M High Performance Research Computing.

NOMENCLATURE

OPB	Out of Plane Bending
IPB	In Plane Bending
UCS	Underwater Chain Stopper
SPMB	Single Point Mooring Buoy
JIP	Joint Industry Project
FEM	Finite Element Method
TAMU	Texas A&M University
DOF	Degree of Freedom
MBL	Minimum Breaking Load
EI	Bending Stiffness
BM	Bending Moment
UCS	Underwater Chain Stopper
UCSBRK	Underwater Chain Stopper Breakout angle
JONSWAP	Joint North Sea Wave Project
API	American Petroleum Institute
ML	Mooring Line
PSD	Power Spectrum Density
ABS	American Bureau of Shipping
STD	Standard Deviation
TLP	Tension Leg Platform

FOWT	Floating Offshore Wind Turbine
FEA	Finite Element Analysis
NDT	Non Destructive Test
VIV	Vortex Induced Vibration
VCG	Vertical Center of Gravity
ANN	Artificial Neural Network
MR	Multivariate Regression
MWL	Mean Water Level
B.C.	Boundary Conditions
JONSWAP	Joint North Sea Wave Project
GOM	Gulf of Mexico

TABLE OF CONTENTS

Page

LIST OF FIGURES

Page

LIST OF TABLES

Page

1. INTRODUCTION

Due to world economic growth, the global consumption of oil and gas has continuously been increased. Many experts expect that this long-term trend will not change in the near future. In the oil and gas production, offshore structures have played an important role as a significant energy supply source. However, all kind of offshore system failures such as chain mooring OPB (Out of Plane Bending)-induced failure and riser breakdown are still reported to the industry. Thus, the performance assessment and monitoring of those offshore structures will continuously be a very critical issue in the offshore oil and gas industry. With this background, the research motivation and purpose of chain mooring OPB-induced failure assessment and riser structure health monitoring will be explained in the following.

1.1 Chain Mooring OPB-induced Failure

Chain mooring system with underwater-chain-stopper (UCS) has been used in many offshore platforms. Even though its design has been based on standard guidelines, numerous accidents of mooring rupture have been reported during the past twenty years. The chain OPB (out of plane bending) / IPB (in plane bending)-induced fatigue drew industry's attention after the report of Girasol SPMB (single-point-mooring-buoy) chain-mooring failure in 2002 [1]. The "OPB" and "IPB" terminology mean the bending caused by the relative rotational angles between any two neighboring chain links [2]. Furthermore, due to the restrictive links near fairlead with large tension and friction,

critical bending moment occurs at the fairlead connection [3]. Usually, IPB-induced fatigue damage is much smaller than that by OPB in chain bending failure [2]. Offshore industry launched several JIPs (joint-industry-projects) to further investigate the key features and physics of the OPB-induced mooring failure through numerical and experimental investigations [2, 4]. Despite those efforts, the details of the procedure and methodology to reliably check the possible OPB-induced failure are not fully established yet. Thus, many researchers are still making effort to develop more rigorous approach.

Since most OPB-induced failures happen locally near fairlead, high-fidelity FEM analysis can be used for more detailed structural analysis there. Based on this background, many researchers focused on that kind of local FEM analysis. For example, [5] suggested a novel procedure for predicting OPB-induced failure using the stress at the last step. Structure failure detection methodology based on the first- and second-order of reliability was reported by [6]. [7] studied OPB-induced failure on 7 pocket roller type fairlead structure. To increase the accuracy of local FEM results, a new non-linear contact model was suggested by [8]. To investigate the difference between tensile stress and bending stress, another FEM model was established by [9].

However, for the rigorous estimation of the OPB-induced stresses, both local FEM analysis and global mooring dynamics should be coupled at the same time and solved simultaneously. The approach to solve OPB/IPB-induced failure by mainly focusing on the local behavior was suggested by [10]. Also, [11] introduced a de-coupled approach for the interlink-angle calculation with respect to the mooring-global-performance analysis. Furthermore, [12-15] underscored the importance of the rigorous modeling of local-

connection complexity including fairlead bearing friction in assessing OPB-induced failure.

However, [10, 11, 16] pointed out that the chain interlink bending stiffness was changed according to the interlink angle and its tension in time-stepping procedure. Thus, first, I developed the most rigorous multi-scale approach considering the time-varying chain interlink bending stiffness obtained from detailed local FE analysis at the critical point in the time marching of global-line simulation. The importance of floater connection boundary condition (B.C.) for fatigue damage is also underscored.

Furthermore, I also developed a rigorous approach that considers the UCS breakout angle effect caused by fairlead bearing friction. During the time-stepping procedure in global mooring simulation, the time-varying fairlead boundary condition and time-varying chain interlink bending stiffness at UCS exit are simultaneously considered at each time step, which has rarely been attempted in the previous studies. That fairlead modeling was done according to the results of instantaneous UCS and breakout angles. Furthermore, since line-discontinuity can be varied by UCS (or chain-hawse) design, the corresponding sensitivity is checked with varying UCS and fairlead-connection parameters to better understand their effects on OPB-induced failure.

For the proposed multi-scale approach, in this research, in-house hull-mooring-riser fully-coupled dynamics solver CHARM3D (TAMU in-house program) [17-20] was used for the global mooring simulation. A commercial non-linear FEM program Abaqus 6.12 was used for the detailed local structural analyses of chain links near the target point (UCS exit).

1.2 Riser Structure Health Monitoring using Numerical Sensors

As explained previously, due to fast global economic expansion, energy demand has increased a lot, and this trend will likely continue in the near future. With this background, offshore energy sources can be divided into two categories such as offshore platform and ocean renewable energy converter (wind turbine or wave energy converter).

Generally, offshore structures including FOWT monitoring methodology can be divided into two categories: sensor based and NDT (Non-Destructive Testing), In deep water, the latter typically uses ROVs (Remotely Operated underwater Vehicle) [21], which is costly, and limited in structural assessment. For example, in fatigue failures of base material, most of the stress cycles usually occur before a detectable crack appears. After that, failure occurs fast, and thus fatigue failures may not be prevented by NDT.

Thus, sensor-based monitoring is a more attractive low-cost health-monitoring option with automation potential [22]. Simple sensors such as accelerometers, inclinometers, and/or strain gauges are installed and their signals are analyzed by analytical or numerical methods to estimate the structural integrity. However, the sensors require continuous power supply to generate and transmit signals, which is also challenging in deeper waters. So far, many sensor-based monitoring technologies and methodologies have been developed and reported. [23] tested their monitoring program using localized strain and motion measurement. Also, scaled model experiments were conducted by [24] to evaluate the dynamic responses of FOWT and validate sensor-measurement strategies. [25] investigated piezo-electric converters as an energy supplying method for subsea sensors. In addition, [26] utilized operational modal analysis coupled with accelerometer data for

wind-turbine structural health monitoring. Using acceleration and angular-rate data, a decision-making methodology for riser angles was proposed by [27]. Also, an acoustic-telemetry-based riser fatigue monitoring system was suggested by [28]. [29] researched a methodology for flexible riser monitoring using hybrid magnetic/optical strain gauges. For slender structures, VIV (vortex-induced vibration) responses, an adopted methodology using modal decomposition and linear regression was presented by [30] including sensitivity tests. Also, the statistical-pattern-recognition paradigm was also introduced by [31]. [32] employed an ANN (artificial neural network)-based technology for a rigorous monitoring of FOWT fatigue.

In this research, first, I introduce the new algorithms that can do real-time riser or mooring monitoring including tensions, internal stresses, and accumulated fatigue damage by using a top-tension-meter and a series of bi-axial inclinometers along the line. The validity of the developed algorithms is demonstrated by using the CHARM3D (TAMU in-house program) for floater-turbine-mooring fully-coupled dynamic simulation [33]. As a validation example, the tendon monitoring of a TLP (Tension Leg Platform)-type FOWT (Floating Offshore Wind Turbine) is selected [34, 35].

Furthermore, the algorithms for the real-time tracing of riser profiles and internal stresses are developed by using multiple inclinometers along the riser. Since accelerometers are not used, double time integration is not necessary to obtain riser's real-time displacements. As a result, the profile tracing method is much more robust than the accelerometer-based approach. In addition, the real-time estimation of internal stresses and accumulated fatigue damages are also possible, which has rarely been reported in the open literature. To

validate the developed algorithms, riser dynamics of a FPSO under typical sea environments are simulated by using a commercial software (OrcaFlex). Then, numerical inclinometers are distributed along the riser and they provide sensor signals like physical sensors. Subsequently, the inputted sensor signals are applied to the developed algorithms to enable the real-time prediction of instantaneous riser profiles and internal stresses. Lastly, the real-time predicted profiles and internal stresses are compared with the originally generated ones to validate the accuracy of the developed methodologies and algorithms. Since CHARM3D (TAMU in-house program) will use mainly in this research, the theoretical description of numerical software (CHARM3D) will be explained at Appendix.

2. MULTI-SCALE APPROACH FOR CHAIN-MOORING OPB-INDUCED FAILURE CONSIDERING TIME-VARYING INTERLINK BENDING STIFFNESS AND FAIRLEAD CONDITION*

2.1 Description of High-Fidelity Nonlinear FEM Model for Local Analysis

There are several papers related to chain-mooring OPB/IPB phenomena using non-linear FEM [10, 12, 16, 36] For chain-mooring, proof-load test is performed to check its structural robustness during chain manufacturing stage. Usually, proof-load is applied at 70% of Minimum Breaking Load (MBL). As a result, it may cause permanent deformation of chain link surface. This permanent deformation and the corresponding residual stress can be one of important factors relevant to chain-mooring OPB/IPB-induced failure (see Figure 1). To consider the processes from manufacturing stage to on-site operation, four sequential loading steps (Figure 1) are applied in the non-linear FEM model. The boundary condition of the left end of the chain links is assumed to be fixed considering the restrictions by stopper inside chain-hawse. Sequential loadings (proof-test loading, unloading, and operational loadings (tension and bending moment) are applied at the right side of the chain link. The interlink angles, corresponding bending moment and resulting stresses can then be calculated based on the non-linear FEM program. Here, a commercial non-linear FEM program, ABAQUS, is used and the results are compared with those of [12] for the exactly same case and material properties. Figure 2 shows the computed relationship between OPB chain interlink angle and OPB moment for various applied

* Parts of this chapter are previously published from [15].

tensions. The general trend (3 stages of sticking-rotating-sliding) agrees well with that of other published results and the case of tension=2250 kN agrees well with that of [12].

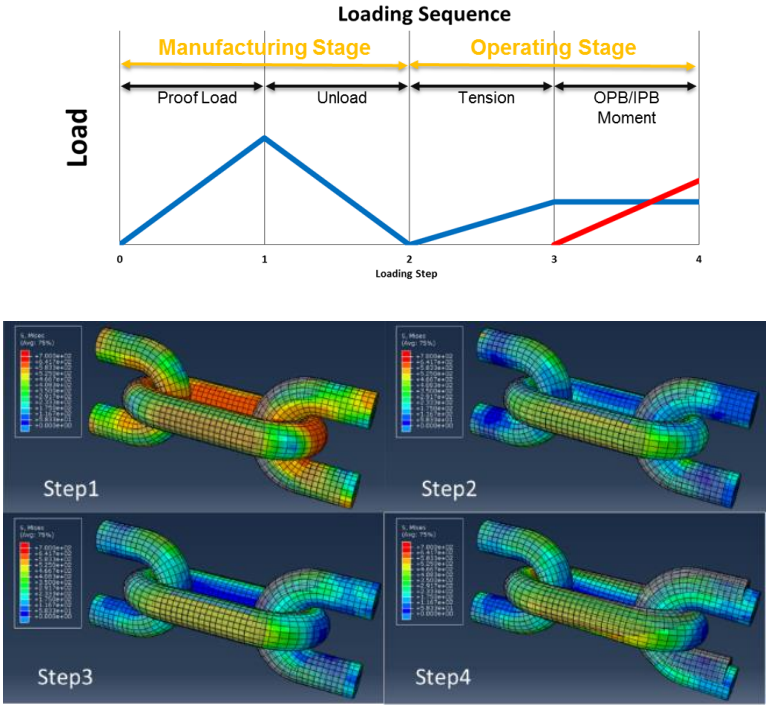

Figure 1 Loading Steps in non-linear FEM computation, Reprinted with permission from [15]

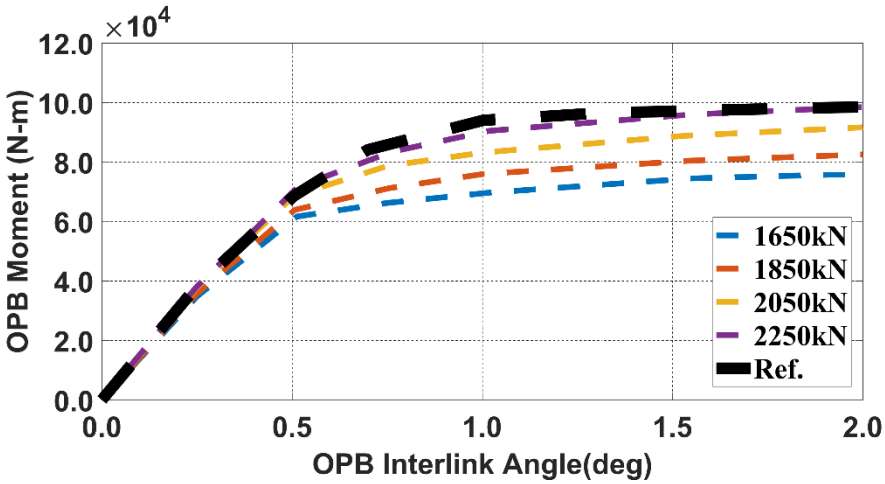

Figure 2 Results of OPB interlink angles vs. Moments for various tensions (Studless, Chain Grade R3, Friction Coefficient = 0.7, Ref.=[12] , Reprinted with permission from [15]

2.2 Description of Low-Fidelity Global Line Dynamics Program

2.2.1 CHARM3D

CHARM3D is TAMU-in-house computer program that has been developed by the TAMU OSCL during the past 20 years for multi-hull-mooring-riser fully-coupled nonlinear dynamic analysis in time domain [33]. The computer simulation program has been extensively validated against various experimental and field data (e.g.[18]). In CHARM3D, the slender-elastic-rod theory developed by Garrett [37] is used for risers and mooring lines. Their governing equations are derived with respect to the position vector r(s, t) which is function of arc length (s) in general coordinate and time (t).

$$-(Pr'')'' + (\lambda r')' + q = \rho \ddot{r}$$

$$P = EI$$

$$r' \cdot r' = (1 + \frac{T}{A_I E})^2 \approx 1 + 2\frac{\lambda}{A_I E} \quad (2.1)$$

In Eq. (2.1), E=Young's modulus, I=sectional moment of inertia, q =distributed load, ρ = rod density, λ = Lagrangian multiplier, T = tension, A_I=effective cross-sectional area, primes represent derivative with respect to arc length (s) and dot represent differentiation with respect to time (t). The distributed load (q) is composed of rod element weight (w), hydrostatic load (F^s), and hydrodynamic load(F^d). Those loads are based on the unit length of the rod. Also, hydrostatic load (F^s) can be estimated using Eq. (2.2).

$$F^s = \text{Buoyancy} - (HA_I r')' \quad (2.2)$$

where, H = hydrostatic pressure at position r

In addition, hydrodynamic load can be computed following Eq. (2.3).

$$F^d = -C_A \rho A_I \ddot{r}^n + \left[(C_A + 1)\rho A_I \dot{V}^n\right] + \frac{1}{2} C_D \rho A_D |V^n - \dot{r}^n|(V^n - \dot{r}^n) \quad (2.3)$$

In Eq. (2.3), V^n , $\dot{V}^n$ are velocity and acceleration vectors of fluid which are normal to the center line of the rod. The symbols $\dot{r}^n$, $\ddot{r}^n$ are velocity and acceleration vectors of rod element which are normal to the center line of the rod. Also, C_A, C_D, A_D, ρ represent added mass coefficient, drag coefficient, projected area of line, seawater density, respectively. The first term in (2.3) is to be moved to the left-hand side to be combined with line mass.

Through Eq. (2.1) ~ (2.3), the final equation of motion for rod element (Eq. (2.4)), can be derived as below.

$$m\ddot{r} + C_A\rho A_I\ddot{r}^n + (EIr'')'' + \left(\tilde{\lambda}r'\right)' = \tilde{w} + \tilde{F}^d \quad (2.4)$$

where m = mass per unit length of the rod element

$\tilde{\lambda} = \tilde{T} - EIk^2$

$\tilde{T}$ = effective tension of the rod element

k = local curvature of the rod element

$\tilde{w}$ = net weight of the rod element

$\tilde{F}^d = \left[(C_A + 1)\rho A_I\dot{V}^n\right] + \frac{1}{2}C_D\rho A_D|V^n - \dot{r}^n|(V^n - \dot{r}^n)$

The external dynamic loads are evaluated at instantaneous position of the lines at each time step. Once this final non-linear equation of motion is solved with respect to r and λ, the displacements and forces of the rod element can be found respectively. To solve the line dynamics in time, high-order FEM was used. The banded matrix for line dynamics is combined with the full matrix of 6DOF platform dynamics through proper connection conditions. The combined full-matrix equation is solved at each time step and the time-marching continues.

2.2.2 OrcaFlex

OrcaFlex [38] is a popular commercial program developed by Orcina. One of main differences between OrcaFlex and CHARM3D is the way to make the line element model. In OrcaFlex, lumped-mass elements are continuously connected by massless

springs/dampers at each node to represent axial, torsional, and bending properties of the line elements [38]. In addition, mass, net buoyancy, and drag forces for line elements can be inputted into each node/element. The distributed hydrodynamic load can be estimated in a similar way as presented in Eq. (2.5). In addition, the final equation of motion for line elements considers axial tension, buoyancy, gravity, torsion, and bending effects. In this study, torsion (or twisting) effect is not considered, as in CHARM3D modeling, since its effect is negligible for long mooring lines. The final dynamic behavior is to be solved from

$$\mathrm{M}(\mathrm{p},\mathrm{a}) + \mathrm{C}(\mathrm{p},\mathrm{v}) = \mathrm{F}(\mathrm{p},\mathrm{v},\mathrm{t}) - \mathrm{K}(\mathrm{p}) \tag{2.5}$$

where M = inertia load, C = damping load, K = stiffness load, p, v, a represent the position, velocity, and acceleration vectors, respectively, with t as time. To solve the equation of motion, implicit scheme (Generalized-α integration scheme) using constant time step is selected. More details about the program can be found in OrcaFlex manual.

2.3 Description of Target Model (Semi-Submersible)

As pointed out in the previous section, a generic drilling semi-submergible is taken as the target rig. 3D diffraction/radiation panel program (WAMIT) was used for the calculation of hydrodynamic coefficients (added mass, radiation damping, and first- & second-order wave forces) [39]. Since the semi-submersible model is symmetric with respect to X and Y axes, only 1 quadrant of the hull below mean water level (MWL) is discretized with 1308 quadrilateral elements. The configuration is shown in Figure 3. Convergence tests were performed with increasing panel numbers until reasonably good accuracy was obtained. In addition, Morison drag formula was applied to the columns and pontoons to

capture viscous cross-flow-drag effects on the hull. At each time step, the fully-coupled dynamic response of hull-mooring-riser system is solved from the combined matrix equation of the overall system.

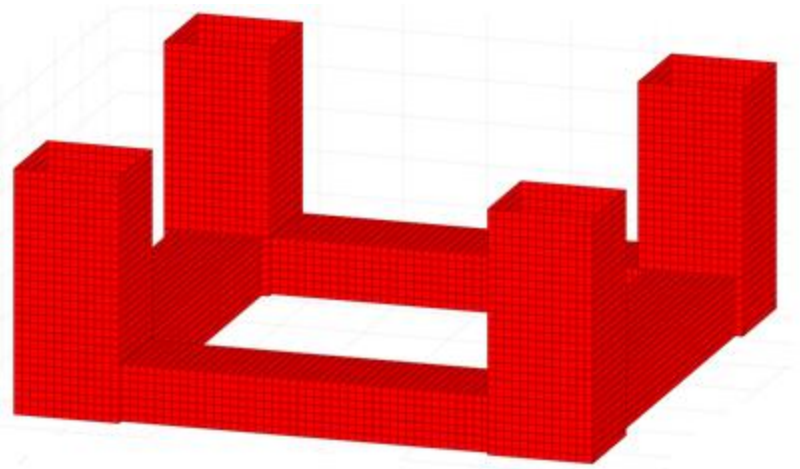

Figure 3 The configuration and numerical modelling of the generic semi-submersible, Reprinted with permission from [15]

Mooring lines and risers are also employed in the fully-coupled numerical model as shown in Figure 4. Twelve mooring lines form four groups at each corner with 5-degree intervals. Each mooring leg has chain-polyester rope-chain combination. The top portion of the chain mooring near fairlead is guided by 3.1m-long chain-hawse. At the outlet of the chain-hawse, the discontinuity of mooring chain is expected, where the bending-induced chain failure problem is the most seriously anticipated. In addition, four steel catenary risers (SCR) are considered in this study, as shown in Figure 4, and the water depth is 1,219 m. More detailed particulars of the hull are given in [40].

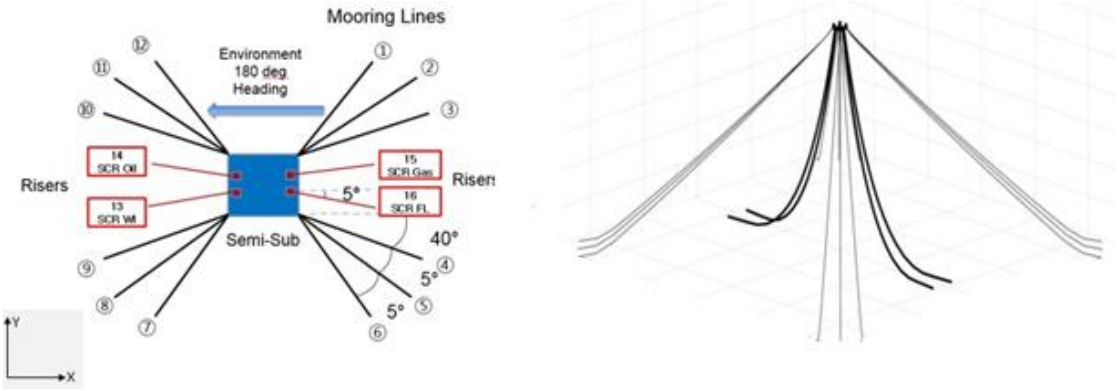

Figure 4 Arrangement of mooring lines and risers and direction of environmental heading, Reprinted with permission from [15]

The material properties of chain, polyester rope, risers, and chain-hawse used in this study are presented in Table 1 and Table 2. To analyze the OPB/IPB problems for chain mooring near fairlead, the detailed modeling of the fairlead and chain-hawse is very crucial. In this study, it is assumed that the chain-hawse is a circular steel tube with 10mm wall thickness that has a chain stopper at its outlet. The chain stopper holds the chains tightly inside. Each mooring line has one chain-hawse of 3.1m length at its top. Polyester rope is used between the top (near fairlead) chain blocks and bottom (near anchor) chain blocks. The chain-hawse is connected to the hull by freely-rotating pin-joint. Other connection conditions, such as friction-induced fixed B.C are also tested to consider floater-connection effect. The initial fairlead-anchor coordinates of lines are as shown in Table 3 along with their pretensions. Figure 5 and Figure 6 illustrate fairlead, chain-hawse, mooring line, and cross-section of chain-hawse.

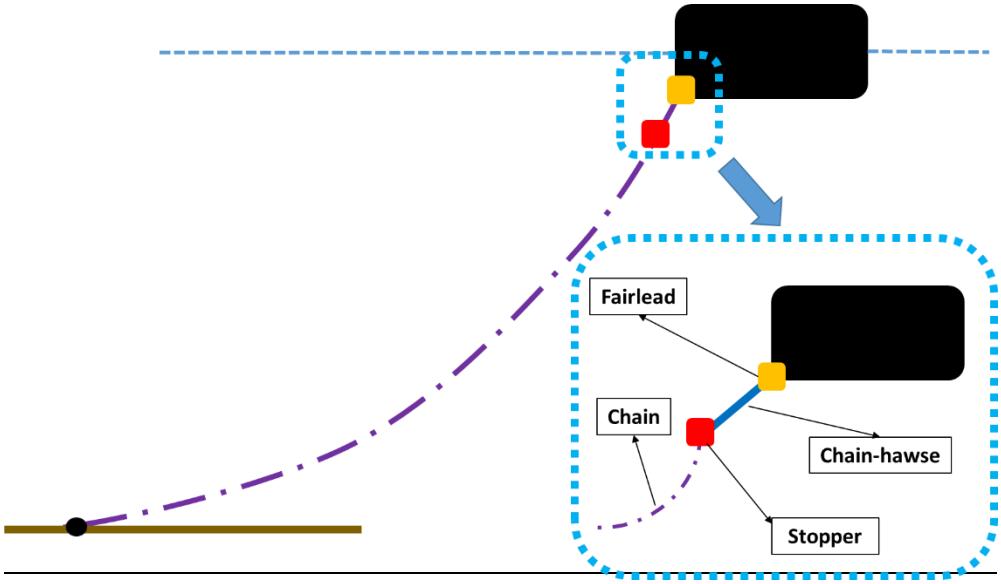

Figure 5 Modeling of chain-hawse and mooring line near fairlead, Reprinted with permission from [15]

Table 1 Mooring Material Properties, Reprinted with permission from [15]

Mooring Material Properties				
	Unit	Chain	Rope	Chain-hawse
Type	[-]	R3 Studless	Polyester	Circular Tube
Diameter	[mm]	147	220	290
Mass in Air	[kg/m]	430	39	499
Displaced Mass	[kg/m]	56	29.2	124
MBL(Min. Braking Load)	[kN]	14700	8250	14700
Axial Stiffness (EA)	[MN]	1845.4	52.76	1845.4
Bend Stiffness (EI)	[MN-m^2]	0	0	18.3
Drag coefficient	[-]	2.4	1.2	1.2

Table 2 SCR Material Properties, Reprinted with permission from [15]

SCR Material Properties					
	Unit	SCR_Oil	SCR_Gas	SCR_WI	SCR_FL
Diameter	[mm]	457.2	355.6	273.1	219.1
Mass in Air	[kg/m]	335.25	141.61	233.74	171.07
Displaced Mass	[kg/m]	186.95	39.79	173.7	132.43
Axial Stiffness (EA)	[MN]	5660	3390	4810	3740
Bend Stiffness (EI)	[MN-m^2]	135	49	36	17

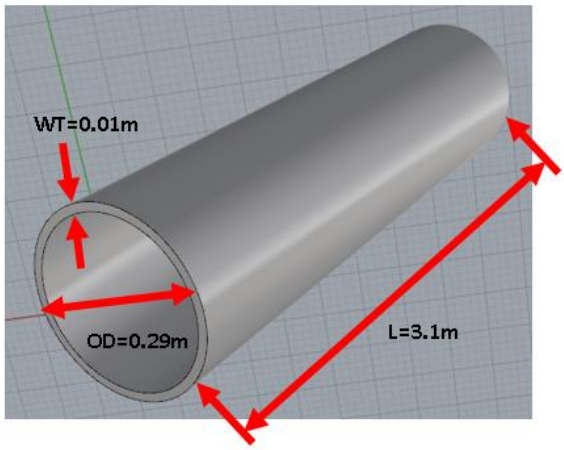

Figure 6 3D view of chain-hawse shape , Reprinted with permission from [15]

Table 3 Coordinates of the mooring lines and risers , Reprinted with permission from [15]

Kinds	Line No.	Fairlead Point			Anchor Point			Pre-Tension
		X	Y	Z	X	Y	Z	
		m	m	m	m	m	m	kN
Mooring Lines	1	34.44	31.25	-22.25	1122.22	1327.61	-1219.20	1993.9
	2	34.44	28.20	-22.25	1234.06	1224.82	-1219.20	1995.3
	3	34.44	25.15	-22.25	1330.80	1112.93	-1219.20	1996.5
	4	34.44	-25.15	-22.25	1330.80	-1112.93	-1219.20	1984.6
	5	34.44	-28.20	-22.25	1231.06	-1224.82	-1219.20	1982.1
	6	34.44	-31.25	-22.25	1122.22	-1327.61	-1219.20	1979.5
	7	-34.44	-31.25	-22.25	-1122.22	-1327.61	-1219.20	1923.5
	8	-34.44	-28.20	-22.25	-1231.06	-1224.82	-1219.20	1922.1
	9	-34.44	-25.15	-22.25	-1330.80	-1112.93	-1219.20	1920.8
	10	-34.44	25.15	-22.25	-1330.80	1112.93	-1219.20	1933.6
	11	-34.44	28.20	-22.25	-1231.06	1224.82	-1219.20	1936.3
	12	-34.44	31.25	-22.25	-1122.22	1327.61	-1219.20	1939.1
Risers	SCR_WI	-33.53	-5.00	-22.10	-962.82	-86.30	-1219.20	2572.6
	SCR_Oil	33.53	-5.00	-22.10	962.74	-86.30	-1219.20	2786.6
	SCR_Gas	33.53	5.00	-22.10	962.46	86.27	-1219.20	593.2
	SCR_FL	-33.53	5.00	-22.10	-962.61	26.28	-1219.20	1961.4

2.4 Time-Varying OPB/IPB Chain Interlink-Angle Assessment

Interlink angle measuring methodology in the fully-coupled global performance simulation [41] is shown in Figure 7. The definition of chain interlink angle in the fully-coupled global performance simulation is similar as that in high-fidelity non-linear FEM analysis. The relative angle of two adjoining vectors in the localized horizontal plane (xy plane) is the OPB chain interlink angle. Similarly, by changing the reference plane to the localized vertical plane (xz plane), IPB angle also can be measured. As shown in Figure 7, the end of chain-hawse where first free-to-rotate chain link which is prone to bending-induced failure is the target reference point. It can be measured at each time step during the hull-mooring-riser fully-coupled global performance simulation.

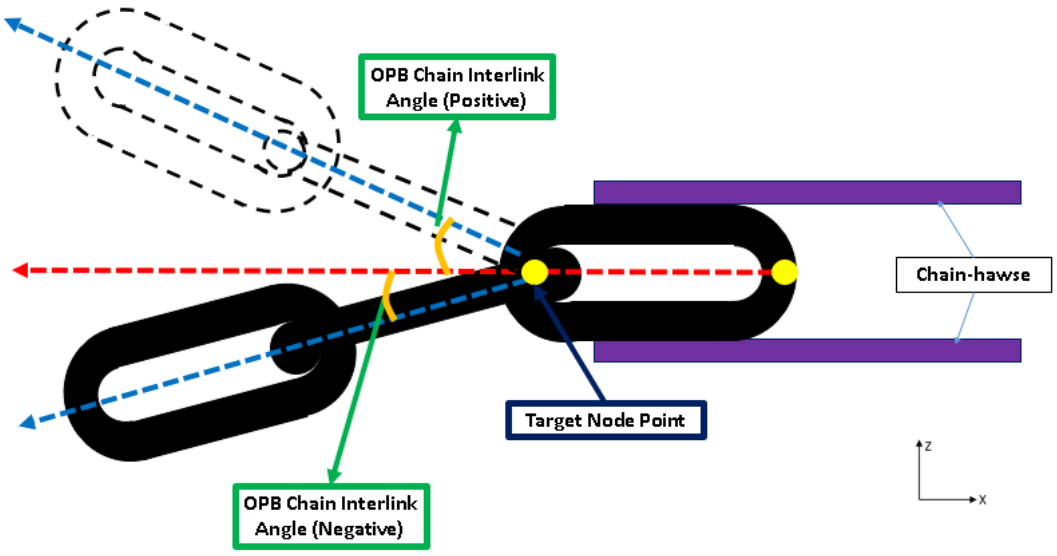

Figure 7 Definition of OPB Chain Interlink Angle – Global Performance Simulation, Reprinted with permission from [15]

OrcaFlex and CHARM3D are used to cross-check OPB/IPB chain-mooring interlink-angle calculations in time-domain global-performance analysis as described in the previous section. To maintain consistency, the fully-coupled platform motions with risers and mooring lines are first simulated for the given environmental conditions by CHARM3D. The motion of a target fairlead point is recorded in time. Then, the same target mooring line is also modeled by OrcaFlex and its dynamics for the prescribed fairlead motion is simulated under the given environmental condition.

First, both cases are simulated under the same regular head-wave condition (H=5m, T=10s, Heading =180^{o}). The 6DOF vessel motions under the given wave condition are presented in Figure 8. As expected in head waves, sway-roll-yaw motions are very small compared to surge-heave-pitch motions due to the hull-mooring geometric symmetry. However, the riser arrangement and its pretension are asymmetric with respect to the x-axis causing small non-zero mean values for the horizontal-plane motions.

To evaluate the local vectors (directional-cosine) of mooring lines near the target point (the discontinuity caused by the chain-hawse), a post-process using 3 neighboring nodal displacements was devised for OrcaFlex because OrcaFlex does not compute them directly. In case of CHARM3D, the local vectors (directional-cosine) for each node are directly outputted. In the post-process, the interval between each point near the target node is 0.9 m. To observe the effects of chain-hawse on OPB/IPB interlink angles, the chain mooring lines with and without the chain-hawse were identically modeled and the results are compared. In the case of with chain-hawse, it is assumed that the chain-mooring inside chain-hawse moves with chain-hawse due to the stopper inside. In the initial chain-

mooring global-performance simulation, it is also assumed that the bending stiffness of the chain-mooring can be neglected, which is actually true for the entire length of long chain-mooring.

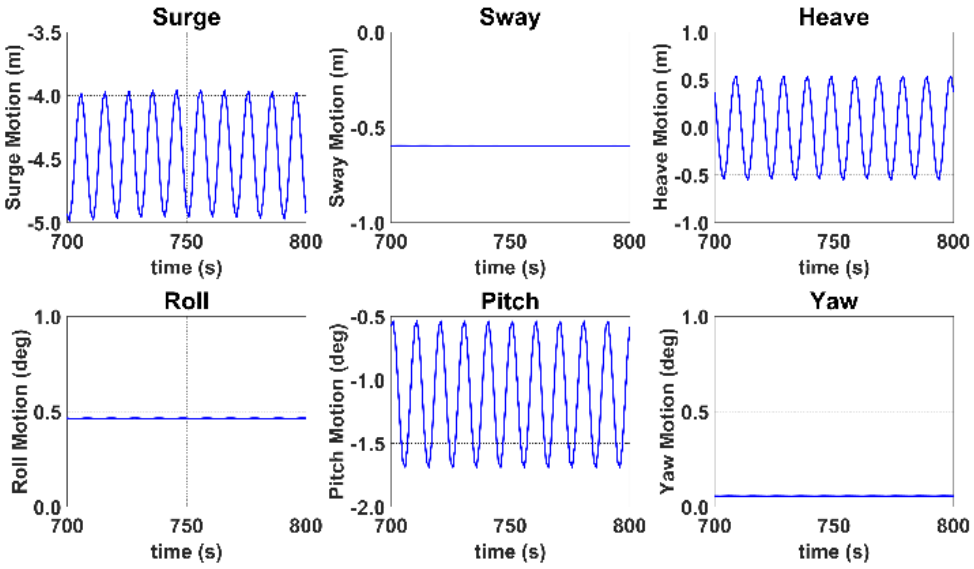

Figure 8 6DOF Platform Motion Time History in Regular Wave (H=5m, T=10s, Heading =180º) , Reprinted with permission from [15]

Figure 9 shows the results of OPB/IPB chain-interlink angles at the target point by OrcaFlex and CHARM3D without chain-hawse. It is confirmed that both results are matched well. We can also see that OPB/IPB chain interlink angles without chain-hawse are typically very small because there is no abrupt line discontinuity. It means that OPB/IPB-induced failure hardly occurs along the continuous chain mooring line without sudden connections or restrictions. With the chain-hawse, the interlink angles are significantly increased. Therefore, from this point on, only the case with chain-hawse will be considered.

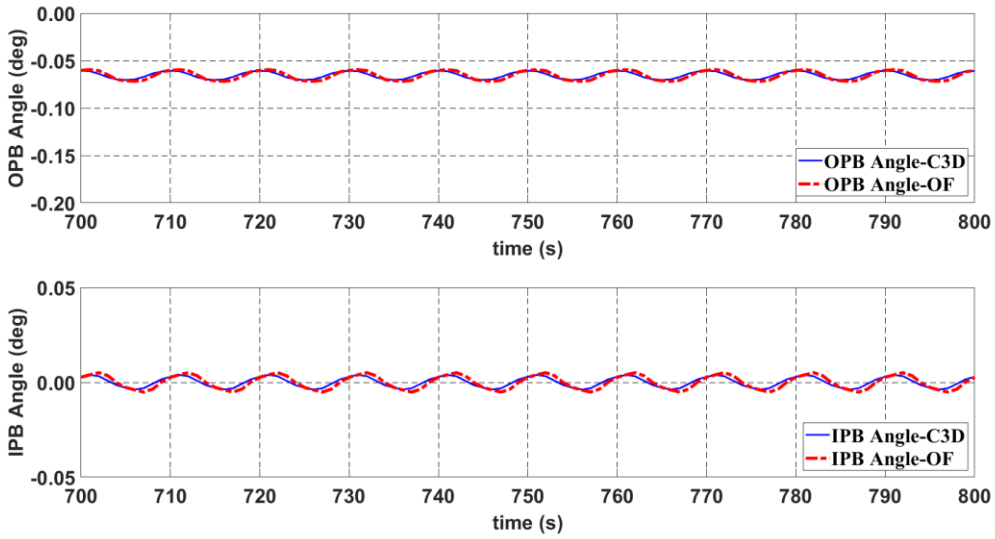

Figure 9 Comparison of OPB(Up) / IPB(Down) chain-interlink angles without chain-hawse by CHARM3D (C3D) vs. OrcaFlex (OF), ML09: Regular Wave (H=5m, T=10s, Heading =180º) , Reprinted with permission from [15]

For comparison, Figure 10 shows the interlink-angle results at the target point after including chain-hawse. Compared to Figure 9, the OPB chain interlink angles at the target point are significantly increased. Both CHARM3D and OrcaFlex show the same trend. In this case, the IPB interlink angles are very small as expected. The two computer programs produce almost identical results for OPB/IPB chain-interlink angles when conventional approach is used. When considering time-varying interlink bending stiffness approach is used, only CHARM3D can produce the results. Therefore, from this point on, only the CHARM3D results will be presented for various case studies.

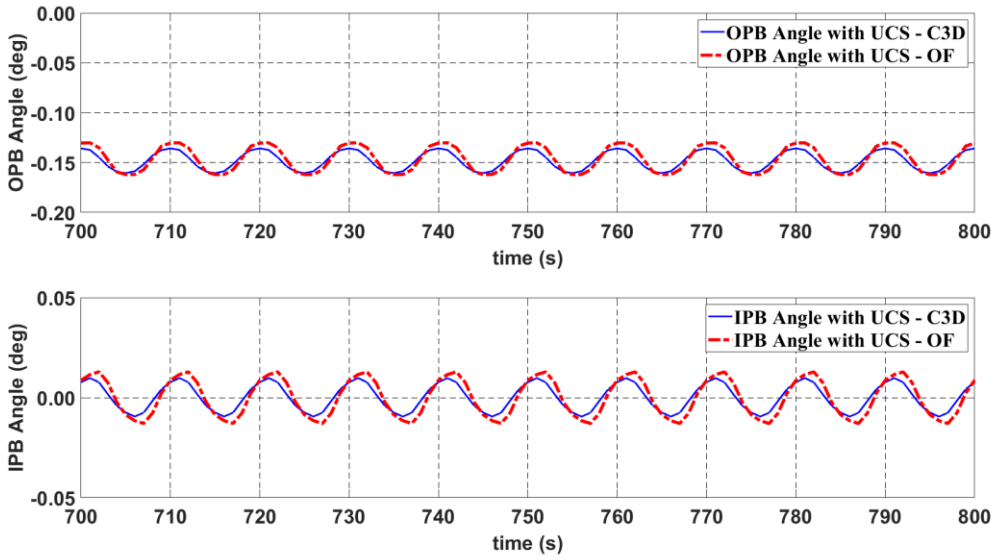

Figure 10 Comparison of OPB(Up) / IPB(Down) chain-interlink angles with chain-hawse by CHARM3D (C3D) vs. OrcaFlex (OF), ML09: Regular Wave (H=5m, T=10s, Heading =180º) , Reprinted with permission from [15]

2.5 Chain Interlink-Angle Variation among Mooring Lines

Figure 11, Figure 12 and Figure 13 plot OPB/IPB chain interlink angles of all mooring lines at the target point with chain-hawse under the same regular-wave condition (H=5m, T=10s, Heading =180deg). It is clearly seen that the variations of interlink angles for lee-side slack lines (ML07~12) are greater than those of taut-side lines (ML01~06). Table 4 shows the initial equilibrium position of the platform before any environmental loads are applied. The platform has small negative (downstream) mean surge-offset and mean pitch angle due to the non-symmetric riser pre-tensions. The mean pitch angle and downstream surge mean offset cause the downstream mooring lines slack, which results in larger dynamic interlink angles. Whereas, there are little differences in IPB interlink angles among the mooring lines. Actually, the bending-induced failure of chain is related to both

tension and interlink angle, as shown in Figure 2. For slack-side lines, interlink angles are larger but tensions are smaller compared to those of taut-side lines. As shown in Figure 11 and Figure 13, ML03 is the most critical line in terms of tension and ML 09 is the most critical line in terms of OPB/IPB interlink angles. Usually, IPB interlink angles play much less role for failure. From this point on, only the ML03, 09 OPB interlink angles will be tracked.

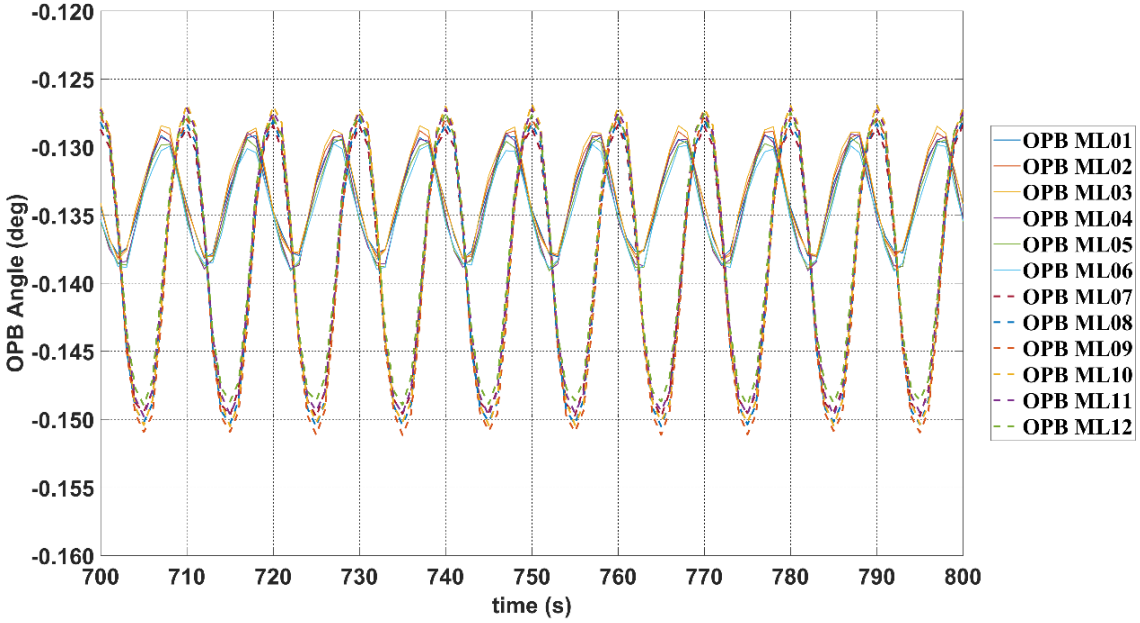

Figure 11 OPB Interlink Angles for All Mooring Lines, Reprinted with permission from [15]

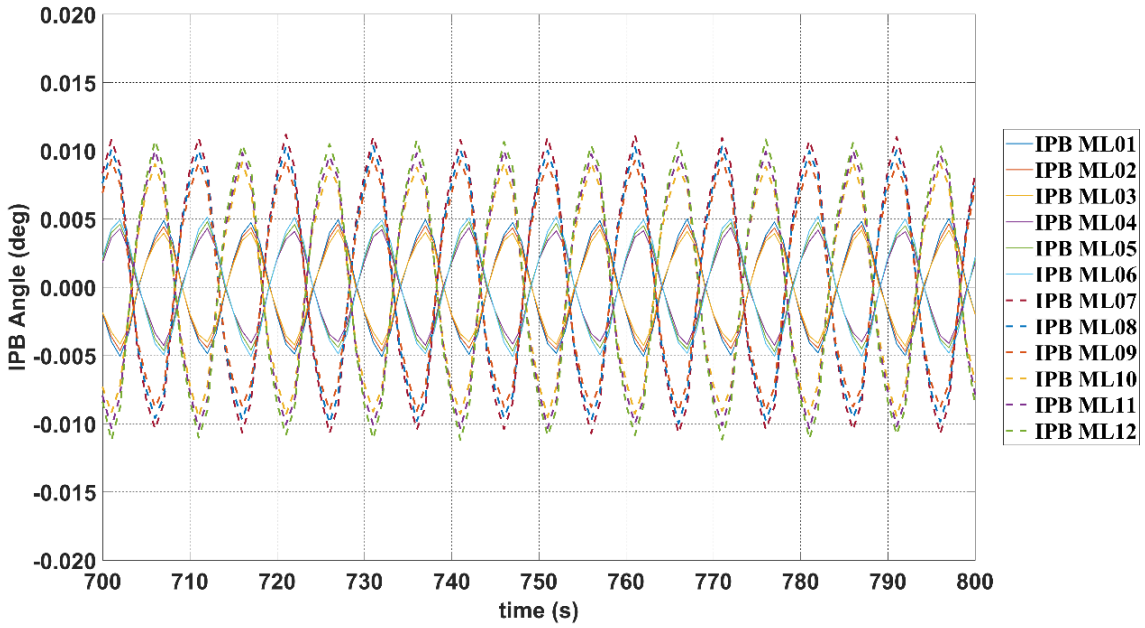

Figure 12 IPB Interlink Angles for All Mooring Lines, Reprinted with permission from [15]

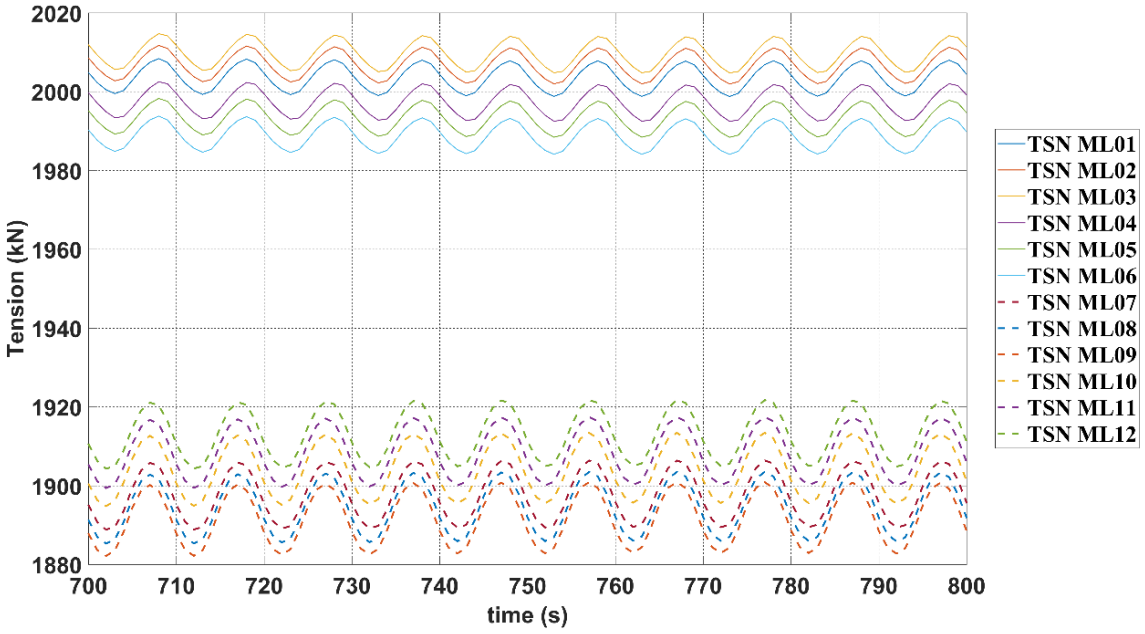

Figure 13 Tensions for All Mooring Lines, Reprinted with permission from [15]

Table 4 Platform Initial Position without environmental loadings, Reprinted with permission from [15]

Surge	Sway	Heave	Roll	Pitch	Yaw
m	m	m	deg	deg	deg
-2.67	-0.61	-0.04	0.47	-1.09	0.05

The above argument “slacker lines tend to have larger OPB interlink angles” can further be supported by showing the trend of dynamic interlink angles of the ML03 and ML09 line with increasing the initial pretension, as presented in Figure 14. With increasing the line pre-tension, both mean and dynamic interlink angles are decreased, while there is virtually no difference in IPB angles.

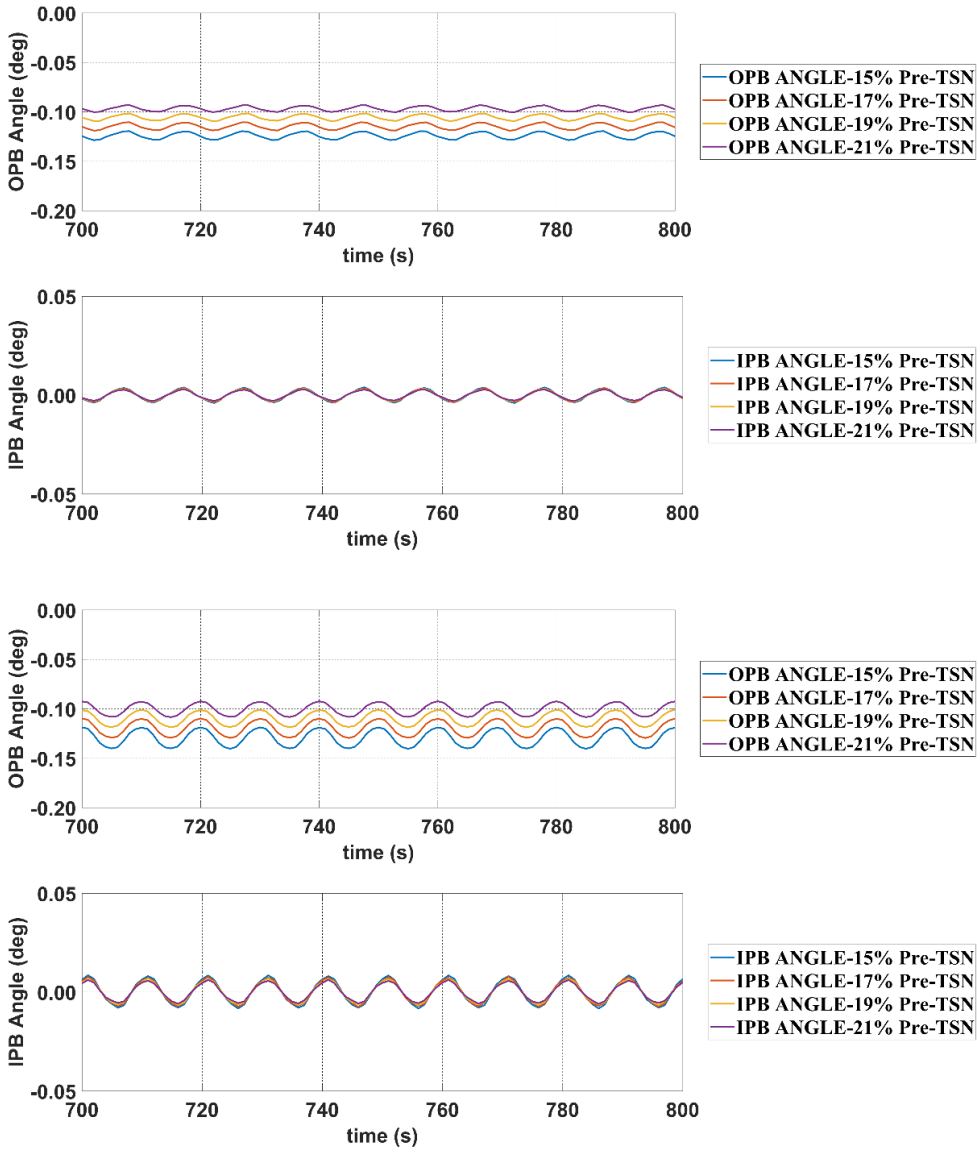

Figure 14 OPB/IPB angles for ML03 (Up), ML09 (Down) for various initial pre-tensions (with chain-hawse): Regular Wave (H=5m, T=10s, Heading =180º) , Reprinted with permission from [15]

2.6 Coupled Analysis between Low-Fidelity and High-Fidelity Analysis

Figure 15 represents flow chart for the multi-scale approach with the simultaneous use of high- and low-fidelity models with time-varying chain interlink bending stiffness and the 3D picture for pre-calculated chain interlink bending stiffness as function of tension and interlink angle in the expected range of variations. At each time increment, the interlink angle and tension at the target point, which is at the chain-hawse outlet in this research, can be computed. Those results can be used as the inputs to high-fidelity (local-FEM) analysis to obtain the corresponding interlink bending stiffness. Then, the new interlink bending stiffness that was read from Figure 15 is to be inputted to the low-fidelity global simulation by CHARM3D software. By using this mutually interfaced time-stepping procedure, the non-linear and time-varying nature of chain interlink bending stiffness can be considered in the time-domain simulation.

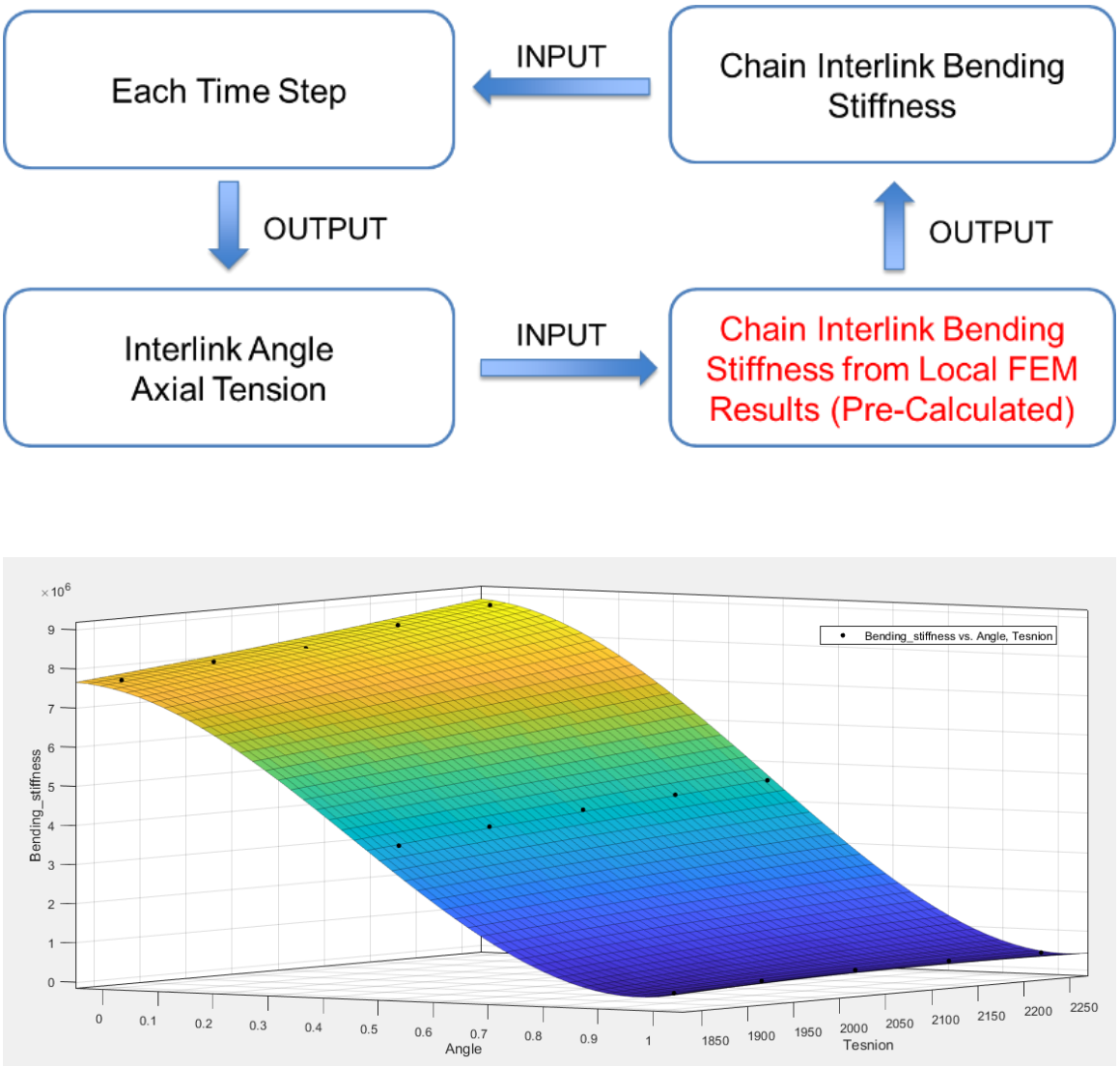

Figure 15 Consideration of Time-varying Chain Interlink Bending Stiffness and 3D Picture from FEA (Pre-Calculated with friction coefficient=0.7), Reprinted with permission from [15]

2.7 Effects of Time-varying Interlink Bending Stiffness

2.7.1 Case 1: Frictionless hinged fairlead connection B.C

As mentioned previously, the accurate modelling of fairlead portion of chain mooring in low-fidelity global-system simulation and analysis can be critical to assess the resulting OPB-induced fatigue damage. To increase the modelling accuracy, the time-varying interlink bending stiffness can be employed. It is a function of time-varying tension and interlink angle (Figure 15). The friction-induced interlink bending stiffness can be pre-estimated by high-fidelity nonlinear-FEM program for various combinations of tensions and interlink angles. Then, the proper value at each time step can be selected from the pre-calculated table and inputted to the time-marching process of the global simulation program.

A typical irregular wave condition is applied as an example, as shown in Table 5. Similar fatigue estimations can be continued for a series of sea conditions. In random waves, slowly-varying surge vessel motions occur due to second-order difference frequency wave loadings, which is accounted for through Newman's methodology [39]. Steady shear currents and dynamic winds are also included in the present simulation as shown in Table 5. JONSWAP wave spectrum (Figure 16) and API wind spectrum are employed to generate random waves and winds.

Figure 17 and Figure 18 show OPB angle time history and power spectral density (PSD) comparisons between conventional approach (basic: zero interlink bending stiffness) and present approach (time-varying interlink bending stiffness) under frictionless hinged fairlead connection B.C for ML03 and 09 lines. By considering time-varying interlink

bending stiffness effect, both mean (about 6.4% and 6.2% for ML03 and 09) and dynamic interlink angles are slightly decreased (about 20% and 13% for ML03 and 09) at wave frequency region. The interlink-angle variation of taut mooring line (=ML03) is much smaller than that of slack mooring line (=ML09), as already evidenced in Figure 14. If the floater-connection B.C is changed to fixed B.C, the trend can be different, which is to be discussed in the next section.

Tension comparisons are also given in Figure 19 and Figure 20 for ML03 and ML09. The effect of time-varying interlink bending stiffness on dynamic tension is generally small although there is appreciable difference at the peak near 0.05 rad/s. The peak is associated with slowly-varying surge responses of the semisubmersible in irregular waves [40]. The difference in mean tension between the taut and slack lines is clearly seen as expected. In the wave-frequency region, the tension variation at slack mooring line (=ML09) is slightly higher than that of taut mooring line (=ML03).

The corresponding bending moments for both mooring lines are presented in Figure 21 and Figure 22. While we use zero interlink bending stiffness in the global mooring dynamics, the bending moment is calculated from the local FE analysis based on the calculated dynamic tension and interlink angles at each time. Similar trends can be observed between the basic and time-varying interlink bending stiffness cases in both time histories and spectra. The time-varying interlink bending stiffness case gives slightly smaller values in both time histories and spectra, which means that the present, more rigorous approach is not supposed to significantly influence the fatigue-damage estimation. The trends of bending moment results are similar to those of interlink angles

(Figure 17 and Figure 18). The mean value of bending moment, as a function of mean tension and interlink angle, is slightly reduced for both mooring lines if the time-varying interlink bending stiffness is considered. Judging from the bending-moment results, taut lines (ML03) are less vulnerable to accumulated fatigue damage than slack lines (ML09). In Figure 21 and Figure 22, it is of interest to notice the presence of bending moment at higher frequencies than input wave frequencies, which is related to mooring-line dynamics. Although their magnitudes are not large, the high-frequency bending moments can play a role in fatigue damage due to higher number of cycles.

Figure 23 shows the time histories of time-varying interlink bending stiffness at the chain-hawse outlet for both mooring lines. Taut line (=ML03) has larger mean value than slack line (=ML09) because of larger mean tension. The bending stiffness definition is a function of tension and interlink angle, as shown in Figure 15. As for the variation of bending stiffness values with time, slack lines have larger values.

Floater motions are little affected by the basic or time-varying interlink bending stiffness modeling, as shown in Figure 24. Due to the head sea condition, only surge, heave, and pitch are presented. Their natural frequencies are 0.05 rad/s, 0.6 rad/s, 0.18 rad/s, respectively. The pitch response spectrum shows peaks at such three natural frequencies due to mode coupling.

Table 5 Environmental Condition, Reprinted with permission from [15]

Wave				Current		Wind		
Gamma	Direction from TN	Significant Wave (Hs)	Spectral Period (Tp)	Depth	Vel.	Spectrum	10 min@+10m elevation	Direction from TN
(-)	(deg)	(m)	(s)	(m)	(m/s)	(-)	(m/s)	(deg)
2.2	Omni	5.5	10.1 (0.62 rad/s)	0	0.5	API	19.9	Omni
				63	0.375			
				126	0			
				mud	0			

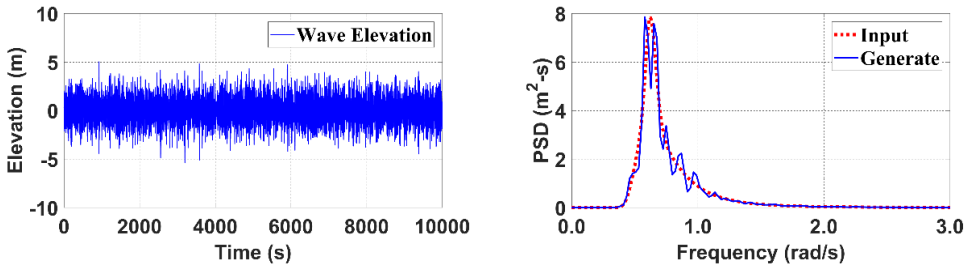

Figure 16 Incident Wave Elevation Time History and Spectrum (Input vs Regenerated) , Reprinted with permission from [15]

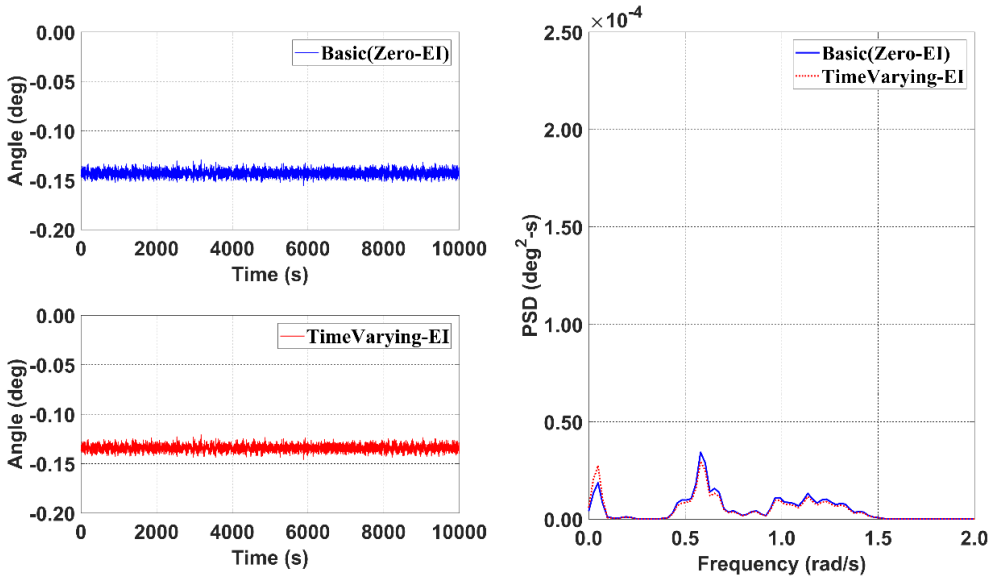

Figure 17 OPB interlink angles comparison for ML03 (taut), Basic VS Time-Varying Interlink Bending Stiffness - Frictionless Hinged BC , Reprinted with permission from [15]

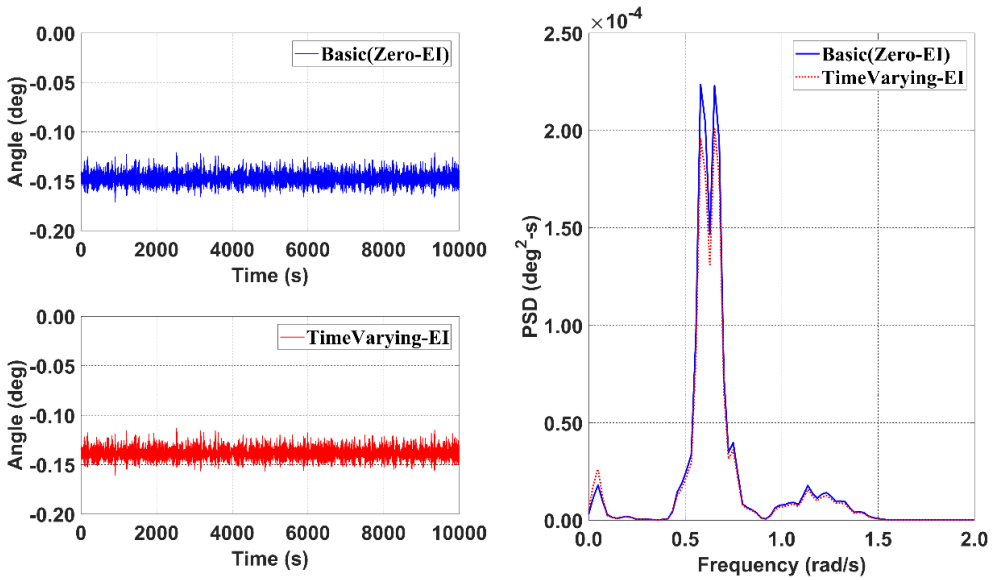

Figure 18 OPB interlink angles comparison for ML09 (slack), Basic VS Time-Varying Interlink Bending Stiffness - Frictionless Hinged BC, Reprinted with permission from [15]

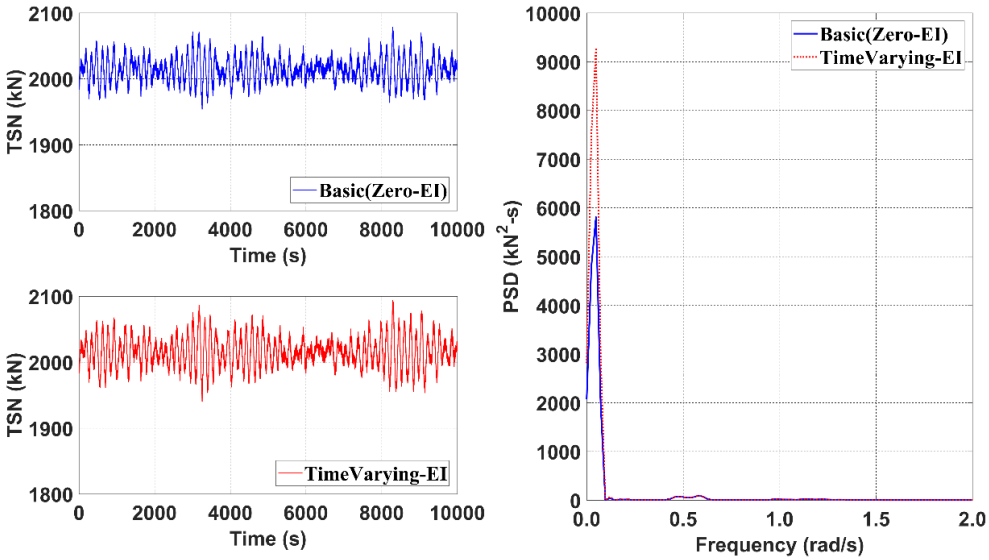

Figure 19 Tension comparison for ML03 (taut), Basic VS Time-Varying Interlink Bending Stiffness - Frictionless Hinged BC, Reprinted with permission from [15]

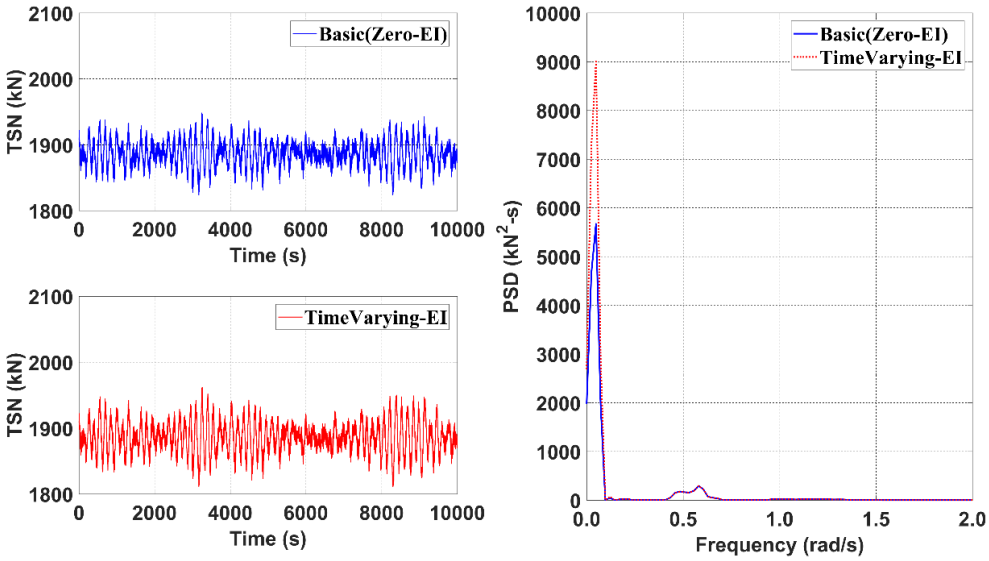

Figure 20 Tension comparison for ML09 (slack), Basic VS Time-Varying Interlink Bending Stiffness - Frictionless Hinged BC, Reprinted with permission from [15]

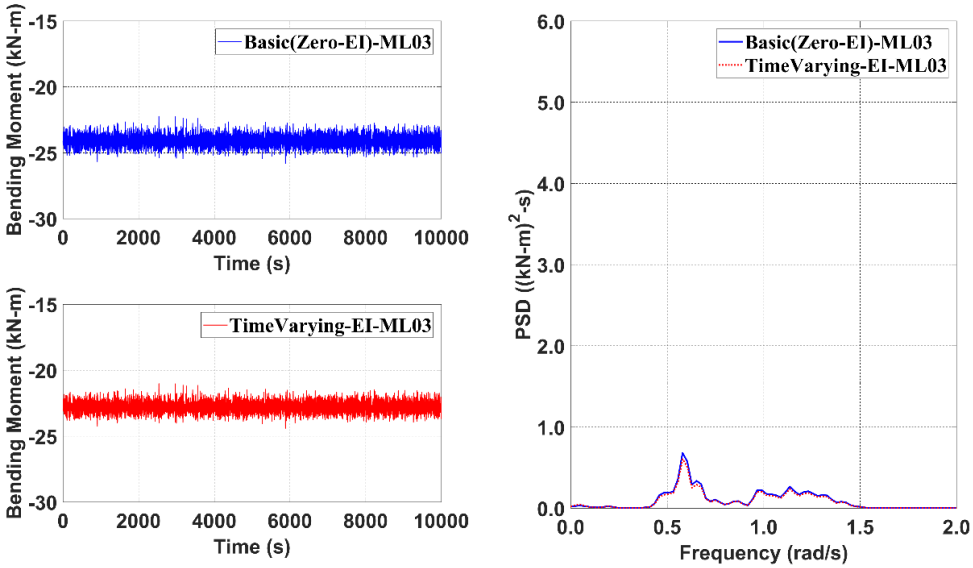

Figure 21 Bending Moment comparison for ML03 (taut), Basic VS Time-Varying Interlink Bending Moment - Frictionless Hinged BC, Reprinted with permission from [15]

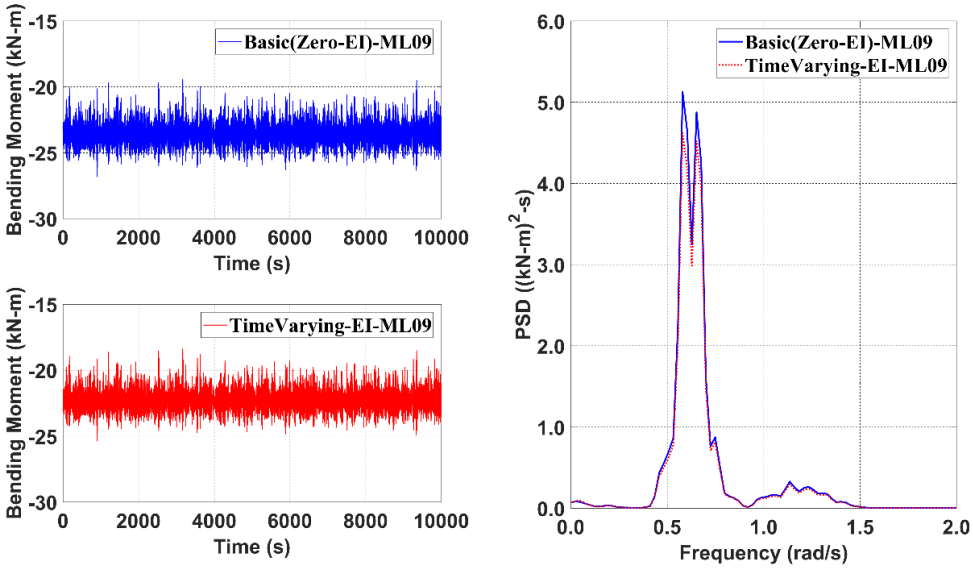

Figure 22 Bending Moment comparison for ML09 (slack), Basic VS Time-Varying Interlink Bending Moment - Frictionless Hinged BC, Reprinted with permission from [15]

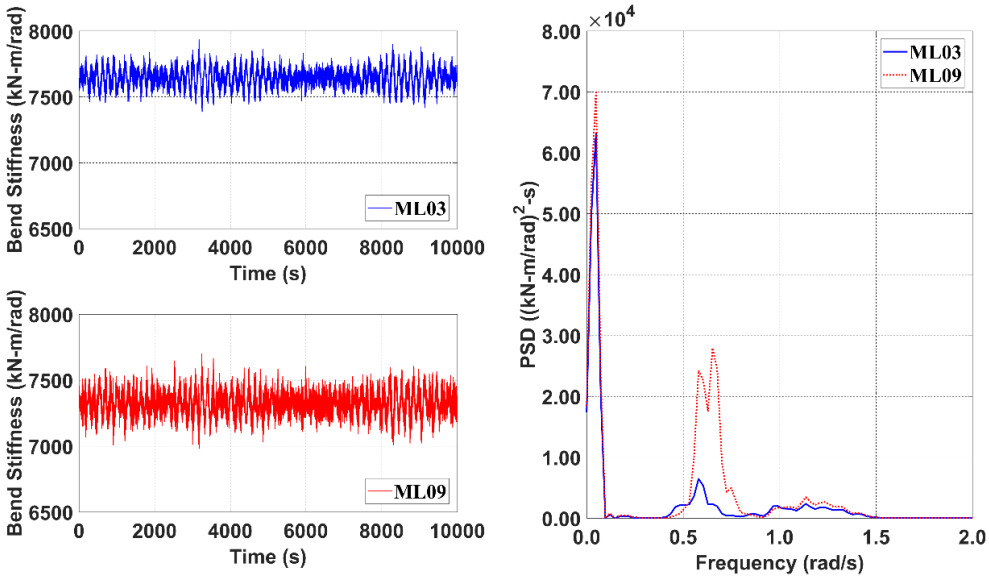

Figure 23 Interlink Bending Stiffness Time History for ML03 (taut), ML09 (slack) - Frictionless Hinged BC, Reprinted with permission from [15]

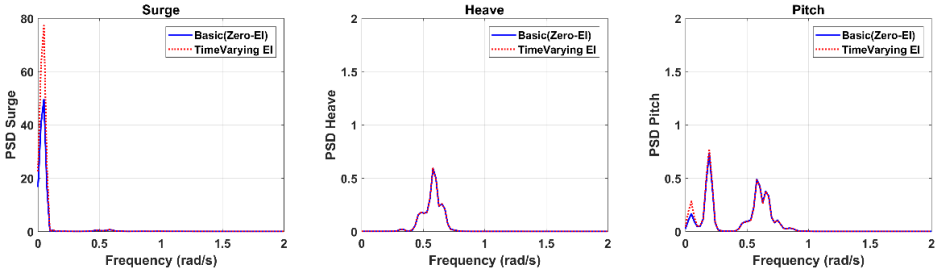

Figure 24 Comparison: Surge-heave-pitch Motion PSD, Basic vs Time-Varying Interlink Bending Stiffness - Hinged fairlead connection , Reprinted with permission from [15]

2.7.2 Case 2: Fixed fairlead connection B.C.

In this section, the effect of different fairlead connection (fixed B.C) is investigated. Practicing engineers suggest that the fairlead connection to platforms can be more restrictive than frictionless pin-joint due to increased friction by marine growth or corrosion during operation [12, 14]. It may cause additional external bending effect on chains near underwater chain-stopper to significantly increase the OPB-induced fatigue damage. Therefore, to see the effect of restriction at the fairlead connection as another extreme, fixed B.C is adopted in this section. The case of fairlead connection through a chain-wheel without using movable chain-hawse is close to this fixed BC. The increased restriction between hull and chain-hawse connection by marine growth and corrosion should be between the two extreme cases. In a sequel research, a sophisticated numerical modeling of fairlead connection considering friction and breakout angle effect is to be detailed.

Figure 25 and Figure 26 show OPB-interlink-angle comparisons between basic (zero interlink bending stiffness) and time-varying interlink bending stiffness for ML03 and ML09 under fixed fairlead connection B.C. Compared to the previous frictionless hinged connection, the variations of interlink angles are significantly increased for both mooring lines. This is expected since the chain-hawse in this case moves with the platform to have larger relative angles against mooring lines. On the other hand, the mean angles are decreased especially at taut side since the chain-hawse angle is initially aligned with the mooring line. On the contrary to the previous case, the variations of interlink angles at taut side are generally greater than those at slack side, which means that the taut-side mooring

is more vulnerable to OPB-induced failure. Taut mooring system is more affected by floater motion than slack mooring system.

Figure 27 and Figure 28 show tension comparisons for both mooring lines (=ML03 and ML09). The results are very similar to those of Figure 19 and Figure 20. This means that the mooring tension is little affected by the change of fairlead connection.

Figure 29 and Figure 30 show bending moment comparisons between basic and time-varying interlink bending stiffness cases for both mooring lines (=ML03, ML09). The dynamic bending moments are significantly increased after fixing the fairlead connection, which is consistent with the witness of practicing engineers during the past two decades. Interestingly, the dynamic bending moment at taut side is significantly larger than that at slack side, which is opposite to the previous trend of frictionless fairlead connection (Figure 21 and Figure 22).

In addition, in this case, the results of constant-interlink-bend-stiffness in the global simulation are added in the spectrum plot of Figure 30-31. The average value of bending stiffness was used in the new case (ML03, ML09 = 8.68E+06 kN-m/rad, 7.75E+06 kN-m/rad). The resulting spectra are closer to the time-varying-EI curves when frequency>0.3 rad/s and the opposite is true otherwise.

The time-varying interlink bending stiffness with fixed fairlead connection is given in Figure 31 for both mooring lines. It is seen that both the mean values and time variations of bending stiffness are significantly increased compared to the previous frictionless fairlead connection (Figure 23). Similar to the previous case (Figure 23), the bending stiffness variation of slack-side mooring is larger than that of taut-side mooring.

Figure 32 shows the surge-heave-pitch response spectra for the surface platform. As compared to Figure 24, there is no apparent change, which means that the platform motion is little affected by the fairlead joint condition of chain-hawse.

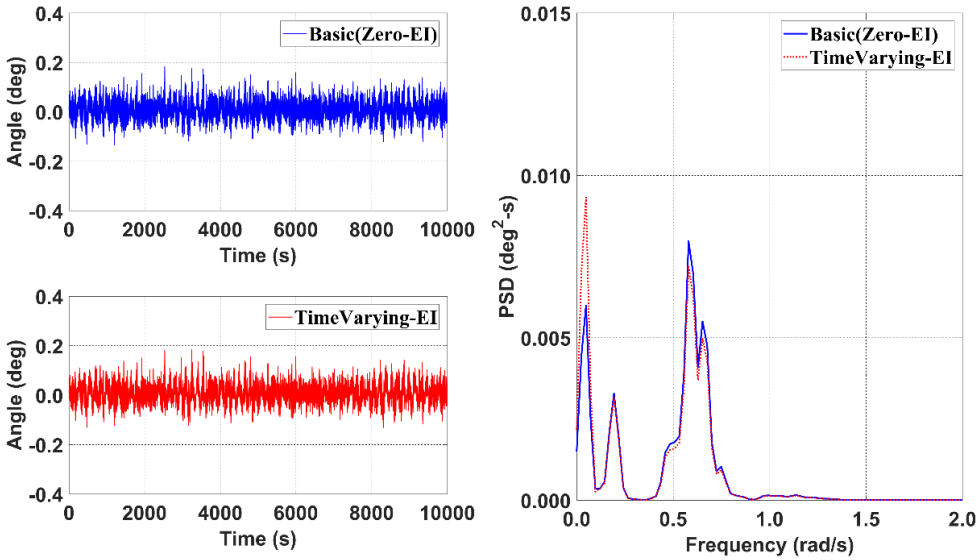

Figure 25 OPB interlink angles comparison for ML03 (taut), Basic VS Time-Varying Interlink Bending Stiffness - Fixed BC, Reprinted with permission from [15]

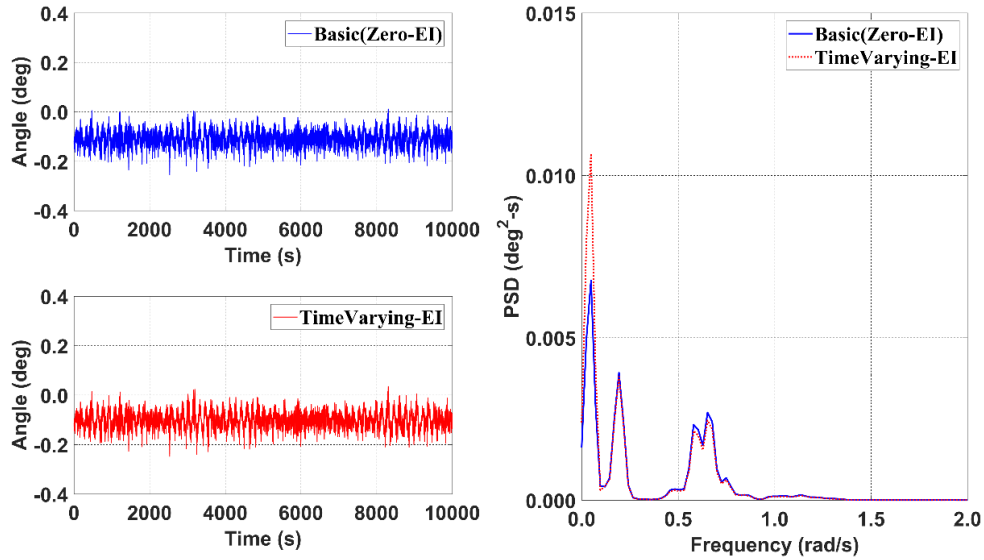

Figure 26 OPB interlink angles comparison for ML09 (slack), Basic VS Time-Varying Interlink Bending Stiffness - Fixed BC, Reprinted with permission from [15]

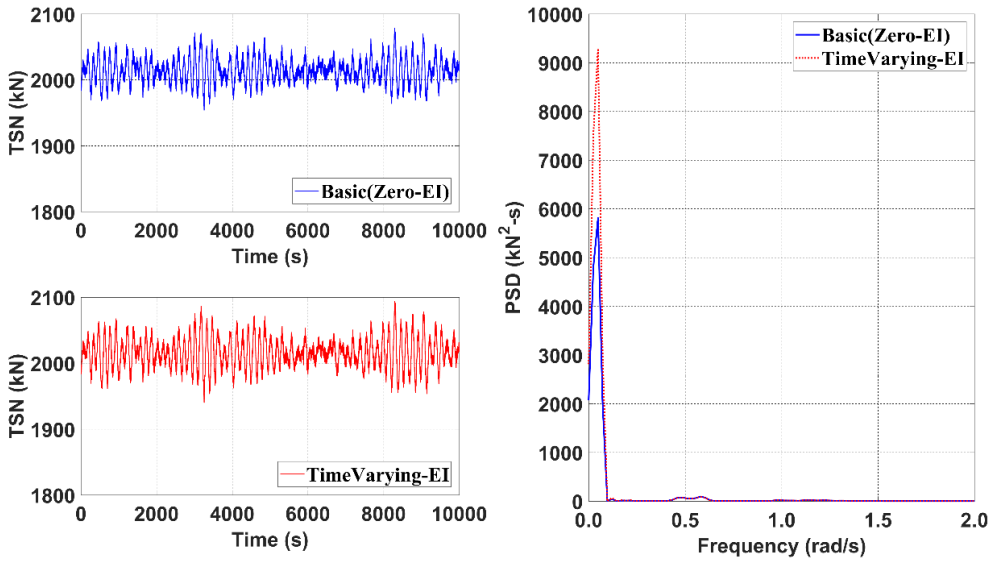

Figure 27 Tension comparison for ML03 (taut), Basic VS Time-Varying Interlink Bending Stiffness - Fixed BC, Reprinted with permission from [15]

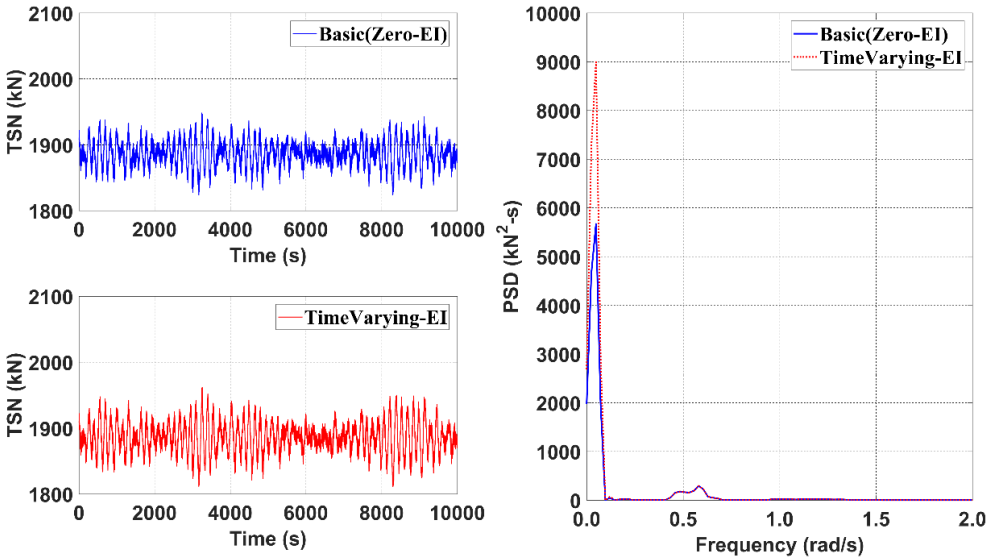

Figure 28 Tension comparison for ML09 (slack), Basic VS Time-Varying Interlink Bending Stiffness –Fixed BC, Reprinted with permission from [15]

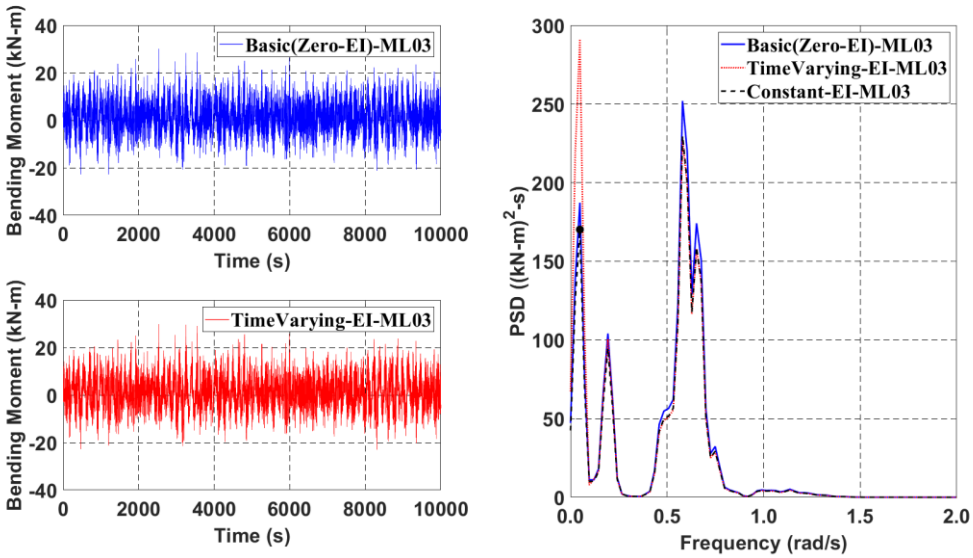

Figure 29 Bending Moment comparison for ML03 (taut), Basic vs Time-Varying Interlink Bending Stiffness vs Constant Interlink Bending Stiffness – Fixed BC, Reprinted with permission from [15]

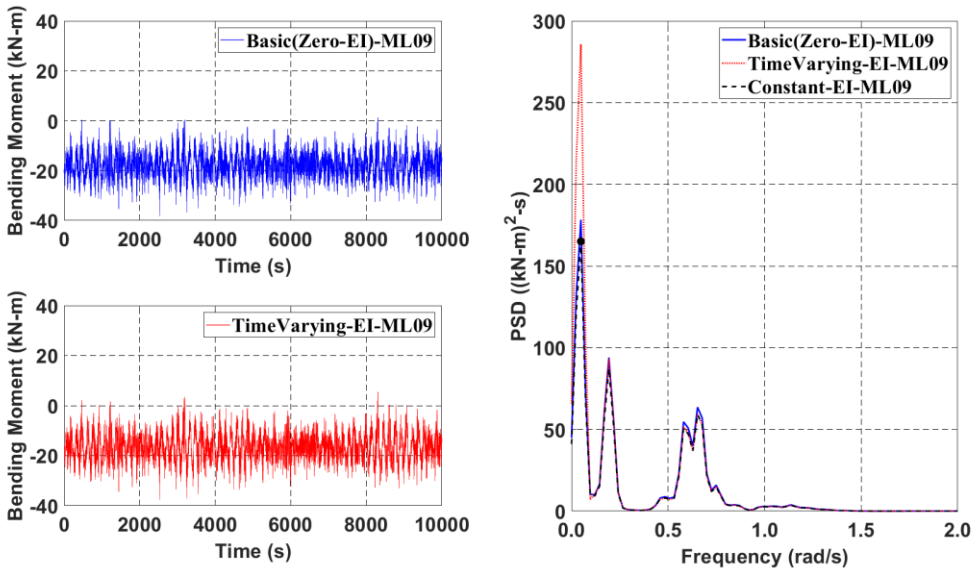

Figure 30 Bending Moment comparison for ML09 (slack), Basic vs Time-Varying Interlink Bending Stiffness vs Constant Interlink Bending Stiffness – Fixed BC, Reprinted with permission from [15]

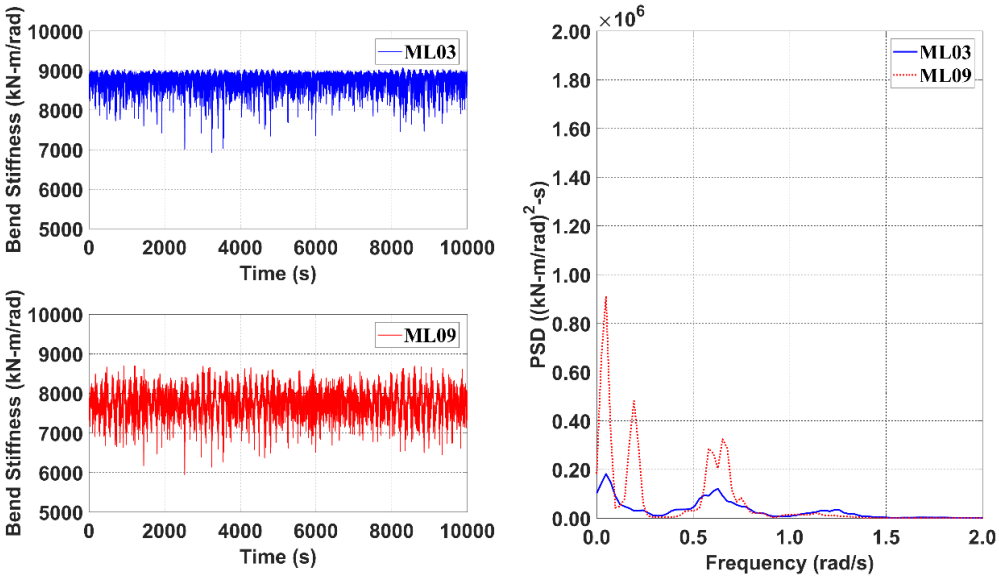

Figure 31 Interlink Bending Stiffness Time History for ML03 (taut), ML09 (slack) - Fixed BC, Reprinted with permission from [15]

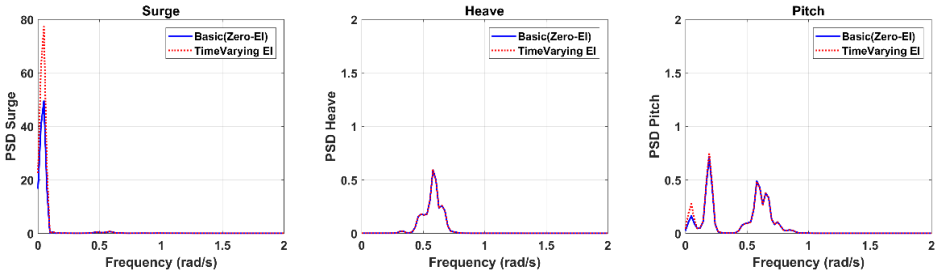

Figure 32 Comparison: Surge-heave-pitch Motion PSD, Basic vs Time-Varying Interlink Bending Stiffness - Fixed fairlead connection, Reprinted with permission from [15]

2.8 Comparisons of Short-term Fatigue Damage

2.8.1 Hotspot Location

As previously explained, many researchers investigated hotspot locations of chain links [3, 10]. In this research, only short-term fatigue during storm duration (3 hours) is considered. The present calculations for the areas of maximum stress are also consistent with those references. Based on those, four points are selected as hotspot locations, as shown in Figure 33. At each hotspot location, maximum principle stress can be estimated to generate the corresponding stress concentrate factor (SCF). Since non-linear FE is used with the sequential loading procedure, as given in Figure 1, residual stresses are also included in the SCF calculation. The accumulated fatigue damage with/without the residual stresses were calculated and compared. Once SCF is pre-calculated as function of tensions and interlink angles, the total stress time history can be generated by using eq.2.6 with low-fidelity global-analysis results. Figure 34 shows the general procedure of fatigue damage calculation. After the total stress time history at each hotspot location is generated, Gerber mean stress correction model is applied as shown in eq. 2.7. Then, stress range-cycle histogram is made by rain-flow counting method which is widely adapted. Finally, fatigue damage index (or accumulated damage) can be calculated using S-N curve and Palmgen-Miner's accumulative fatigue damage rule (eq. 2.8). In this study, ABS-FC (Free Corrosion) curve is used as S-N curve to estimate cumulative fatigue damage.

$$\sigma_{Total}(t) = SCF_{TT+OPB}(T(t), \alpha(t)) \cdot \frac{T(t)}{2A} \tag{2.6}$$

T = tension, A = chain section area, α = OPB interlink angle

Gerber model: $\frac{\sigma_a}{\sigma_e^{'}} + \left(\frac{\sigma_m}{\sigma_u}\right)^2 = 1$ (2.7)

where, σ_m, σ_u = mean stress and tensile strength, respectively

σ_a = stress amplitude

$\sigma_e^{'}$ = effective alternating stress at failure for a lifetime of N cycles

Damage Index $D = \sum_{i=1}^{k} \frac{n_i}{N_i}$ (2.8)

where, n_i = the number of cycles of the (effective) stress range

N_i = the ultimate number of cycles of the (effective) stress range before fatigue failure

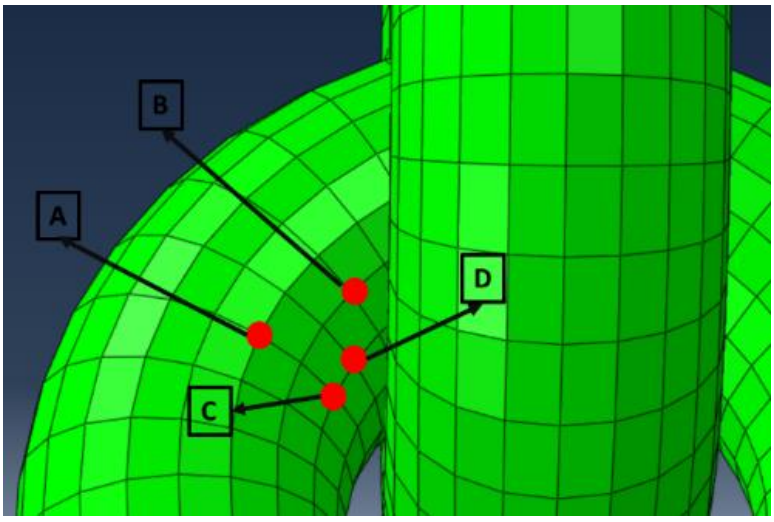

Figure 33 Hotspot locations from Local FEM model, Reprinted with permission from [15]

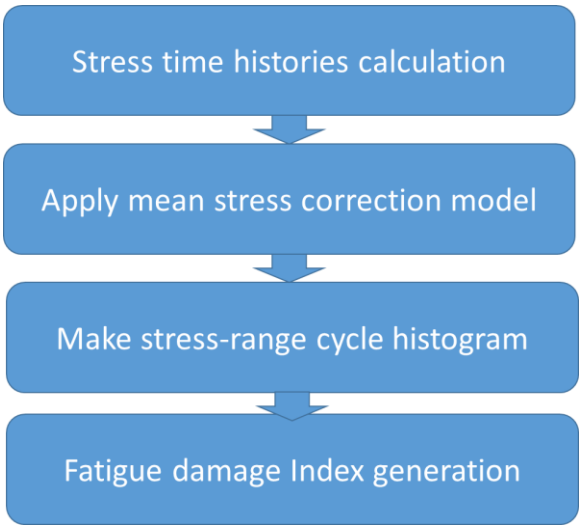

Figure 34 Flow chart of fatigue damage estimation, Reprinted with permission from [15]

Table 6 and Table 7 show the short-term fatigue estimation for the given system and sea condition. The same procedure can be repeated for various sea environments to estimate the accumulated fatigue damage. In the table, 'basic' means conventional approach with zero interlink bending stiffness and 'time-varying' means present approach with time-varying interlink bending stiffness. Results are also given for two fairlead-connection conditions, frictionless hinged and fixed joints and for two mooring lines, ML03 (taut) and ML09 (slack). In Table 6 and Table 7, residual stresses after proof-loading test are included.

As for fatigue damage with hinged fairlead connection (Table 6), the maximum fatigue damage occurs at slack-side B location by the basic and present approaches. The corresponding magnitude of basic approach is larger than that of present approach. In case of fixed fairlead connection (Table 7), both basic and time-varying-EI approaches produce the maximum fatigue damage at taut-side B location and basic approach gives larger value

than present approach. The corresponding maximum fatigue damage is greatly (order of 100 times) increased when compared to the case of hinged fairlead connection. As pointed out earlier, the actual condition, with friction and given rotational-angle restriction, should be between the two extreme cases. The above conclusions are for four potential hot spots and more points need to be checked with more environmental loads.

In Table 8, the residual stresses of the hot spots are given. It is interesting that the residual stress of point A is 44% larger than that of point B. However, as discussed in the above, the short-term fatigue damage of B is larger than A after continuous loading by time-varying tension and OPB bending.

Table 9 and Table 10 show the accumulated fatigue damages without residual stress effect. Again, the maximum fatigue damage occurs at slack-side B for hinged fairlead connection and taut-side B for fixed fairlead connection. However, when the residual stress effects are not accounted for, the fatigue damage is underestimated by 41% for hinged fairlead connection and by 33% for fixed fairlead connection. These differences are, however, much less when compared to the effect of fairlead-connection condition. The above procedure can repeatedly be used for various sea conditions during the service life to obtain the actual accumulated fatigue damage.

Table 6 Damage Index comparison Basic VS Time-Varying Interlink Bending Stiffness, Frictionless hinged floater connection B.C., ML03 and ML09, Residual stress included, Reprinted with permission from [15]

Frictionless hinged floater connection B.C., ML03				
	A	B	C	D
Basic	3.99E-08	3.73E-08	1.66E-08	2.40E-08
Time-Varying Interlink Bending Stiffness	3.54E-08	3.61E-08	2.01E-08	2.44E-08
Frictionless hinged floater connection B.C., ML09				
	A	B	C	D
Basic	4.08E-07	4.27E-07	1.99E-07	2.83E-07
Time-Varying Interlink Bending Stiffness	3.58E-07	3.84E-07	1.88E-07	2.57E-07

Table 7 Damage Index comparison Basic VS Time-Varying Interlink Bending Stiffness, Friction-induced fixed floater connection B.C., ML03 and ML09, Residual stress included, Reprinted with permission from [15]

Friction-induced fixed floater connection B.C., ML03				
	A	B	C	D
Basic	6.31E-05	6.44E-05	2.73E-05	4.44E-05
Time-Varying Interlink Bending Stiffness	5.88E-05	6.04E-05	2.57E-05	4.15E-05
Friction-induced fixed floater connection B.C., ML09				
	A	B	C	D
Basic	2.97E-05	2.96E-05	1.15E-05	1.88E-05
Time-Varying Interlink Bending Stiffness	3.04E-05	3.07E-05	1.22E-05	1.96E-05

Table 8 Residual Stress at each Potential Hot Spot Location, Reprinted with permission from [15]

Residual Stress			
A	B	C	D
MPa	MPa	MPa	MPa
196.55	136.22	45.31	136.21

Table 9 Damage Index comparison between Basic vs Time-Varying Interlink Bending Stiffness, Frictionless hinged floater connection B.C., ML03 and ML09, Residual stress excluded, Reprinted with permission from [15]

Frictionless hinged floater connection B.C., ML03				
	A	B	C	D
Basic	1.78E-08	2.13E-08	1.47E-08	1.44E-08
Time-Varying Interlink Bending Stiffness	1.60E-08	2.08E-08	1.78E-08	1.48E-08
Frictionless hinged floater connection B.C., ML09				
	A	B	C	D
Basic	1.87E-07	2.48E-07	1.78E-07	1.74E-07
Time-Varying Interlink Bending Stiffness	1.66E-07	2.25E-07	1.69E-07	1.59E-07

Table 10 Damage Index comparison Basic VS Time-Varying Interlink Bending Stiffness, fixed floater connection B.C., ML03 and ML09, Residual Stress excluded, Reprinted with permission from [15]

Friction-induced fixed floater connection B.C., ML03				
	A	B	C	D
Basic	3.53E-05	4.31E-05	2.51E-05	3.11E-05
Time-Varying Interlink Bending Stiffness	3.28E-05	4.03E-05	2.37E-05	2.90E-05
Friction-induced fixed floater connection B.C., ML09				
	A	B	C	D
Basic	1.42E-05	1.77E-05	1.05E-05	1.19E-05
Time-Varying Interlink Bending Stiffness	1.47E-05	1.86E-05	1.11E-05	1.24E-05

3. EFFECTS OF VARIOUS FAIRLEAD-CONNECTION PARAMETERS ON CHAIN-MOORING OPB-INDUCED FAILURE*

3.1 Explanation of Target System (Semi-Submersible with UCS)

As a target structure, semi-submersible system with 12 mooring lines and 4 risers is selected in 1219.2 m water depth. The potential-theory-based diffraction and radiation panel program WAMIT, which is widely used in the offshore industry, is selected to calculate the hydrodynamic coefficients such as added mass, radiation damping, first-order and second-order-mean wave forces [39]. The geometric configuration and distribution of panels for the hydrodynamic-coefficient calculation is presented in Figure 35 after checking its convergence. The subsequent time-domain hull-mooring-riser coupled-dynamics simulation was done by CHARM3D program. It is TAMU-in-house computer program that has been developed by TAMU OSSL lab during the past 20 years for multi-hull-mooring-riser fully-coupled nonlinear dynamic analysis in time domain [33]. The computer simulation program has been extensively validated against various experimental and field data (e.g.[18]). In CHARM3D, the slender-elastic-rod theory developed by Garrett [37] is used for risers and mooring lines. The line dynamics are solved by rod-element FE (finite element) method using high-order elements and generalized coordinate. The detailed formulas and numerical implementation are given in [19, 40]. The external dynamic loads are evaluated at instantaneous position of the lines at each time step by using Morison equation [43]. The banded matrix for line dynamics is

* Parts of this chapter are previously published from [42]

combined with the full matrix of 6DOF platform dynamics through proper connection conditions. The combined full-matrix equation is solved at each time step and the time-marching continues.

The details of the target semi-submersible floater are explained in [40]. As shown in Figure 36, each mooring group consists of 3 mooring lines and 4 mooring groups (total 12 mooring lines) are installed to enhance station-keeping capability and 4 risers are employed at each side. Due to riser pre-tension imbalance, initial floater displacements are slightly tilted so that ML01~06 is taut-side and ML07~12 is slack-side. For wave direction, head sea (180 deg) condition is considered. Each mooring line is modelled by the combination of chain and polyester rope. The length for chain-polyester-chain portion is 130m-1720m-250m. Each mooring line is modeled by 29 quadratic elements with cubic variation of external loading. For chain-stopper, underwater-chain-stopper (UCS) connected to fairlead is adopted as shown in Figure 37. It is assumed that the underwater-chain-stopper (or chain-hawse) is circular steel-pipe type with outer diameter 0.29m and wall thickness 10mm and chain inside is held by the chain stopper so that they move together. Furthermore, the friction coefficient of 0.7 is used in the high-fidelity local-FEM computation. The mooring and UCS properties and configuration are given in

Table 1 and Table 12. The information about risers can be found in [15, 41]. To check the effects of UCS modeling on OPB-induced failure, numerous simulations were conducted with varying the approaches and parameters. In the following, the simulation results are presented only for ML03 (taut) and ML09 (slack) as representative taut-side and slack-side lines.

The chain material properties are shown in Table 13. For the elastoplastic behavior of material at high fidelity local FEM computation, the multi-linear and isotropic hardening law proposed by Ramberg-Osgood was used as shown in eq.3.1 [44-46].

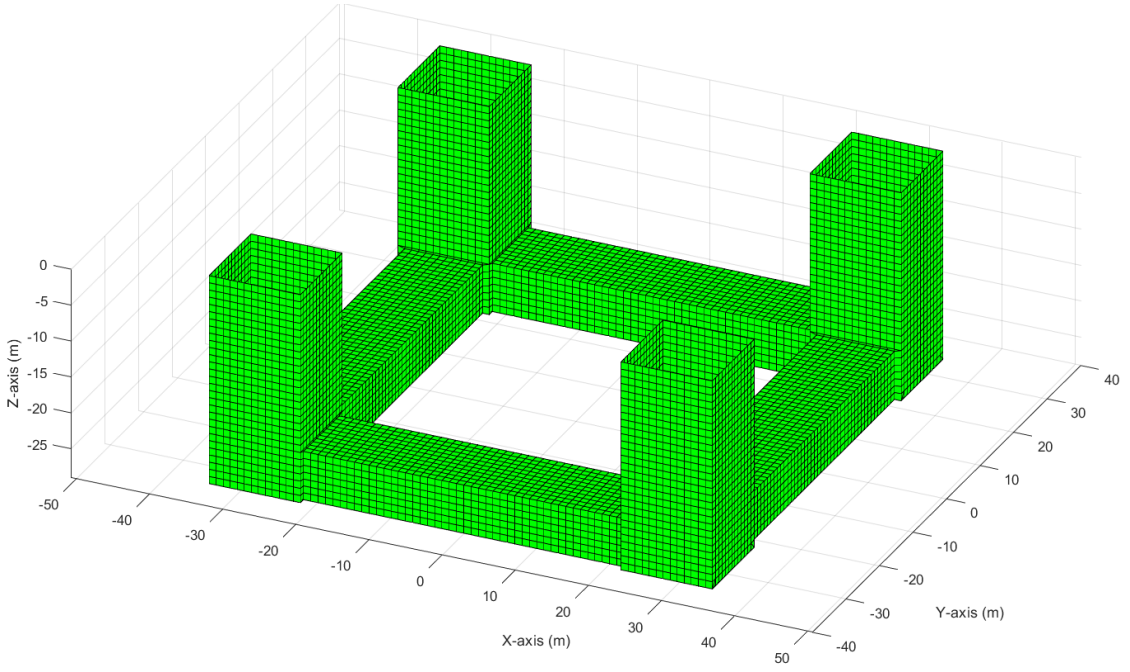

Figure 35 Panel Discretization of Semi-Submersible Model, Reprinted with permission from [42]

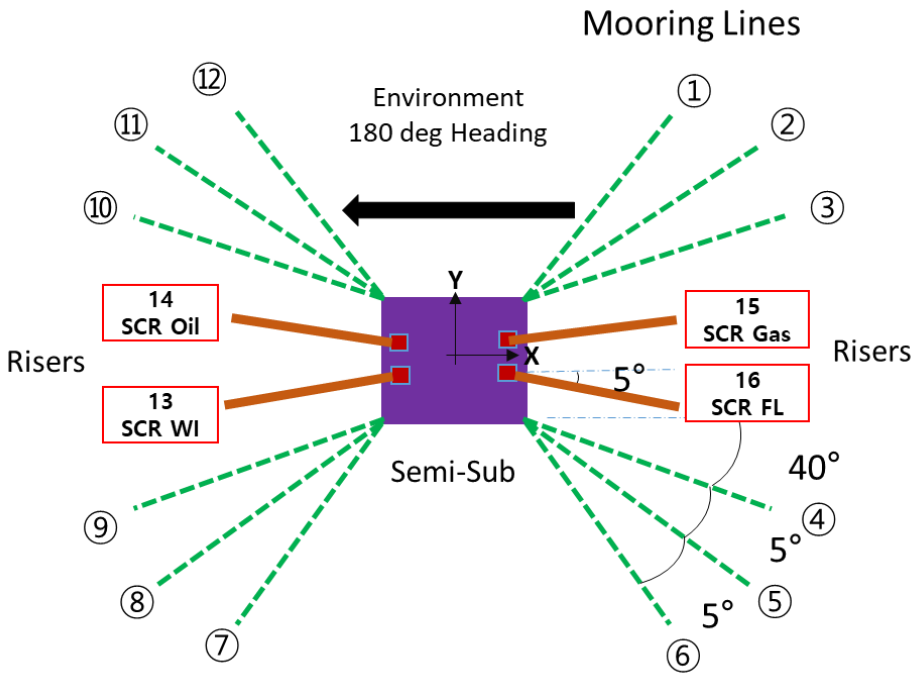

Figure 36 Configuration of Semi-Submersible System with 12 Mooring Lines and 4 Risers, Reprinted with permission from [42]

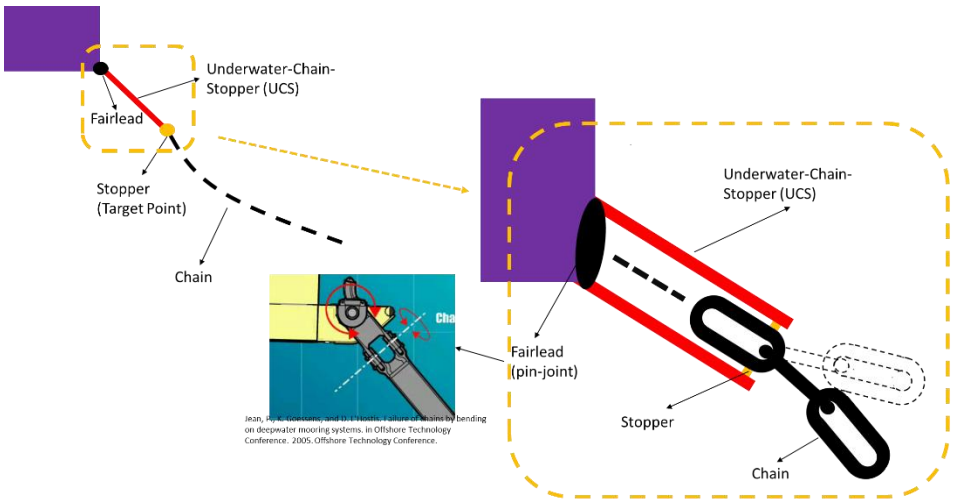

Figure 37 Configuration of Underwater-Chain-Stopper System [1] , Reprinted with permission from [42]

Table 11 Mooring and UCS (or Chain-Hawse) Modelling Properties , Reprinted with permission from [42]

Mooring and UCS (or Chain-Hawse) Modelling Properties				
	Unit	Chain	Rope	UCS (or Chain-Hawse)
Type	[-]	R3 Studless	Polyester	Circular Tube
Diameter	[mm]	147	220	290
Mass in Air	[kg/m]	430	39	499
Displaced Mass	[kg/m]	56	29.2	124
MBL(Min. Braking Load)	[kN]	14700	8250	14700
Axial Stiffness (EA)	[MN]	1845.4	52.76	1845.4
Bend Stiffness (EI)	[MN-m^2]	time-varying or 0	0	18.3
Drag coefficient	[-]	2.4	1.2	1.2

Table 12 Coordinates and pretensions of the mooring lines, Reprinted with permission from [42]

Kinds	Line No.	Fairlead Point			Anchor Point			Pre-Tension
		X	Y	Z	X	Y	Z	
		m	m	m	m	m	m	kN
Mooring Lines	1	34.44	31.25	-22.25	1122.22	1327.61	-1219.20	1993.9
	2	34.44	28.20	-22.25	1234.06	1224.82	-1219.20	1995.3
	3	34.44	25.15	-22.25	1330.80	1112.93	-1219.20	1996.5
	4	34.44	-25.15	-22.25	1330.80	-1112.93	-1219.20	1984.6
	5	34.44	-28.20	-22.25	1231.06	-1224.82	-1219.20	1982.1
	6	34.44	-31.25	-22.25	1122.22	-1327.61	-1219.20	1979.5
	7	-34.44	-31.25	-22.25	-1122.22	-1327.61	-1219.20	1923.5
	8	-34.44	-28.20	-22.25	-1231.06	-1224.82	-1219.20	1922.1
	9	-34.44	-25.15	-22.25	-1330.80	-1112.93	-1219.20	1920.8
	10	-34.44	25.15	-22.25	-1330.80	1112.93	-1219.20	1933.6
	11	-34.44	28.20	-22.25	-1231.06	1224.82	-1219.20	1936.3
	12	-34.44	31.25	-22.25	-1122.22	1327.61	-1219.20	1939.1

$$\varepsilon_n = \frac{\sigma_n}{E} + 0.804\frac{\sigma_y}{E}\left(\frac{\sigma_n}{\sigma_y}\right)^n$$

σ_n = Nominal Stress

ε_n = Nominal Strain (3.1)

σ_y = Yield Stress

E = Young's Modulus

n = Hardening Exponent of Material (=15.84)

Table 13 Chain Material Properties, Reprinted with permission from [42]

Chain Grade	Yield Strength	Ultimate Tensile Strength	Ultimate Tensile Strain	Young's Modulus	Poisson Ratio
[-]	MPa	MPa	[-]	MPa	[-]
R3	520	690	0.18	2.09E+05	0.3

3.2 Chain Interlink Time-Varying EI (Bending Stiffness) at UCS Outlet

The diagram below (Figure 38) represents flow chart for the 'time-varying EI' approach with the simultaneous use of high- and low-fidelity models with time-varying chain interlink bending stiffness. The 3D picture for the pre-calculated chain interlink bending stiffness as function of tension and interlink angle by using local-FEM program is shown in Figure 39. The convergence of the FEM meshes was also checked. The interlink angles can be measured using the relative angles between two localized neighboring directional vectors at each time step in the low-fidelity global simulation (Figure 40). More detailed explanation is given in [15]. In Figure 38, at each time increment, the interlink angle and

tension at the target point, which is at the UCS (or chain-hawse) outlet in this research, can be computed. Then, the instantaneous interlink stiffness can be read from Figure 39 using the instantaneous tension and interlink angle. Then, the new interlink bending stiffness that was read from Figure 39 is to be inputted to the low-fidelity global simulation by CHARM3D software. By using this mutually interfaced time-stepping procedure, the non-linear and time-varying nature of chain interlink bending stiffness can be considered in the time-domain simulation.

On the other hand, the 'basic' approach uses zero chain interlink bending stiffness while considering the discontinuity of material at the target point, as in existing commercial program such as OrcaFlex. In [15], the present CHARM3D result was compared with OrcaFlex result in the case of 'basic' approach and they agreed very well. However, at the target point, due to the material discontinuity, the variation of interlink angle there can be large and then the corresponding EI variation can matter. So, 'time-varying EI' approach is devised. No existing commercial mooring dynamics software has the capability of 'time-varying EI' or 'time-varying fairlead bearing friction (next section)' models, so comparisons cannot be made in this regard. However, in the case of basic approach, comparison with the commercial program OrcaFlex is possible. The two independent results for the given system agreed well [15].

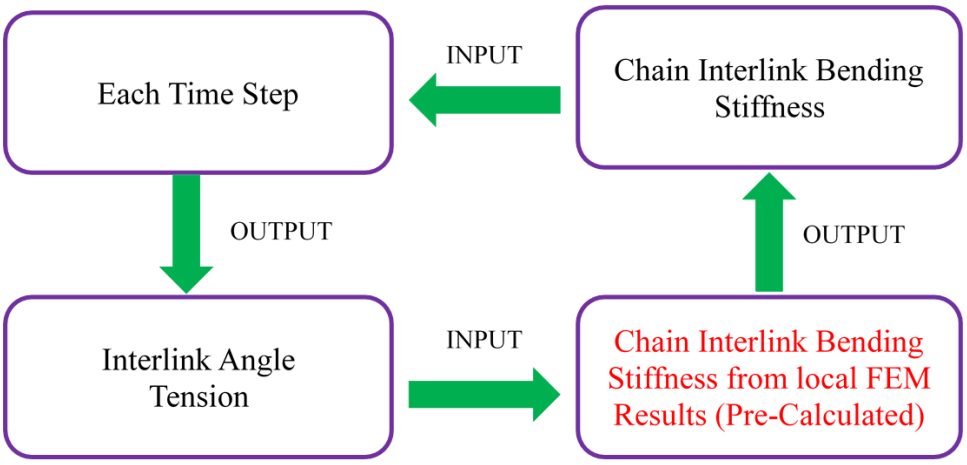

Figure 38 Process flow chart of time-varying EI approach, Reprinted with permission from [42]

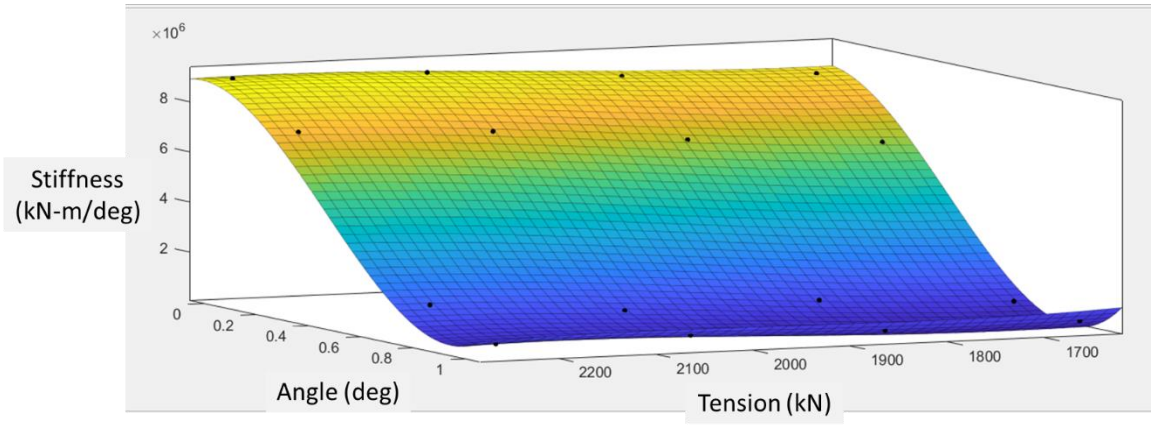

Figure 39 3D plots of bending stiffness as function of tension and interlink angle, Reprinted with permission from [42]

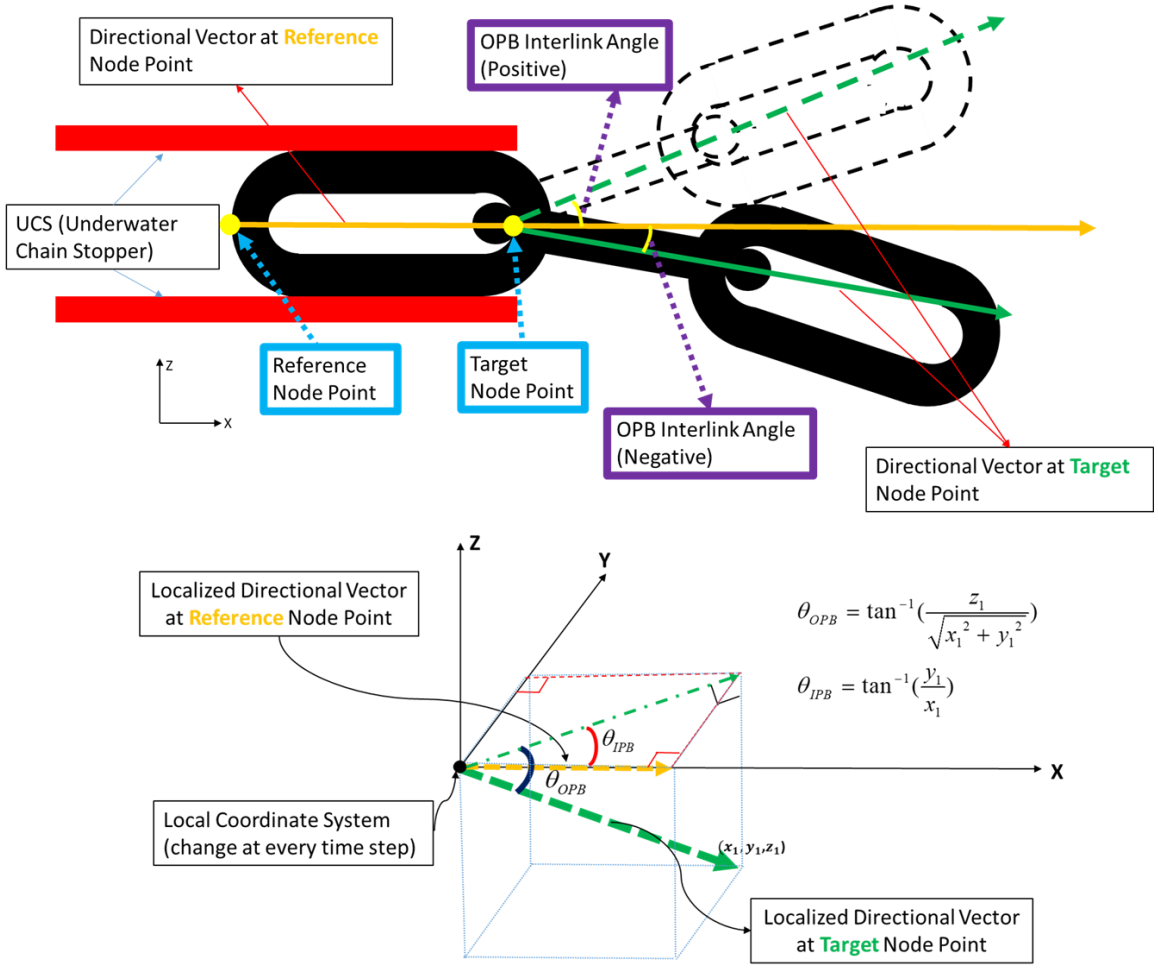

Figure 40 OPB/IPB Interlink Angle Measuring Configuration, Reprinted with permission from [42]

3.3 UCS Bearing Friction Effect at Fairlead

In this section, we consider the effect of UCS bearing friction at fairlead. In this regard, three different approaches, such as basic, time-varying EI, UCSBRK will be compared (Table 14). In Table 14, 'TimeVarying-EI' means that we consider time-varying interlink bending stiffness but time-varying bearing-friction effect is not taken into consideration. On the other hand, 'UCSBRK' represents the approach considering both time-varying

interlink bending stiffness and time-varying UCS bearing friction effect at fairlead. The term ‘basic’ means that neither of time-varying interlink bending stiffness nor UCS bearing friction effect at fairlead is considered.

In the ‘TimeVarying-EI’ approach, the locally detailed nonlinear-FEM (finite element method) structural analysis near fairlead is coupled with global mooring dynamics simulation so that time-varying interlink bending stiffness can be used at each time step [15]. In addition to this non-linear effect, we can also consider another time-varying non-linear effect in ‘UCSBRK’ approach due to UCS bearing friction at fairlead, as shown in Figure 41. At the fairlead connection, the UCS does not rotate when the UCS angle, which is the relative angle between initial (static) UCS position vector and current time-step position vector, is smaller than the breakout angle which is the reference angle to start the slide of UCS [12, 14]. Based on this background, if UCS angle is smaller than breakout angle, there is no rotation and additional secondary bending moment is generated at the target point, which is located at the exit of UCS. To simulate this non-linear mechanism during the global mooring dynamics simulation, the time-varying boundary condition at the fairlead connection needs to be applied at each time step along with the comparison between UCS angle and breakout angle. As shown in Figure 42, fixed B.C. was used if UCS angle is smaller than breakout angle (sticking mode). Whereas, hinged B.C. was imposed when UCS angle is greater than breakout angle (rotation mode). Of course, the sticking mode happens by large bearing-friction force when large tension is applied. In this research, 0.5 deg is used as the reference breakout angle [12]. The criterion can be changed depending on the type of bearing friction. Also, 0.12 is used as UCS bearing

friction coefficient with 0.05m radius of bearing pin. The value corresponds to the fairlead sliding stiffness of 1.0E+06 N-m/rad during the sticking mode, as inputted in this study [13]. On the other hand, frictionless hinged B.C. is imposed at the fairlead connection for both 'basic' and 'time-varying EI' cases.

To observe the differences caused by the three different approaches, the time-domain dynamics simulations of the semi-submersible system in random waves are conducted. As summarized in Table 15, collinear (wind-wave-current from the same direction) 1-yr storm is selected as an environmental condition. JONSWAP wave spectrum [47] and API wind spectrum (wind speed of 10m/s at 10m altitude) [48] were used to generate the corresponding random-wave and wind-velocity signals. To confirm the correctness of the relevant procedure, the comparison results between the input spectrum and re-generated spectrum (from the generated time series) are presented in Figure 43. The wave-wind-current are co-linear and from head direction (180 degrees), as shown in Figure 36. A steady storm-induced shear current is also applied, as presented in Table 15. In the following sections, the same environmental loadings will repeatedly be applied to maintain consistency.

The statistical values including mean value of interlink angle in both ML03 (taut) and ML09 (slack) are tabulated in Table 16. The absolute mean value of interlink angle is decreased especially in ML03 (taut) when the UCSBRK approach is applied compared to the other two approaches. It means that ML03 (taut) is more affected by UCS bearing friction at fairlead than ML09 (slack) due to larger bearing-friction with higher tension.

Figure 44 and Figure 45 show OPB interlink angle results (time history and spectra) at the target point for ML03 (taut) and ML09 (slack). As shown in Figure 44, the differences between basic and time-varying EI results are small compared to the differences between time-varying EI and UCSBRK results. Similar trend can also be observed in ML09 (slack) results. The interlink angles at the target point by the UCSBRK model are the largest. Furthermore, due to additional secondary bending moment (caused by fairlead bearing friction) at the target point, high frequency components related to UCS bending and high-mode mooring dynamics can be observed in the UCSBRK case of ML03 (taut) while it is not clearly seen in ML09 (slack). In the case of slack-side mooring with UCSBRK approach, on the other hand, two peaks are shown in the low frequency region; lowest one associated with floater's slowly-varying surge motion and second one associated with floater's pitch natural frequency (see Figure 50). The trend related to floater's pitch natural frequency (second peak) does not appear in basic and time-varying-EI cases due to the frictionless hinged B.C. In this case, the wave-frequency components of interlink-angle variation is significant due to floater's heave motion (see Figure 50).

Tension comparison results are shown in Figure 46 and Figure 47. Tension has a dominant peak at the low frequency close to floater's surge natural frequency i.e. tension variation in this case is almost static and mainly caused by slowly-varying large-amplitude floater's surge motions. The variation of tension magnitude is less affected by fairlead bearing friction and more influenced by time-varying-EI effect. In the simplest case of basic approach, the tension magnitude is underestimated.

Bending moment at the target point, which is post-calculated using 3D plot of bending moment as function of OPB interlink angle and line tension is given in Figure 48 and Figure 49. The general trend of bending moment is similar to that of interlink angle, as bending moment initially increases with OPB interlink angle. In the taut-side case of UCSBRK approach, there exists significant peak near 2.8 rad/s, as in the corresponding figure in Figure 44, which is related to the transient response of UCS when sudden transition occurs from sticking mode to rotation mode at the fairlead connection. The high-frequency large-magnitude bending moment generates the corresponding bending stress, which will be a big problem in fatigue in view of high number of cycles. Judging from the bending moment results, with basic and time-varying EI approaches, the bending moments at the target point are significantly underestimated. This will result in serious under-estimation of the OPB-induced accumulated fatigue damage there. Therefore, the accurate modeling of fairlead connection and time-varying EI is very important for reliable OPB-induced failure. In the case of basic and time-varying EI approaches, the bending moment of ML03 (taut) is less compared to that of ML09 (slack) while the opposite is true when UCS bearing friction effect at fairlead is considered. Since IPB-induced moments play less role for chain bending failure, only OPB-induced moment is considered [2].

Floater motion spectra are presented in Figure 50. Due to head wave condition (180 deg), only surge-heave-pitch motion spectra are plotted. As expected, the differences between three different approaches are small except the slowly-varying surge motion. It means that the accurate modeling of fairlead connection and time-varying EI is important for mooring OPB-induced failure but it makes little influence on floater motions.

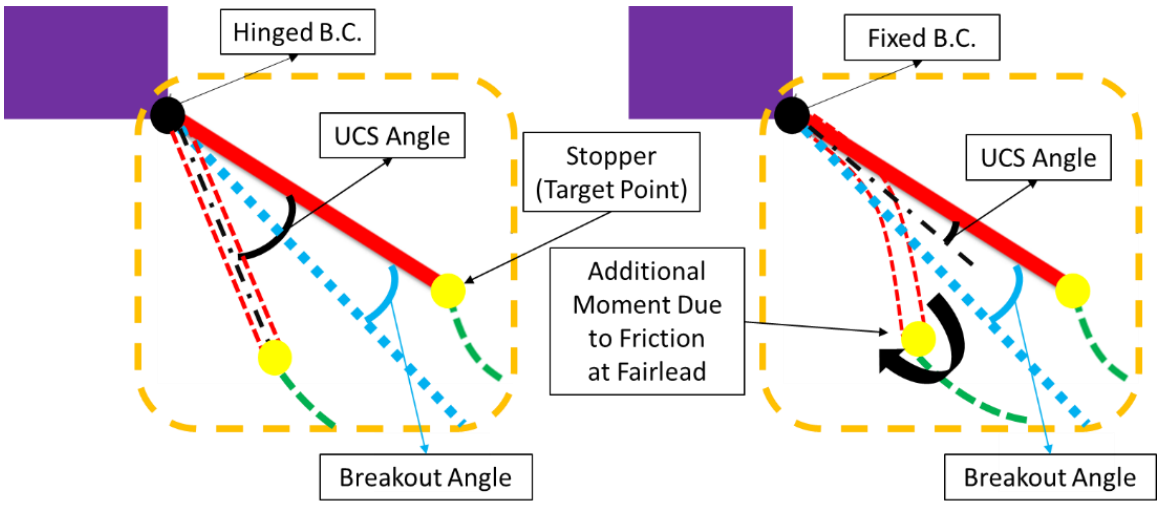

Figure 41 Configuration of Consideration of UCS Bearing Friction at Fairlead (UCSBRK) , Reprinted with permission from [42]

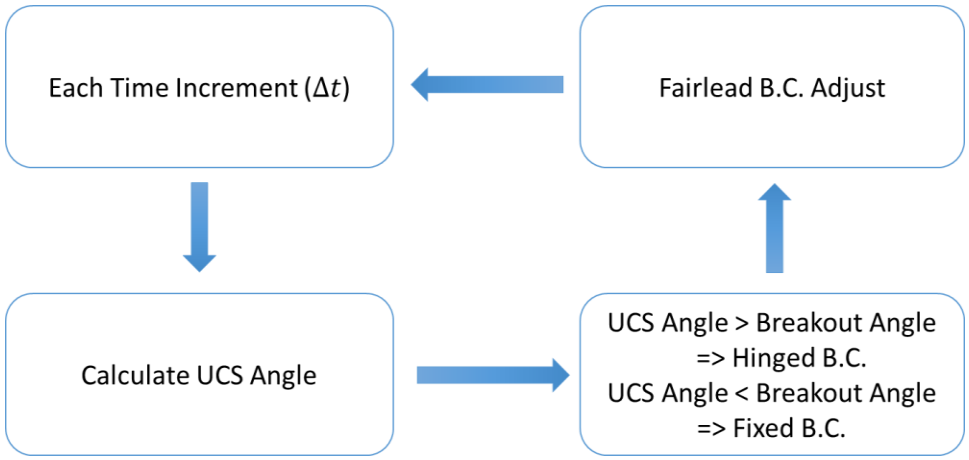

Figure 42 Chart for Consideration of UCS Bearing Friction at Fairlead (UCSBRK) , Reprinted with permission from [42]

Table 14 Consideration Chart for Basic vs Time-varying - EI vs UCSBRK, Reprinted with permission from [42]

CASE	Consideration	
	Time-Varying Interlink Bending Stiffness	Fairlead Bearing Friction
BASIC	X	X
TIMEVARYING-EI	O	X
UCSBRK	O	O

Table 15 Environmental Condition (1-year storm) , Reprinted with permission from [42]

Wave				Current		Wind		
Gamma	Direction from north	Significant Wave (Hs)	Spectral Period (Tp)	Depth	Vel.	Spectrum	10-min average at 10m elevation	Direction from north
(-)	(deg)	(m)	(s)	(m)	(m/s)	(-)	(m/s)	(deg)
2.4	180 (uni-directional)	3.1	8.4 (0.75 rad/s)	0	0.5	API	10.0	180 (uni-directional)
				63	0.375			
				126	0			
				mud	0			

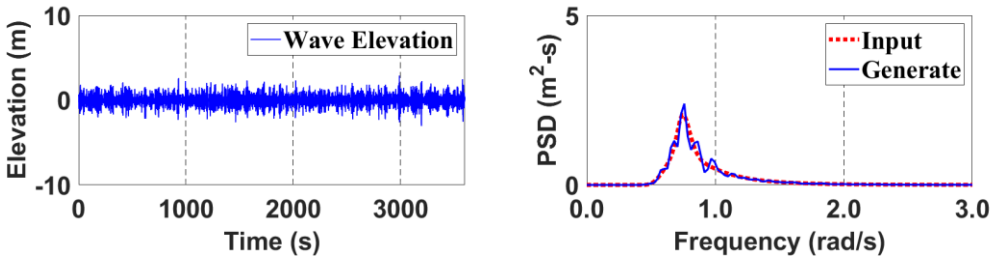

Figure 43 Incident Wave Elevation Time History and Spectrum (Input vs Regenerated) , Reprinted with permission from [42]

Table 16 Statistical Value Comparisons for Basic vs Time-varying - EI vs UCSBRK, 180deg, Reprinted with permission from [42]

			STD	Mean	Max.	Min.
ML03	Basic	Tension (kN)	18.39	2009.92	2073.01	1963.37
		OPB Angle (deg)	0.0020	-0.1429	-0.1340	-0.1496
		OPB Moment (kN-m)	0.26	-24.05	-22.86	-25.03
	TimeVaryingEI	Tension (kN)	27.65	2011.74	2100.79	1933.83
		OPB Angle (deg)	0.0022	-0.1342	-0.1246	-0.1412
		OPB Moment (kN-m)	0.25	-22.75	-21.60	-23.65
	UCSBRK	Tension (kN)	27.80	2011.87	2103.47	1931.49
		OPB Angle (deg)	0.0845	0.0358	0.6264	-0.6783
		OPB Moment (kN-m)	12.93	6.44	73.92	-77.10
ML09	Basic	Tension (kN)	18.29	1890.52	1939.98	1828.41
		OPB Angle (deg)	0.0029	-0.1473	-0.1379	-0.1591
		OPB Moment (kN-m)	0.39	-23.61	-21.91	-25.14
	TimeVaryingEI	Tension (kN)	27.30	1889.58	1969.85	1801.22
		OPB Angle (deg)	0.0029	-0.1386	-0.1291	-0.1497
		OPB Moment (kN-m)	0.38	-22.32	-20.78	-23.80
	UCSBRK	Tension (kN)	27.29	1889.55	1971.44	1801.10
		OPB Angle (deg)	0.0348	-0.1403	0.0227	-0.4251
		OPB Moment (kN-m)	5.24	-22.48	3.37	-56.88

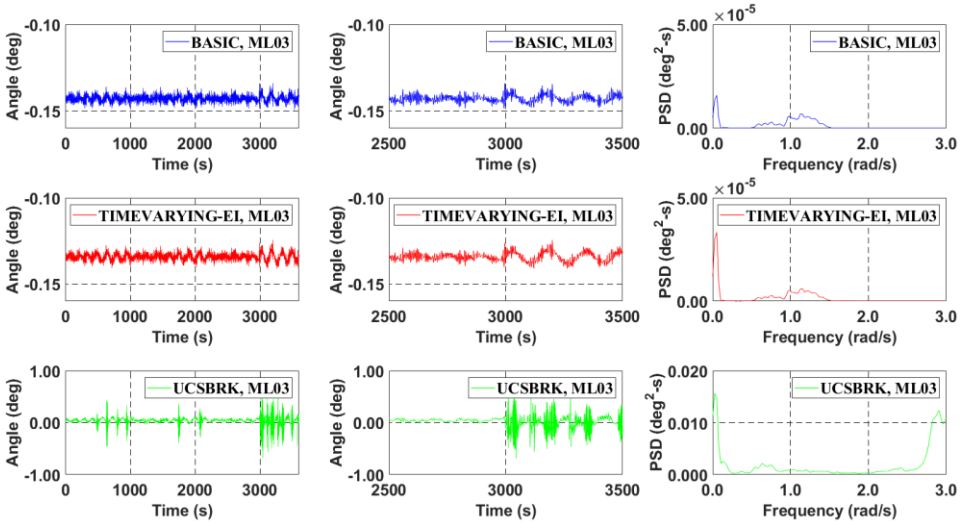

Figure 44 OPB interlink angle comparison for ML03 (taut), Basic vs TimeVarying-EI vs UCSBRK, 180deg, Reprinted with permission from [42]

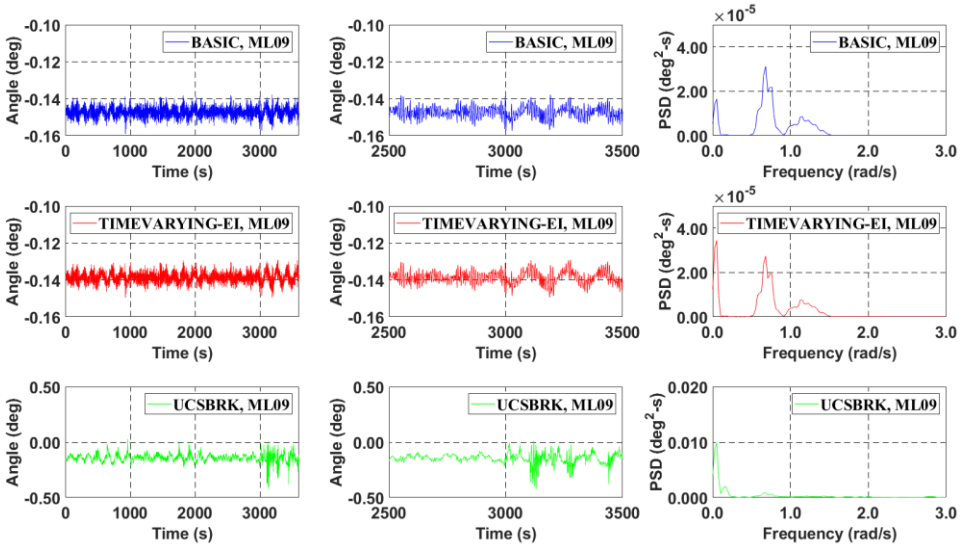

Figure 45 OPB interlink angle comparison for ML09 (slack), Basic vs TimeVarying-EI vs UCSBRK, 180deg, Reprinted with permission from [42]

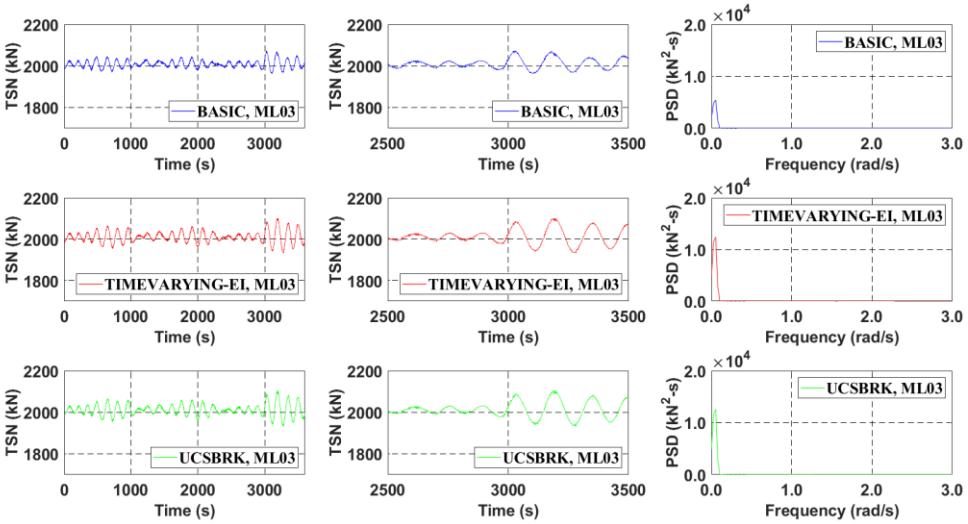

Figure 46 Tension comparison for ML03 (taut), Basic vs TimeVarying-EI vs UCSBRK, 180deg, Reprinted with permission from [42]

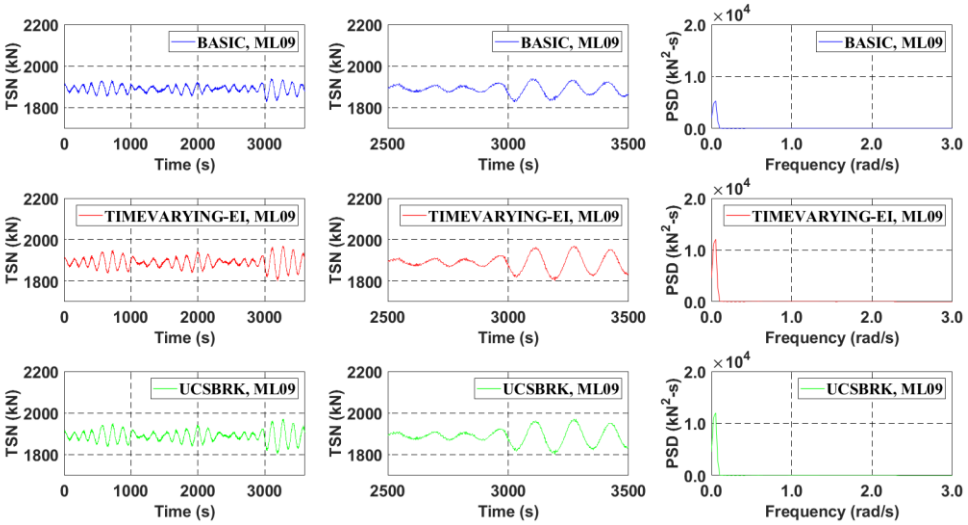

Figure 47 Tension comparison for ML09 (slack), Basic vs TimeVarying-EI vs UCSBRK, 180deg, Reprinted with permission from [42]

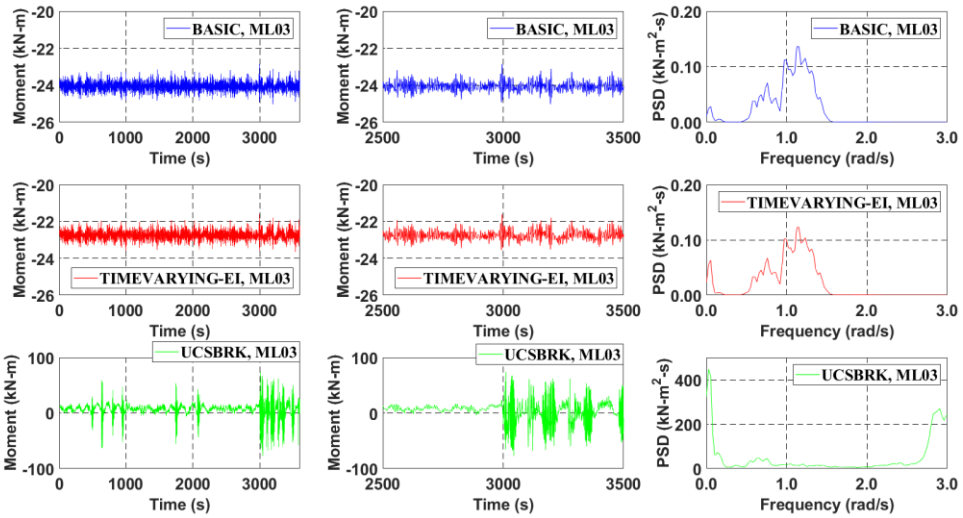

Figure 48 Bending Moment comparison for ML03 (taut), Basic vs TimeVarying-EI vs UCSBRK, 180deg, Reprinted with permission from [42]

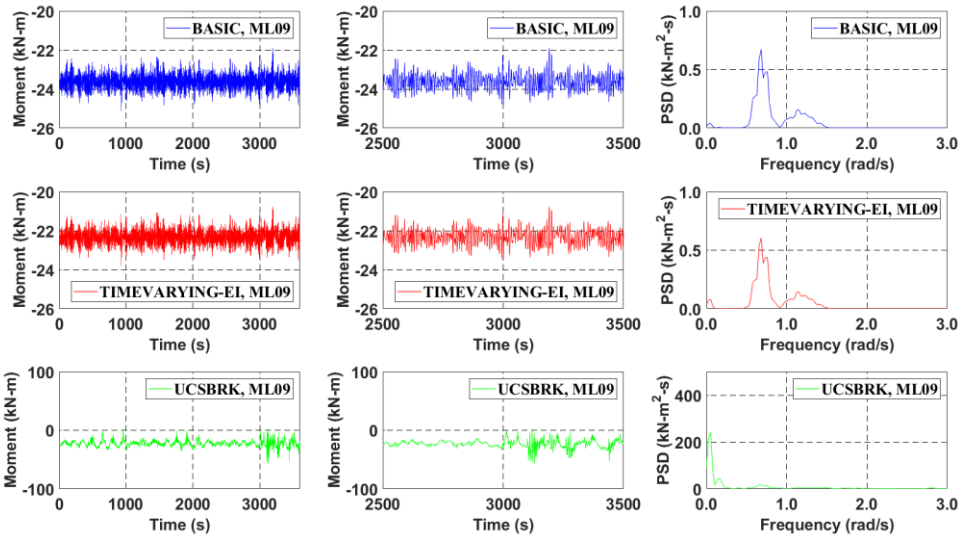

Figure 49 Bending Moment comparison for ML09 (slack), Basic vs TimeVarying-EI vs UCSBRK, 180deg, Reprinted with permission from [42]

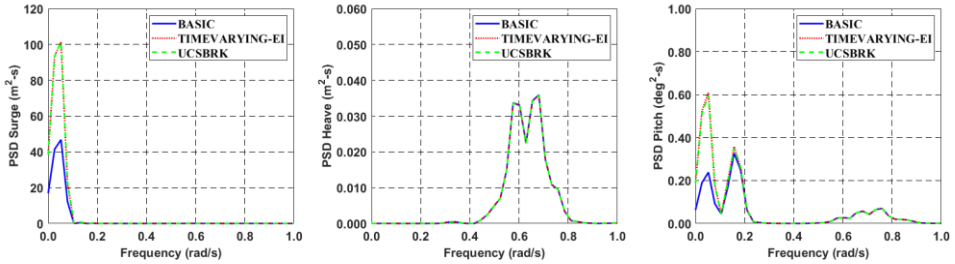

Figure 50 Comparison: Surge-heave-pitch Motion PSD, Basic vs TimeVarying-EI vs UCSBRK, 180deg, Reprinted with permission from [42]

3.4 Accumulated Short-term Fatigue Estimation

Only short-term fatigue within one-hour duration by the three different approaches is considered in this research under 1-yr storm condition (Table 15). This kind of comparison pattern will be repeated for other sea states to generate accumulated long-term fatigue damage. Many researchers reported and published about stress-hot-spot location based on their local FEM results [3, 10]. Based on those references, seven points are selected as hot-spot locations, as shown in Figure 51. The hot-spot selection is also consistent with the present simulation results. At each hotspot location, the corresponding time histories of axial stress and OPB bending stress are combined and added into the existing residual stress. The residual stress was caused by the manufacturing process (loading up to 70% of MBL (minimum breaking load) during proof-load test and subsequently unloaded) and can be estimated from the detailed local modeling of chain link using nonlinear FEM program, such as Abaqus 6.12. Then the residual stress can be obtained as maximum principle stress. Subsequently, with the combination of low-fidelity global mooring simulation and pre-calculated axial/bending stress as function of tension magnitude and interlink angle based on local FEM analysis, as shown in eq.3.2, the total stress as well as SCF time series can be re-generated. To apply the corresponding mean-stress-correction effect, Gerber model is selected (eq. 3.3). Then, stress range-cycle histogram is made by rain-flow counting method which is widely adopted [49]. Lastly, using S-N curve (eq. 3.4) (ABS-FC (Free Corrosion) the "W" curve ($A = 5.33 \cdot 10^{10},\ m = 3.0$)) [50] and Palmgen-Miner's accumulative fatigue damage rule (eq. 3.5), the accumulated fatigue damage can be calculated.

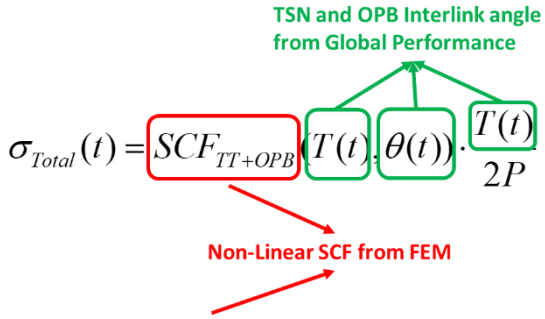

$$SCF_{TT+OPB} = \frac{\text{Max. Principle Stress }_{TT+OPB}}{\text{Normal Stress}} \tag{3.2}$$

T = tension, P = chain section area, θ = OPB interlink angle

Gerber model: $\frac{\sigma_a}{\sigma_e'} + \left(\frac{\sigma_m}{\sigma_u}\right)^2 = 1$ (3.3)

where, σ_m, σ_u = mean stress and tensile strength, respectively

σ_a = stress amplitude

σ_e' = effective alternating stress at failure for a lifetime of N cycles

$$N = A \cdot S^{-m} \tag{3.4}$$

N => Number of cycles to failure
S => Stress Range
A, m => Fatigue strength coefficient and exponent

Damage Index $D = \sum_{i=1}^{k} \frac{n_i}{N_i}$ (3.5)

where, n_i = the number of cycles of the (effective) stress range

N_i = the ultimate number of cycles of the (effective) stress range before fatigue failure

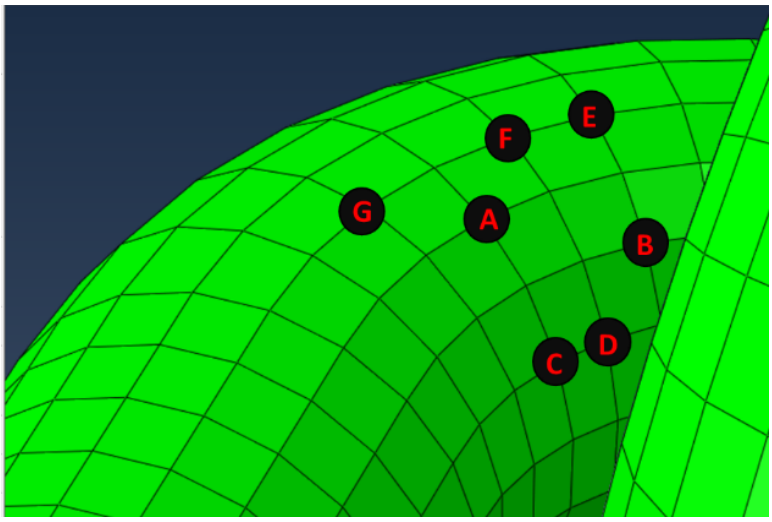

Figure 51 Hotspot locations from FEM model, Reprinted with permission from [42]

The short-term cumulative fatigue damage for the given system and sea condition including residual stress at seven hot spots is summarized in Table 17 (ML03) and Table 18 (ML09). As shown in Table 17 and Table 18, G location has the maximum fatigue damage regardless of different approaches for both taut (ML03) and slack-side mooring line (ML09). When UCSBRK is used, the corresponding maximum fatigue damage at every hot spot of ML03 (taut) and ML09 (slack) mooring is greatly increased compared to basic and time-varying EI approaches. Furthermore, ML09 (slack) is much more vulnerable to OPB-induced failure than ML03 (taut) when basic approach is used while the opposite is true when time-varying EI and UCSBRK approaches are applied. Thus, it can be concluded that OPB-induced failure at target point (out of UCS) is mainly governed by the UCS bearing friction effect at fairlead rather than time-varying interlink-bending-stiffness effect. The above example underscores the importance of the accurate modeling of fairlead-connection condition in global mooring-dynamics simulation for the prediction

of OPB-induced fatigue failure. With crude mooring model without the details of fairlead connection and UCS, the OPB-fatigue prediction can be meaningless. The above conclusions need to be checked for other environmental loads and their directions. Also, to assess long-term fatigue damage, the above procedure has to be repeatedly applied for numerous environmental conditions of any given site. In the following section, residual stress due to proof load during manufacturing process will be compared and discussed.

Table 17 Fatigue damage comparison, Basic vs TimeVarying-EI vs UCSBRK, ML03 (taut), 180deg, Reprinted with permission from [42]

Fatigue Damage, Basic VS TimeVarying-EI VS UCSBRK, ML03, 180deg							
	A	B	C	D	E	F	G
Basic_ML03	3.6924E-09	4.1019E-09	2.7200E-09	2.9089E-09	1.6199E-09	1.5308E-08	2.5848E-08
TimeVarying-EI_ML03	4.0929E-09	6.1003E-09	6.3629E-09	4.9724E-09	2.8454E-09	4.5524E-08	7.2007E-08
UCSBRK=0.5deg_ML03	7.0685E-04	7.0075E-04	2.8245E-04	4.5565E-04	3.5497E-04	3.8066E-04	7.9853E-04

Table 18 Fatigue damage comparison, Basic vs TimeVarying-EI vs UCSBRK, ML09 (slack), 180deg, Reprinted with permission from [42]

Fatigue Damage, Basic VS TimeVarying-EI VS UCSBRK, ML09, 180deg							
	A	B	C	D	E	F	G
Basic_ML09	1.1655E-08	1.2414E-08	6.6389E-09	8.3845E-09	4.7596E-09	1.4851E-08	2.7951E-08
TimeVarying-EI_ML09	1.1260E-08	1.4259E-08	1.0643E-08	1.0430E-08	6.1371E-09	3.0918E-08	5.1664E-08
UCSBRK=0.5deg_ML09	2.0632E-05	2.0238E-05	8.3251E-06	1.3081E-05	7.1269E-06	9.7865E-06	2.4289E-05

3.5 Effects of UCS Bending Stiffness and Residual Stress

In the previous section, it is seen that the largest OPB-fatigue damage occurs when the fairlead B.C is UCSBRK. Also, we observe that high-frequency bending moment can be generated at the taut side of mooring due to the UCS transient responses when sudden change of fairlead B.C. happens after friction resistance is released. Therefore, the high-frequency bending moment may be influenced by UCS bending stiffness. In this regard, by using UCSBRK approach, four simulations are conducted for four different UCS bending stiffness, such as 0.5EI=9.15E+06, EI=1.83E+07, 2EI=3.66E+07, and 10EI=1.83E+08. All the other UCS parameters and environmental loadings are kept the same.

The bending-moment time histories and corresponding spectra are presented in Figure 52 and Figure 53. It is expected that the bending moment at the target point is governed by interlink angles since tension is almost identical regardless of UCS bending stiffness. In the case of taut-side mooring ML03, the spectral area of high-frequency components increases as UCS-EI increases but eventually decreases when EI is further increased. The corresponding spectral peak is also slightly shifted to higher frequency as UCS becomes stiffer. At the slack-side mooring ML09, the general trends of time series and spectra remain the same while the lowest-frequency spectral peak is slightly increased as UCS-EI increases. However, the differences are not significant, which means that the bending moment and fatigue damage at the target point are not sensitive to the UCS-EI.

The corresponding accumulated short-term fatigue damage for various UCS bending stiffness (0.5EI, EI, 2EI, 10EI) is tabulated in Table 19 and Table 20 . As before, we have the maximum fatigue damage in ML03 (taut) with UCS bending stiffness=2EI. As was observed in the bending moment, the differences in fatigue damage for different UCS-EI are not that significant. Judging from the presented results, the maximum fatigue occurs at the taut-side G location when UCS bending stiffness=2EI. Due to the non-linearity of fairlead bearing friction and time-varying interlink EI, the above conclusions need to be checked with more UCS EI and environmental loads.

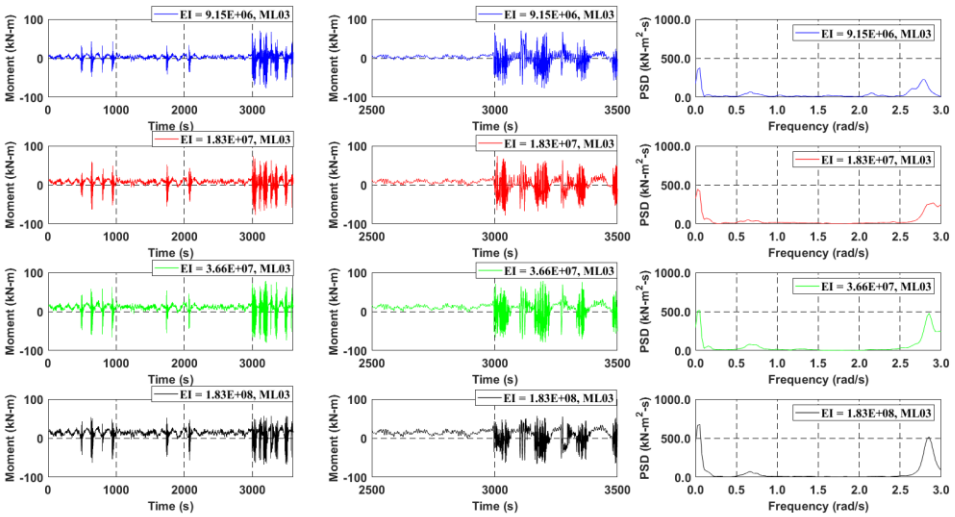

Figure 52 Bending Moment comparison for ML03 (taut), for various UCS Bending Stiffness, 180deg, Reprinted with permission from [42]

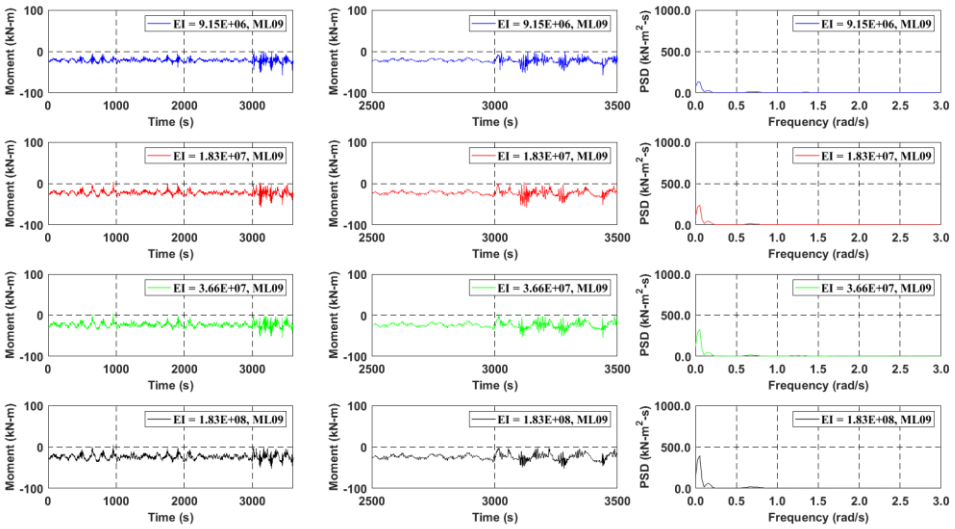

Figure 53 Bending Moment comparison for ML09 (slack), for various UCS Bending Stiffness, 180deg, Reprinted with permission from [42]

Table 19 Fatigue damage comparison for various UCS Bending Stiffness, ML03 (taut), 180deg, Reprinted with permission from [42]

Fatigue Damage UCS Bending Stiffness, ML03, Included Residual Stress							
	A	B	C	D	E	F	G
EI=9.15E06_ML03	4.6246E-04	4.5685E-04	1.8421E-04	2.9660E-04	2.2671E-04	2.4512E-04	5.2336E-04
EI=1.83E07_ML03	7.0685E-04	7.0075E-04	2.8245E-04	4.5565E-04	3.5497E-04	3.8066E-04	7.9853E-04
EI=3.66E07_ML03	9.1799E-04	9.0853E-04	3.7031E-04	5.8854E-04	4.9888E-04	4.9630E-04	1.0267E-03
EI=1.83E08_ML03	6.0076E-04	5.9991E-04	2.5280E-04	3.9874E-04	2.7792E-04	3.2862E-04	6.6560E-04

Table 20 Fatigue damage comparison for various UCS Bending Stiffness, ML09 (slack), 180deg, Reprinted with permission from [42]

Fatigue Damage UCS Bending Stiffness, ML09, Included Residual Stress							
	A	B	C	D	E	F	G
EI=9.15E06_ML09	1.7833E-05	1.7460E-05	7.1212E-06	1.1289E-05	6.2788E-06	8.8309E-06	2.1926E-05
EI=1.83E07_ML09	2.0632E-05	2.0238E-05	8.3251E-06	1.3081E-05	7.1269E-06	9.7865E-06	2.4289E-05
EI=3.66E07_ML09	1.9342E-05	1.9116E-05	7.8371E-06	1.2319E-05	6.7560E-06	9.6134E-06	2.3971E-05
EI=1.83E08_ML09	1.6385E-05	1.6320E-05	6.7357E-06	1.0521E-05	5.7659E-06	8.4934E-06	2.1137E-05

Finally, let us consider the effects of residual stress on the fatigue damage. As was pointed out before, chain mooring has to go through proof-loading test (loading up to 70% of MBL and unloading) before installation. If the chain is perfectly elastic, then after unloading the residual stress should be zero. However, due to material nonlinearity, there exist residual stresses after unloading [46]. There may be additional residual stress due to chain-curve-forming process, which is not considered here. The magnitudes of the residual stresses on hot-spots can be calculated by using nonlinear FE program, such as Abaqus 6.12. The residual-stress results are given in Figure 54 at seven points around the hot-spots. The corresponding short-term fatigue damages without considering the residual-stress effects are given in Table 21. In taut-side case, the maximum fatigue damage occurs at point B and it is only about half of the case including residual stresses (see Table 19). We can also observe the similar amount of underestimation of short-term fatigue damage even at slack-side mooring (see Table 20) when proper residual stresses are not taken into consideration.

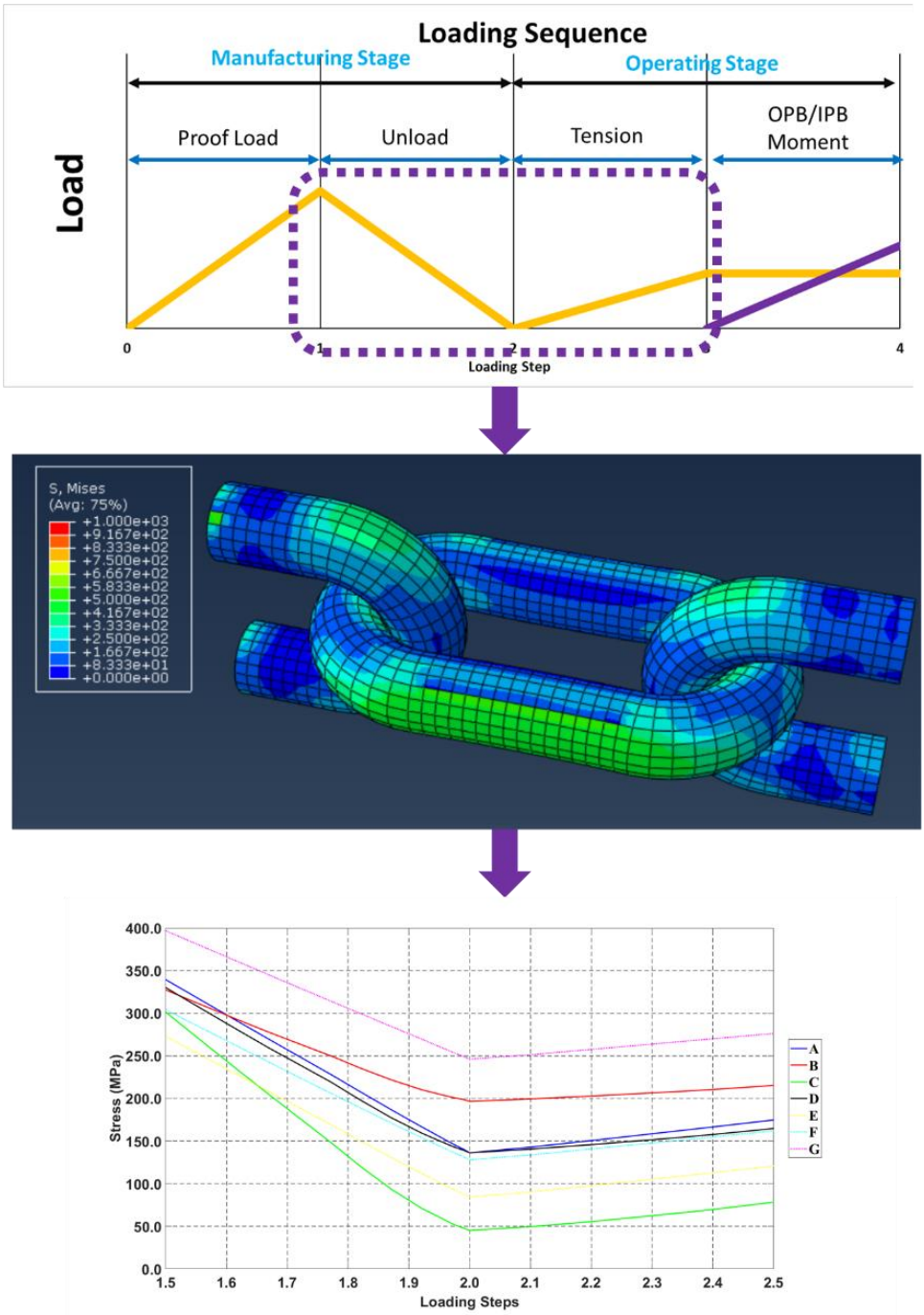

Figure 54 Proof loading test (top) and the residual stresses after unloading at each hot spot points A, B, C, D, E, F and G (middle & bottom) , Reprinted with permission from [42]

Table 21 Fatigue damage without residual stresses, 180deg, Reprinted with permission from [42]

Fatigue Damage UCSBRK Approach with 2EI UCS Bending Stiffness Excluding Residual Stress							
	A	B	C	D	E	F	G
EI=3.66E07 (2EI)_ML03 (taut)	5.2584E-04	6.2004E-04	3.4216E-04	4.1497E-04	4.1272E-04	3.3572E-04	4.4097E-04
EI=3.66E07 (2EI)_ML09 (slack)	8.8654E-06	1.1163E-05	7.0362E-06	7.5806E-06	5.2179E-06	6.3135E-06	7.2213E-06

3.6 Effect of Environmental-Loading Direction

Furthermore, since environmental heading can affect the OPB-induced failure, additional fatigue damage results under 135 deg heading are presented in this section (Table 22 and Table 23). As expected, the OPB-induced fatigue damage is decreased compared to the head-wave (=180deg) results (Figure 50) since the floater motions are reduced (Figure 55). The G location still has the maximum fatigue damage in the three different approaches. Since head wave is the critical case for OPB-induced failure, only the head wave (=180deg) results will be considered in the ensuing sections.

Table 22 Fatigue damage comparison, Basic vs TimeVarying-EI vs UCSBRK, ML03 (taut), 135deg, Reprinted with permission from [42]

Fatigue Damage, Basic vs TimeVarying-EI vs UCSBRK, ML03, 135deg							
	A	B	C	D	E	F	G
Basic_ML03	2.6351E-10	4.5259E-10	5.1922E-10	3.7982E-10	2.2060E-10	4.2632E-09	6.8369E-09
TimeVarying-EI_ML03	1.9835E-10	2.9789E-10	2.9428E-10	2.3728E-10	1.3704E-10	2.1836E-09	3.5360E-09
UCSBRK=0.5deg_ML03	4.1361E-07	4.4260E-07	1.7893E-07	2.9081E-07	1.4778E-07	2.3874E-07	5.1579E-07

Table 23 Fatigue damage comparison, Basic vs TimeVarying-EI vs UCSBRK, ML09 (slack), 135deg, Reprinted with permission from [42]

Fatigue Damage, Basic vs TimeVarying-EI vs UCSBRK, ML09, 135deg							
	A	B	C	D	E	F	G
Basic_ML09	1.8571E-10	3.7590E-10	4.8139E-10	3.2470E-10	1.9937E-10	2.6640E-09	4.0554E-09
TimeVarying-EI_ML09	1.3067E-10	2.3056E-10	2.6435E-10	1.9156E-10	1.1696E-10	1.4371E-09	2.1732E-09
UCSBRK=0.5deg_ML09	2.2350E-07	2.2651E-07	9.6182E-08	1.4758E-07	8.1740E-08	1.3771E-07	3.3595E-07

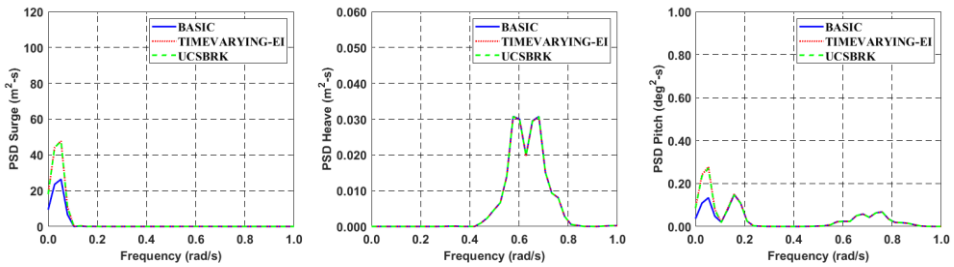

Figure 55 Comparison: Surge-heave-pitch Motion PSD, Basic vs TimeVarying-EI vs UCSBRK, 135deg, Reprinted with permission from [42]

3.7 Comparison between UCSBRK and BV methodology

In this section, the present approach (UCSBRK) is compared with the methodology by Bureau Veritas (BV methodology) [3] which is widely adopted by practicing engineers. In BV methodology, the non-linear effect of chain-interlink bending stiffness (= "time-varying EI") is ignored and the breakout-angle effect can be considered as post-process. Whereas, the time-varying EI can be considered in the present approach during the time-marching step of low fidelity global analysis. The details of BV methodology are given in [3]. As shown in Table 24 and Table 25, BV methodology gives more conservative accumulated fatigue damage than UCSBRK in all hot spots for both ML03(taut) and ML09 (slack). Also, the difference between UCSBRK and BV methodology in ML03 (taut) is smaller than ML09 (slack).

Table 24 Fatigue damage comparison, UCSBRK vs BV methodology, ML03 (taut), 180deg, Reprinted with permission from [42]

Fatigue Damage, UCSBRK vs BV methodology, ML03, 180deg							
	A	B	C	D	E	F	G
UCSBRK_ML03	7.0685E-04	7.0075E-04	2.8245E-04	4.5565E-04	3.5497E-04	3.8066E-04	7.9853E-04
BV methodology ML03	1.9609E-03	1.8575-03	7.1101E-04	1.1934E-03	7.3346E-04	8.4282E-04	2.0661E-03

Table 25 Fatigue damage comparison, UCSBRK vs BV methodology, ML09 (slack), 180deg, Reprinted with permission from [42]

Fatigue Damage, UCSBRK vs BV methodology, ML09, 180deg							
	A	B	C	D	E	F	G
UCSBRK_ML09	2.0632E-05	2.0238E-05	8.3251E-06	1.3081E-05	7.1269E-06	9.7865E-06	2.4289E-05
BV methodology ML09	1.9415E-03	2.0238E-03	7.1637E-04	1.1826E-03	1.5994E-03	8.5583E-04	1.7016E-03

4. STRUCTURAL HEALTH MONITORING FOR TLP-FOWT (FLOATING OFFSHORE WIND TURBINE) TENDON USING SENSORS

4.1 Methodology

The objective of the present study is to develop algorithms to trace lines in real time by using a series of inclinometers including the corresponding real-time internal stresses and accumulated fatigue. As shown in Figure 56, the algorithm starts from a two-dimensional beam element. Using basic FEM beam theory, displacements along the beam can be interpolated between sensor (or node) locations by a third-order polynomial (eq.4.1). Denoting s as the arc-length coordinate along the length L between both end nodes of the beam, v(s) is the normal displacement of a point at s, and $\frac{dv}{ds}$ is the inclination at the same location. The boundary conditions (eq. 4.2) are displacements and inclinations given at both ends.

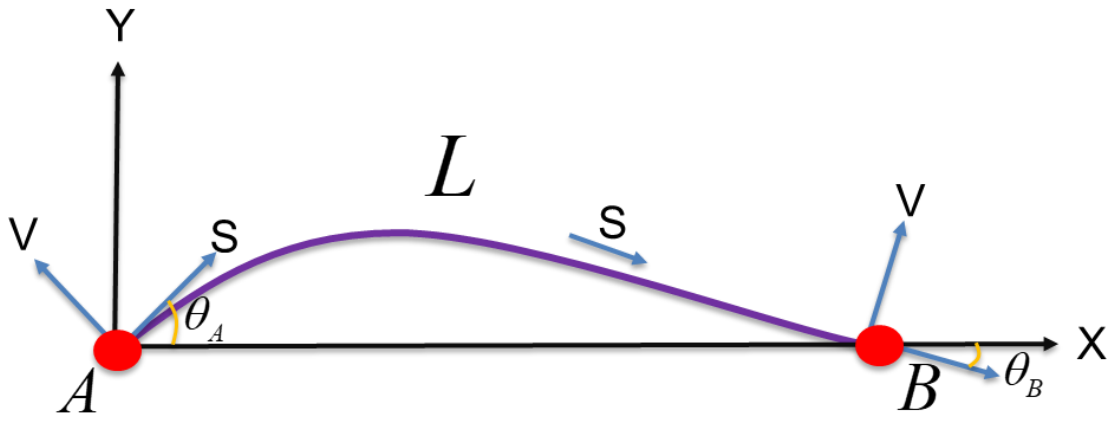

Figure 56 Basic FEM Beam Model

$$v(s) = f(v_A, v_B, \theta_A, \theta_B, s) = a_0 + a_1 s + a_2 s^2 + a_3 s^3 \tag{4.1}$$

$$v(s = s_A) = v_A,\ v(s = s_B) = v_B,\ \left.\frac{dv}{ds}\right|_{s=s_A} = \theta_A,\ \left.\frac{dv}{ds}\right|_{s=s_B} = \theta_B \tag{4.2}$$

Applying four boundary conditions (eq. 4.2) to the third-order polynomial equation (eq. 4.1), the four coefficients of eq. 4.1 can be calculated as shown in eq. 4.3, which is a function of arc length s. This third-order polynomial equation can be expressed in matrix form as shown in eq. 4.4, where N_1, N_2, N_3, N_4 represent shape functions and ξ express the nodal displacement and inclination vectors.

$$v(s) = (1 - \frac{3s^2}{L^2} + \frac{2s^3}{L^3})v_A + (s - \frac{2s^2}{L} + \frac{s^3}{L^2})\theta_A + (\frac{3s^2}{L^2} - \frac{2s^3}{L^3})v_B + (\frac{s^3}{L^2} - \frac{s^2}{L})\theta_B \tag{4.3}$$

$$v(s) = [\mathrm{N}_1 \mathrm{N}_2 \mathrm{N}_3 \mathrm{N}_4] \begin{Bmatrix} v_A \\ \theta_A \\ v_B \\ \theta_B \end{Bmatrix} = [\mathrm{N}]\{\xi\} \tag{4.4}$$

Using linearized beam theory, the bending moment can be derived as shown in eq. 4.5.

$$M = EI \frac{d^2[\mathrm{N}]}{ds^2}\{\xi\} = EI[(\frac{12s}{L^3} - \frac{6}{L^2})v_A + (\frac{6s}{L^2} - \frac{4}{L})\theta_A + (\frac{6}{L^2} - \frac{12s}{L^3})v_B + (\frac{6s}{L^2} - \frac{2}{L})\theta_B] \tag{4.5}$$

where E = Young's modulus, I = the second moment of the sectional area

To estimate the bending moment at the mid-point of the beam element, let $\frac{s}{L} = 0.5$ in eq. 4.5, resulting in eq. 4.6 below:

$$M = EI[\frac{1}{L}(\theta_B - \theta_A)] \tag{4.6}$$

Once bending moment is obtained, the corresponding maximum bending stress can be estimated from eq. 4.7

$$\sigma_S(s) = \frac{M \cdot y_{\max}}{I} = y_{\max} \cdot E \cdot [\frac{1}{L}(\theta_B - \theta_A)] \tag{4.7}$$

where $y_{\max}$ is the largest distance from the neutral axis. As can be seen in eq. 4.5, the bending moment at the mid-point of the beam element is independent of the displacements v_A and v_B. In other words, by using a series of inclinometers along the line, the bending moment and stress along the line at the discrete points (mid-length of each element) can directly be calculated even without tracing the actual instantaneous shape of the line. Then, the continuous bending moment distribution along the line can also be constructed by interpolation to find the value at other points.

The formulas for eqs. 4.1 to 4.7 are derived for 2D case [51]. For small angles (less than 10 degrees) with respect to the vertical axis, 3D bending moment can be estimated by decomposing the measured inclinations at the discrete points in two orthogonal directions, applying the formulas to both directions, and vector summing the results. In the present research, the 3D extension is made in such a way and all the example cases are calculated from the 3D algorithm. Once bending moment distribution is estimated, the corresponding bending stress and the cumulative fatigue damage by it can be obtained in real time, respectively.

Tension is also important for internal stress and fatigue, so its estimation is also critical to the structural integrity management. When the top tension can be monitored in real time

by strain-gauge based load cells or other type of monitoring at the tendon/hull interface, the corresponding tension distribution along the line can also be estimated as shown in [52] assuming small angles with respect to the vertical axis.

As shown in Figure 57, the tension difference between the top and bottom is estimated by subtracting the beam effective weight (structural weight plus internal fluid weight minus displaced external fluid weight) from the top tension. In the case of TLP, the dynamic variation of tension is relatively much smaller than the effects of pretension and effective weight. As the present methodology is focused on TLP tendons, their axial responses, axial inertia and damping forces can be assumed to be small and neglected.

The inclination sensors can be installed at the set intervals to provide θ_A and θ_B readings at their sampling rate. By exploiting the inclinometer signals with the top-tension measurement, the above methodology can produce the corresponding bending moment and tension distribution along the line in real time. To validate the developed algorithm, a TLP-type FOWT with tendons is numerically modeled using our in-house simulation program CHARM3D, a fully-coupled hull-mooring-riser dynamic analysis software [33]. The CHARM3D program has extensively been validated through comparisons with other commercial software, experimental and field measurements during the past two decades [18]. The inclinometer signals are generated by picking up the simulation results at the corresponding sensor locations, which may be called numerical-sensor signals. The top-tension signal was also generated by the same way, which may be called numerical tensioner. In case of real measurement, the signals may be contaminated by noises, which is assumed to be pre-filtered in the following simulation results. Then, the explained

algorithm is applied to those angle-sensor signals to produce the corresponding estimated bending moments, tensions, and internal stresses along the line and they are compared with their actual values calculated from CHARM3D.

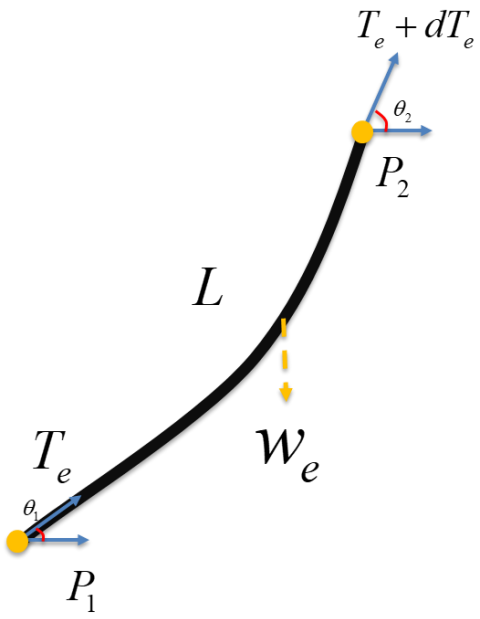

Figure 57 Tension distribution estimation model

$$T_e = T_{tw} + (-p_i A_i) - (-p_e A_e) \tag{4.8}$$

where $T_e = effective\ tension,\ T_{tw} = true\ wall\ tension,$

$p_i, p_e = inner, external\ pressure,\ A_i, A_e = inner, external\ area$

$$w_{effective} = w_{tw} + w_i - w_e \tag{4.9}$$

$w_{effective} = effective\ weight$

$w_{tw} = true\ wall\ weight$

$w_e, w_i = inner, external\ weight$

$$dT_e = (w_{effective}) \cdot L \cdot \sin(\theta_2) \tag{4.10}$$

4.2 TLP-FOWT Numerical Model

To test the proposed methodology, a FOWT with mini-TLP hull and tendon is selected. Its hull discretization is shown in Figure 58. The detailed particulars and characteristics of this FOWT are given in [35]. The hydrodynamic coefficients, such as added mass, radiation damping, first/second-order wave forces, are estimated by using the potential-based diffraction and radiation software, WAMIT, which is widely adopted in the offshore industry [39, 53]. Since the modeled hull is symmetric with respect to both X and Y axes, only a quarter of its surface below mean water level (MWL) is discretized by using 686 quadrilateral elements. Subsequently, the dynamic response of the fully coupled hull-mooring system is obtained by integration in time domain. To consider the viscous drag force on the hull, Morison drag element is used for the column. The drag force is calculated at the instantaneous hull position. At each time step, the entire system equations are assembled in a matrix form and solved. In this study, for simplicity, the dynamic interaction between the wind turbine and the hull is not considered assuming that the FOWT is idle and not generating power. Since we focus on the monitoring of tendon dynamics by a series of inclinometers, the numerical results are presented only for the tendons.

The applied wave direction and tendon numbering are shown in Figure 59. The water depth of 200m is considered. 10 bi-axial inclinometers are placed along the line to measure bi-axial slope angles. Table 26 shows the coordinates of tendon fairleads and anchor points and the pre-tensions. The tendon structural properties are given in Table 27. Several case

studies with different regular/irregular waves are presented in the following sections to assess the applicability of the proposed algorithm.

The locations of inclinometers are shown in Figure 60. As pointed out in the previous section, the bending moment is estimated along the tendon at the mid-point between the sensors, while tension can be obtained continuously along the line. To demonstrate the accuracy of the predicted tension and bending moment distribution from sensor signals against the actual values, three representative points, top, middle, and bottom, are selected. Given the considered wave direction, tendon number five is the most critically loaded, so it is focused in this study. In the present case study, the second-order sum-frequency wave loads and dynamic coupling with the elastic modes of turbine [54] were not included since they are not directly related to the objective of the present study. However, the second-order slowly-varying wave forces causing large-amplitude horizontal hull motions are included, as described in [35], since they are important in generating the bending of tendons.

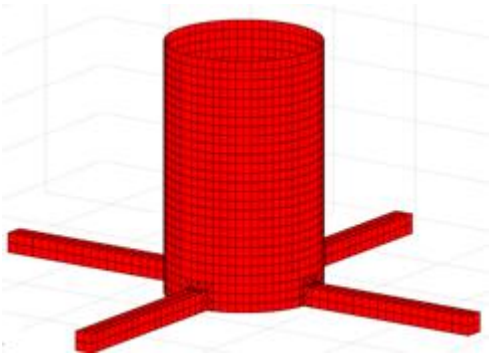

Figure 58 TLP Configuration

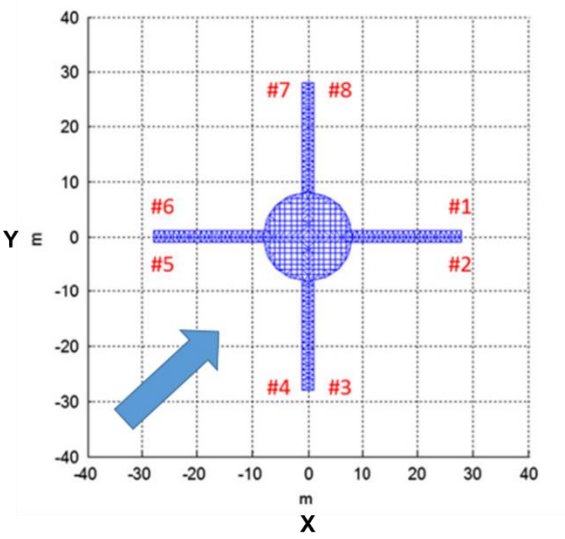

Figure 59 Wave direction (=45deg) and tendon numbering

Table 26 Tendon fairlead/anchor points and pre-tension

	Line No.	Fairlead Point			Anchor Point			Pre-Tension
		X	Y	Z	X	Y	Z	
		m	m	m	m	m	m	kN
Tendon	1	28.00	1.00	-24.00	28.00	1.00	-200.00	2008.816
	2	28.00	-1.00	-24.00	28.00	-1.00	-200.00	2008.816
	3	1.00	-28.00	-24.00	1.00	-28.00	-200.00	2008.816
	4	-1.00	-28.00	-24.00	-1.00	-28.00	-200.00	2008.816
	5	-28.00	-1.00	-24.00	-28.00	-1.00	-200.00	2008.816
	6	-28.00	1.00	-24.00	-28.00	1.00	-200.00	2008.816
	7	-1.00	28.00	-24.00	-1.00	28.00	-200.00	2008.816
	8	1.00	28.00	-24.00	1.00	28.00	-200.00	2008.816

Table 27 Tendon material properties

Tendon Structural Properties					
Outer Diameter	Wall Thickness	Mass in Air	Submerged Weight	Axial Stiffness (EA)	Bend Stiffness (EI)
[mm]	[mm]	[kg/m]	[kN/m]	[MN]	[MN-m^2]
457.2	100	335.25	1.454	5660	135

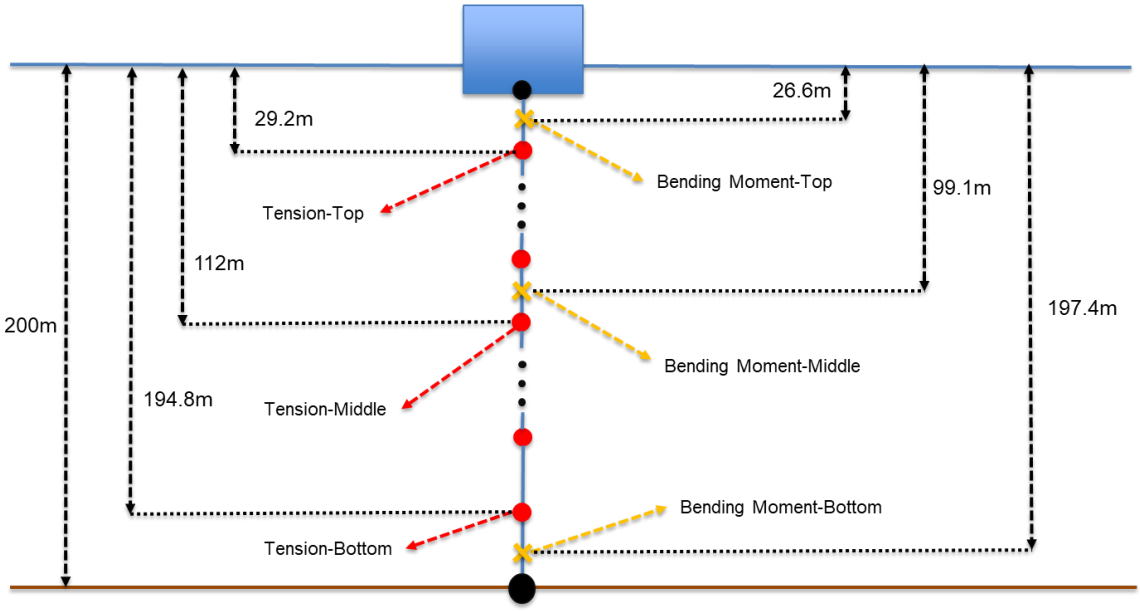

Figure 60 Measuring Location of Tension and Bending Moment

4.3 Numerical Results and Discussions

4.3.1 Case 01 – Sensor Interval Effect

First, sensor-positioning effects on the performance of the algorithm are assessed in the case of regular waves. Generally, near the top and bottom connections of the tendon, larger variation of bending moment occurs due to the imposed restrictions and denser distribution of sensors is needed. As shown in Table 28, two (uniform and variable) sensor distributions are considered for the 10 sensors. A regular wave (H=5m, T=10s) with 45-degree heading is inputted as environmental loading. Also, hinged boundary conditions are employed at both ends of the tendon.

Figure 61 and Figure 62 show tension and bending moment time series at three target points (top, middle, and bottom), comparing uniformly-distributed and top-bottom-clustered sensor positions. As expected, the mean tension decreases with water depth due to the reduction of effective weight. Whereas, the dynamic tension remains similar along the length. The predicted tension results by the proposed algorithm agree well with the actual values by the FEA dynamics simulation program. This means that the tension variation is mainly caused by the hull motions (or forced oscillation of its top point), which can be captured by the top-tension measurement, with negligible effect from the axial inertia or frictional forces on the tendon itself. In case of tension prediction, the two different sensor distributions produce almost the same results. As for bending moment distribution, as the tendon is pinned (moment-free) at both ends, larger bending-moment variations can be seen in the middle section. However, as lateral wave loads are higher at

the top section of the riser, larger difference in bending moment at that region between the predicted (by algorithm) and actual (by FEA program) values can be noticed for the uniform-sensor- distribution case. By using denser sensor distribution at the top region with the same number of sensors, better accuracy can be achieved there, as evidenced in Figure 62, while maintaining the same accuracy for the remaining part of the tendon. Therefore, from this point on, top and bottom clustered sensor distribution is used.

Table 28 Sensor installation location, Uniform VS Optimized

Sensor Location along the length	Uniform Distribution (uniform interval)	Optimized Distribution (variable interval)
[-]	m	m
#1 (top)	17.6	5.2
#2	17.6	5.2
#3	17.6	25.87
#4	17.6	25.87
#5 (middle)	17.6	25.87
#6	17.6	25.87
#7	17.6	25.87
#8	17.6	25.87
#9	17.6	5.2
#10 (bottom)	17.6	5.2

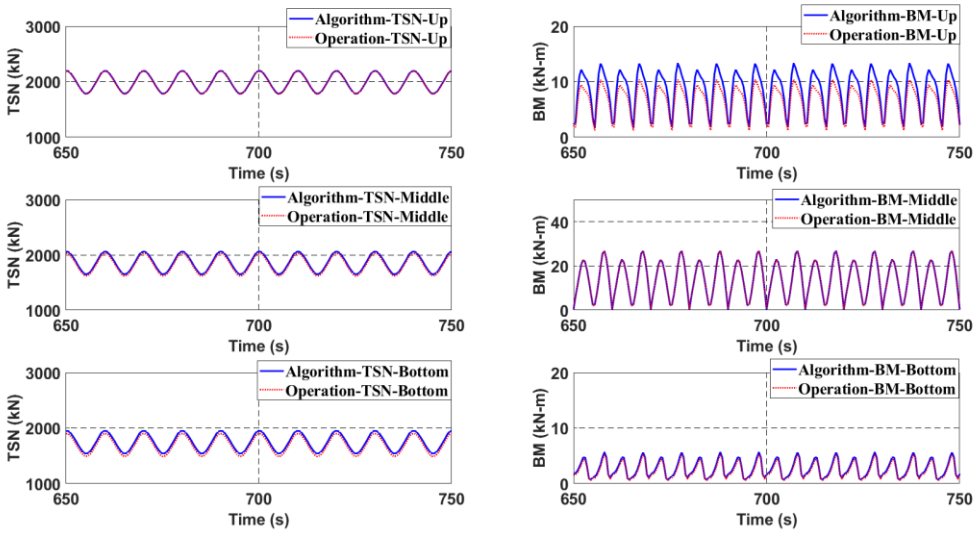

Figure 61 Tension and bending moment at 3 target points by uniform sensor distribution; comparison between the present algorithm and actual FEA calculation

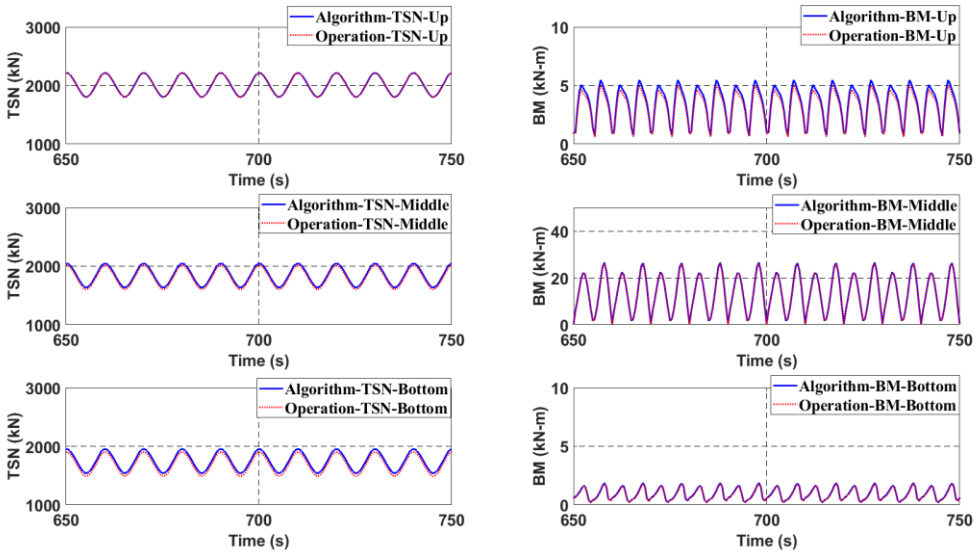

Figure 62 Tension and bending moment at 3 target points by variable sensor distribution; comparison between the present algorithm and actual FEA calculation

4.3.2 Case 02 – Tendon Failure Detection

An important goal of structural health monitoring by sensors is real-time failure detection. Since the TLP-FOWT is unmanned, the early detection of one-tendon failure from the sensor signals is critical to prevent further failures. Thus, in this section, we investigate whether the tendon failure and the resulting instantaneous increases in tensions and bending moments can be detected/assessed by the present method. In this regard, sudden failure of tendon (#4) is considered to demonstrate the algorithm's failure-detection capability. The model is setup so that tendon (#4) fails at 700s during the simulation. Figure 63 shows the corresponding results in tendon (#5). It can be seen that the mean tension suddenly increases after the failure, as expected, to keep the same hull buoyancy with less tendons. In addition, high-frequency transient responses happen at the system's natural frequency due to the impulse-kind-of loading right after the failure (Yang & Kim, 2010). Since it is transient response, it quickly dissipates by system damping. However, its initial overshoot in magnitude can be dangerous. From Figure 63 and Figure 64, we can see that the detailed physics of line tensions and bending moments can excellently be predicted by the present algorithm compared with the actual values. Interestingly, there is no increase in bending moment after one-line failure, as shown in Figure 63. On the other hand, the effects of the transient high-frequency tension variations are reflected, especially for top and bottom portions, on the bending moment after the time of failure. The decay rate of the transient signal in the bending moment is higher than that of tension since the lateral hydrodynamic damping is larger than the axial one.

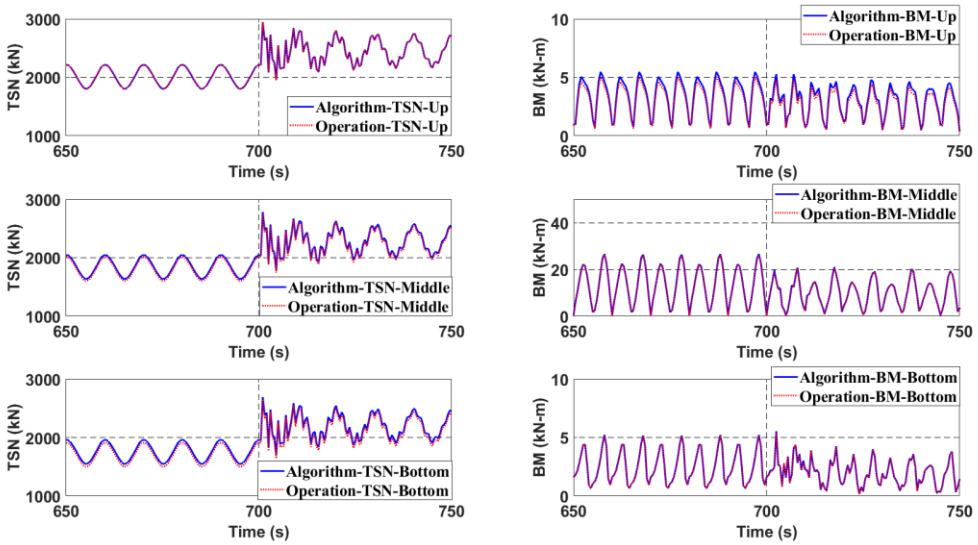

Figure 63 Tension and bending moment time series at 3 target points of tendon #5 after the sudden failure of tendon #4; comparison between the present algorithm and actual FEA calculation

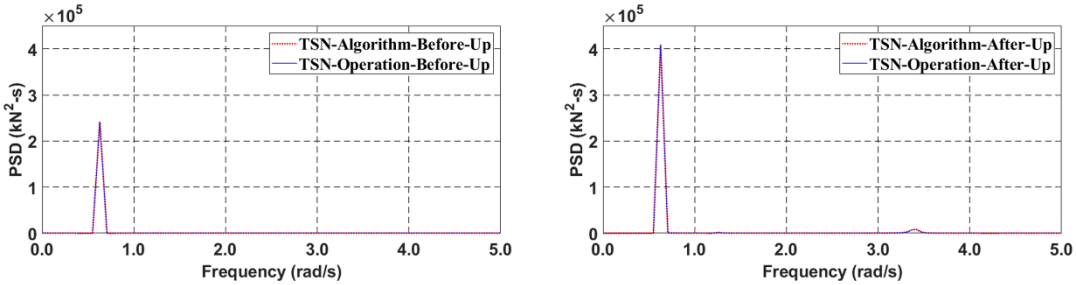

Figure 64 Tension spectra at the top point of tendon #5 before and after the sudden failure of tendon #4; comparison between the present algorithm and actual FEA calculation

4.3.3 Case 03 – Boundary-Condition Effect

In a real design, different boundary conditions may be used in the tendon-hull interface, such as stress joints, flex joints or roto-latches. As such, the algorithm is checked when the hull-joint BC is changed to fixed B.C. instead of hinged joint. Figure 65 shows the comparison between the hinged and fixed B.C. As expected, tension results are not sensitive to the boundary-condition change. However, bending moment results show significant differences, especially at the top region. The big increase of bending moment near the hull joint is clearly demonstrated in Figure 7.10 when compared with Figure 62. The present algorithm is able to capture the change of BCs with good accuracy.

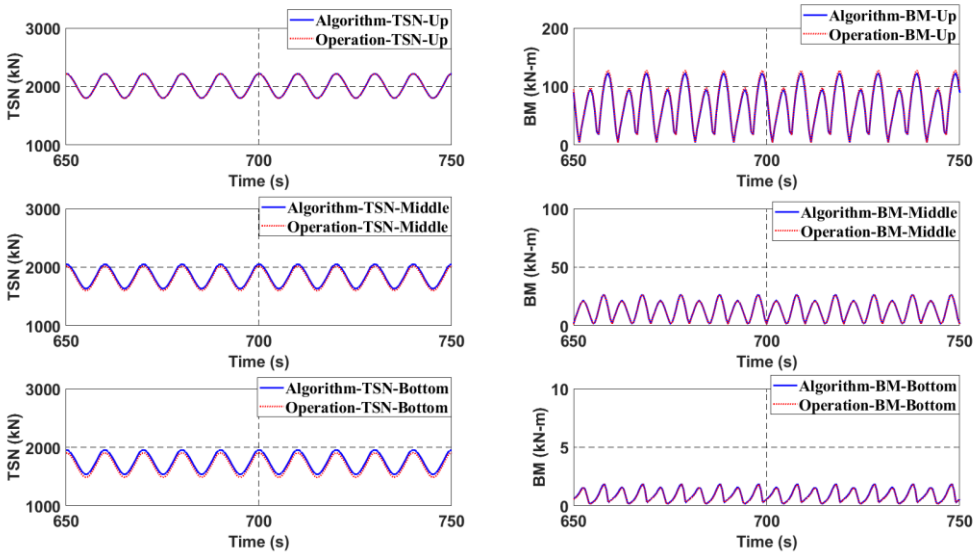

Figure 65 Tension and bending moment at 3 target points with the change of top BC to fixed one; comparison between the present algorithm and actual FEA calculation

4.3.4 Case 04 – Irregular Wave (10-yr storm)

So far, we investigated the performance of the developed algorithm in regular waves. The ensuing case studies 04, 05 and 06 are for more realistic irregular waves. To assess tendon's service life, tracking cumulative fatigue damage is needed. Fatigue damage is usually calculated using Miner's rule, as accumulated damage by stress variations and their occurrences for continuously varying environmental conditions. As such, continuously estimating bending moment and tension and the resulting bending and axial stresses at several hot spots is essential, which can effectively be done by the present algorithm. In this regard, most severe operational condition and extreme survival condition are employed to assess the accuracy and practicality of the developed algorithm. A typical 10yr-storm environment is given in Table 29. JONSWAP wave spectrum and API wind spectrum (wind speed of 19.9m/s at 10m altitude) were used to generate the corresponding random wave and wind signals. Figure 66 shows a comparison between the original spectrum and the regenerated spectrum from the generated irregular-wave time series, which confirms the correctness of the relevant procedure. The wave-wind-current are collinear and their heading is 45 degrees. Steady storm-induced shear current is also applied.

The resulting floater-motion time histories and spectra are presented in Figure 67. The results show that the natural frequencies are 0.08 rad/s for surge and sway, 1.65 rad/s for heave, 4.04 rad/s for roll and pitch, 0.35 rad/s for yaw, respectively. Heave motions have three peaks; the low-frequency peak is associated with the set-down effect caused by

slowly-varying horizontal motions, the second peak is at peak wave frequency, and the third peak is at heave natural frequency.

The corresponding tension and bending moment time histories and spectra for three target locations (top, middle, bottom) are shown in Figure 68, Figure 69, and Figure 70. The mean tension decreases with water depth due to less submerged weight below the point, while dynamic tension caused by hull heave-pitch motions remains similar along the length. The mean and dynamic bending moments are the largest at the middle location, as was the case of regular wave. Towards the top and bottom ends, bending moments decrease since hinged boundary conditions are applied at both ends. As the heading of environmental loading is 45 degrees and hull is symmetric with respect to the x and y axes, the resulting bending moment of the tendon should have about the same values with respect to the x-z and y-z planes. Also, it can be noticed that the dynamic bending moment has two peaks, one at very low frequency by floater's slowly-varying horizontal motions (surge and sway) and the other at the floater's heave natural frequency (1.65 rad/s). The effects of rotational motions (roll, pitch, yaw) on bending moments are small due to the hinged boundary conditions. Rotational motions are expected to more significantly affect dynamic bending moments if fixed B.C. is used, as shown later in Case 06. Examining the bending moment spectra, there is little energy near the peak wave frequency while tension energy is significant there by the combined effects of heave, roll, and pitch there.

Overall, the monitoring algorithm by sensors excellently captured the actual behaviors of tensions and bending moments along the tendons even without measuring the hull motions. The predicted and actual time series and spectra are almost identical (2.80% mean error for tension estimation and 1.60% for bending-moment estimation in time histories).

Table 29 Operating Design Condition Environmental Data (10yr-return period)

Wave				Current		Wind		
Gamma	Direction from TN	Significant Wave (Hs)	Spectral Period (Tp)	Depth	Vel.	Spectrum	10 min@+10m elevation	Direction from TN
(-)	(deg)	(m)	(s)	(m)	(m/s)	(-)	(m/s)	(deg)
2.4	Omni	6.58	8.2 (0.77 rad/s)	0	1.54	API	19.9	Omni
				25	1.00			
				50	0.50			
				mud	0.00			

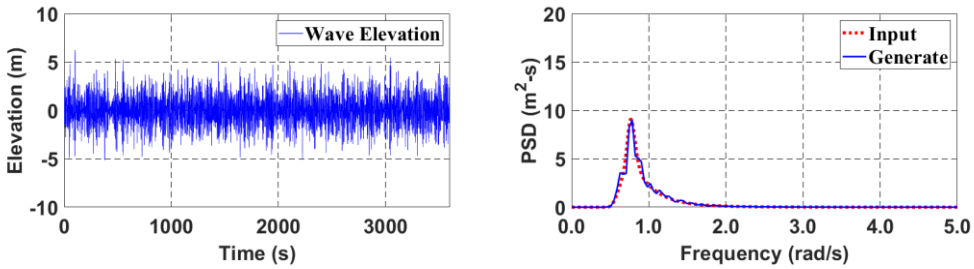

Figure 66 Generated irregular-wave time series and the corresponding wave spectrum for 10-yr storm

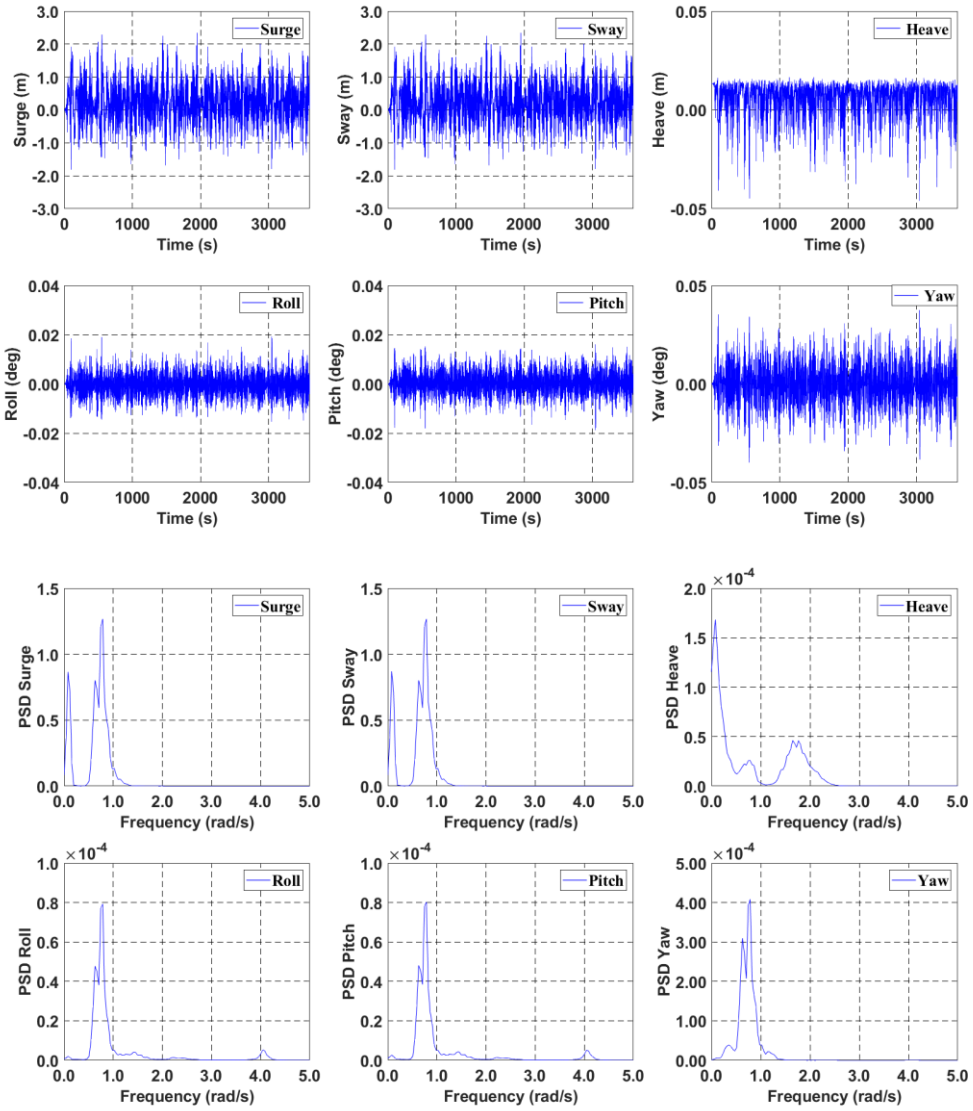

Figure 67 Floater 6DOF Motions; Time History (Up) and PSD (Down)

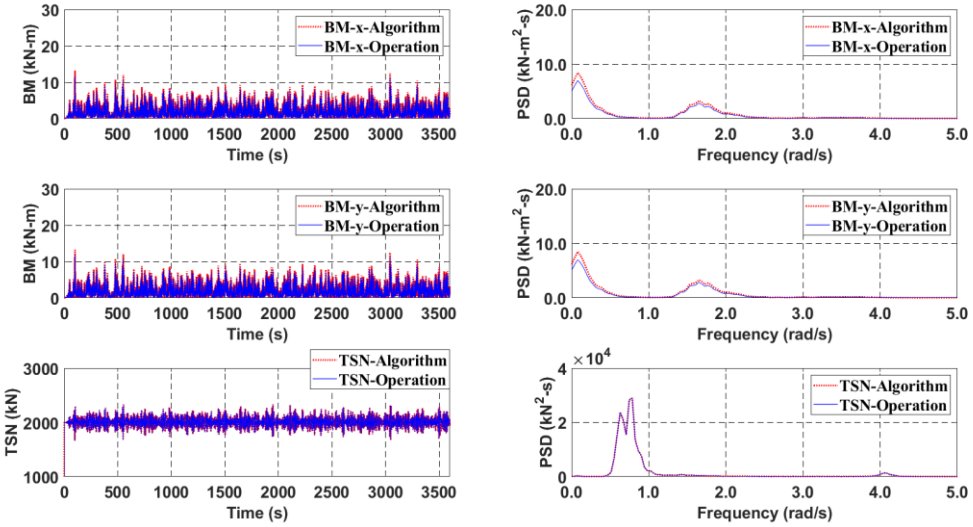

Figure 68 Tension & bending moment time histories and spectra at top target point of tendon #5

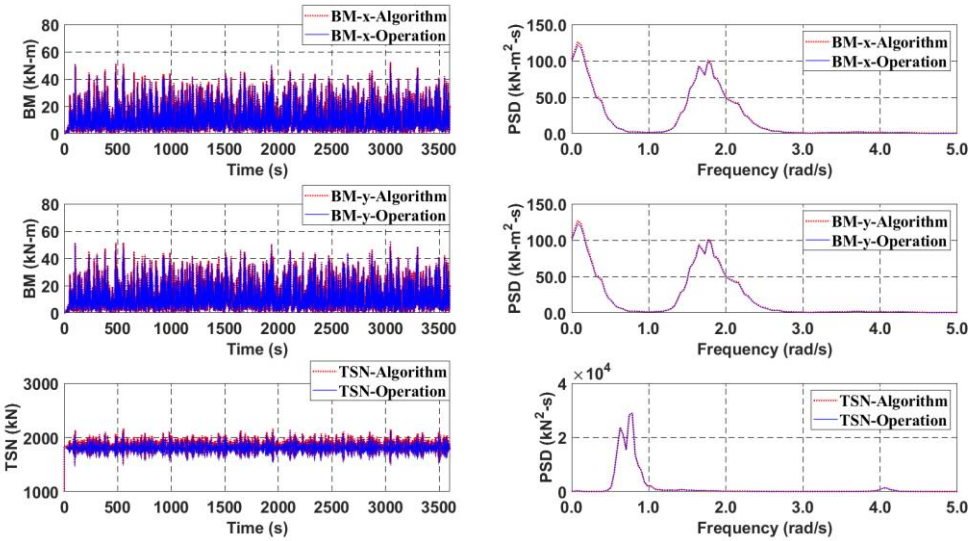

Figure 69 Tension & bending moment time histories and spectra at middle target point of tendon #5

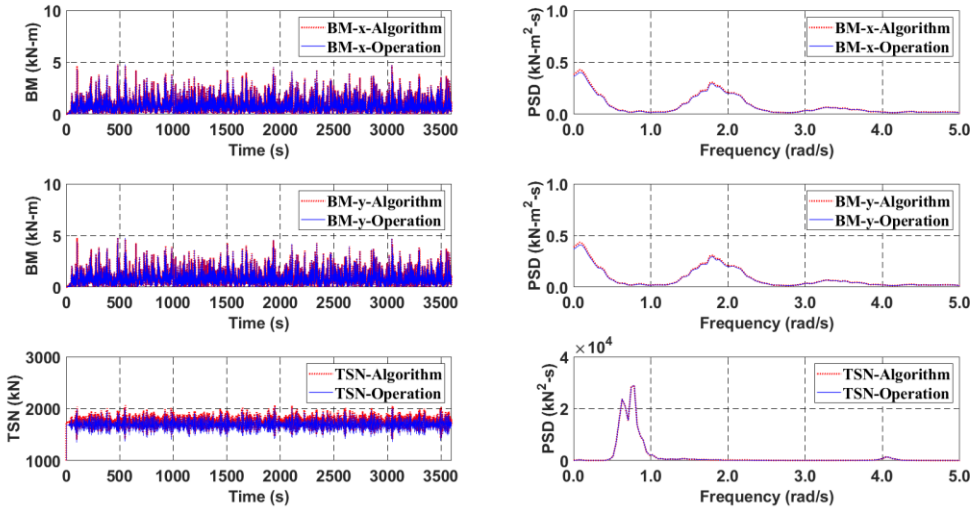

Figure 70 Tension & bending moment time histories and spectra at bottom target point of tendon #5

4.3.5 Case 05 – One-Line Failure Detection during 10-yr storm

As in Case 02, a sudden failure of one-line is simulated under 10-yr storm to verify if the developed monitoring algorithm can still detect the suddenly changed dynamic pattern effectively. Tendon #4 is intentionally broken at 1800s to check its detection capability. The floater motion time histories and spectra (before/after failure) are shown in Figure 71 and Figure 72. Comparing with the intact case (Figure 67), the mean heave suddenly increases after the failure due to the sudden weakening of the total vertical stiffness of tendons. Similarly, the roll mean is suddenly changed due to the imbalance in roll restoring moment.

Generally, a sudden change of trend after failure can clearly be detected in the time series of heave, roll, and yaw motions while those in surge-sway-pitch are less conspicuous. When the heave-motion signal is examined, downward motions are much greater than upward motions. After failure, the increased mean tensions on the remaining tendons tend to reduce their heave motions. The biggest changes after failure happen in roll and yaw responses mainly due to the change in restoring moments and loss of symmetrical balance. The sudden appearance of the dominant peak in the roll spectrum at the heave natural frequency after failure is an interesting asymmetric coupling phenomenon. It is seen that the roll natural frequency decreases from 4.04 rad/s to 3.5 rad/s after failure.

The corresponding tendon bending moment and tension signals for tendon #5 at the middle target points are presented in Figure 73 and Figure 74. The developed prediction algorithm

by sensors reproduce almost the same bending moment and tension signals compared to the actual values. The difference in time series is less than 1.2% in tension and 1.3% in bending moment. The general trends and accuracy for the top and bottom target points are similar to those of the middle target point. It is very clear that the developed real-time tendon-monitoring algorithm can produce even the details of the variations of tendon internal stresses in random waves including such a transient effect.

As expected, both mean and dynamic tensions increase after the failure. The increase in dynamic tension after failure is caused by that the new heave-pitch-roll natural frequencies get closer to the input wave spectrum. On the other hand, the dynamic bending moments decrease after failure because the mean tensions of the remaining tendons become higher and contribute to the reduction of dynamic bending moment.

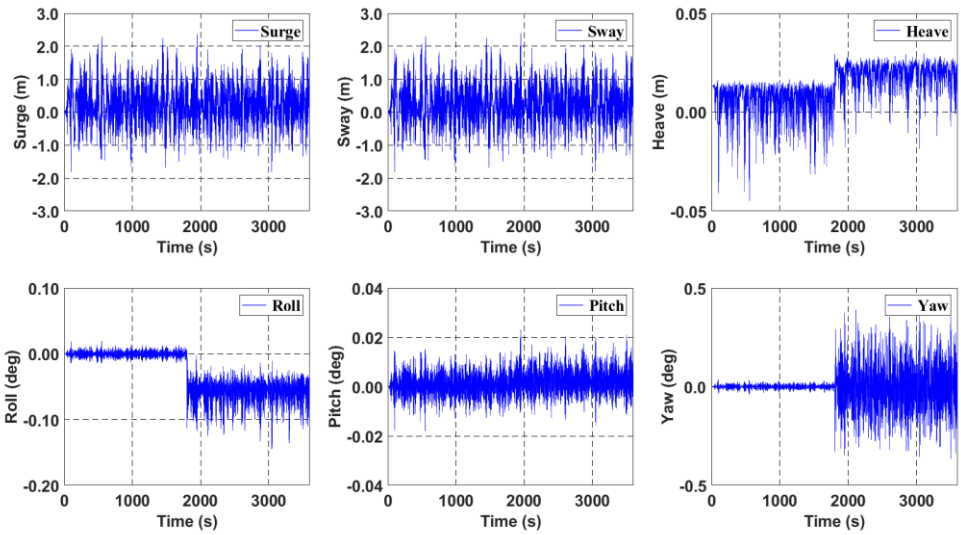

Figure 71 Floater 6DOF motion time series before and after failure

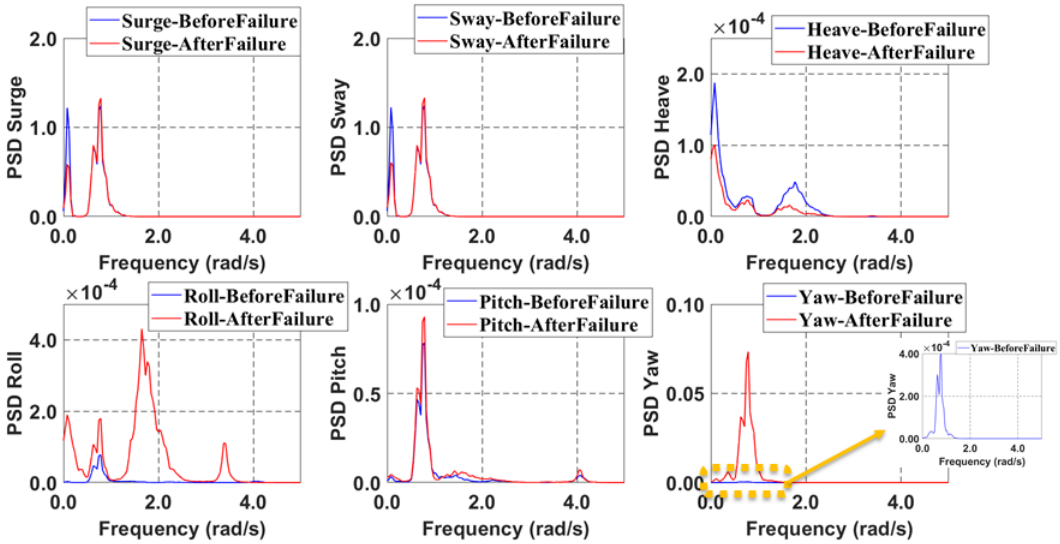

Figure 72 Floater 6DOF motion spectra before and after failure

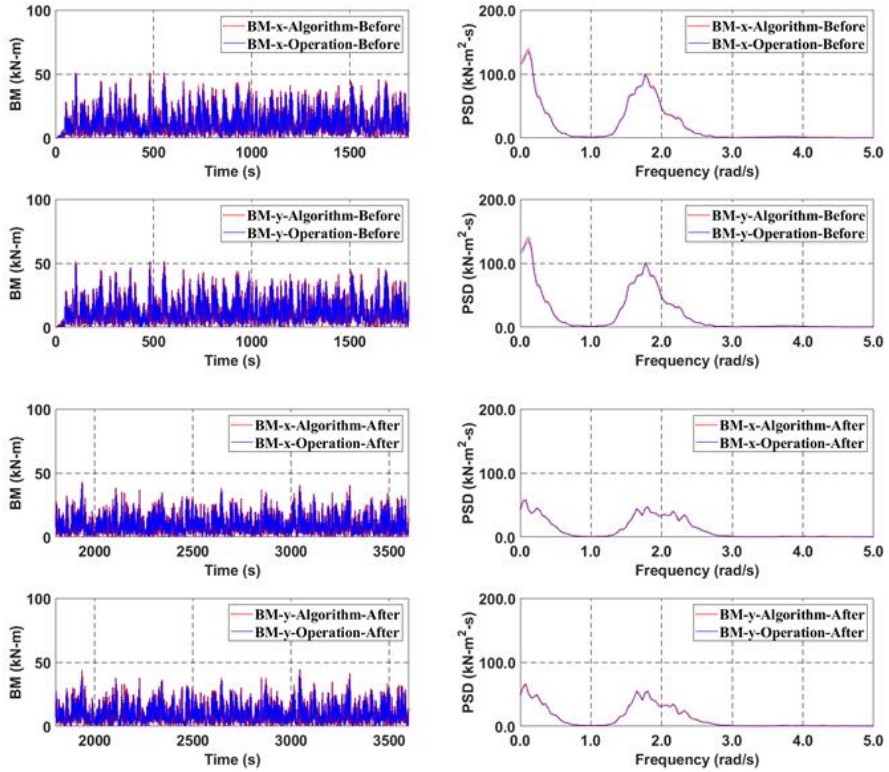

Figure 73 Bending moment time series and spectra of tendon #5 before and after tendon #4 failure

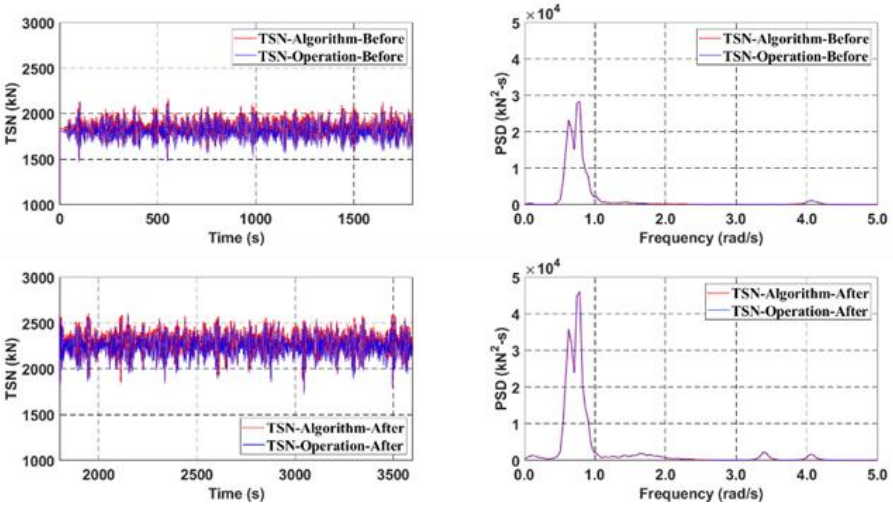

Figure 74 Tension time series and spectra of tendon #5 before and after tendon #4 failure

4.3.6 Case 06 – Extreme Condition (100-yr storm)

Finally, the monitoring capability of the developed algorithm for an extreme condition is investigated. Table 30 presents the extreme survival environmental conditions with 100yr return period in GOM (Gulf of Mexico). As expected, compared to the maximum operational condition (Figure 67), the floater motions are significantly increased while the overall trends are similar. To observe the sensitivity of tendon's bending moment for different boundary conditions, the top-end condition is changed to fixed BC. Similar to Case 04, tension and bending moment comparisons are shown in Figure 76 (top), Figure 77 (middle) and Figure 78 (bottom). As in previous simulations, the dynamic tension does not vary significantly along depth. Due to the fixed top B.C., larger bending moments are observed near the top, as floater rotational (pitch and roll) responses are more directly transmitted to the tendon. The bending moments near the bottom remain small due to the moment-free hinged boundary condition. The general trends for bending moments are similar to those of 10-yr storm showing three peaks; first at low frequency associated with slowly varying surge-sway motions, second at wave peak frequency, third at wave peak frequency. The results show that the developed algorithm can monitor the actual values of tensions and bending moments even in the extreme environmental condition, with the errors smaller than 5.13% in tension time series and 1.62% in bending-moment time series. Through the previous six case studies, it is clearly shown that the developed algorithms have the capability of highly accurate real-time monitoring of tendon's internal stresses (axial and bending stresses) along the line for various ocean environments. This capability

enables the real-time monitoring of accumulated fatigue damage at hot-spots by adding the corresponding fatigue-calculation algorithm, which is not presented in this research.

Table 30 Extreme Design Condition Environmental Data (100yr-return period)

Wave				Current		Wind		
Gamma	Direction from TN	Significant Wave (Hs)	Spectral Period (Tp)	Depth	Vel.	Spectrum	10 min@+10m elevation	Direction from TN
(-)	(deg)	(m)	(s)	(m)	(m/s)	(-)	(m/s)	(deg)
2.4	Omni	16.2	12.1 (0.52 rad/s)	0	3.00	API	60.0	Omni
				25	2.50			
				50	2.00			
				100	1.00			
				mud	0.00			

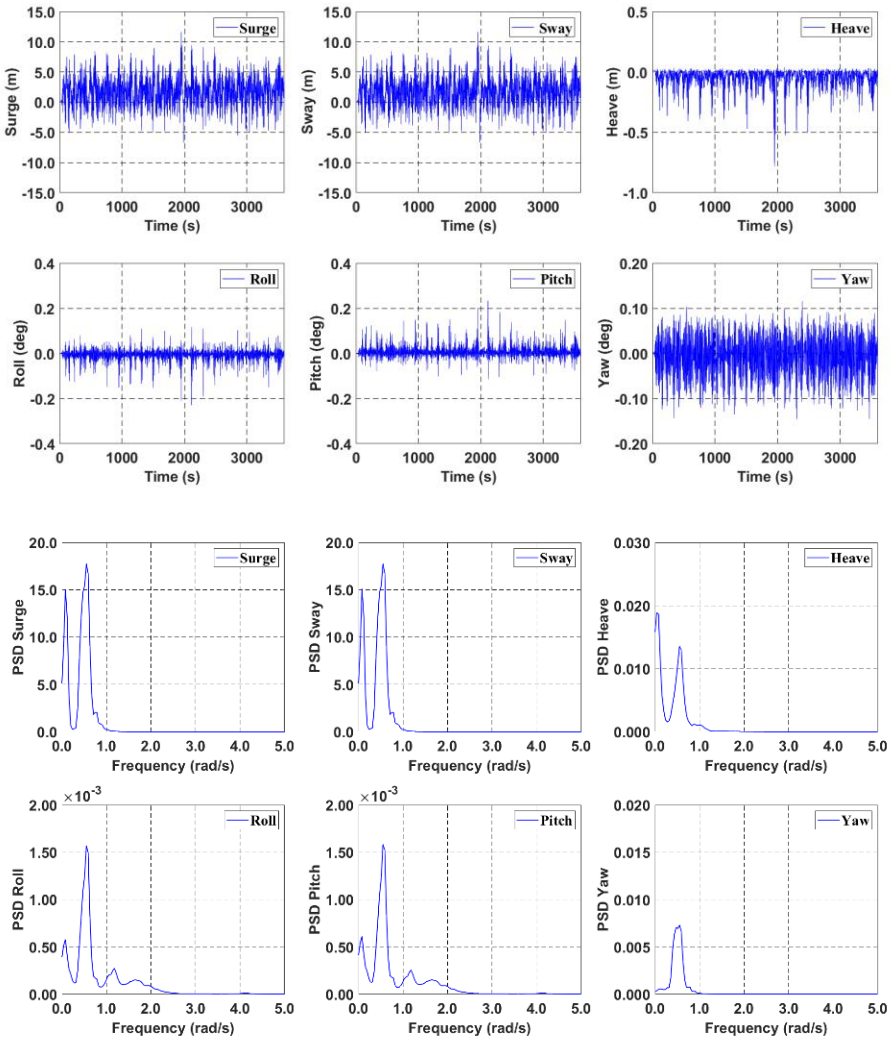

Figure 75 Floater 6DOF Motions; Time History (Up) and PSD (Down)

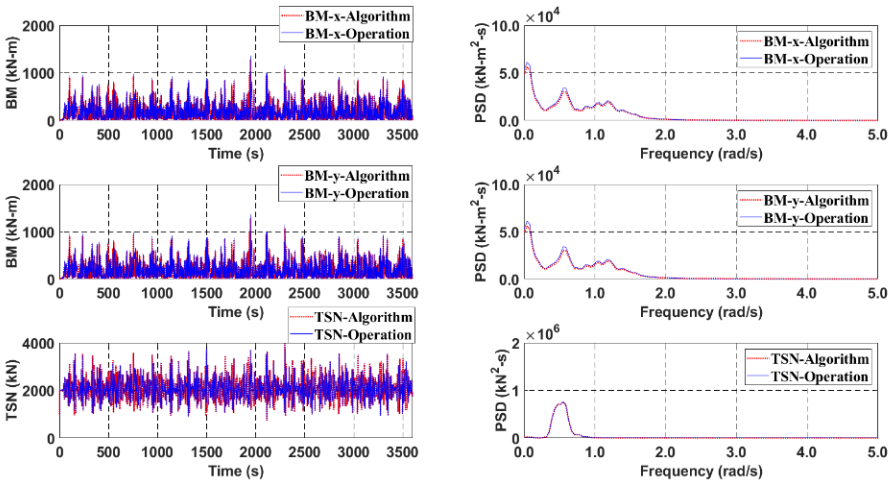

Figure 76 Tension & bending moment time histories and spectra at top target point of tendon #5

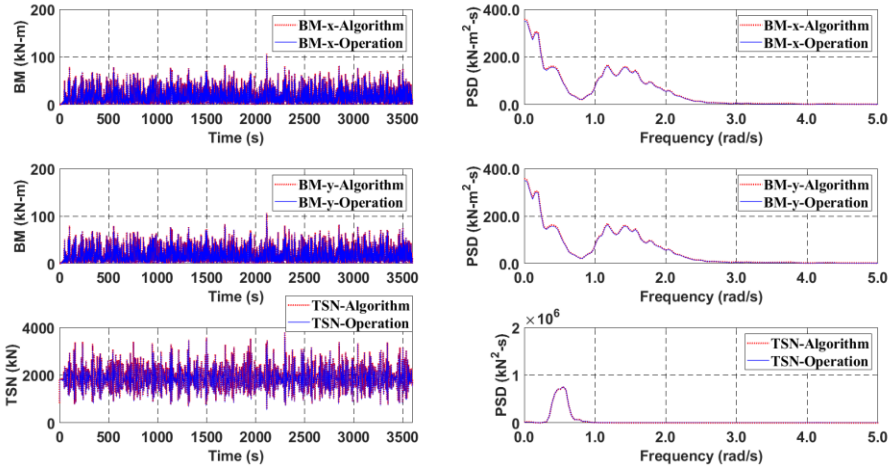

Figure 77 Tension & bending moment time histories and spectra at middle target point of tendon #5

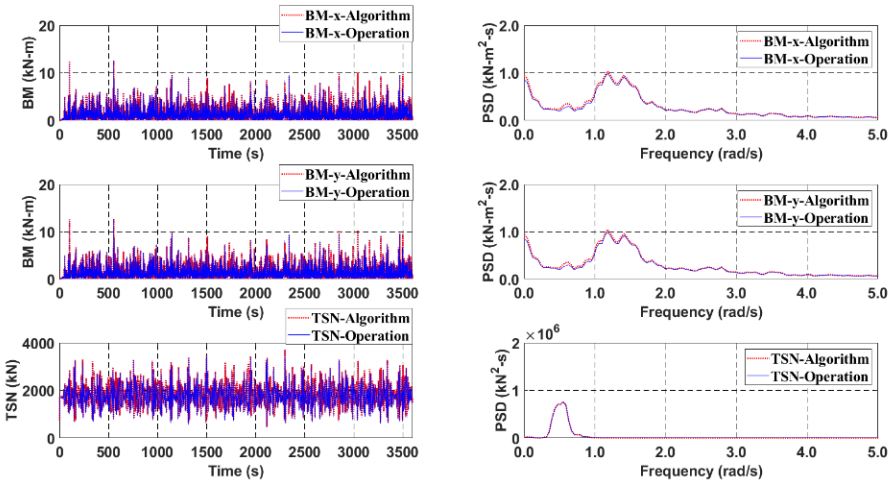

Figure 78 Tension & bending moment time histories and spectra at bottom target point of tendon #5

5. REAL-TIME TRACE OF RISER PROFILE AND BENDING MOMENT WITH INCLINOMETERS

5.1 Methodology – Riser Profile (Node Displacements) Tracing

5.1.1 Derivation of Line Length Equation in 3D

In this section, an analytical solution for node displacements calculation for riser profile tracing using an inclinometer will be explained. First, let's start derivation of the line length equation in 3D space as shown in Figure 79. The entire line length ($L_{P_AP_B}$) can be calculated by the summation of linearized small segments (L_i) length as shown in eq.5-1. Linearized each small segment length can be obtained (eq.5-2). By applying the mean value theorem (eq.5-3) with the decomposed arbitrary quadratic interpolation function (Figure 80), a small segment length equation (eq.5-2) can be re-written as shown in eq.5-4. By substituting the derivative of arbitrary quadratic interpolation function (eq.5-5) into Eq.5-4, the small segment length equation (eq.5-2) is re-arranged with arbitrary coefficients (eq.5-6). After applying the basic infinite integral theorem, the entire line length ($L_{P_AP_B}$) in 3D space can be expressed with respect to the only single variable (x). This derived line length equation (a function of only single variable) in 3D space will be used to resolve the quadratic interpolation function for riser node displacements calculation in the next section.

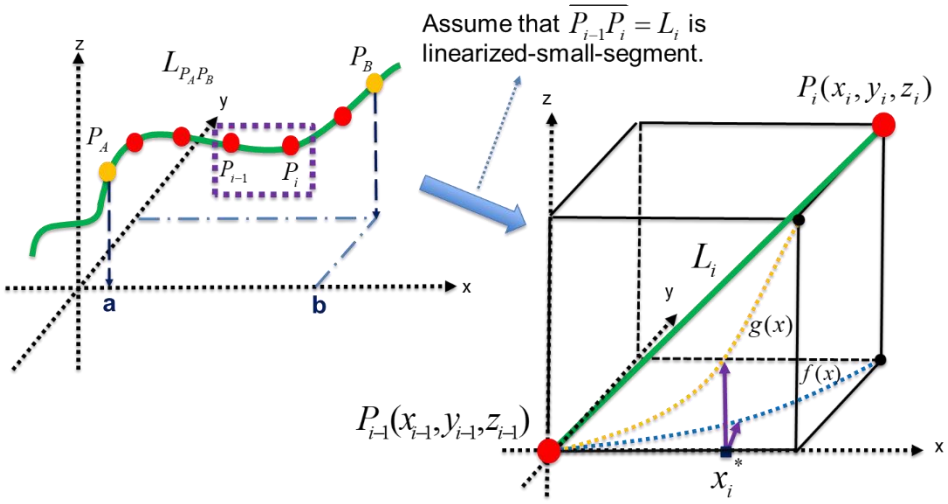

Figure 79 Configuration for Derivation of Line Length Equation in 3D

$$L_{P_AP_B} = \sum_{i=1}^{n} |P_{i-1}P_i| \tag{5-1}$$

$$L_i = |P_{i-1}P_i| = \sqrt{(x_{i-1} - x_i)^2 + (y_{i-1} - y_i)^2 + (z_{i-1} - z_i)^2} = \sqrt{(\Delta x_i)^2 + (\Delta y_i)^2 + (\Delta z_i)^2} \tag{5-2}$$

Mean Value Theorem

$$\Delta y_i = f'(x_i^*) \cdot \Delta x_i, \quad \text{where} \quad x_i^* \text{ in } [x_{i-1}, x_i] \tag{5-3}$$
$$\Delta z_i = g'(x_i^*) \cdot \Delta x_i, \quad \text{where} \quad x_i^* \text{ in } [x_{i-1}, x_i]$$

$$|P_{i-1}P_i| = \sqrt{(\Delta x_i)^2 + (\Delta y_i)^2 + (\Delta z_i)^2} = \sqrt{(\Delta x_i)^2 + (f'(x_i^*) \cdot \Delta x_i)^2 + (g'(x_i^*) \cdot \Delta x_i)^2} \tag{5-4}$$
$$= \sqrt{(1 + (f'(x_i^*))^2 + (g'(x_i^*))^2} \cdot \Delta x_i$$

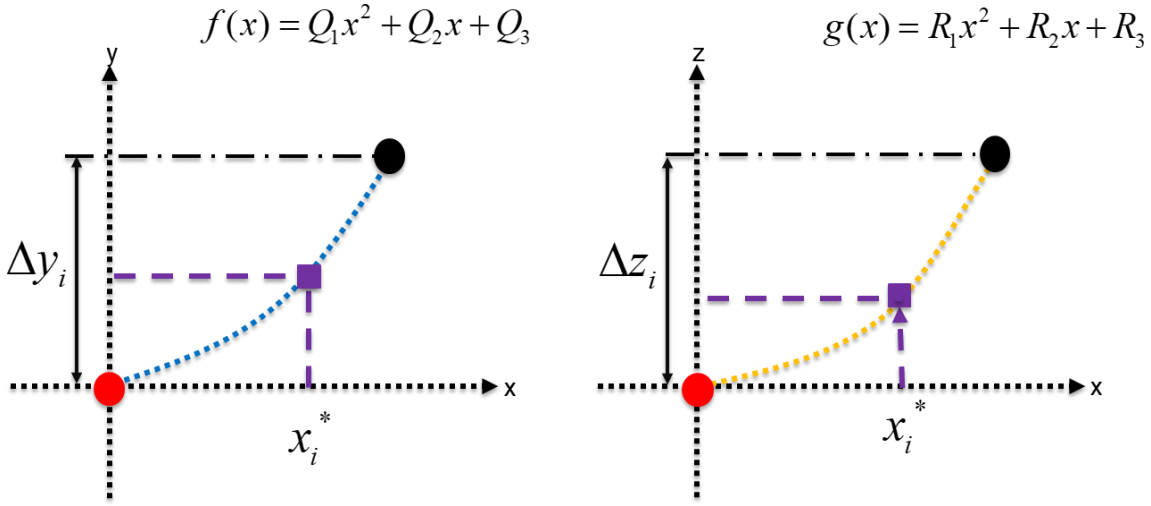

Figure 80 Decomposed Quadratic Interpolation function for small segment (xy plane(left), xz plane(right))

$$f'(x_i^*) = 2Q_1x_i^* + Q_2$$
$$g'(x_i^*) = 2R_1x_i^* + R_2 \qquad (5\text{-}5)$$

$Q_1,\ Q_2,\ R_1, R_2$ are arbitary coeficients

$$|P_{i-1}P_i| = \sqrt{(1 + (A\cdot(x_i^*)^2 + B\cdot(x_i^*) + C)} \cdot \Delta x_i,$$

where $\overline{A}=4\cdot(Q_1^2 + R_1^2),\ \ \overline{B} = 4\cdot(Q_1Q_2 + R_1R_2),\ \ \overline{C} = Q_2^2 + R_2^2$ (5-6)

$\overline{A}, \overline{B}, \overline{C}$ are also arbitary coeficients

$$L_{P_AP_B} = \lim_{\Delta x\to 0}\sum_{i=1}^{n}|P_{i-1}P_i| = \lim_{\Delta x\to 0}\sum_{i=1}^{n}\sqrt{(1 + (\overline{A}\cdot(x_i^*)^2 + \overline{B}\cdot(x_i^*) + \overline{C})} \cdot \Delta x$$

$$\Rightarrow \int_a^b \sqrt{(1 + (2Ax + B)^2} \cdot dx \qquad (5\text{-}7)$$

A, B are also arbitary coeficients

5.1.2 Node Displacements Calculation

Continually, the derivation of an analytical solution for node displacement tracing will be introduced. Usually, based on the basic FEM (Finite Element Method) beam theory, displacements along the beam can be obtained using interpolation function and it can be resolved with four boundary conditions. With the assumption that the riser is modeled with several beam segments connection, riser node displacements can be traced if the required information is given. But, in this research, it is assumed that only inclinometer data at both ends of each riser segment and hang-off and anchor positions are available.

Configuration for node displacements tracing is presented in Figure 81. The interpolation function between each sensor and its boundary conditions are tabulated in Table 31. Also, Eq. 5-8 represents the interpolation function and its spatial derivative equation with respect to the global coordinate system. By applying boundary conditions at the first segment endpoint (hang-off), the third coefficient (C) of the interpolation function can be derived (eq.5-9). Continually, with a combination of eq. 5-8 and third boundary condition, the second coefficient (B) also can be estimated. Now, one more condition is required to obtain the first coefficient (A). As explained in the previous section, the equation for line length (eq.5-12) between two points (sensor interval) can be applied here. By using the equation of line length (eq.5-12) and fourth boundary condition (eq.5-11), the first coefficient of interpolation function (A) finally can be obtained as shown in eq.5-13. If then, the interpolation function can be expressed as a function of only declinations (

θ_{xz_A}, θ_{xz_B}) as shown in eq.5-13. Finally, two displacements of other ends (x and z) can be obtained (eq.5-14) firstly.

Similarly, by repeating the same process with respect to the y-direction, the coefficients for interpolation function with respect to the xy-direction can be also obtained (eq.5-15) and another displacement of other end in y-direction finally can be calculated (eq.5-16) using same x displacement which is obtained previously. Those obtained node displacements can be used as an input again for the calculation of the next node displacements with the other riser segment. By repeating the above process, the entire riser node displacements can be traced in order of sequence from the top. Finally, the entire riser profile also will be generated with a combination of inclinometers and sensor interval.

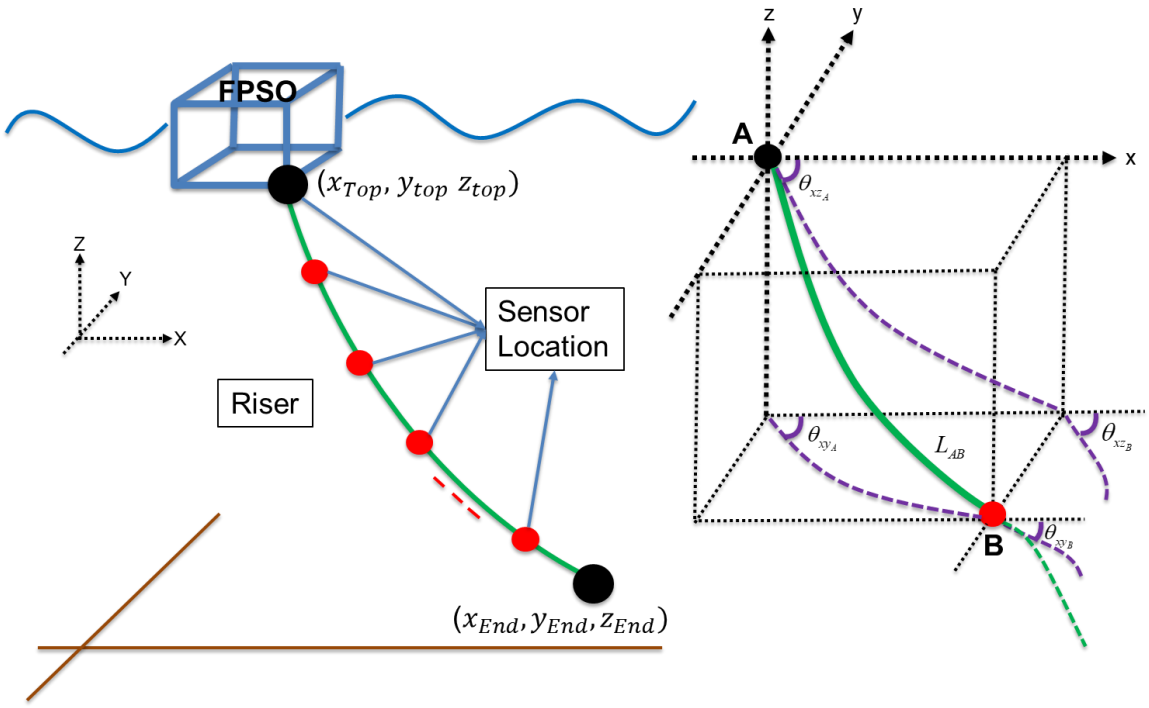

Figure 81 Configuration for Node Displacements Tracing

Table 31 Interpolation Function & Boundary Conditions, Node Displacements Calculation for Riser Profile Tracing, xz-direction

Quadratic Interpolation Function	$F_{xz}(x) = A_{xz} \cdot x^2 + B_{xz} \cdot x + C_{xz}$ A_{xz}, B_{xz}, C_{xz} are arbitary coeficients
Boundary Conditions	• $F_{xz}(x = x_A) = x_A \Rightarrow F_{xz}(x = 0) = 0$ • $F_{xz}(x = x_B) = z_B$ • $\left.\frac{dF_{xz}}{dx}\right\|_{x=x_A=0} = \theta_{xz_A} \Rightarrow B_{xz} = \theta_{xz_A}$ • $\left.\frac{dF_{xz}}{dx}\right\|_{x=x_B} = \theta_{xz_B} \Rightarrow A_{xz}x_B + B_{xz} = \theta_{xz_B}$

$$F_{xz}(x) = A_{xz}x^2 + B_{xz}x + C_{xz}, \quad \frac{dF_{xz}}{dx} = 2A_{xz}x + B_{xz} \tag{5-8}$$

$$F_{xz}(x = x_A) \Rightarrow F_{xz}(x = 0) = 0 \quad \Rightarrow C_{xz} = 0 \tag{5-9}$$

$$\left.\frac{dF_{xz}}{dx}\right|_{x=x_A=0} = \theta_{xz_A} \Rightarrow B_{xz} = \theta_{xz_A} \tag{5-10}$$

$$\left.\frac{dF_{xz}}{dx}\right|_{x=x_B} = \theta_{xz_B} \Rightarrow 2A_{xz}x_B + B_{xz} = \theta_{xz_B} \Rightarrow 2A_{xz}x_B + \theta_{xz_A} = \theta_{xz_B} \tag{5-11}$$

$$L = \int_{x_A}^{x_B} \sqrt{(1 + (A_{xz} \cdot x + B_{xz})^2} \cdot dx = \int_0^{x_B} \sqrt{(1 + (A_{xz} \cdot x + \theta_{xz_B})^2} \cdot dx \tag{5-12}$$

$$F_{xz}(x) = A_{xz}x^2 + B_{xz}x + C_{xz}$$

where,

$$A_{xz} = \frac{1}{4 \cdot L}[(\sqrt{\theta_{xz_B}{}^2 + 1} \cdot \theta_{xz_B} + \sinh^{-1}(\theta_{xz_B})) - (\sqrt{\theta_{xz_A}{}^2 + 1} \cdot \theta_{xz_A} + \sinh^{-1}(\theta_{xz_A}))] \tag{5-13}$$

$$B_{xz} = \theta_{xz_A}, \quad C_{xz} = 0$$

$$x_B = \frac{\theta_{xz_B} - \theta_{xz_A}}{2A_{xz}} \tag{5-14}$$

$$z_B = F_{xz}(x_B) = A_{xz}x_B{}^2 + B_{xz}x_B + C_{xz}$$

$$F_{xy}(x) = A_{xy}x^2 + B_{xy}x + C_{xy}$$

where,

$$A_{xy} = \frac{1}{4 \cdot L}[(\sqrt{\theta_{xy_B}{}^2 + 1} \cdot \theta_{xy_B} + \sinh^{-1}(\theta_{xy_B})) - (\sqrt{\theta_{xy_A}{}^2 + 1} \cdot \theta_{xy_A} + \sinh^{-1}(\theta_{xy_A}))] \quad (5\text{-}15)$$

$$B_{xy} = \theta_{xy_A}, \quad C_{xy} = 0$$

$$y_B = F_{xy}(x_B) = A_{xy}x_B{}^2 + B_{xy}x_B + C_{xy} \quad (5\text{-}16)$$

5.2 Methodology – Riser Discretized BM (bending moment)

In this section, the analytical solution for riser bending moment estimation will be explained. As explained previously, if the quadratic interpolation function is used, the curvature which is double spatial-derivative of interpolation function becomes constant. Therefore, it cannot be used for proper bending-moment distribution continuous at each nodal point. Thus, the cubic interpolation function with respect to the generalized s-coordinate system with directional cosine angles ($\theta_{x_A}, \theta_{x_B}$) is employed (eq. 5-17) here with corresponding boundary conditions (eq. 5-18). This is possible since all the instantaneous nodal positions can be determined as explained in the previous section.

$$v_x(s) = f(v_{x_A}, v_{x_B}, \theta_{x_A}, \theta_{x_B}, s) = a_0 + a_1 s + a_2 s^2 + a_3 s^3 \tag{5-17}$$

$$v_x(s = s_A = 0) = v_{x_A},\ v_x(s = s_B = L) = v_{x_B},$$
$$\frac{dv}{ds}_{s=s_A=0} = \theta_{x_A},\ \frac{dv}{ds}_{s=s_B=L} = \theta_{x_B} \tag{5-18}$$

Applying boundary conditions (eq. 5-18) to the third-order polynomial equation (eq.5-17), the eq. 5-17 can be re-written as (eq. 5-19). The third-order polynomial equation can be re-constructed as matrix form as shown in eq. 5-20. In eq. 5-20, N_1, N_2, N_3, N_4 represent shape functions and ξ expresses the nodal displacements and inclinations.

$$v_x(s) = (1 - \frac{3s^2}{L_{AB}{}^2} + \frac{2s^3}{L_{AB}{}^3})v_{x_A} + (s - \frac{2s^2}{L_{AB}} + \frac{s^3}{L_{AB}{}^2})\theta_{x_A}$$
$$+(\frac{3s^2}{L_{AB}{}^2} - \frac{2s^3}{L_{AB}{}^3})v_{x_B} + (\frac{s^3}{L_{AB}{}^2} - \frac{s^2}{L_{AB}})\theta_{x_B} \tag{5-19}$$

$$v_x(s) = [\mathrm{N}_1\mathrm{N}_2\mathrm{N}_3\mathrm{N}_4]\begin{Bmatrix} v_{x_A} \\ \theta_{x_A} \\ v_{x_B} \\ \theta_{x_B} \end{Bmatrix} = [\mathrm{N}]\{\xi\} \tag{5-20}$$

By substituting eq. 5-20 to normal stress for beam bending (eq.5-21), eq. 5-22 is derived. Then, the beam bending moment equation can be derived as shown in eq. 5-23.

$$\sigma_x(s) = \frac{M_x y_{\max}}{I} = y_{\max} E \frac{d^2[\mathrm{N}]}{ds^2}\{\xi\} \tag{5-21}$$

$$\begin{aligned} \sigma_x(s) = y_{\max} E[&(\frac{12s}{L_{AB}^{\ 3}} - \frac{6}{L_{AB}^{\ 2}})v_{x_A} + (\frac{6s}{L_{AB}^{\ 2}} - \frac{4}{L_{AB}})\theta_{x_A} \\ &+(\frac{6}{L_{AB}^{\ 2}} - \frac{12s}{L_{AB}^{\ 3}})v_{x_B} + (\frac{6s}{L_{AB}^{\ 2}} - \frac{2}{L_{AB}})\theta_{x_B}] \end{aligned} \tag{5-22}$$

$$\begin{aligned} \mathrm{M}_x = \mathrm{EI}\cdot[&(\frac{12s}{L_{AB}^{\ 3}} - \frac{6}{L_{AB}^{\ 2}})v_{x_A} + (\frac{6s}{L_{AB}^{\ 2}} - \frac{4}{L_{AB}})\theta_{x_A} \\ &+(\frac{6}{L_{AB}^{\ 2}} - \frac{12s}{L_{AB}^{\ 3}})v_{x_B} + (\frac{6s}{L_{AB}^{\ 2}} - \frac{2}{L_{AB}})\theta_{x_B}] \end{aligned} \tag{5-23}$$

Eq (5-23) represents the distribution of bending moment along the line. It is interesting to see that the bending moment at the mid-point of each element can be obtained in a greatly simplified form as shown in eq. 5-24 by inputting $\frac{s}{L_{AB}} = 0.5$ to eq. 5-23.

$$M_x = EI \cdot [\frac{1}{L_{AB}}(\theta_{x_B} - \theta_{x_A})]$$
$$M_y = EI \cdot [\frac{1}{L_{AB}}(\theta_{y_B} - \theta_{y_A})] \quad (5\text{-}24)$$
$$M_z = EI \cdot [\frac{1}{L_{AB}}(\theta_{z_B} - \theta_{z_A})]$$

For those points other than the mid-length point, the second spatial derivative (curvature) of the cubic shape function can be used. In the following section, we will prove whether the derived analytical solutions for node displacements and bending moments can actually be used for the real-time tracing of riser profile and bending moment from inclinometer signals only. In the present numerical experiment, the actual riser profile and bending moment were taken from the time-domain system simulation by the commercial program OrcaFlex (widely adapted in oil & gas industry). Then the numerical riser inclination signals at the inclinometer locations were taken and inputted with the given top point (from GPS) to the developed algorithm to see whether it can actually reproduce the actual riser profile and stress at each time step. The numerical experiment closely emulates the real situation except that the physical sensor is replaced by the numerical sensor. For simplicity, the potential detrimental effect of small physical sensor noise is not considered here. However, it was shown that the present algorithm is much more robust against sensor noises than the accelerometer-based method since double time integration is not needed at each time step.

5.3 Explanation of Target Structure – FPSO with SCR and SLWR

As a target structure, FPSO (Floating Production Storage and Offloading) system with SCR (Steel Catenary Riser) or SLWR (Steel Lazy Wave Riser) is adopted in this research. It is well known that the SCR may experience local dynamic buckling near touch-down zone under extreme storm conditions [55]. To circumvent the problem, lazy-wave risers are frequently employed.

Figure 82 and Figure 83 present the configuration of the FPSO system with SCR or SLWR. The sensor distribution along the riser with 10-m interval is presented in Figure 84. As a floater, the default FPSO given by OrcaFlex was selected with the corresponding added mass, radiation damping, first- and second-order wave loads [38]. Furthermore, a total of 12 spread mooring lines (with four groups) are employed for the station-keeping in 100m water depth. Each mooring line consists of chain components for entire arc length. For the SCR and SLWR, steel tube pipe with 356mm outer diameter is used. In the SLWR case, buoyancy modules are attached to make a lazy wave shape along the riser at arc length 100m ~ 110m. The details of the mooring and riser properties and SLWR buoyancy modules are tabulated in Table 32 and Table 33. For SCR and SLWR line segment modelling, each segment length of 0.1m was used for OrcaFlex. Furthermore, to represent seabed for the seabed-touching riser elements, the seabed stiffness of 50 kN/m^3 is considered. For simplicity, the seabed induced Coulomb friction and damping effect are not considered in the numerical simulations. For the boundary conditions at the hang-off and anchor points, frictionless-hinged boundary condition (B.C.) is used as a typical condition of the riser. The 1-yr and 50-yr storm conditions with a co-linear WWC (wind-

wave-current) heading of 45 degrees are considered as detailed in Table 34. For the wave and wind spectra, JONSWAP wave and API wind spectra are adopted. For the corresponding current profile, 1/7 power law is applied as shown in eq. 5-25. To demonstrate the prediction capability, all the results are plotted for 200s simulation duration.

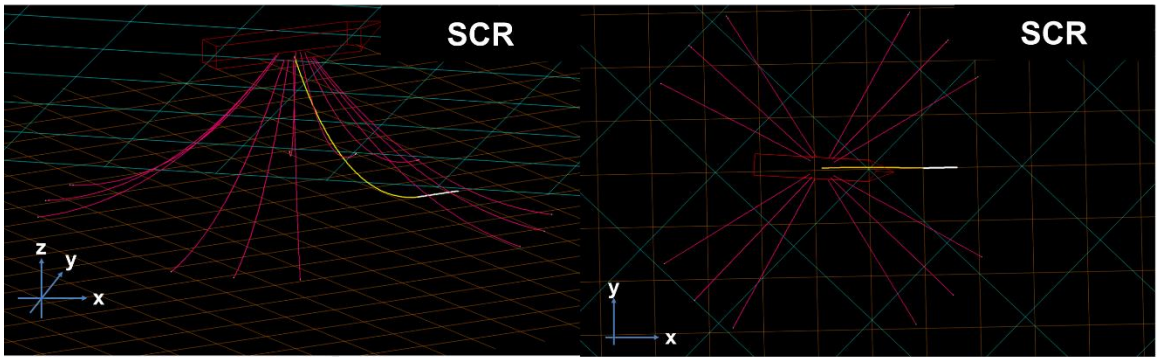

Figure 82 Configuration of FPSO with SCR

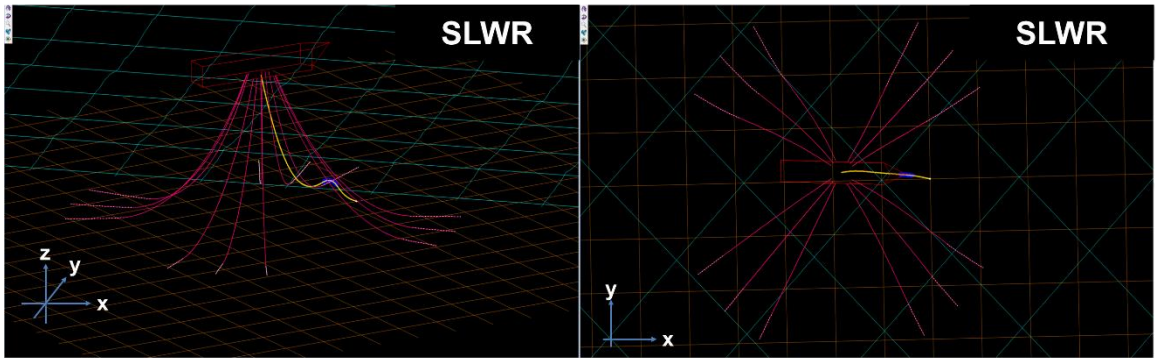

Figure 83 Configuration of FPSO with SLWR

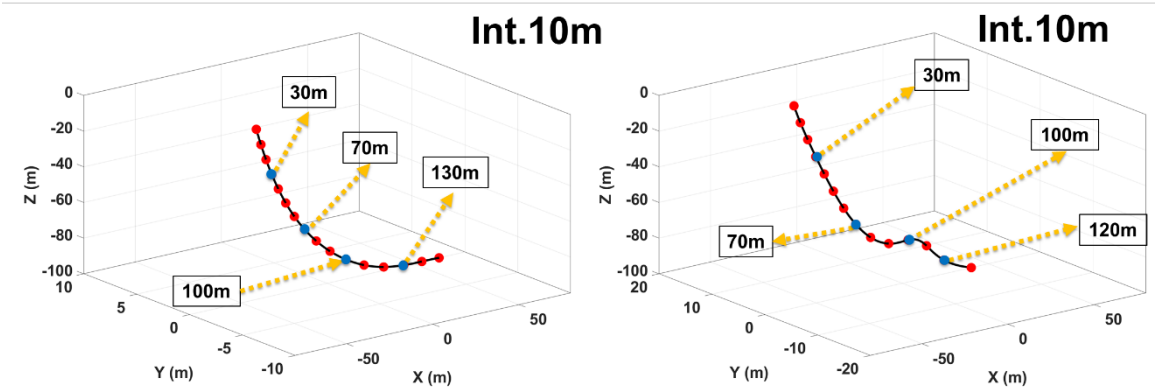

Figure 84 Sensor Distribution for SCR and SLWR, Coarse Interval (=10m)

Table 32 Mooring Chain and Riser Material Properties

Mooring Chain			Riser (SCR and SLWR)		
Type	[-]	R3 Studless	Outer Diameter	[mm]	356
Bar Diameter	[mm]	140	Inner Diameter	[mm]	254
Mass in Air	[kg/m]	390	Mass in Air	[kg/m]	335.3
Displaced Mass	[kg/m]	51	Displaced Mass	[kg/m]	184
MBL (Min. Breaking Load)	[MN]	17.6	Axial Stiffness (EA)	[MN]	711.2
Axial Stiffness (EA)	[MN]	1674	Bend Stiffness (EI)	[kN-m^2]	124.9
Bend Stiffness (EI)	[kN-m^2]	0	Arc Length (SCR/SLWR)	[m]	150/130
Arc Length (SCR/SLWR)	[m]	160/170	[-]	[-]	[-]

Table 33 Buoyancy Module (SLWR) Material Properties

Buoyancy Module (SLWR)		
Mass	[te]	0.6
Volume	[m^3]	1.032
Height	[m]	1

Table 34 Environmental Condition (1-yr and 50-yr storms)

Wave					**Current**		**Wind**		
Spectrum	Gamma	Direction from North	Significant Wave (Hs)	Spectral Period (Tp)	Depth	Vel	Spectrum	10 min at 10m elevation	Direction from North
(-)	(-)	(deg)	(m)	(s)	(m)	(m/s)	(-)	(m/s)	(deg)
JONSWAP	2.2	45	3.5	10.3	Surface	0.3	API	20	45
					1/7 law is used				
JONSWAP	2.2	45	7.5	14.3	Surface	0.5	API	26	45
					1/7 law is used				

$$V = V_{sb} + (V_{sf} - V_{sb}) \cdot [\frac{(z - z_{sb})}{(z_{sf} + z_{sb})}]^{1/7} \quad (5\text{-}25)$$

V_{sb}, V_{sf} = current velocity at seabed and surface

z_{sb}, z_{sf} = vertical coordinate of seabed and surface

5.4 Comparisons between the predicted and actual riser profiles and BM

In this section, various comparisons between the predicted and actual profiles and bending moments will be presented and discussed. It is assumed that the bi-axial inclinometers are attached uniformly along the entire riser arc length. Furthermore, two different sensor intervals (compact interval=2m, coarse interval=10m) are selected to show the sensor-interval effect for both SCR and SLWR.

The FPSO system with the respective riser is simulated first by the OrcaFlex computer program with the given inputs and parameters. Then, the inclination- and azimuthal-angle signals are collected from the sensor locations. Next, the developed algorithms are run by using the numerical-sensor signals to trace the instantaneous riser profile and bending moments at any location along the riser. Finally, the reconstructed riser profiles and bending moments are compared with the actual values at the respective time steps to assess the capability of the developed algorithms. Here, the possible sensor noises are not considered.

First, the riser-profile-tracing capability by the presently developed algorithm for the SCR case is discussed. For the time history of riser displacements, four representative locations are selected i.e. 30m (upper), 70m (middle), 100m (lower), and 130m (on seabed). In Figure 85 and Figure 86, the respective x-y-z locations' time histories for both compact (Int. =2m) and coarse (Int. =10m) sensor intervals are plotted. Both 1-yr and 50-yr storms are employed and both algorithm-predicted and actual profiles are compared. For both

storm conditions, the predicted riser movements at the upper-middle-lower locations excellently agree with the actual movements both for coarse and compact riser arrangements. This implies that longer than 10-m interval can also be used for practical applications depending on the level of target accuracy. At arc length 130m location, which is laid down on the seabed, the profile-tracing accuracy is still good even for 10-m sensor interval.

In the case of SCR on the seabed, the seabed stiffness causes the sudden change of riser curvature near the touch-down zone, and thus the accuracy of the prediction algorithm is affected. To further explain this, the same SCR cases without seabed stiffness are presented in Figure 87. It is confirmed that there is almost no difference between the predicted and actual profiles regardless of the sensor interval since the curvature of the SCR smoothly changes with hanging profile below seabed if seabed stiffness is not considered (Figure 87). This is true even for the case of sparse sensor interval. Therefore, the sensors need to be arranged with smaller spacing when the curvature changes rapidly and high accuracy is needed.

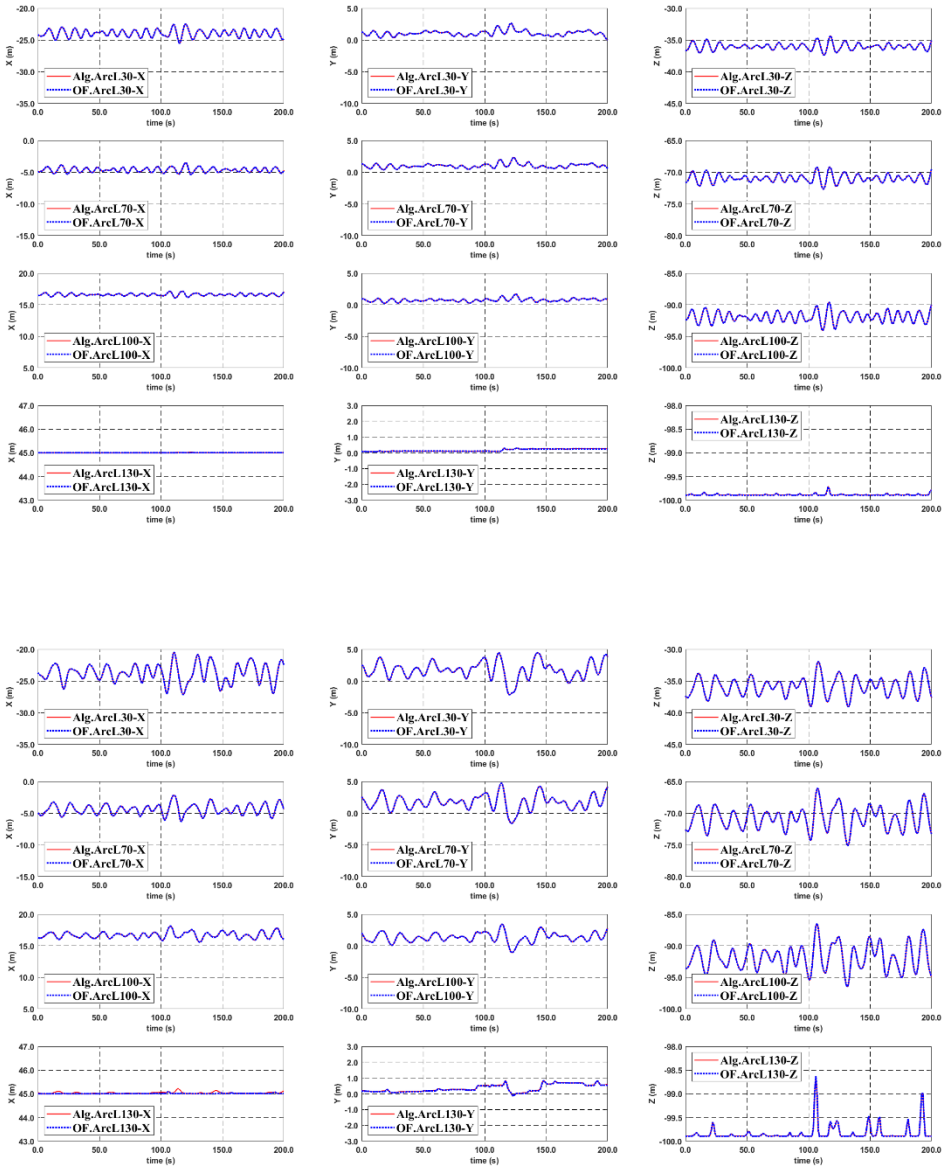

Figure 85 SCR motion time histories at various locations with compact sensor interval=2m (with seabed stiffness), 1-yr (Up) 50-yr (Down)

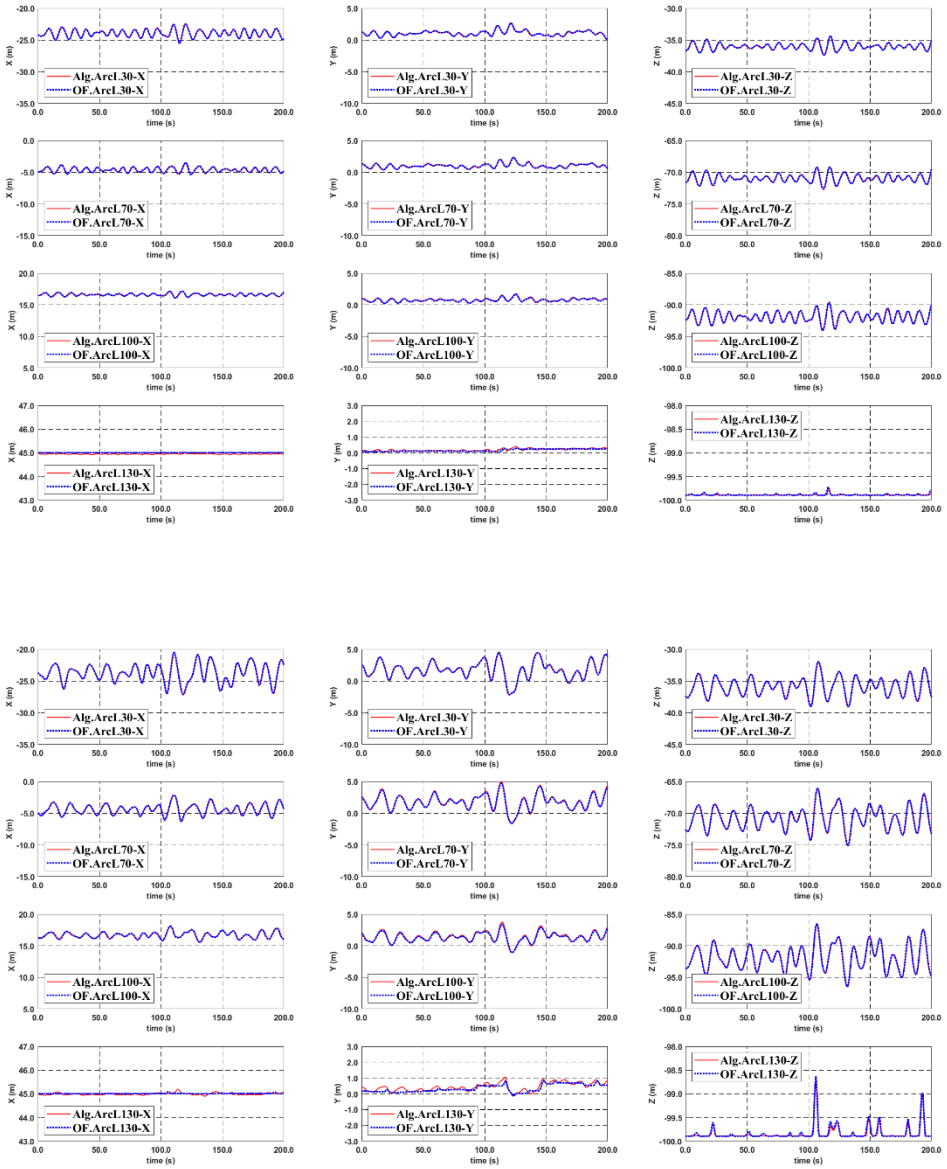

Figure 86 SCR motion time histories at various locations with coarse sensor interval=10m (with seabed stiffness), 1-yr (Up) 50-yr (Down)

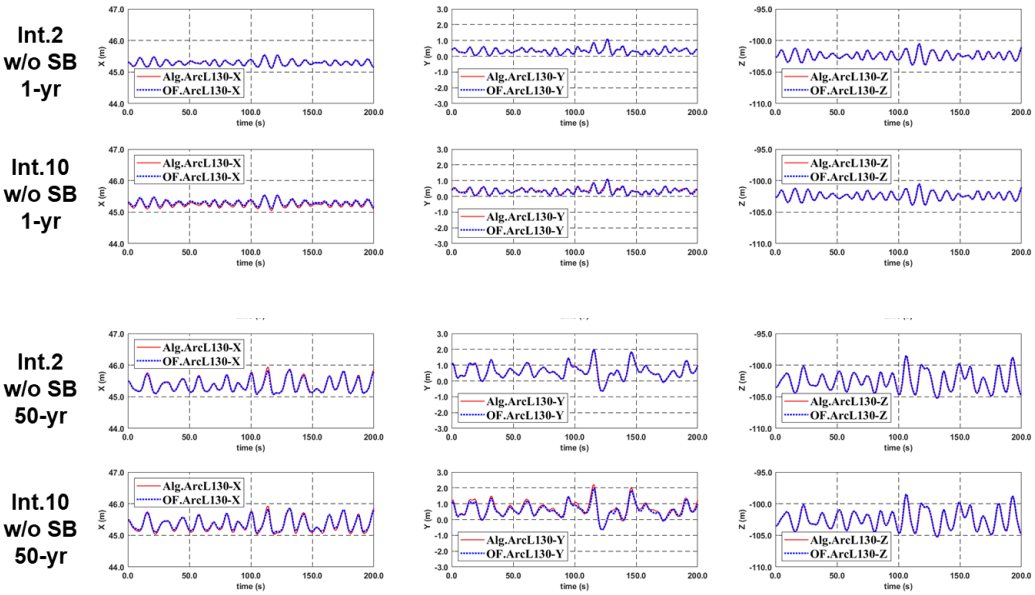

Figure 87 SCR motion time histories at various locations near touch-down point for two different sensor intervals (without seabed stiffness), 1-yr (Up) 50-yr (Down)

In Figure 88 and Figure 89, the corresponding bending-moment comparisons at the middle point and off-middle point of each element (s/L=0.5 and 0.75) are presented. For each figure, the results for mid-arc-length point at 75m and 3 near-touch-down locations are plotted. Since the TDP (Touch Down Point) near the arc length of about 124m is the most critical region in view of bending stress, three locations near TDP are selected (arc length 115m, 125m, and 135m). As was pointed out in the theoretical description, simple analytical results are available for the bending moment at the middle of each sensor interval while for other locations, the bending moment can be obtained by differentiating twice the cubic shape function of riser profile. In all cases, we observe the excellent

recovery of actual bending moments at both the middle (s/L=0.5) and off-mid locations (s/L=0.75) by the developed algorithm. As can intuitively be expected, the compact interval produces more accurate prediction than sparse interval. More interestingly, even the sparse cases give good recovery of actual values, which is very important in practical applications for saving budget. For both 1-yr and 50-yr storms, the predicted bending moments by the developed algorithm reasonably well follow the actual bending moments. The prediction accuracy of the coarse interval case near TDP and on seabed is slightly worse than that of other upper locations, as was already seen in the displacement-tracing examples. That can be attributed to the sudden change of line curvature at the TDP. To double-check this, another set of simulations without seabed stiffness were conducted in Figure 90. In this case, the agreement between the predicted and actual bending moments is excellent even for 10-m sensor interval regardless of the locations and storm conditions.

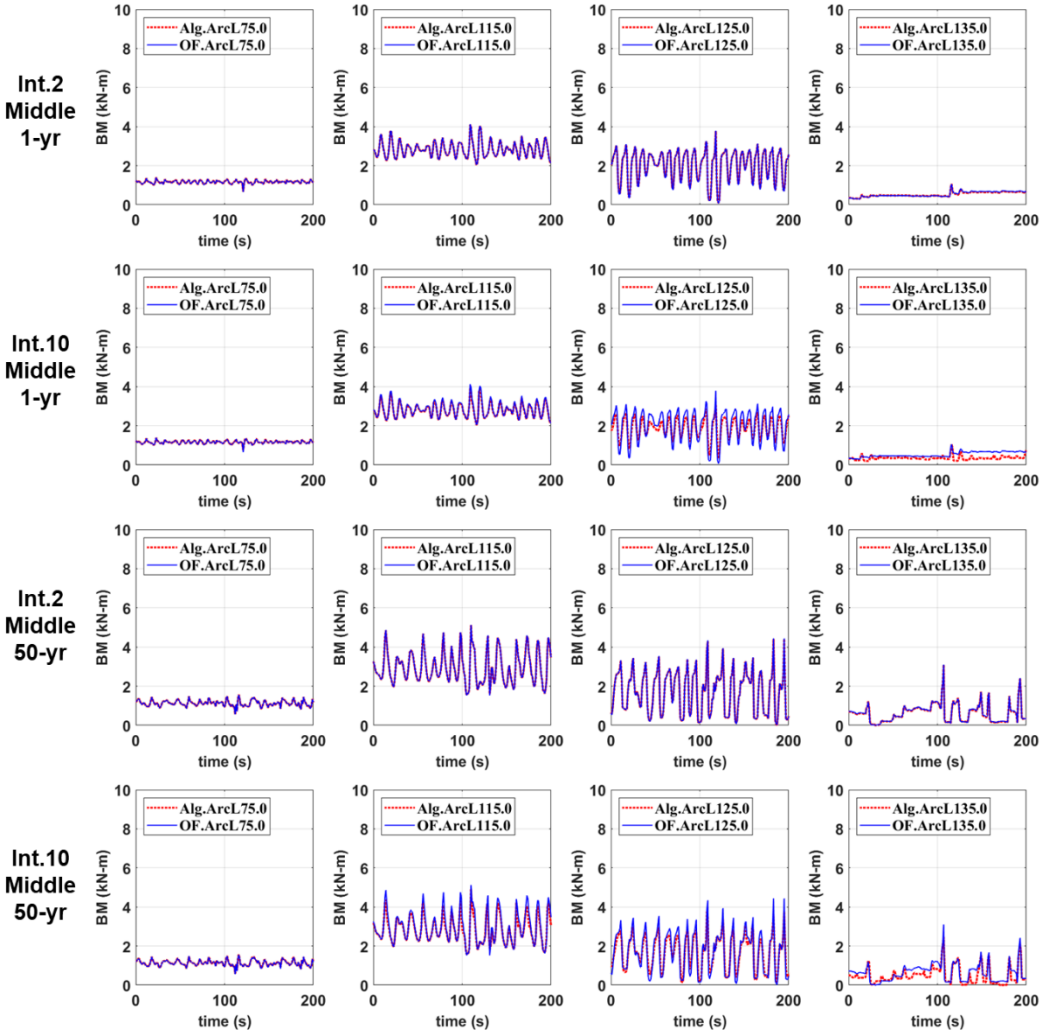

Figure 88 SCR bending moment time histories at the middle of sensor interval (s/L=0.5) with seabed stiffness, 1-yr (Up) 50-yr (Down)

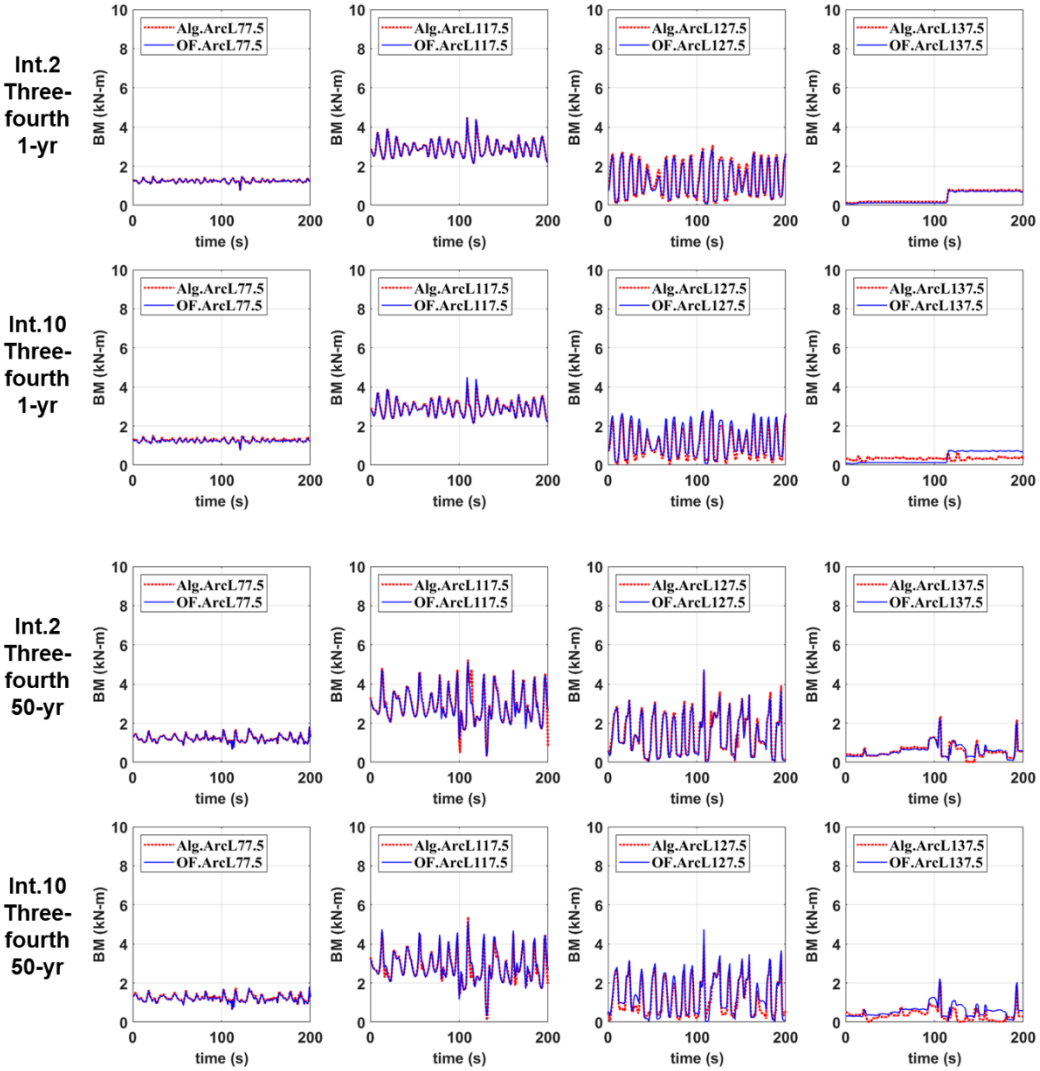

Figure 89 SCR bending moment time histories at the off-middle point of sensor interval (s/L=0.75) with seabed stiffness, 1-yr (Up) 50-yr (Down)

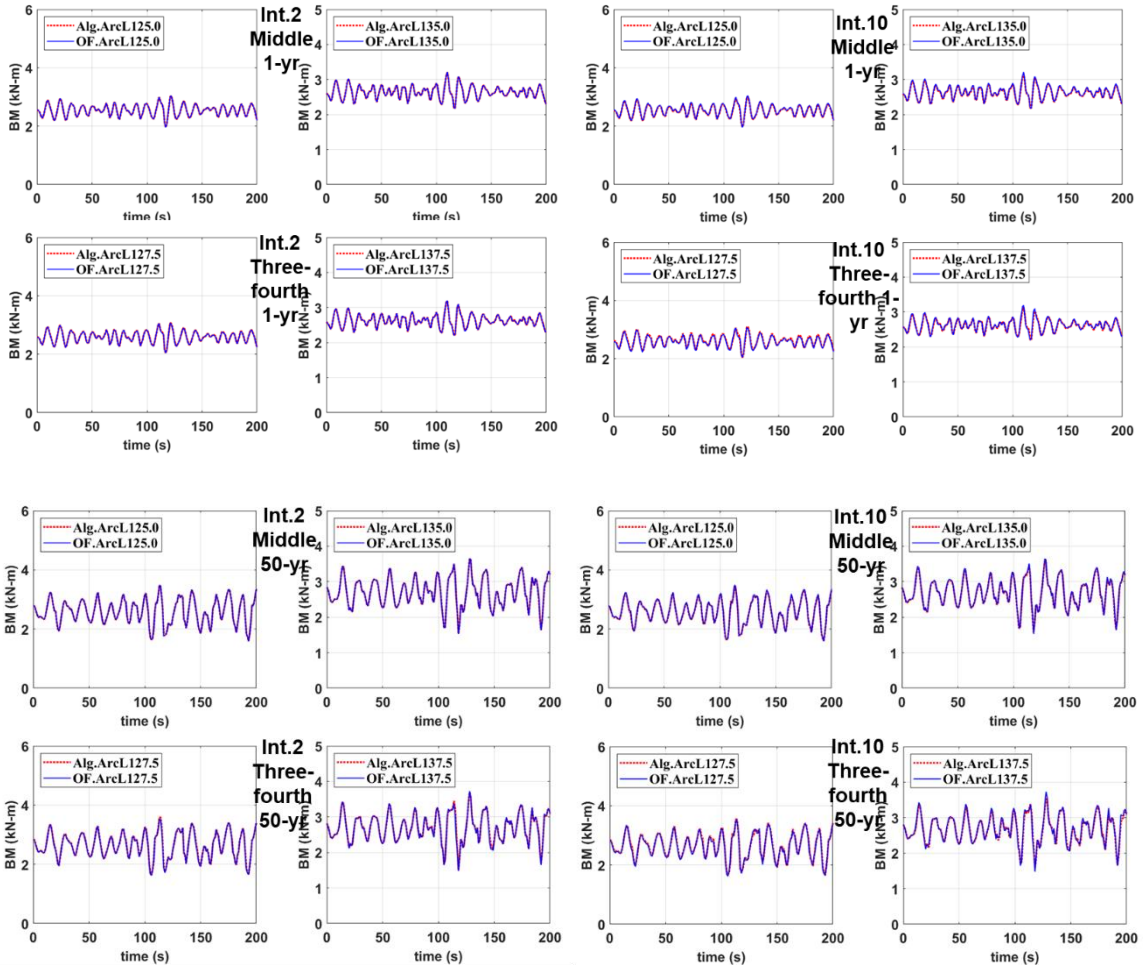

Figure 90 SCR bending moment time histories at the middle point and ¾ of sensor interval, without seabed stiffness, 1-yr (Up) 50-yr (Down)

Next, let us consider the SLWR instead of SCR. The SCR may experience local-dynamic buckling problem when hull heave-pitch motions are excessive [55]. In this case, to avoid that kind of problem, SLWR needs to be used although it is more expensive and problematic in flow assurance. Since the developed algorithms can be applied to any types of line shapes, the prediction capability for a SLWR is also examined in the following.

Intuitively, it is required that the sensors should be arranged densely around the highly curve-reversed lazy wave zone (arc length 100m ~ 110m) to have good prediction accuracy. The same algorithms and sensor intervals are applied to the SLWR movements and the results are compared at four locations i.e. at arc length 30m, 70m, 100m, and 120m with compact and coarse sensor distributions. The corresponding time histories are presented in Figure 91 (compact interval = 2m) and Figure 92 (coarse interval = 10m).

Due to the geometric characteristic of the lazy wave shape, the dynamic motions of the SLWR in x, y, and z directions near concave and TDP (at 90m and 128m) are significantly reduced compared to those of SCR (at 124m). Also, the compact interval case can follow the rapid change of riser curvature in the lazy wave zone much better than the course-interval case. As for the upper portion above the lazy wave zone, even the coarse interval case can predict the overall shape very well. Therefore, sensor distribution can be coarse for the upper portion but needs to be denser around the lazy wave zone to achieve high accuracy. In the case of coarse sensor interval, if a point of inflection exists within the element, the representation of line by quadratic shape function may not be accurate.

Therefore, adjusted sensor arrangement may be needed near the lazy wave zone with double reverse curvature. In this regard, the case of optimal sensor arrangement with variable intervals is also presented by green-dashed line for 100m and 120m arc lengths. In the adjusted sensor arrangement, 10m interval is used except for near the lazy wave zone (arc length 90m~110m) for which 2m interval is applied. As can be seen in the same figure (Figure 92), the adjusted sensor location (green-dashed-line) can produce satisfactorily high accuracy. Since the bottom touching portion of the SLWR is small, the modeling of the seabed stiffness in this case is not an important issue.

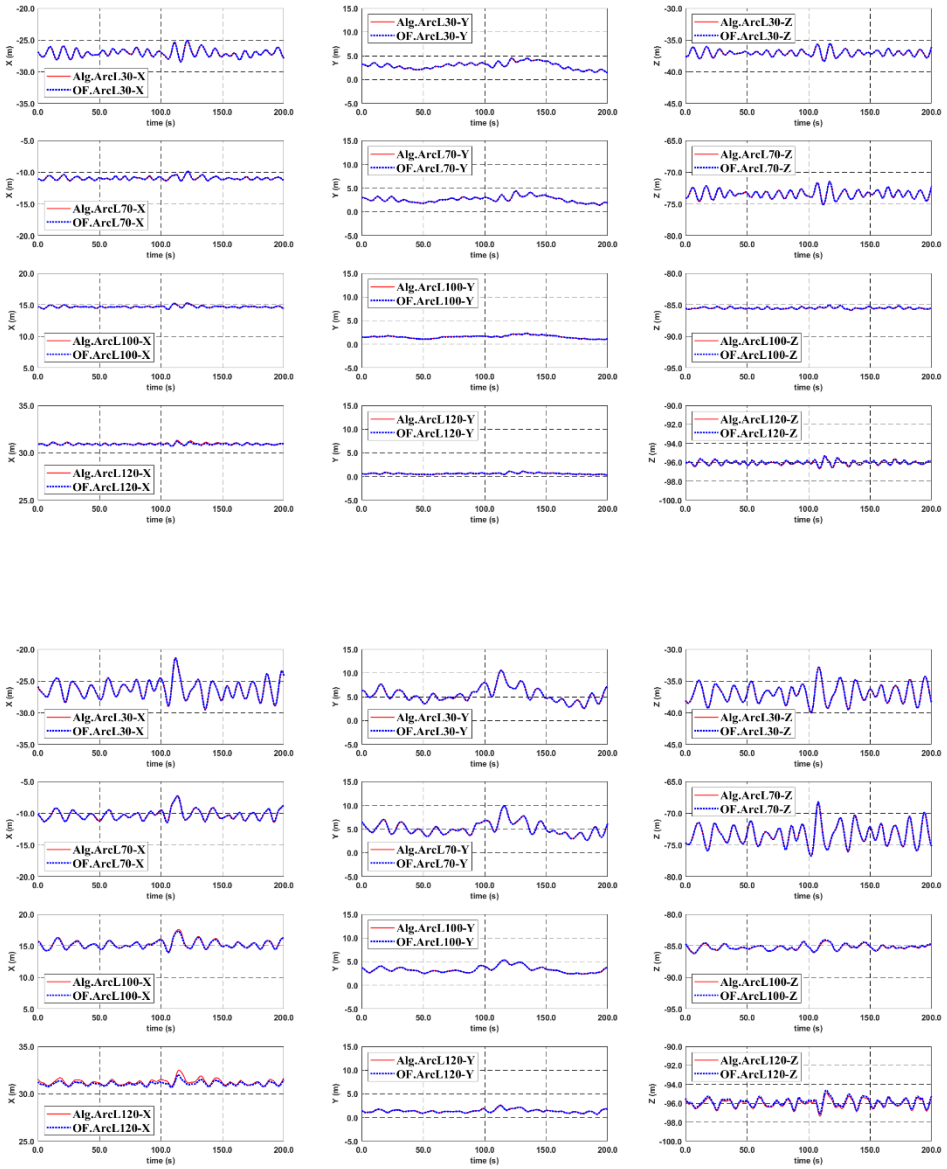

Figure 91 SLWR motion time histories at various locations with compact sensor interval=2m (with seabed stiffness), 1-yr (Up) 50-yr (Down)

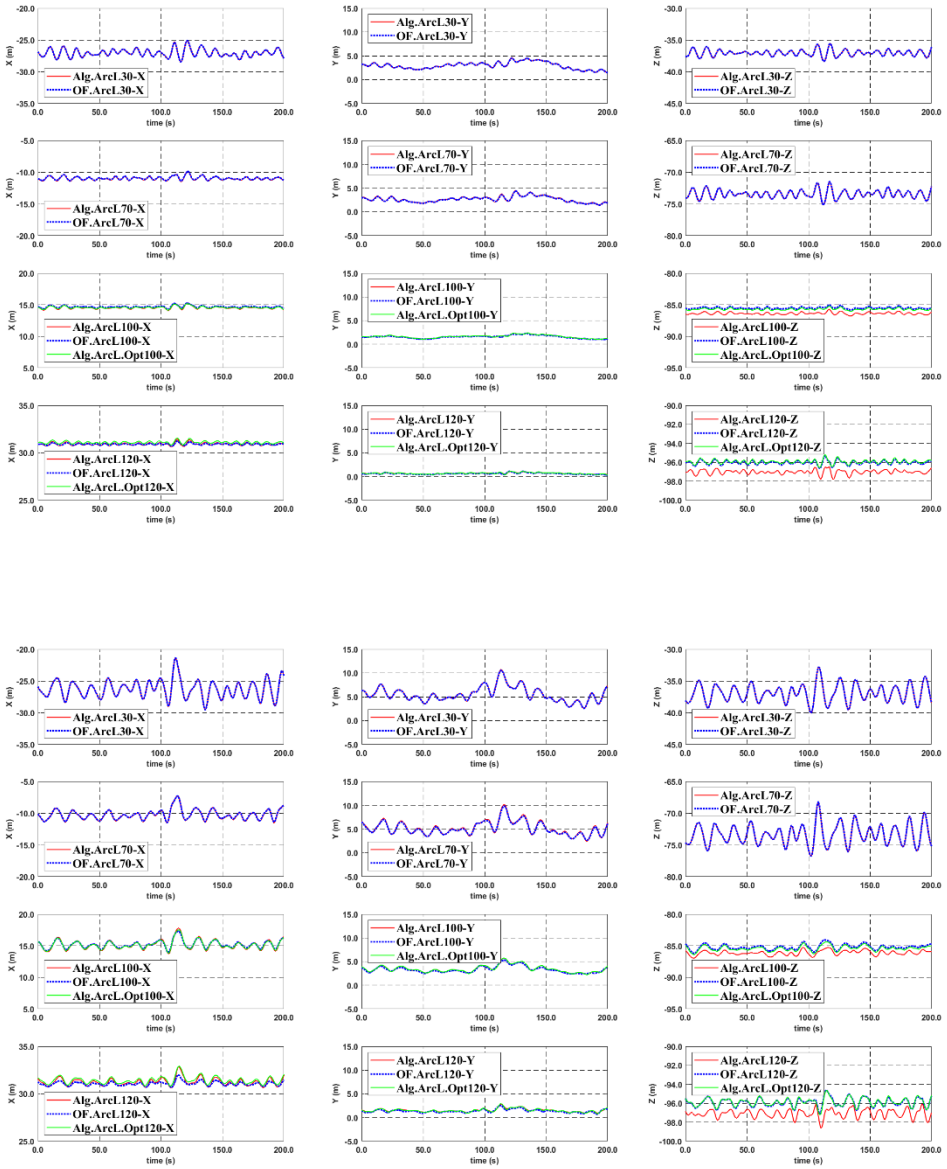

Figure 92 SLWR motion time histories at various locations with coarse sensor interval=10m (with seabed stiffness), 1-yr (Up) 50-yr (Down)

Finally, the bending moment time histories of the SLWR at three locations (= arc length 55m, 85m, and 105m) are presented in Figure 93 and Figure 94. Figure 93 is for the mid-point of the respective elements and Figure 94 is for the 3/4 point of each element. Both figures show the comparisons for compact and coarse intervals. The 85m and 105m locations are around the lazy wave zone since it is the most critical region in view of high bending stresses. Since the curvature variation of the lazy wave zone is relatively large, so denser sensor arrangement is needed there to capture the rapid change and improve the prediction accuracy (green-dashed line) as shown in Figure 93 and Figure 94. However, for the upper portions of the SLWR, even the coarse sensor arrangement gives good enough prediction accuracy, which helps the sensor designers to devise the most cost-effective sensor-based monitoring methodology. So far, the tracing of riser profile and bending moment along the riser by using multiple bi-axial inclinometers was presented. The developed algorithms can in principle also be applied when additional riser-motion complexity exists due to VIV (vortex induced vibration).

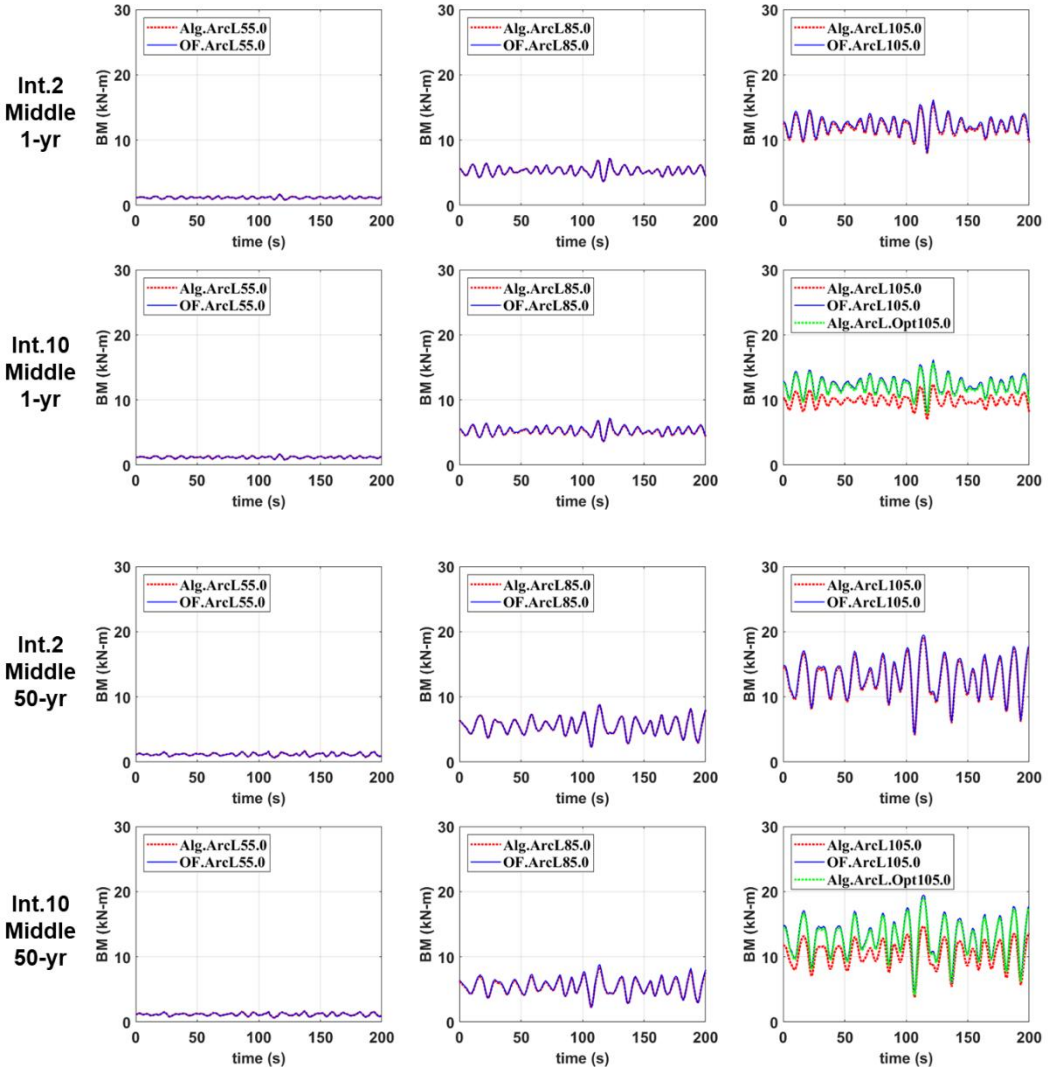

Figure 93 SLWR bending moment time histories at the middle of sensor interval (2m and 10m sensor interval) at three locations (with seabed stiffness), 1-yr (Up) 50-yr (Down)

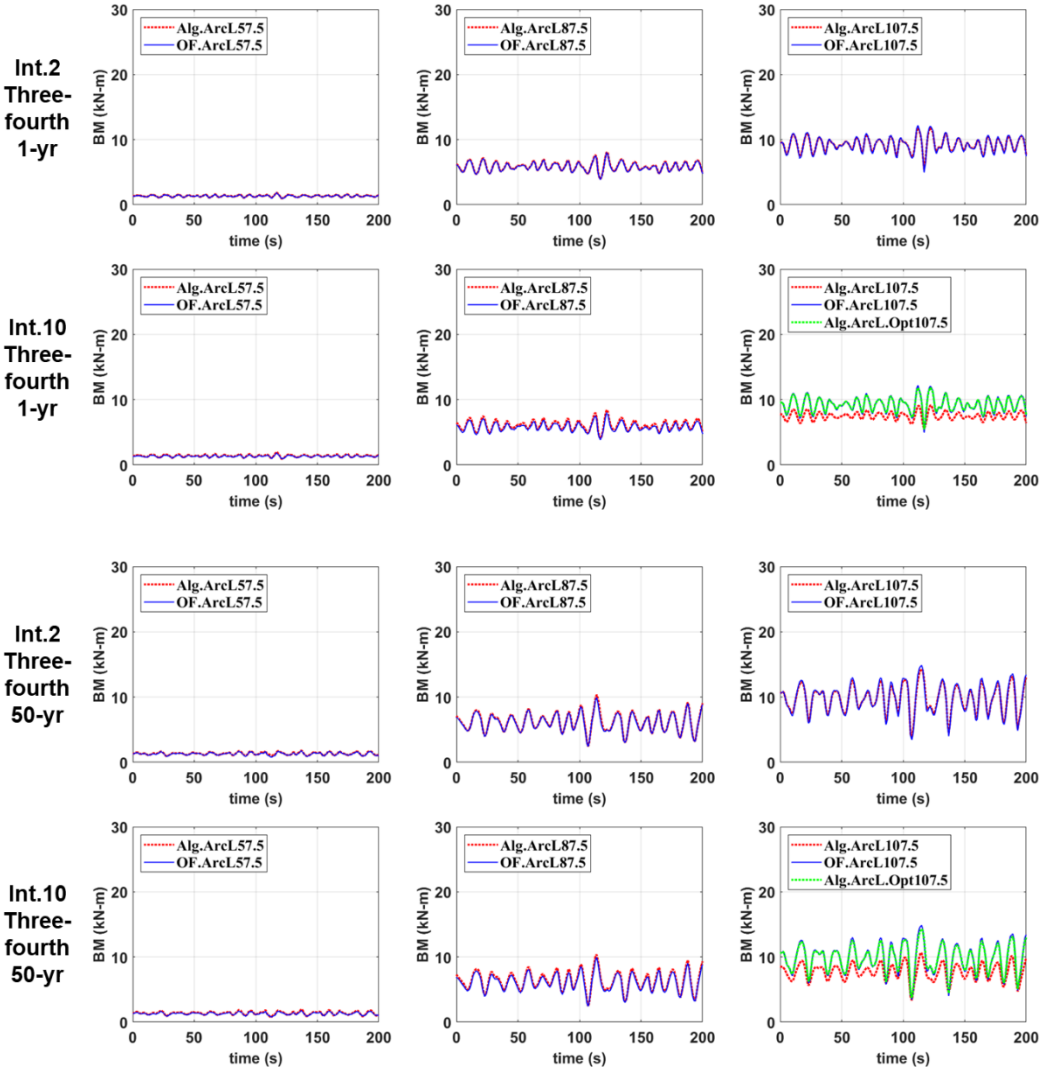

Figure 94 SLWR bending moment time histories at the 3/4 of sensor interval (2m and 10m sensor interval) at three locations (with seabed stiffness), 1-yr (Up) 50-yr (Down)

Finally, Figure 95 shows several snapshots of SCR and SLWR profiles with 10-m sensor interval for SCR and optimized interval for SLWR under 50-yr storm at different time steps. It demonstrates that the whole profile can reliably be traced in real time by the developed algorithms.

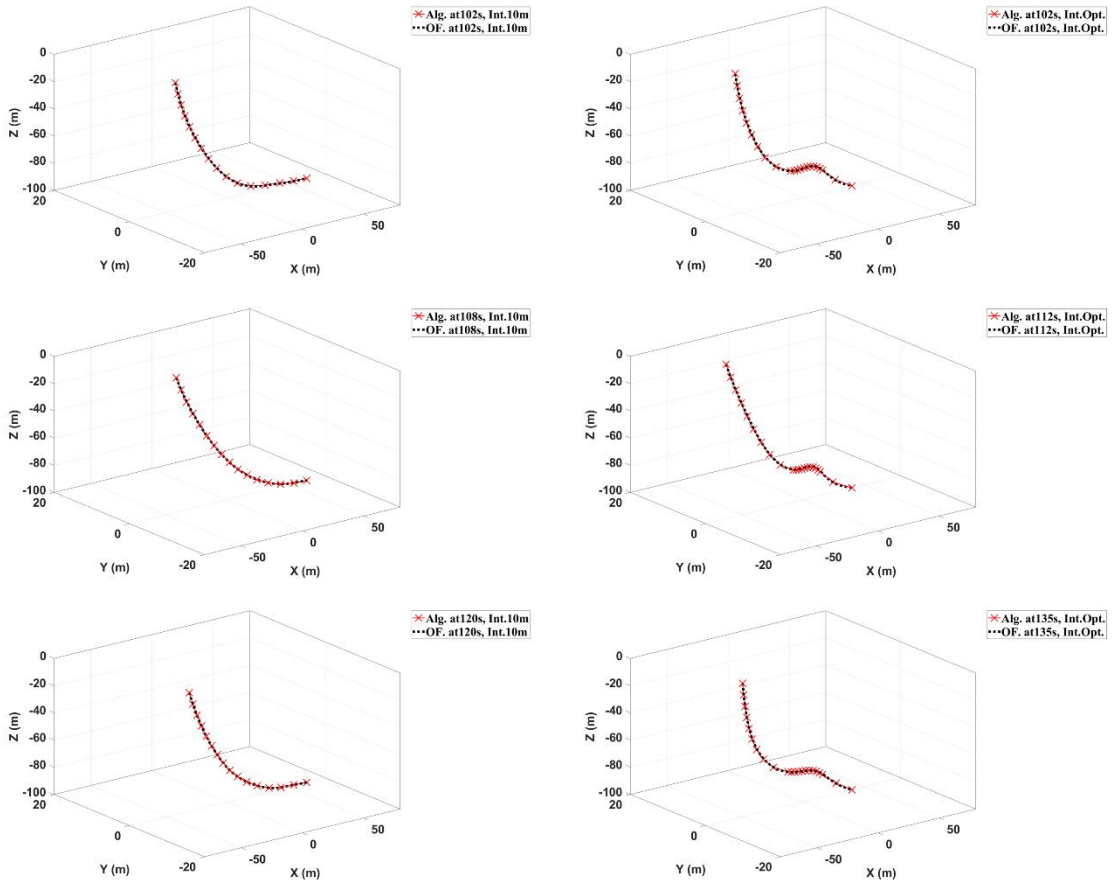

Figure 95 Snapshots of SCR (Left) and SLWR (Right) entire profiles, Int.10m (SCR), Optimization Int. (SLWR), 50-yr

6. DIGITAL TWIN METHODOLOGY FOR RISER STRUCTURE HEALTH MONITORING WITH MINIMUM SENSORS

6.1 Digital Twin Approach for Riser Structure Health Monitoring

In this section, for the comparison purpose, two different approaches such as digital twin (DT) and forced floater oscillation (FFO) will introduce to discuss advantages of digital twin approach (Figure 96). As shown in Table 35, since original (Ori) model will be used as real-field operating system in this study so that all kinds of environmental loadings (wind, wave and current) should be considered. However, for both approaches, it can be claimed that both wind and current loads effect will be considered in digital twin approach whereas only wind effect can be considered for forced floater oscillation approach. Furthermore, since wind loading will affect to floater motion and it is related to dynamic response of inclinometers attached along the top part of the riser, it can be asserted that wind effect is also considered in digital twin (DT) approach. Continually, the overview of digital twin approach for riser structure health monitoring with minimum sensors on the top part presented in Figure 97. First, signal data from sensors attached along the top part of the riser can be acquired. Then, the measured sensing data can be used as an input file for inverse current profile prediction using machine learning and it also can apply to trace node displacements and tension at target point (same location with last sensor attached). With assumption that there is a significant wave excitation load reduction below certain water depth, digital twin model can be established and implemented using traced target node displacements, tension and predicted current profile. As a floater, the default FPSO

given by OrcaFlex was selected with the corresponding added mass, radiation damping, first- and second-order wave loads. Furthermore, a total of 12 spread mooring lines (with four groups) are employed for the station-keeping in 100m water depth. Each mooring line consists of chain components for entire arc length. Also, it is assumed that only five inclinometers are attached along the top part of riser with 5m interval. Detailed mooring and riser material properties are summarized in Table 36. For forced floater oscillation approach, it is assumed that floater displacements can be traced directly by GPS (Global Positioning System) and traced floater displacements can be inputted to the system under calm water (no wave and current).

In the following section, since riser near the touch down point (TDP) can be a critical region during the operation, three arc length locations near the TDP can be selected for comparison. Furthermore, each of required information for digital twin approach such as node displacement and tension tracing algorithm and inverse current profile prediction process using multivariate regression will be explained in detail, accordingly.

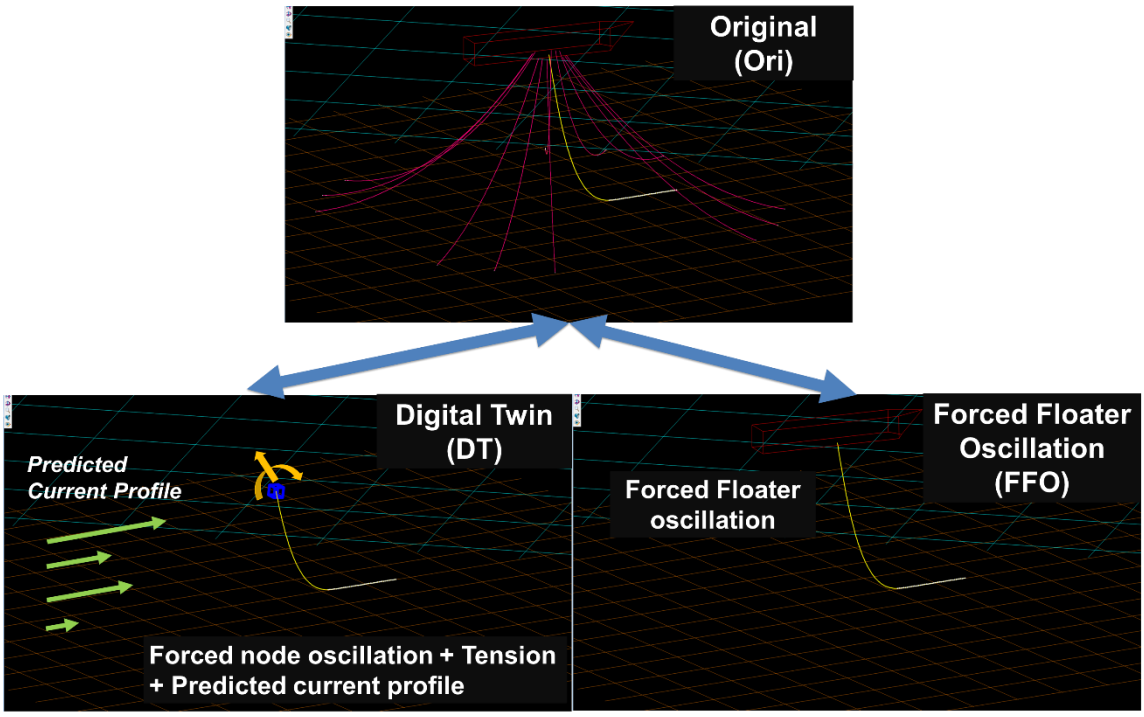

Figure 96 Schematic view of Digital Twin Model and Forced Floater Oscillation

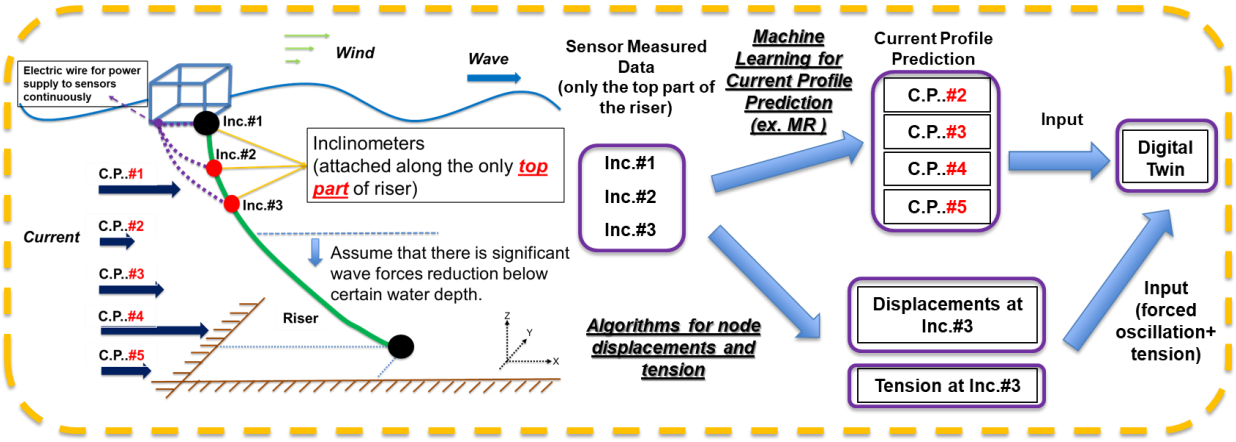

Figure 97 Configuration for Digital Twin Model for Riser Structure Health Monitoring with Minimum Sensors

Table 35 Environmental Loadings Consideration

	Original	Digital Twin	Forced Floater Oscillation
Wave	O	X	X
Current	O	O	X
Wind	O	O	O

Table 36 Mooring Chain and Riser Material Properties

Mooring Chain			Riser		
Type	[-]	R3 Studless	Outer Diameter	[mm]	356
Bar Diameter	[mm]	140	Inner Diameter	[mm]	254
Mass in Air	[kg/m]	390	Mass in Air	[kg/m]	335.3
Displaced Mass	[kg/m]	51	Displaced Mass	[kg/m]	184
MBL (Min. Breaking Load)	[MN]	17.6	Axial Stiffness (EA)	[MN]	711.2
Axial Stiffness (EA)	[MN]	1674	Bend Stiffness (EI)	[kN-m^2]	124.9
Bend Stiffness (EI)	[kN-m^2]	0	Arc Length	[m]	150
Arc Length	[m]	160	[-]	[-]	[-]

6.2 Methodology – Inverse Current Profile Prediction using MR

In this section, inverse current profile prediction process with minimum sensors on the top part of riser will be discussed in this section. Here, Multivariate Regression (MR) model is selected as a machine learning algorithm [56]. Generally, MR model can be written N-dimensional using linear combinations of continuous response vectors and residual (error) vector (eq. 6-1)

$$Y = \alpha_0 + \alpha_1 X_1 + \alpha_2 X_2 + \bullet\bullet\bullet + \alpha_N X_N + \varepsilon$$

α_0 = intercept (6-1)
α_i = multivariate regression coefficients, i=1,...,N
ε = residual (error)

In eq. 6-1, X_i $(i = 1 \sim N)$ is "independent" variables, Y is "dependent" variable. In this study, measured inclinometer signals can be used as an "independent" variables and current velocity at each water depth can be inputted as a "dependent" variable. To find MR coefficients, least square method will be used with correlated error variance-covariance matrix to find best fit to minimize sum of the residuals [57]. Furthermore, as shown in Figure 98, to build multivariate regression model, massive training data should be generated at first. To do this, OrcaFlex which is widely adopted commercial tool in the offshore industry is used. For the training data generation, original approach model is used as a basement. As shown in Figure 98, fully-coupled FPSO system will be simulated within environmental loading condition boundary at first and then average of declination value at each inclinometer can be computed and stored as an output for each corresponding environmental loading conditions. For wave and wind, JONSWAP and API spectra is used

as corresponding wave and wind spectrum, respectively. Furthermore, 4m to 10m with 0.5m interval is selected as a significant wave height boundary whereas another boundary (8s to 16s) with 0.5s interval is selected in peak period case. Also, for wind training boundary, 10 m/s to 40 m/s with 5 m/s interval is selected as shown in Table 37. Thus, applying each boundary combination, total 1547 load cases are generated and simulated. However, for current profile generation for training, random generation based on Gaussian distribution is used. Table 38 present mean and standard deviation (STD) for current profile random generation for training. Once training data sets generation and simulation is completed, the training process is applied and finally the coefficients in eq. 9-1 can be obtained. Using this trained multivariate regression model (eq. 9-1), current profile can be predicted inversely (Figure 99). In the following section, validation results for inverse current profile prediction will be presented.

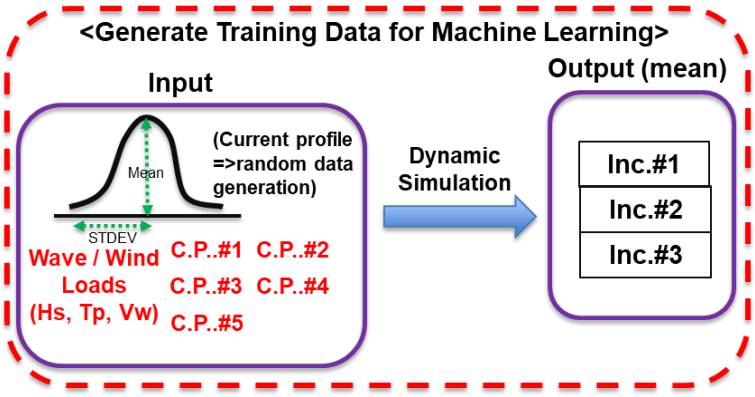

Figure 98 Training Data Generation for Multivariate Regression

Table 37 Wave and Wind Conditions for Training Data Generation (total 1547 sets)

		Min.	Max.	Int.	Sets #
Wave	Hs(m)	4	10	0.5	13
	Tp(s)	8	16	0.5	17
Wind	Speed(m/s)	10	40	5	7
Total	[-]	[-]	[-]	[-]	1547

Table 38 Random Generation for Current Profile, Training data

Current Profile	Water Depth	Mean	STD
[-]	[m]	[m/s]	[-]
1	0	1.2	0.3
2	25	1	0.2
3	50	0.8	0.2
4	75	0.6	0.2
5	100	0.4	0.2

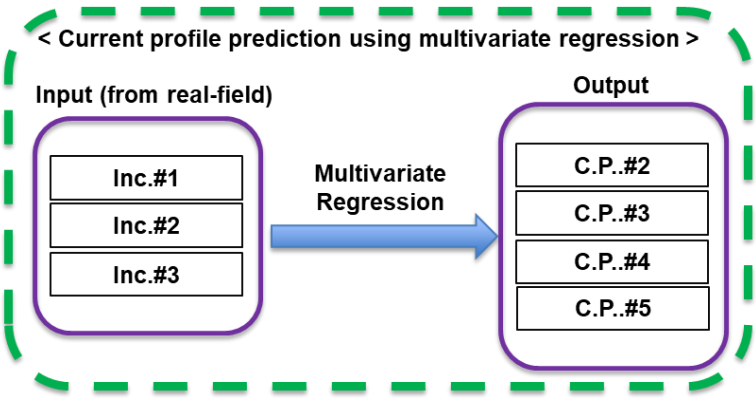

Figure 99 Current Profile Prediction with Multivariate Regression

6.3 Numerical Results Comparisons for Riser Structure Health Monitoring

In this section, numerical results comparison between digital twin approach and forced floater oscillation approach for riser structure health monitoring will be presented and discussed. For target environmental condition, 100-yr return period storm condition is selected as summarized in Table 39. However, for inverse current profile prediction, nine load cases are generated randomly (same process with training data generation) for validation purpose of trained multivariate regression model (Figure 100). As shown in Figure 101, it is confirmed that there is a good agreement between randomly generated current profile for validation and its corresponding predicted current profile inversely. Thus, it can be claimed that current profile can be traced well using and multivariate regression inversely with minimum sensors. Continually, to confirm digital twin approach for riser structure health monitoring, LC08 among inverse current profile prediction load cases is selected. Since current profile cannot be changed rapidly (steady) even in real-field, it is assumed that predicted current profile is the same for duration of simulation in this research. Furthermore, node displacements should be traced to build digital twin model. As previously explained, using quadratic interpolation function and curve length equation in 3D space, node displacement can be traced progressively from the top with assumption that hang off location can be given in real-time by GPS signal (Figure 102). Additionally, tension information is also needed to build digital twin model. Even though there is a little shift as sensor submerged depth goes to deep, overall trend can be captured well with suggested algorithm until certain submerged depth (at least last sensor attached) as shown in Figure 103. Now, all required information to build digital twin approach such

as node displacements, tension and predicted current profile below certain water depth is obtained from measured signal of inclinometers. Since near TDP (touch down point) which is the 100m arc length in this FPSO system is the most critical region during SCR operation, three neighboring locations (95m, 100m, 105m) near the TDP are selected to assess riser structure performance. In Figure 104, time history of tension and bending moment at three locations are presented. As it can expected, wave impact can be negligible based on the comparison result between original model and digital twin approach whereas there is a small difference in forced floater oscillation compared to the others due to current loading effect. Continually, statistical characteristic comparison is tabulated in Table 40. Also, the difference comparison with original model is summarized in Table 41. It can be confirmed that both mean and STD (greatly affect to accumulative fatigue calculation) monitoring accuracy of riser can be significantly increased if several additional inclinometers are attached only top part of the riser (easy maintenance and continuous power supply) compared to forced floater oscillation approach.

Table 39 Environmental Conditions (100-yr)

Wave					Wind		
Spectrum	Gamma	Direction from North	Significant Wave (Hs)	Spectral Period (Tp)	Spectrum	10 min at 10m elevation	Direction from North
(-)	(-)	(deg)	(m)	(s)	(-)	(m/s)	(deg)
JONSWAP	2.2	45	9.4	15.2	API	35	45

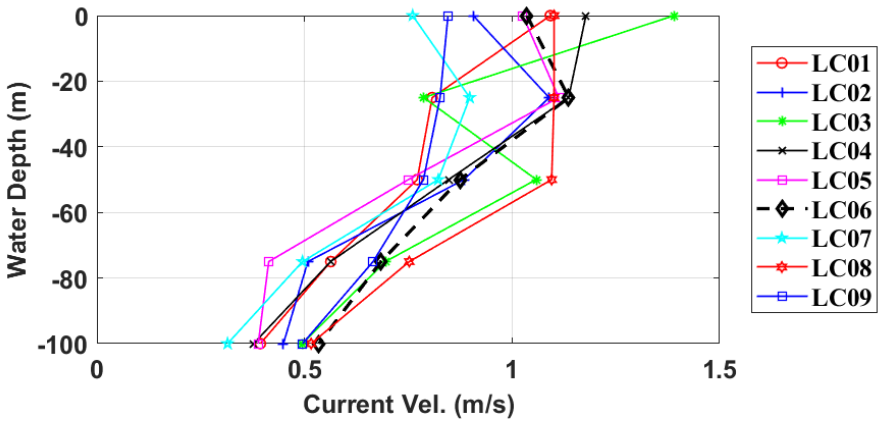

Figure 100 Current Profiles for MR Validation

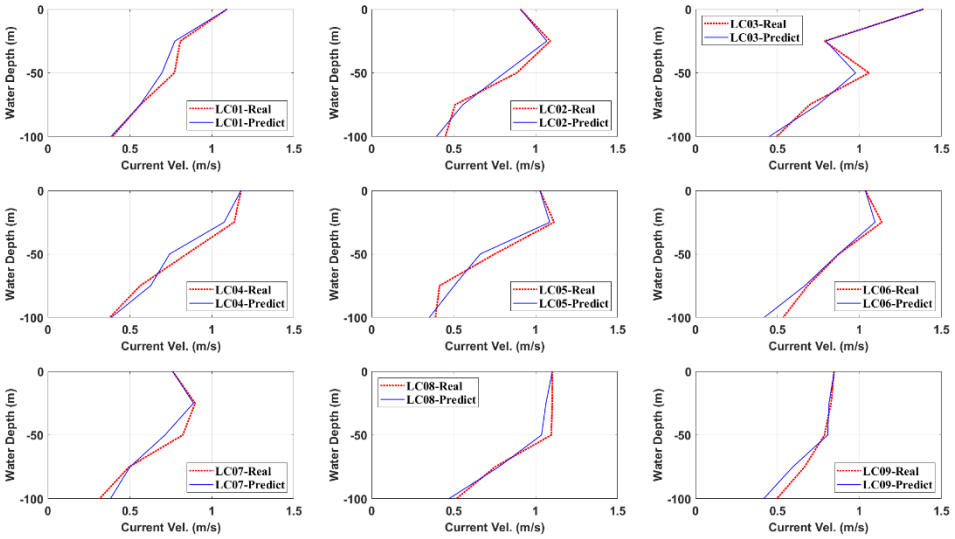

Figure 101 Current Profile Prediction, Multivariate Regression (MR), SCR

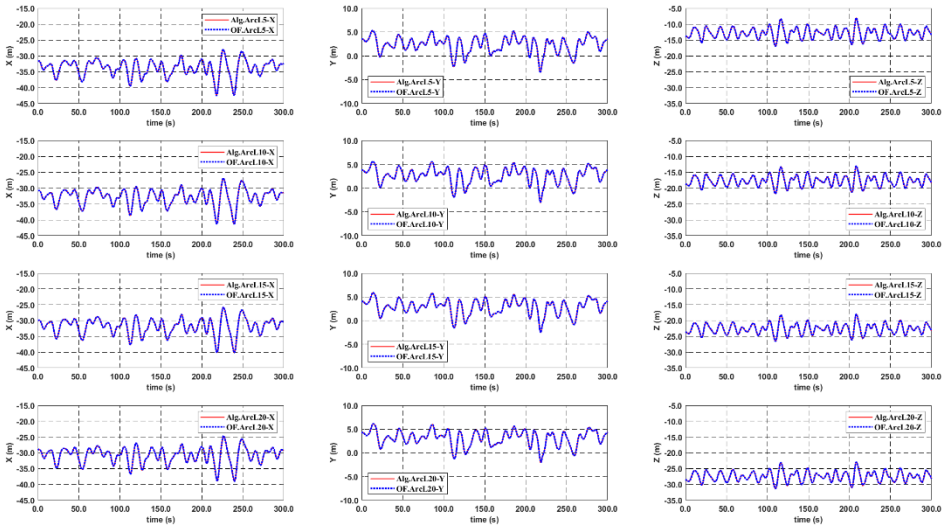

Figure 102 Displacement Tracing, 100-yr, WD100, LC08, SCR

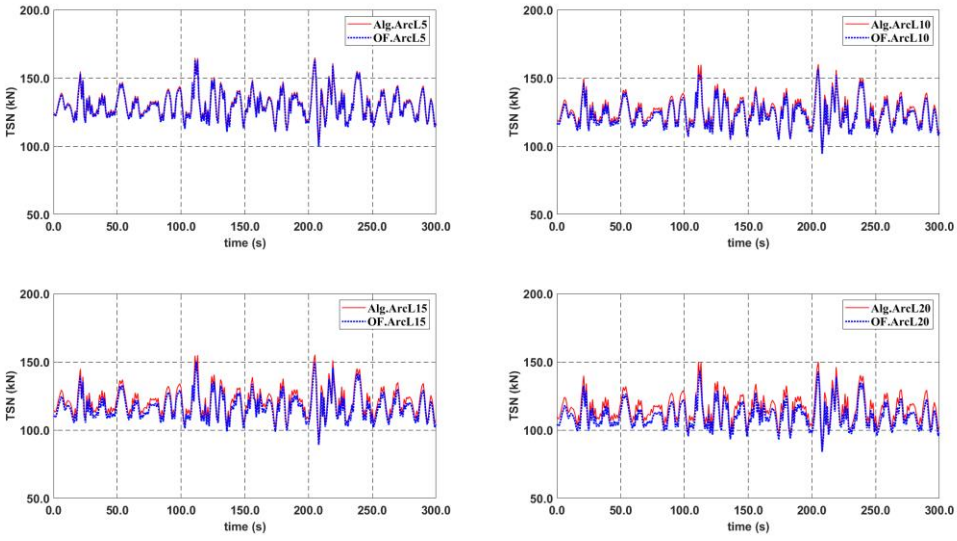

Figure 103 Tension Estimation, 100-yr, WD100, LC08, SCR

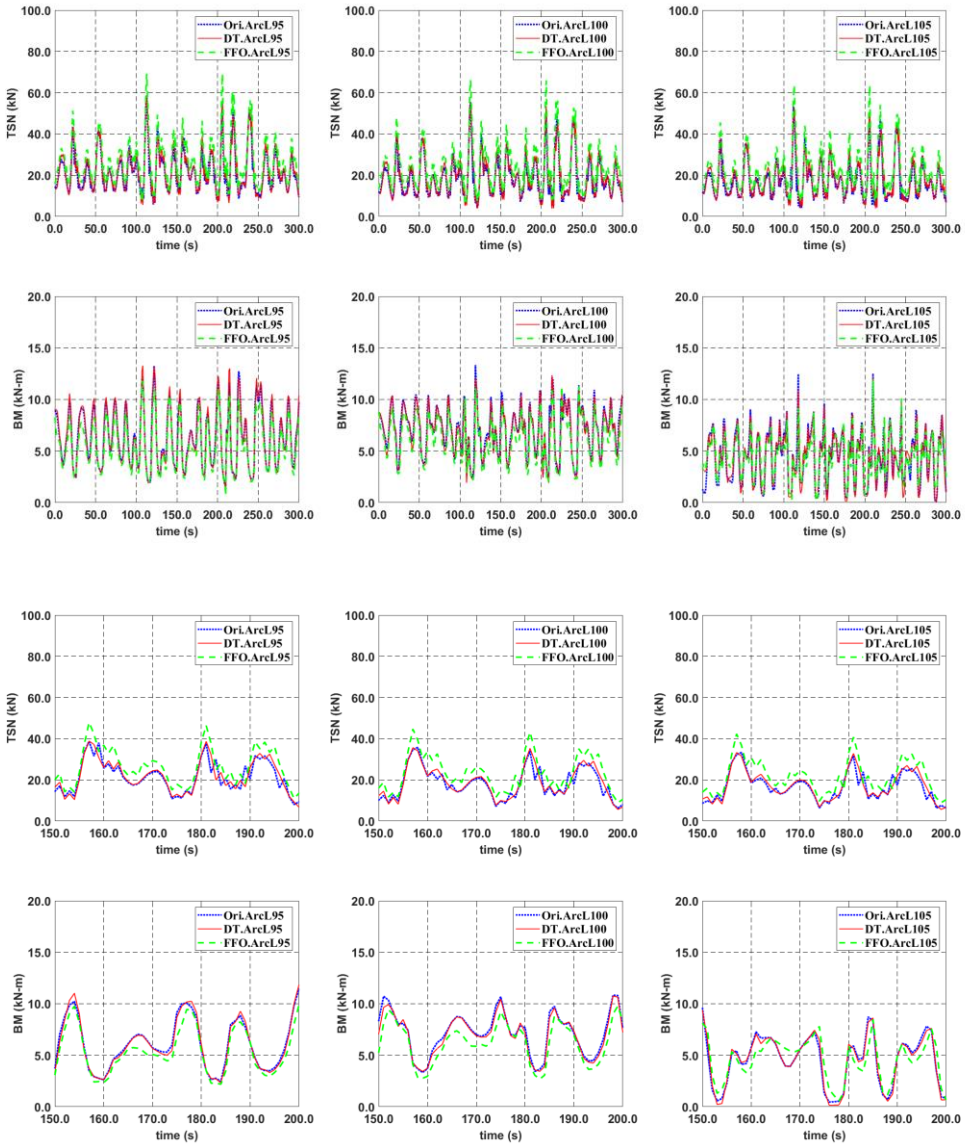

Figure 104 Performance Monitoring Comparison between Digital Twin and Forced Floater Oscillation, Near TDP (=arc length 100m), 100-yr, WD100, LC08, SCR

Table 40 Statistical Characteristics Comparison, Original VS Digital Twin VS Forced Floater Oscillation, 100-yr, WD100, LC08, SCR

	Arc Length 95m, SCR					
	Original (Ori.)		Digital Twin (DT)		Forced Floater Oscillation (FFO)	
	TSN (kN)	BM (kN-m)	TSN (kN)	BM (kN-m)	TSN (kN)	BM (kN-m)
Mean	21.1191	6.5983	21.5372	6.5698	26.0730	5.7411
Std. Dev.	9.4012	2.6629	9.4814	2.7460	10.5081	2.3060
Max.	58.0527	13.4566	57.9200	13.7716	68.5442	11.9160
Min.	5.0806	1.6604	5.2423	1.6733	7.5351	0.7493
	Arc Length 100m, SCR					
	Original (Ori.)		Digital Twin (DT)		Forced Floater Oscillation (FFO)	
	TSN (kN)	BM (kN-m)	TSN (kN)	BM (kN-m)	TSN (kN)	BM (kN-m)
Mean	18.3278	6.8188	18.7595	6.6372	23.2460	6.0596
Std. Dev.	9.0855	2.0621	9.0827	1.9995	10.2045	1.8599
Max.	55.1152	13.1828	54.6946	12.1941	65.5812	11.4439
Min.	4.1406	1.1176	3.8889	0.4988	7.0750	1.2401
	Arc Length 105m, SCR					
	Original (Ori.)		Digital Twin (DT)		Forced Floater Oscillation (FFO)	
	TSN (kN)	BM (kN-m)	TSN (kN)	BM (kN-m)	TSN (kN)	BM (kN-m)
Mean	17.1357	3.9212	17.5593	3.9127	21.8606	4.1037
Std. Dev.	8.5446	2.3601	8.4675	2.3172	9.5975	1.9577
Max.	52.9389	10.7697	52.2340	11.3296	63.2775	11.5567
Min.	4.1430	0.2028	4.0144	0.1898	6.9408	0.1863

Table 41 Difference Comparison with Original VS Digital Twin, Original VS Forced Floater Oscillation, 100-yr, WD100, LC08, SCR

	Arc Length 95m, SCR			
	Digital Twin (DT)		Forced Floater Oscillation (FFO)	
	TSN (%)	BM (%)	TSN (%)	BM (%)
Mean	-1.98	0.43	-23.46	12.99
Std. Dev.	-0.85	-3.12	-11.77	13.40
Max.	0.23	-2.34	-18.07	11.45
Min.	-3.18	-0.78	-48.31	54.87
	Arc Length 100m, SCR			
	Digital Twin (DT)		Forced Floater Oscillation (FFO)	
	TSN (%)	BM (%)	TSN (%)	BM (%)
Mean	-2.36	2.66	-26.83	11.13
Std. Dev.	0.03	3.04	-12.32	9.80
Max.	0.76	7.50	-18.99	13.19
Min.	6.08	55.37	-70.87	-10.96
	Arc Length 105m, SCR			
	Digital Twin (DT)		Forced Floater Oscillation (FFO)	
	TSN (%)	BM (%)	TSN (%)	BM (%)
Mean	-2.47	0.22	-27.57	-4.66
Std. Dev.	0.90	1.82	-12.32	17.05
Max.	1.33	-5.20	-19.53	-7.31
Min.	3.10	6.42	-67.53	8.12

7. CONCLUSIONS

7.1 Multi-scale Approach for Chain-Mooring OPB-induced Failure

In chapter 2, a multi-scale approach of using both local-high-fidelity and global-low-fidelity computational models is introduced to best estimate the OPB-induced chain-failure assessment by numerical-simulation tools. At each time step of global-line simulation, by calculating the time-varying tension and OPB interlink angles at the target spot, the actual time-varying bending stiffness (as function of tension magnitude and interlink angle) between adjacent chains was read from the pre-calculated 3D plots from high-fidelity non-linear FEM calculation. For the global-system-simulation computation, hull-mooring-riser fully-coupled in-house time-domain simulation program, CHARM3D, was used. The results were double checked by a commercial program (OrcaFlex) when comparison is possible for the simpler case of constant interlink bending stiffness. For the high-fidelity local structural analysis, a commercial non-linear FEM program (ABAQUS) was used.

From the present study, it is found that the accurate modeling of chain-hawse and fairlead connection in the global-dynamics simulation is very critical for the reliable OPB-induced failure assessment. Several conclusions from the present case study can be drawn as follows:

- Without modeling the actual chain-hawse in the global analysis, the OPB/IPB angles can significantly be under-estimated.

- The mean and variation of interlink angles at the critical point are increased with smaller pretension (slack-side) with frictionless hinged connection.
- Residual stresses after proof-loading test by manufacturers play a role in OPB-induced failure.
- Mooring tensions change little due to the change of fairlead connection but bending moments on the chain are significantly affected.
- In case of fixed fairlead connection, bending moments and interlink-angle variations at taut side are greater than those at slack side, which means that the taut-side mooring is more vulnerable to OPB-induced failure. In case of frictionless hinged fairlead connection, the opposite is true.
- The dynamic bending moments are significantly increased after fixing the fairlead connection, which is consistent with the witness of practicing engineers during the past two decades
- In case of fixed fairlead connection, the fatigue damage is greatly (order of 100 times) increased compared to the hinged fairlead connection.
- When the residual stress effects are not accounted for, the fatigue damage is underestimated by 41% for hinged fairlead connection and by 33% for fixed fairlead connection. These differences are, however, much less when compared to the effect of fairlead-connection condition.

7.2 Effects of Fairlead-Connection Parameters on Mooring OPB-induced Failure

In chapter 3, the effects of underwater-chain-stopper (UCS) bearing friction at fairlead connection and time-varying interlink EI (bending stiffness) at the UCS exit on the OPB-induced-fatigue chain failure were investigated. To demonstrate their effects through numerical simulations, three different approaches, only considering time-varying EI, considering both time-varying EI and fairlead bearing friction, and neither considered, were modeled and the results were systematically compared. The "time-varying EI" was the multi-scale approach of using both local-high-fidelity and global-low-fidelity so that they were mutually interfaced at each time step. With fairlead bearing friction, the fairlead boundary condition was adjusted during the time-marching simulation depending on the instantaneous UCS angle and breakout angle. The simultaneous use of "time-varying fairlead bearing friction" and "time-varying EI" was not attempted by other researchers. In addition, the effect of different environmental heading (135deg) on the OPB stress was investigated. Also, the present UCSBRK approach (considering both time-varying EI and fairlead bearing friction) was compared with widely accepted BV methodology and the latter gave more conservative fatigue results.

In addition, since fairlead bearing friction is affected by UCS bending stiffness directly, UCS bending stiffness sensitivity test were modelled and analyzed.

From present research, several conclusions can be drawn as follows:

- OPB-induced short-term fatigue damage is significantly increased when "UCSBRK" approach is used compared to the "basic" and "time-varying EI"

approaches. It can be concluded that OPB-induced failure at target point (UCS exit) is mainly governed by UCS bearing friction at fairlead.

- When "basic" and "time-varying EI" approaches are used slack-side mooring is more vulnerable to OPB-induced failure than taut-side mooring while the opposite is true when "UCSBRK" approach is used.
- When "UCSBRK" approach is used high-frequency large-magnitude bending moments and stresses are generated at the target point, which can be a big problem in fatigue in view of high stress level and high number of cycles.
- The floater motions and mooring tension magnitudes are not appreciably affected by the three different approaches.
- Head environmental condition (=180deg) produced larger OPB-induced fatigue damage than 135-deg heading.
- BV methodology gave more conservative fatigue results than the present "UCSBRK" approach.
- With "UCSBRK" approach, the short-term fatigue damage can be increased by factor of 2 depending on UCS bending stiffness.
- With "UCSBRK" approach, the short-term fatigue damage can be underestimated by factor of 2 when residual stresses from nonlinear FEM are not considered.

7.3 Structural Health Monitoring for TLP-FOWT Tendon using Sensors

In chapter 4, an algorithm for the real-time structural health monitoring of TLP tendons using bi-axial slope sensors and top tension-meter was presented. Based on a generalized-coordinate-based FEM theory with high-order rod elements, essential equations were derived for estimating the variations of tensions and bending moments along the tendon. The simplified tension formula was derived by assuming small angles (less than 10 degrees) of tendon with respect to the vertical axis and the results turned out to be highly reliable. To validate the algorithm, several case studies were performed for various regular and irregular waves. The slope-sensor distribution is not necessarily uniform; instead, denser (or coarser) distribution for higher (or smaller) variation was recommended. The estimated tension and bending-moment signals by using the developed algorithms with numerical-sensor signals matched excellently against the actual values proving the accuracy and effectiveness of the proposed methodology.

To observe whether the developed algorithms can monitor even the details of the transient variations in tensions and bending moments, a special case of sudden one-line failure was also tested and it was confirmed that the algorithm can successfully capture the resulting transient responses, and thus be used as the basis of a failure detection system. Furthermore, the change of boundary conditions (B.C.) by unexpected circumstances can also be detected by examining the patterns of stress signals. When tested for maximum operational and extreme survival storm conditions, the algorithm predicted the tension and bending moment with 97-98% accuracy in the operational condition and 95-98% in the extreme condition.

The demonstrated capability of real-time monitoring of axial and bending stresses by the developed algorithms enables the real-time monitoring of accumulated fatigue damage at hot-spots by adding the corresponding fatigue-calculation algorithm, which can straightforwardly be added.

7.4 Real-Time Trace of Riser Profile and bending moment with Inclinometers

In chapter 5, to monitor or predict riser dynamic responses and the corresponding bending moments by using multiple-inclinometer signals, unique algorithms were developed based on the high-order rod-element FE formulas and analytic curve-length equation. The top and bottom points were assumed to be known. For riser x-y-z displacement tracing, quadratic interpolation functions for each line element between two neighboring bi-axial inclinometers were employed with respect to the global coordinate system. Then, from the analytic solutions for given boundary conditions, the node positions along the riser were sequentially obtained node by node at each time step. To solve the quadratic interpolation function, the analytic curve length formula in 3D space was used. As for bending moments, cubic interpolation function with respect to the generalized coordinate system was employed to allow double spatial derivative of shape function. With the given scheme, a simplified analytic formula for the bending moment at the mid-point of each riser segment can be obtained. Furthermore, through double spatial derivative of the shape function, the bending moments (or stresses) at any points along the riser can be obtained at each time step.

To validate the developed real-time riser-monitoring algorithms, a FPSO system with SCR or SLWR was simulated for 1-yr and 50-yr collinear wind-wave-current conditions with 45-deg heading and the corresponding numerical sensor signals were inputted to the algorithms for reproducing the real-time riser profiles and bending moments (or stresses). As a numerical tool, OrcaFlex, widely adopted commercial program in the oil & gas industry, was used. Two different sensor intervals, (compact (Int.=2m) and coarse (Int.=10m)), were tested.

Several conclusions can be drawn based on the presented results as below.

- Overall, the real-time prediction of riser profiles and bending moments (or stresses) by using the inclinometer signals with the developed algorithms agrees well with the actual values for both SCR and SLWR regardless of sea-environmental conditions.
- The computational time for the algorithm is minimal so that the real-time riser monitoring is possible. The developed algorithm is general, so it can be applied to any types of risers, mooring lines, and cables.
- The coarse sensor interval (10m) performed well compared to the compact sensor interval (2m) if riser shape varies smoothly along the arc length. If there is an inflection point within the interval around which curvature rapidly changes, high accuracy is not necessarily warranted. In this case, adjusted sensor arrangement is recommended for the high-curvature-varying region.
- The bending moments and bending stresses can be predicted equally well as the riser profiles when proper sensor arrangement is used.

7.5 Digital Twin Model for Riser Health Monitoring with Minimum Sensors

In chapter 6, novel riser structure health monitoring methodology with minimum sensors using digital twin and multivariate regression is suggested. First, to implement digital twin approach with minimum sensors, algorithms and methodology to obtain required information such as node displacements and tension and current profile prediction are explained. Node displacements can be traced in real-time using derived curve length equation in 3D space and inclinometers signal. Furthermore, tension also can be traced using sensing signals and intervals. Lastly, current profile below certain water depth is predicted applying multivariate regression algorithm inversely. Using those gathered information, digital twin is modelled and simulated. To claim the advantage of presented methodology, two different approaches such as innovative digital twin and typical forced floater oscillation are systemically compared and discussed. As a target structure, FPSO system with SCR is selected under 100-yr return period storm condition. It is confirmed that accuracy of performance assessment is greatly increased by the suggested methodology (digital twin) compared to the typical approach (forced floater oscillation).

REFERENCES

1. Jean, P., K. Goessens, and D. L'Hostis., Failure of chains by bending on deepwater mooring systems, Offshore Technology Conference, 2005, Houston, TX, USA

2. Rampi, L., F. Dewi, Vargas, P., Chain out of plane bending (OPB) joint industry project (JIP) summary and main results, Offshore Technology Conference, 2015, Houston, TX, USA

3. Bureau Veritas, Fatigue of Top Chain of Mooring Lines due to In-plane and Out-of-plane Bendings, Guidance Note NI, 2014

4. Rampi, L., Dewi, F., Vargas, P., Chain out of plane bending (OPB) fatigue joint industry project (JIP) static test program and OPB interlink stiffness, The 35th International Conference on Ocean, Offshore and Arctic Engineering, 2016, Busan, Korea

5. Choung, J. and J.-b. Lee, Out-of-plane bending stiffness and hotspot stress based on advanced numerical analysis techniques, Ships and Offshore Structures, 2019

6. Lee, C.-H. and Y. Kim, Probabilistic flaw assessment of a surface crack in a mooring chain using the first-and second-order reliability method, Marine Structures, 2019

7. Luo, M. and C. Heyl, Numerical Study on the Out-of-Plane Bending (OPB) Behaviors of Studless Mooring Chain Links in Fairlead Structures, The 27th International Ocean and Polar Engineering Conference, 2017, San Franscisco, CA,

USA

8. Hou, H.-M., Dong, G.-H., Xu, T.-J., Zhao, Y.-P., Bi, C.-W., Fatigue Reliability Analysis for Mooring Chain of Fish Cages Considering Corrosion Effect, The 27th International Ocean and Polar Engineering Conference, 2017, San Franscisco, CA, USA

9. Qiao, D., Kang, Z., Yan, J., Ma, Z., Li, Y., Influence of Out-of-Plane Bending to the Wear Analysis for Mooring Chain Link, The 27th International Ocean and Polar Engineering Conference, 2017, San Franscisco, CA, USA

10. Choung, J. and S. Han, A Novel Procedure for Mooring Chain Fatigue Prediction based on Maximum Principal Stress Considering Out-of-Plane and In-Plane Bending Effects, Journal of the Society of Naval Architects of Korea, 2016

11. Kim, Y., M.-S. Kim, and M.-J. Park, Fatigue analysis on the mooring chain of a spread moored FPSO considering the OPB and IPB, International Journal of Naval Architecture and Ocean Engineering, 2018

12. Hwang, O., Fatigue Assessment for Mooring Chain Link of Spread-Moored FPSO in Deepwater Considering Bending Phenomenon, Korea Maritime University, 2012 Busan, Korea

13. Lassen, T., J. Aarsnes, and E. Glomnes., Fatigue Design Methodology for Large Mooring Chains Subjected to Out-of-Plane Bending, The 33rd International Conference on Ocean, Offshore and Arctic Engineering, 2014, San Franscisco, CA,

USA

14. Amir, I., Caspar, H., Vargas, P., Zou, J., Guidance For Assessing Out-of-Plane Bending Fatigue on Chain Used in Permanent Mooring Systems, SNAME 23th Offshore Symposium, 2018, Houston, TX, USA

15. Chung, W.C., H.Y. Kang, and M.H. Kim, Multi-scale approach for chain-mooring OPB-induced failure considering time-varying interlink bending stiffness and fairlead condition, Applied Ocean Research, 2020

16. Kim, S.J. and D.-H. Won, Bending Behavior of the Mooring Chain Links Subjected to High Tensile Forces, Journal of Korean Society of Steel Construction, 2017

17. Kang, H.Y. and M.H. Kim, Safety assessment of Caisson transport on a floating dock by frequency-and time-domain calculations, Ocean Systems Engineering, 2014

18. Kim, M.H., Koo, B.J., Mercier, R., Ward, E., Vessel/mooring/riser coupled dynamic analysis of a turret-moored FPSO compared with OTRC experiment, Ocean Engineering, 2005

19. Ran, Z. and M.H. Kim, Nonlinear coupled responses of a tethered spar platform in waves, International Journal of Offshore and Polar Engineering, 1997

20. Yang, C.K. and M.H. Kim, Transient effects of tendon disconnection of a TLP by hull–tendon–riser coupled dynamic analysis, Ocean Engineering, 2010

21. Anderson, M., Nondestructive testing of offshore structures, NDT International, 1987

22. Ziegler, L. and M. Muskulus., Lifetime extension of offshore wind monopiles: Assessment process and relevance of fatigue crack inspection, The 12th EAWE PhD Seminar, 2016, DTU Lyngby, Denmark

23. Karayaka, M., W. Ruf, and S. Natarajan., Steel catenary riser response characterization with on-line monitoring devices, 28th International Conference on Ocean, Offshore and Arctic Engineering, 2009

24. O'Donnell, D., Srbinovsky, B., Murphy, J., Popovici, J., Pakrashi, V., Sensor measurement strategies for monitoring offshore wind and wave energy devices, Journal of Physics: Conference Series, 2015

25. Jahangiri, V., Mirab, H., Fathi, R., Ettefagh, M. M., TLP structural health monitoring based on vibration signal of energy harvesting system, Latin American Journal of Solids and Structures, 2016

26. Kim, H.-C., M.H. Kim, and D.-E. Choe, Structural health monitoring of towers and blades for floating offshore wind turbines using operational modal analysis and modal properties with numerical-sensor signals, Ocean Engineering, 2019

27. McNeill, S., Angehr, P., Kluk, D., Saruhashi, T., Sawada, I., Kyo, M., Yamazaki, Y., A Method for Determining Quasi-Static and Dynamic Riser Inclination Using Collocated Accelerometers and Angular Rate Sensors, The 33rd International

Conference on Ocean, Offshore and Arctic Engineering, 2014, San Franscisco, CA, USA

28. Li, B., Wang, H., Shen, X., Yan, Y., Yang, F., Hua, F., Deep-water riser fatigue monitoring systems based on acoustic telemetry, Journal of Ocean University of China, 2014

29. Pipa, D., Morikawa, S., Pires, G., Camerini, C., Santos, J., Flexible riser monitoring using hybrid magnetic/optical strain gage techniques through RLS adaptive filtering, EURASIP Journal on Advances in Signal Processing, 2010

30. Natarajan, S., Howells, H., Deka, D., Walters, D., Optimization of sensor placement to capture riser VIV response, The 25th International Conference on Offshore Mechanics and Arctic Engineering, 2006, Hamburg, Germany

31. Sohn, H., Farrar, C. R., Hunter, N. F., Worden, K., Structural health monitoring using statistical pattern recognition techniques, Journal of Dynamic Systems, Measurement, and Control, 2001

32. Kim, H.-J., Jang, B.-S., Park, C.-K., Bae, Y. H., Fatigue analysis of floating wind turbine support structure applying modified stress transfer function by artificial neural network, Ocean Engineering, 2018

33. Kim, M.H., CHARM3D User's Manual, Texas A&M University, 1997, College Station, TX, USA

34. Bae, Y.H. and M.H. Kim, Rotor-floater-mooring coupled dynamic analysis of

mono-column-TLP-type FOWT (Floating Offshore Wind Turbine), Ocean System Engineering, 2011

35. Bae, Y.H. and M.H. Kim, Rotor-floater-tether coupled dynamics including second-order sum–frequency wave loads for a mono-column-TLP-type FOWT (floating offshore wind turbine), Ocean Engineering, 2013

36. Lim, Y.-C., Kim, K.-S., Choung, J.-M., Kang, C.-H., A study on out-of-plane bending mechanism of mooring chains for floating offshore plants, Journal of the Society of Naval Architects of Korea, 2010

37. Garrett, D., Dynamic analysis of slender rods, Journal of energy resources technology, 1982

38. Orcina Ltd., OrcaFlex User Manual, Orcina Ltd, 2006, UK

39. Lee, C.-H. and J.N. Newman, WAMIT User manual, WAMIT, Inc., 2006

40. Kang, H.S., Semi-active magneto-rheological damper and applications in tension leg platform/semi-submersible, Texas A&M University, 2015, College Station, TX, USA

41. Chung, W.C., H.Y. Kang, and M.H. Kim., Numerical Study on OPB/IPB Interlink Angle with Underwater Chain Stopper System, SNAME 24th Offshore Symposium, 2019, Houston, TX, USA

42. Chung, W.C. and M.H. Kim, Effects of various fairlead-connection parameters on chain-mooring OPB-induced failure, Marine Structures, 2021

43. J.R. Morison, J.W. Johnson, S.A. Schaaf, The force exerted by surface waves on piles, Journal of Petroleum Technology, 1950

44. Ramberg, W. and W.R. Osgood, Description of stress-strain curves by three parameters, National Bureau of Standards, 1943

45. Zarandi, E.P. and Skallerud, B.H., Cyclic behavior and strain energy-based fatigue damage analysis of mooring chains high strength steel, Marine Structures, 2020

46. Zarandi, E.P. and Skallerud, B.H., Experimental and numerical study of mooring chain residual stresses and implications for fatigue life, International Journal of Fatigue, 2020

47. Hasselmann, K., Barnett, T., Bouws, E., Carlson, H., Cartwright, D., Enke, K., Kruseman, Measurements of wind-wave growth and swell decay during the Joint North Sea Wave Project (JONSWAP), Ergänzungsheft zur Deutschen Hydrographischen Zeitschrift, Reihe A, Nr. 12., 1973

48. American Petroleum Institute (API), Recommended practice for planning, designing and constructing fixed offshore platforms—Working stress design, 2A-WSD, American Petroleum Institute (API), 1993

49. Matsuishi, M. , T. Endo, Fatigue of metals subjected to varying stress, Japan Society of Mechanical Engineers, 1968 Fukuoka, Japan

50. American Bureau of Shipping (ABS), Guide for Building and Classing Floating Production Installations, American Bureau of Shipping (ABS), 2013

51. Chung, W.C., Kang, H.Y., Kim, M.H., Pestana, R. G., Riser Structural Health Monitoring with Numerical Sensors, The 29th International Ocean and Polar Engineering Conference, 2019, Hawaii, USA

52. Sparks, C.P., Fundamentals of marine riser mechanics, PennWell Corporation, 2007

53. Lee, C. and J. Newman, The computation of second-order wave loads, The 10th International Conference on Offshore Mechanics and Arctic Engineering, 1991, Stavanger, Norway

54. Kim, M.H. and Yue, D.K., Sum-and difference-frequency wave loads on a body in unidirectional Gaussian seas, Journal of Ship Research, 1991

55. Kim, S.J. and M.H. Kim, Dynamic behaviors of conventional SCR and lazy-wave SCR for FPSOs in deepwater, Ocean Engineering, 2015

56. Alexopoulos, E.C., Introduction to multivariate regression analysis, Hippokratia, 2010

57. MathWorks.,MATLAB: the language of technical computing. Desktop tools and development environment, version 7. Vol. 9., MathWorks., 2005

58. Ran, Z., Coupled dynamic analysis of floating structures in waves and currents, Texas A&M University, 2001, College Station, TX, USA

59. Bae, Y.H., Coupled dynamic analysis of multiple unit floating offshore wind turbine, Texas A&M University, 2013, College Station, TX, USA

APPENDIX A

WAVE FORCES ON OFFSHORE STURCTURES

In this appendix, linear and second order wave theories will be discussed at first. Furthermore, radiation and diffraction theory for floating structure, first-order wave excitation forces calculation based on potential theory will be introduced.

A.1 Wave Theory

Based on Laplace's equation (A.1), the wave theory can be derived with several assumptions such as incompressible, inviscid, irrotational [40, 58].

$$\nabla^2\Phi = 0 \tag{A.1}$$

To find wave potential in Laplace's equation, several boundary conditions such as kinematic and dynamic on the free surface and bottom can be applied. First, wave particles should be remained within the free surface (kinematic boundary condition)

$$\frac{\partial\eta}{\partial t} + u\frac{\partial\eta}{\partial x} + v\frac{\partial\eta}{\partial y} = \frac{\partial\Phi}{\partial t} \quad \text{at z=}\eta(x,y,t) \tag{A.2}$$

where $\eta(x,y,t)$ is wave elevation on the free surface.

Next, for the dynamic boundary condition which is that there is an agreement between the atmospheric pressure and the pressure along the free surface (A.3)

$$\rho\frac{\partial\Phi}{\partial t} + \frac{1}{2}(\Phi_x{}^2 + \Phi_y{}^2 + \Phi_z{}^2) = -\rho g z \qquad \text{at z=}\eta\text{(x,y,t)} \tag{A.3}$$

For bottom boundary condition which is physically means that wave particles cannot penetrate the seabed (velocity of wave particle in vertical direction is always zero) (A.4).

$$\frac{\partial\Phi}{\partial z} = 0 \qquad \text{at z=-d, d is water depth} \tag{A.4}$$

Even though available boundary conditions are applied, Laplace's equation is still difficult to resolve exactly because of the non-linear terms on the free surface boundary conditions. Thus, here, perturbation approach is adopted with small wave amplitude assumption to estimate approximated solution with a certain level of accuracy [40, 58].

The corresponding first- and second-order wave velocity potentials and free surface elevation are presented as below,

$$\Phi^{(1)} = \mathrm{Re}[-\frac{igA}{\omega}\cdot\frac{\cosh k(z+d)}{\cosh kd}\cdot e^{i(kx\cos\theta+ky\sin\theta-\omega t)}] \tag{A.5}$$

$$\eta^{(1)} = A\cos(kx\cos\theta+ky\sin\theta-wt) \tag{A.6}$$

$$\Phi^{(2)} = \mathrm{Re}[-\frac{3}{8}\cdot\omega A^2\cdot\frac{\cosh 2k(z+d)}{\sinh^4 kd}\cdot e^{i(2kx\cos\theta+2ky\sin\theta-2\omega t)}] \tag{A.7}$$

$$\eta^{(2)} = A^2\cdot\frac{\cosh kd}{\sinh^3 kd}\cdot\cos(2kx\cos\theta+2ky\sin\theta-2\omega t) \tag{A.8}$$

where A is wave amplitude, ω is the wave frequency, k is wave number and θ is wave heading angle.

For generation of random sea environment condition, fully-developed wave model can be modelled using wave spectra. Based on given wave spectrum $S(\omega)$, random wave elevation signal can be generated by combination of a numerous number of linear wave components with random phases [40, 59].

$$\eta(x,t) = \sum_{i=1}^{N} A_i\cos(k_i x+\omega_i t+\varepsilon_i) = \mathrm{Re}[\sum_{i=1}^{N} A_i e^{i(k_i x-\omega_i t+\varepsilon_i)}] \tag{A.9}$$

$$A_i = \sqrt{2S(\omega_i)\Delta\omega} \tag{A.10}$$

where N, ε and $\Delta\omega$ are the number of wave components and random phase angle (generated by random number generation function) and wave frequency intervals, respectively. In this study, adjusted formula will be applied to avoid the repetition of random wave realization with restricted wave components number [40, 58]

$$\eta(x,t) = \mathrm{Re}[\sum_{i=1}^{N} A_i e^{i(k_i x - (\omega_i + \delta\omega_i)t + \varepsilon_i)}] \tag{A.11}$$

where $\delta\omega_i$ is the random perturbation number evenly distributed between $-\frac{\Delta\omega}{2}$ and $\frac{\Delta\omega}{2}$.

A.2 Wave Loads on Floating Structure

Since wave excitation loading calculation on floater is essential for prediction of mooring and riser dynamic response, the methodology using the diffraction and radiation theory (based on previously derived wave velocity potential) and the Morison equation will be explained in this section.

A.2.1 Diffraction and Radiation

Total velocity potential Φ should satisfy the Laplace equation with several boundary conditions such as free surface (kinematic and dynamic) and bottom boundary condition. Furthermore, total velocity potential can be expressed using linear combination of incidental velocity potential Φ_I, diffraction velocity potential Φ_D, radiation potential Φ_R using perturbation approach and wave slope parameter ε [40, 58]

$$\Phi = \sum_{n=1}^{\infty} \varepsilon^n \Phi^{(n)} = \sum_{n=1}^{\infty} \varepsilon^n (\Phi_I{}^{(n)} + \Phi_D{}^{(n)} + \Phi_R{}^{(n)}) \tag{A.12}$$

where $\Phi^{(n)}$ means the n th order of Φ.

In addition, the body boundary condition of floating structure is required to resolve wave excitation loads on the floating structure (A.13).

$$\frac{\partial \Phi}{\partial n} = V_n \qquad \text{on the body surface} \tag{A.13}$$

where n is normal vector on the surface, V_n is the normal velocity vector on the body surface.

Also, the *Sommerfeld* far field radiation condition should be satisfied for the diffraction Φ_D, radiation potential Φ_R [40, 58].

$$\lim_{r\to\infty}\sqrt{r}[\frac{\partial\Phi_{D,R}}{\partial r}\pm ik\Phi_{D,R}]=0 \tag{A.14}$$

where r denotes the radial distance from center of the floating structure.

A.2.2 First Order Boundary Value Problem

Using perturbation approach, the first order wave velocity potential and the first order incident potential $\Phi_I^{(1)}$ can be expressed as below (separating the time dependency explicitly), respectively.

$$\begin{aligned}\Phi^{(1)} &= \varepsilon(\Phi_I^{(1)}+\Phi_D^{(1)}+\Phi_R^{(1)})\\ &= \mathrm{Re}\left\{[\phi_I^{(1)}(x,y,z)+\phi_D^{(1)}(x,y,z)+\phi_R^{(1)}(x,y,z)]\cdot e^{-i\omega t}\right\}\end{aligned} \tag{A.15}$$

$$\phi_I^{(1)}(x,y,z)=\mathrm{Re}[-\frac{igA}{\omega}\frac{\cosh k(z+d)}{\cosh kd}e^{iKx}] \tag{A.16}$$

where k means that a wave number vector under the Cartesian components $(k\cos\theta, k\sin\theta, 0)$, x is the position vector and θ is the incident wave angle (related to x-axis).

The summary of first order diffraction and radiation potential governed by the boundary value problem is presented as below.

$$\nabla^2\phi_{D,R}^{(1)}=0 \qquad \text{within fluid domain (z < 0)} \tag{A.17}$$

$$[-\omega^2+g\frac{\partial}{\partial z}]\cdot\phi_{D,R}^{(1)}=0 \qquad \text{on the free surface (z = 0)} \tag{A.18}$$

$$\frac{\partial \phi_{D,R}^{(1)}}{\partial z} = 0 \quad \text{on the bottom (z = -d)} \tag{A.19}$$

$$\frac{\partial \phi_{R}^{(1)}}{\partial n} = -i\omega \mathbf{n} \cdot [\xi^{(1)} + \alpha^{(1)} \times \mathbf{r}] \quad \text{on the body surface} \tag{A.20}$$

$$\lim_{r\to\infty} \sqrt{r}[\frac{\partial}{\partial r} \pm ik] \cdot \phi_{D,R}^{(1)} = 0 \quad \text{at far field} \tag{A.21}$$

where $\mathbf{r}$ is the position vector on the body surface, r is the radial distance from the center and $\mathbf{n}$ is the unit normal vector (from body surface into the fluid domain).

The corresponding first-order motion of the floating structure in translational $\Xi^{(1)}$ and rotational $\Theta^{(1)}$ are presented as below [40, 59].

$$\Xi^{(1)} = \mathrm{Re}[\xi^{(1)} e^{-i\omega t}], \quad \xi^{(1)} = [\xi_1^{(1)}, \xi_2^{(1)}, \xi_3^{(1)}] \tag{A.22}$$

$$\Theta^{(1)} = \mathrm{Re}[\alpha^{(1)} e^{-i\omega t}], \quad \alpha^{(1)} = [\alpha_1^{(1)}, \alpha_2^{(1)}, \alpha_3^{(1)}] \tag{A.23}$$

In the above equations, the subscripts number means the six degrees of freedom motion direction such as 1,2,3 is for surge, sway and heave and 4,5,6 is for roll, pitch, yaw, correspondingly. Those six degrees of freedom motions can be re-written as below,

$$\zeta_i = \xi_i^{(1)} \quad \text{for i = 1,2,3} \tag{A.24}$$

$$\zeta_i = \alpha_i^{(1)} \quad \text{for i = 1,2,3} \tag{A.25}$$

The radiation velocity potential which is caused by fluid disturbance near floating structure can be presented as below,

$$\phi_R^{(1)} = \sum_{i=1}^{6} \zeta_i \phi_i^{(1)} \tag{A.26}$$

where ϕ_i is the first-order velocity potential under unit amplitude condition in the *i* th mode. Continually, the body boundary condition on the body surface can be re-written as below [40, 59],

$$\frac{\partial \phi_i^{(1)}}{\partial n} = n_i \qquad \text{for i = 1,2,3} \tag{A.27}$$

$$\frac{\partial \phi_i^{(1)}}{\partial n} = [r \times n]_{i-3} \qquad \text{for i = 4,5,6} \tag{A.28}$$

Also, the diffraction velocity potential can be applied the body surface boundary condition [40, 58]

$$\frac{\partial \phi_D^{(1)}}{\partial n} = -\frac{\partial \phi_I^{(1)}}{\partial n} \qquad \text{on the body surface} \tag{A.29}$$

A.2.3 First Order Potential Forces

Using the first order diffraction ($\phi_D^{(1)}$) / radiation ($\phi_R^{(1)}$) velocity potential, wave excitation loads on the floating structure can be obtained. Based on the perturbation approach, the hydrodynamic pressure on the floating structure surface can be written as below [40, 58].

$$P^{(1)} = -\rho \frac{\partial \Phi^{(1)}}{\partial t} \tag{A.30}$$

Using combination of hydrodynamic pressure and wetted body surface S(t), total forces and moments exerted on the floating structure can be obtained as below [40, 59].

$$F(t)_i = \iint_{Sb} Pn_i dS \qquad i = 1,2,3$$
$$F(t)_i = \iint_{Sb} P(r \times n)_i dS \qquad i = 4,5,6 \tag{A.32}$$

Thus, total first order loads can be obtained.

$$F^{(1)} = F_{HS}{}^{(1)} + F_R{}^{(1)} + F_{EX}{}^{(1)} \tag{A.32}$$

where HS, R and EX represents the hydrostatic restoring, the radiation and the wave exciting (the incident and diffraction potentials) force and moments, accordingly.

Here, due to dynamic response (motion) of the floating structure, the change of the first order hydrostatic restoring force and moment $F_{HS}{}^{(1)}$ is occurred.

$$F_{HS}{}^{(1)} = -K[\zeta^{(1)}] \tag{A.33}$$

where K is the hydrostatic restoring stiffness, $\zeta^{(1)}$ is the first order motion.

Continually, the radiation potential induced first order force and moment can be written as below,

$$F_R{}^{(1)} = \mathrm{Re}\left([\mathbf{f}] \cdot \{\zeta^{(1)}\}\right) \tag{A.34}$$

where

$$\mathbf{f} = f_{ij} = -\rho \iint_{S_b} \frac{\partial \phi_i}{\partial n} \phi_j dS \qquad \text{i, j = 1,2, … ,6} \tag{A.35}$$

$$f_{ij} = -\omega^2 M_{ij}{}^a - i\omega C_{ij} \tag{A.36}$$

Thus, radiation potential force and moment can be expressed as below [40, 59].

$$F_R{}^{(1)} = \mathrm{Re}\left([\mathbf{M}^a]\{\ddot{\zeta}^{(1)}\} + [\mathbf{C}]\{\dot{\zeta}^{(1)}\}\right) \tag{A.37}$$

where $\mathbf{M}^a$ is the added mass coefficients and C is the damping (radiation) coefficients.

The force term $F_{EX}{}^{(1)}$ in the below equation which is the first order wave force and moment based on incident and diffraction velocity potential can be defined as below [40, 58].

$$F_{EX}{}^{(1)} = \mathrm{Re}\left(-\rho A e^{i\omega t} \iint_{S_0} (\phi_I + \phi_D) \frac{\partial \phi_j}{\partial n} dS \right) \qquad \mathrm{j} = 1,2, \ldots, 6 \tag{A.38}$$

As shown, the first order wave excitation loads are proportional to the frequency dependent wave amplitude. Thus, Linear Transfer Function (LTF= $F_{EX}{}^{(1)} / A$) represents correlation between incident wave elevation and the first order diffraction forces on the floating structures [40, 59].

A.2.4 Wave Loads in Time Domain Simulation

During the time domain simulation (CHARM3D), the linear wave forces are calculated with given wave frequency, the second order sum and difference frequency forces also can be obtained using the interaction of bi-chromatic waves [40, 58, 59]. Using two Volterra series in the time domain, the linear and second order hydrodynamic loads on the floating structures induced from stationary Gaussian random seas condition can be written [40, 58].

$$F^{(1)}(t) + F^{(2)}(t) = \int_{-\infty}^{\infty} h_1(\tau) \cdot \eta(t-\tau) d\tau + \int_{-\infty}^{\infty} \int_{-\infty}^{\infty} h_2(\tau_1, \tau_2) \cdot \eta(t-\tau_1) \cdot \eta(t-\tau_2) d\tau_1 d\tau_2 \tag{A.39}$$

where $h_1(\tau)$ represents the linear impulse response function and $h_2(\tau_1, \tau_2)$ is the quadratic impulse response function. Furthermore, $\eta(t)$ means the ambient wave free surface location at the reference position.

For N number of wave components under uni-directional sea state, the wave exciting loads from incident and diffraction velocity potential can be written as below [40, 59].

$$F_I^{(1)}(t) = \mathrm{Re}[\sum_{i=1}^{N} A_i \mathbf{L}(\omega_i) e^{i\omega_i t}] \tag{A.40}$$

$$F_I^{(2)}(t) = \mathrm{Re}[\sum_{j=1}^{N}\sum_{k=1}^{N} A_j A_k^{*} \mathbf{D}(\omega_j, -\omega_k) \cdot e^{i(\omega_j-\omega_k)t} + \sum_{j=1}^{N}\sum_{k=1}^{N} A_j A_k \mathbf{S}(\omega_j, \omega_k) \cdot e^{i(\omega_j+\omega_k)t}] \tag{A.41}$$

(*) represent the complex conjugate. Also, **L, D, S** means linear transfer function (LTF), the difference (**D**) and sum (**S**) frequency quadratic transfer function (QTF), accordingly. Furthermore, the wave excitation loads for multi-directional waves can be expressed as below [40, 59].

$$F_I^{(1)}(t) = \mathrm{Re}[\sum_{j=1}^{N}\sum_{l=1}^{M} A_{jl} \mathbf{L}(\omega_j, \theta_l) e^{i\omega_i t}] \tag{A.42}$$

$$\begin{aligned} F_I^{(2)}(t) = \mathrm{Re}[&\sum_{j=1}^{N}\sum_{k=1}^{N}\sum_{l=1}^{M}\sum_{m=1}^{M} A_{jl} A_{km}^{*} \mathbf{D}(\omega_j, -\omega_k, \theta_l, \theta_m) \cdot e^{-i(\omega_j-\omega_k)t} \\ &+ \sum_{j=1}^{N}\sum_{k=1}^{N}\sum_{l=1}^{M}\sum_{m=1}^{M} A_{jl} A_{km}^{*} \mathbf{S}(\omega_j, \omega_k, \theta_l, \theta_m) \cdot e^{-i(\omega_j+\omega_k)t}] \end{aligned} \tag{A.43}$$

For wave load caused by radiation velocity potential in time domain can be expressed as below [40, 58].

$$F_R(t) = -\mathbf{M}^a(\infty) \cdot \ddot{\zeta} - \int_{-\infty}^{t} \mathbf{R}(t-\tau) \cdot \dot{\zeta}(\tau) d\tau \tag{A.44}$$

where $\mathbf{M}^a(\infty)$ is the added mass at infinite wave frequency. Also, the convolution integral term means that the memory effects of the wave loads on the floating structure

prior to time t. Furthermore, **R(*t*)** is called the retardation function which is related to frequency domain solution for radiation problem as follow [40, 59].

$$\mathbf{R}(t) = \frac{2}{\pi}\int_0^\infty C(\omega)\frac{\sin\omega t}{\omega}\,d\omega \tag{A.45}$$

$C(\omega)$ is the wave damping coefficient. The added mass at infinite frequency ($\mathbf{M}^a(\infty)$) is equivalent to constant value [40, 58].

$$\mathbf{M}^a(\infty) = \mathbf{M}^a(\infty) - \int_0^\infty \mathbf{R}(t)\cdot\cos\omega t\ dt \tag{A.46}$$

By summing each force terms, total wave force in the time domain can be calculated [40, 59].

$$\begin{aligned} F_{total}(t) &= F^{(1)}(t) + F^{(2)}(t) \\ &= F_I^{(1)}(t) + F_I^{(2)}(t) + F_R(t) \end{aligned} \tag{A.47}$$

A.2.5 Morison's Formula

Since wave loads based on velocity potential cannot consider viscous effect, Morison's formula is employed additionally [43].

$$F_M = C_m\rho\frac{\pi D^2}{4}\dot{u}_n - C_a\rho\frac{\pi D^2}{4}\ddot{\xi}_n + \frac{1}{2}\rho C_D D_s(u_n - \dot{\zeta}_n)\cdot\left|u_n - \dot{\zeta}_n\right| \tag{A.48}$$

F_M denotes the Morison force, C_m $(=1+C_a)$ is the inertia coefficient, C_a is the added mass coefficient, C_D is the drag coefficient, D_s is diameter or breadth of the floating structure, u_n and $\dot{u}_n$ are the velocity and acceleration of the fluid normal to the structure, $\dot{\zeta}_n$ and $\ddot{\xi}_n$ are normal velocity and acceleration of the floating structure.

A.2.6 Time Domain Solution for Floating Structure Motion

The equation of motion for floating structure in time domain can be expressed as below [40, 58].

$$[\mathbf{M}+\mathbf{M}^{a}(\infty)]\cdot\ddot{\zeta}+\mathbf{K}\cdot\zeta=\mathbf{F}_{I}(t)+\mathbf{F}_{C}(t,\dot{\zeta})+\mathbf{F}_{M}(t,\zeta) \tag{A.49}$$

$$\mathbf{F}_{C}(t,\dot{\zeta})=-\int_{-\infty}^{t}\mathbf{R}(t-\tau)\cdot\dot{\zeta}\;d\tau \tag{A.50}$$

where $\mathbf{F}_{I}(t)$ is the first and second order wave exciting forces and $\mathbf{F}_{M}(t,\zeta)$ is drag forces obtained from Morison Equation.

In the numerical modeling, the second-order *Adams-Moulton* method (or mid-point method) is applied. Because the finite element analysis of the mooring lines and riser in time domain is developed based on this method, the same method should be applied here to resolve together at each time step (fully-coupled equations of mooring lines-riser-hull) [40, 58].

$$\bar{\mathbf{M}}\cdot\dot{\zeta}=\mathbf{F}_{I}(t)+\mathbf{F}_{C}(t,\dot{\zeta})+\mathbf{F}_{M}(t,\zeta)-\mathbf{K}\cdot\zeta \tag{A.51}$$

$$\dot{\zeta}=\xi \tag{A.52}$$

where

$$\bar{\mathbf{M}}=\mathbf{M}+\mathbf{M}^{a}(\infty) \tag{A.53}$$

Apply integration to the above equations from time step $t^{(n)}$ to $t^{(n+1)}$

$$\bar{\mathbf{M}}\cdot\xi^{(n+1)}-\bar{\mathbf{M}}\cdot\xi^{(n)}=\int_{t^{(n)}}^{t^{(n+1)}}(\mathbf{F}_{I}(t)+\mathbf{F}_{C}(t,\dot{\zeta})+\mathbf{F}_{M}(t,\zeta))dt-\int_{t^{(n)}}^{t^{(n+1)}}(\mathbf{K}\cdot\zeta)dt \tag{A.54}$$

$$\zeta^{(n+1)}-\zeta^{(n)}=\int_{t^{(n)}}^{t^{(n+1)}}\xi dt \tag{A.55}$$

Here, using the *Adams-Moulton* scheme: $\int_{t^{(n)}}^{t^{(n+1)}} x\ dt = \frac{\Delta t}{2}[x^{(n)} + x^{(n+1)}]$ (A.56)

$$\bar{\mathbf{M}} \cdot \xi^{(n+1)} = \bar{\mathbf{M}} \cdot \xi^{(n)} + \frac{\Delta t}{2}[\mathbf{F}_I{}^{(n+1)} + \mathbf{F}_I{}^{(n)} + \mathbf{F}_C{}^{(n+1)} + \mathbf{F}_C{}^{(n)} + \mathbf{F}_M{}^{(n+1)} + \mathbf{F}_M{}^{(n)}] - \frac{\Delta t}{2}[\mathbf{K} \cdot (\zeta^{(n+1)} + \zeta^{(n)})] \quad \text{(A.57)}$$

$$\zeta^{(n+1)} - \zeta^{(n)} = \frac{\Delta t}{2}[\xi^{(n+1)} + \xi^{(n)}] \quad \text{--->} \quad \xi^{(n+1)} = \frac{2}{\Delta t}[\zeta^{(n+1)} - \zeta^{(n)}] - \xi^{(n)} \quad \text{(A.58)}$$

In the above equations, there are several unknown terms such as $\xi^{(n+1)}$ and $\zeta^{(n+1)}$, the convolution integral and drag force which are a function of the floater velocity at time step (n1). Thus, an iterative process is required to resolve the equations with initial guess of the $\xi^{(n+1)}$ term within calculation process the $\mathbf{F}_C{}^{(n+1)}$ and $\mathbf{F}_M{}^{(n+1)}$ [40, 58].

Here, using the *Adams-Bashforth* scheme, the iterative procedure can be avoided for below non-linear loads terms [40, 58].

$$\int_{t^{(n)}}^{t^{(n+1)}} F_C\ dt = \frac{\Delta t}{2}[3 \cdot \mathbf{F}_C{}^{(n)} - \mathbf{F}_C{}^{(n-1)}] = \Delta t \cdot \mathbf{F}_C{}^{(0)} \qquad \text{for n=0} \quad \text{(A.59)}$$

$$\int_{t^{(n)}}^{t^{(n+1)}} F_M\ dt = \frac{\Delta t}{2}[3 \cdot \mathbf{F}_M{}^{(n)} - \mathbf{F}_M{}^{(n-1)}] = \Delta t \cdot \mathbf{F}_M{}^{(0)} \qquad \text{for n=0} \quad \text{(A.60)}$$

The floating structure equation of motion in time domain can be expressed as below

$$[\frac{4}{\Delta t^2}\bar{\mathbf{M}} + \mathbf{K}] \cdot \Delta\zeta = \frac{4}{\Delta t}\bar{\mathbf{M}}\xi^{(n)} + [\mathbf{F}_I{}^{(n+1)} + \mathbf{F}_I{}^{(n)}] + [3 \cdot \mathbf{F}_C{}^{(n)} - \mathbf{F}_C{}^{(n-1)}] + [3 \cdot \mathbf{F}_M{}^{(n)} - \mathbf{F}_M{}^{(n-1)}] - 2\mathbf{K}\zeta^{(n)} + 2\mathbf{F}_0 \quad \text{(A.61)}$$

$\mathbf{F}_0$ is a constant load (ex: net buoyancy force)

where $\Delta\zeta = \zeta^{(n+1)} - \zeta^{(n)}$ (A.62)

APPENDIX B

DYNAMICS OF MOORING LINES AND RISER

In this section, based on three-dimensional elastic rod theory [37], the modelling of legs such as mooring lines or riser in the CHARM3D is explained and discussed.

B.1 Theory of Rod

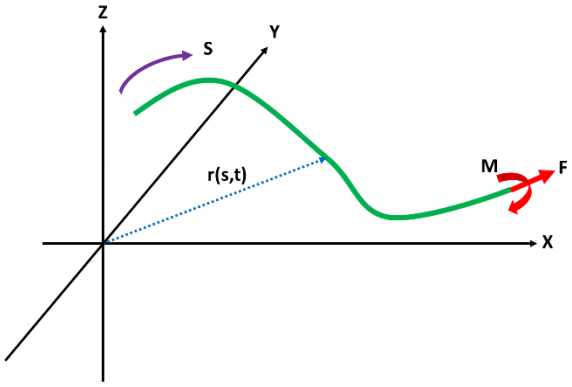

Figure 105 Coordinate system of slender rod

In this section, behavior of slender rod can be described with respect to the center line of the rod. As shown in Figure 105, position vector ($r(s,t)$) which is a function of arc length (s) and time (t) is introduced to define curved line in three-dimensional space. Using assumption that the rod is inextensible, it can be defined that r' is the unit tangent vector and r'' is the principal normal vector and $r' \times r''$ is bi-normal vector where the prime means the differentiate with respect to the arc length whereas the dot means the differentiation with respect to the time in the following.

By applying equilibrium of the linear force and moment at the unit arc length, equation of motion of the rod can be expressed as below:

$$F' + q - \rho \ddot{r} = 0 \tag{B.1}$$

$$M' + r' \times F' + m = 0 \tag{B.2}$$

where q and m are the applied force and moment per unit length of arc length, ρ is the mass per unit length. F and M are the resultant force and moment. The resultant moment M can be re-written as below

$$M' - (r' \times EIr'') - Hr' = 0 \tag{B.3}$$

where EI is bending stiffness of the rod, H is the torque. It shows the relationship between the bending moment and the curvature along the bi-normal direction. Using this relationship, below equation is also derived.

$$r' \times [(EIr'')' + F] + H'r' + Hr'' + m = 0 \tag{B.4}$$

$$H' + m \cdot r' = 0 \tag{B.5}$$

With assumption that the torque effect can be negligible and there is no distributed torsional moment, eq.3.4 can be re-written as

$$r' \times [(EIr'')' + F] = 0 \tag{B.6}$$

Here, introducing the *Lagrangian* multiplier which is a scalar function $\lambda(s,t)$, the force term and the scalar product can be re-written as below.

$$F = -(EIr'')' + \lambda r' \tag{B.7}$$

$$\lambda = F \cdot r' - (EIr'')' \cdot r' \tag{B.8}$$

By introducing the tension (T) and the curvature (κ) of the rod, above equation can be expressed again.

$$\lambda = T - EI \cdot \kappa^2 \tag{B.9}$$

Combining Equation 3.7 with 3.1, the equation of motion can be developed. Furthermore, the inextensible condition of the rod should be satisfied.

$$-(EI \cdot r'')'' + (\lambda \cdot r')' + q = \rho \cdot \ddot{r} \tag{B.10}$$

$$r' \cdot r' = 1 \tag{B.11}$$

Continually, the elongation is infinite small and linear if the rod is extensible. Then, above equation can be approximated as:

$$\frac{1}{2}[r' \cdot r' - 1] = \frac{T}{AE} \approx \frac{\lambda}{AE} \tag{B.12}$$

It can be obtained the position vector ($= r(s,t)$) and the *Lagrangian* multiplier ($\lambda(s,t)$) from above equation if sufficient information is given such as inextensible condition with initial and boundary conditions and applied force vector q. In addition, the gravity of the rod and the hydrostatic/hydrodynamic forces are related to the applied force vector q in offshore systems. Thus, it can be re-written as:

$$q = w + F_s + F_d \tag{B.13}$$

where w is the rod weight per unit length, F_s *and* F_d are the hydrostatic / hydrodynamic forced applied on the rod unit length. Furthermore, hydrostatic force can be re-written as

$$F_s = B - (\mathrm{Pr}')' \tag{B.14}$$

where B is buoyancy force and P is the hydrostatic pressure at point r on the rod.

With combination of the Morison's formula as below,

$$F_d = -C_A \ddot{r}^n + C_M \dot{V}^n + C_D \left| V^n - \ddot{r}^n \right| (V^n - \ddot{r}^n) = -C_A \ddot{r}^n + \bar{F}_d \tag{B.15}$$

where C_A is the added mass coefficient, C_M is the inertia coefficient, C_d is the drag coefficient. V^n and $\dot{V}^n$ are fluid around the structure velocity and acceleration, respectively. Those terms can be expressed as:

$$V^n = (V - \dot{r}) - [[V - \dot{r}] \cdot r'] \cdot r' \tag{B.16}$$

$$\dot{V}^n = \dot{V} - (V \cdot \dot{r}) \cdot \dot{r} \tag{B.17}$$

$$\dot{r}^n = \dot{r} - (\dot{r} \cdot \dot{r}) \cdot r' \tag{B.18}$$

$$\ddot{r}^n = \ddot{r} - (\ddot{r} \cdot r') \cdot r' \tag{B.19}$$

The equation of motion of the rod finally derived with its weight, hydrostatic and hydrodynamic forces in the sea water using combination of other equations (B.13~B.15 and B.1).

$$-\rho\ddot{r} - C_A\ddot{r}^n - (EIr'')'' + (\tilde{\lambda} r_i')' + \bar{w} + F_d = 0 \tag{B.20}$$

$$\tilde{\lambda} = T + P - EI\kappa^2 \tag{B.21}$$

$$\bar{w} = w + B \tag{B.22}$$

$$\bar{T} = T + P \tag{B.23}$$

$\bar{w}$ and $\bar{T}$ are the effective tension / weight of the rod.

Finally, governing equation for the statics or dynamics of the rod is derived with combination equations (B.20) and (B.12).

B.2 Finite Element Modeling of Rod in CHARM3D

The governing equation of the rod in the sea water can be re-written as:

$$-\rho\ddot{r}_i - C_A\ddot{r}_i^n - (EIr_i'')'' + (\bar{\lambda} r_i')' + \bar{w}_i + F_{d_i} = 0 \tag{B.24}$$

Also, inextensible of the rod condition can be expressed as:

$$\frac{1}{2}[r_n' r_n' - 1] - \frac{\lambda}{AE} = 0 \tag{B.25}$$

Using finite element method, the governing equation of the rod can be discretized into several elements which has a finite length. For each element, the variables such as $\lambda(s,t)$ and $r_i(s,t)$ can be approximated as [40, 58].

$$r_i(s,t) = A_l(s) \cdot U_{il}(t) \tag{B.26}$$

$$\lambda(s,t) = P_m(s) \cdot \lambda_m(t) \tag{B.27}$$

where $0 \le s \le L$ and A_l and P_m is called the interpolation function. By applying the *Galerkin's* method along the element length, it can be expressed as [40, 58].

$$\int_0^L \delta r_i[-\rho\ddot{r}_i - C_A\ddot{r}_i^n - (EIr_i'')'' + (\bar{\lambda} r_i')' + \bar{w}_i + F_{d_i}]\, ds = 0 \tag{B.28}$$

With assumption that the term (δU_{ij} in $\delta r_i = A_l \delta U_{il}(t)$) is independent, the above equation can be resolved after integration by parts scheme is applied.

$$\begin{aligned} &\int_0^L [A_l(\rho\ddot{r}_i + C_A\ddot{r}_i^n) + EIA_l'' r_i'' + \bar{\lambda} A_l' r_i' - A_l(\bar{w}_i + F_{d_i})]\, ds \\ &= EIr_i'' \cdot A_l' \Big|_0^L + [\bar{\lambda}_l r_i' - (EIr_i'')'] \cdot A_l \Big|_0^L \end{aligned} \tag{B.29}$$

Furthermore, the stretching condition can be re-written and quadratic and cubic interpolation function can be applied for P_m and A_l [40, 58].

$$\int_0^L P_m[\frac{1}{2}(r_n' r_n' - 1) - \frac{\lambda}{AE}]\, ds = 0 \tag{B.30}$$

$$\begin{aligned} &P_1 = 1 - 3\xi + 2\xi^2,\ \ P_2 = 4\xi - 4\xi^2,\ \ P_3 = 2\xi^2 - \xi \\ &A_1 = 1 - 3\xi^2 + 2\xi^3,\ \ A_2 = L(\xi - 2\xi^2 + \xi^3),\ \ A_3 = 3\xi^2 - 2\xi^3,\ \ A_4 = L(-\xi^2 + \xi^3) \end{aligned} \tag{B.31}$$

$$\xi = \frac{s}{L} \tag{B.32}$$

The parameters such as U_{il} and λ_m can be written with assumptions that the position, tangent, the *Lagrangian* multiplier (r_i, r_i', λ) are continuous between the neighboring elements, respectively [40, 58].

$$U_{i1} = r_i(0,t),\ \ U_{i2} = r_i'(0,t),\ \ U_{i3} = r_i(L,t),\ \ U_{i4} = r_i'(L,t) \tag{B.33}$$

$$\lambda_1 = \lambda(0,t),\ \ \lambda_2 = \lambda(L/2, t),\ \ \lambda_3 = \lambda(L,t) \tag{B.34}$$

Using combination equations (B.19, B.26, B.27 and B.29), the equation of motion of the element can be presented as below:

$$(M_{ijkl} + M_{ijkl}{}^a)\ddot{U}_{jk} + (K^1_{ijkl} + \lambda_n K^2_{ijkl})U_{jk} = F_{il} \tag{B.35}$$

$$\int_0^L A_l \rho \ddot{r}_i\, ds = \int_0^L A_l \rho A_k \delta_{ij}\, ds \ \cdot\ \ddot{U}_{jk} = M_{ijkl} \cdot \ddot{U}_{jk} \tag{B.35a}$$

$$\begin{aligned} &\int_0^L A_l C_A \ddot{r}_i^n\, ds = \int_0^L A_l C_A[\ddot{r}_i - (\ddot{r}\cdot r_i')\cdot r_i']\, ds = C_A[\int_0^L A_l[\ddot{r}]\, ds - \int_0^L A_l[(\ddot{r}\cdot r_i')\cdot r_i']\, ds] \\ &= C_A[\int_0^L A_l A_k \delta_{ij}\, ds - (\int_0^L A_l A_k A_s' A_t'\, ds)\cdot U_{it} U_{js}]\cdot \ddot{U}_{jk} = M^a{}_{ijkl}\cdot \ddot{U}_{jk} \end{aligned} \tag{B.35b}$$

$$\int_0^L EIA_i''r_i''ds = \int_0^L EIA_i''A_k''\delta_{ij}ds \cdot U_{jk} = K^1{}_{ijkl} \cdot U_{jk} \tag{B.35c}$$

$$\int_0^L \bar{\lambda}A_i'r_i'ds = \lambda_n \int_0^L P_n A_i'A_k'\delta_{ij}ds \cdot U_{jk} = \lambda_n K^2{}_{nijk} \cdot U_{jk} \tag{B.35d}$$

$$\int_0^L A_i(\bar{w}_i + F_{d_i})\, ds = F_{il} \tag{B.35e}$$

δ_{ij} is called the *Kronecker* Delta Function. The resultant loads of the last element are not considered in the above equation because they are cancelling out during the derivation process of the final assembly equation. The coefficients of the above equation such as mass, added mass, bending stiffness and axial stiffness are defined as below.

$$M_{ijkl} = \int_0^L A_i \rho A_k \delta_{ij}\, ds \qquad \text{for mass} \tag{B.36}$$

$$M^a{}_{ijkl} = C_A[\int_0^L A_i A_k \delta_{ij} ds - (\int_0^L A_i A_k A_s'A_t'ds) \cdot U_{it}U_{js}] \qquad \text{for added mass} \tag{B.37}$$

$$K_{ijkl}{}^1 = \int_0^L EIA_i''A_k''\delta_{ij}ds \qquad \text{for general stiffness from bending stiffness} \tag{B.38}$$

$$K_{nijkl}{}^2 = \int_0^L P_n A_i'A_k'\delta_{ij}ds \qquad \text{for general stiffness from axial tension and curvature} \tag{B.39}$$

$$F_{il} = \int_0^L A_i(\bar{w}_i + F_{d_i})\, ds \tag{B.40}$$

The imposed stretching condition equation also can be re-written as below with derivation process.

$$G_m = A_{mil}U_{ik}U_{lk} - B_m - C_{mt}\lambda_t \tag{B.41}$$

$$\int_0^L P_m[\frac{1}{2}(r_n' r_n')]\, ds = \frac{1}{2}\int_0^L P_m A_i' A_l'\, ds\; U_{ik}U_{lk} = A_{mil}U_{ik}U_{lk} \tag{B.41a}$$

$$B_m = \frac{1}{2}\int_0^L P_m\, ds \tag{B.41b}$$

$$\int_0^L P_m \lambda\, ds = \int_0^L P_m P_t\, ds\; \lambda_t = C_{mt}\lambda_t AE \tag{B.41c}$$

B.3 Formulation of Static Problem

The above formulas (B.35 and B.41) can be expressed to resolve static problem as below.

$$R_{ij} = F_{il} - (K^1{}_{ijlk} + \lambda_n K^2{}_{ijlk})\cdot U_{jk} = 0 \tag{B.42}$$

$$G_m = 0 \tag{B.43}$$

where F_{il} is the term which is the combination with several loads on the line (rod) such as applied static force, gravity and drag forces. Actually, it is hard to resolve these equations because of the non-linearity terms. Thus, to resolve these equations, the iterative approach (*Newton-Raphson* method) should be applied here. With neglect the higher order terms of the equations which is expanded with *Taylor* series about approximated the solution or previously iterated solution, it can be expressed (n is the number of iteration) as [40, 58].

$$R^{(n+1)}{}_{il} - R^{(n)}{}_{il} - \frac{\partial R_{il}}{\partial U_{jk}}(\Delta U_{jk}) - \frac{\partial R_{il}}{\partial \lambda_n}(\Delta \lambda_n) = 0 \tag{B.44}$$

$$G^{(n+1)}{}_m - G^{(n)}{}_m - \frac{\partial G_m}{\partial U_{jk}}(\Delta U_{jk}) - \frac{\partial G_m}{\partial \lambda_n}(\Delta \lambda_n) = 0 \tag{B.45}$$

It can be reconstructed as matrix form:

$$\begin{bmatrix} K^{t0(n)}{}_{ijlk} & K^{t1(n)}{}_{iln} \\ D^{t0(n)}{}_{mjk} & D^{t1(n)}{}_{mn} \end{bmatrix} \cdot \begin{bmatrix} \Delta U_{jk} \\ \Delta \lambda_n \end{bmatrix} = \begin{bmatrix} -R^{(n)}{}_{il} \\ -G^{(n)}{}_m \end{bmatrix} \tag{B.46}$$

The process of re-numbering is applied to the global degree of freedom related to the parameters such as U_{jk} and λ_n in CHARM3D [40, 58].

For two-dimensions (2D):

$$\text{DOF of } U_{jk} = \text{DOF of } U_{il} = \begin{bmatrix} 1 & 2 & 7 & 8 \\ 3 & 4 & 9 & 10 \end{bmatrix} \text{ for } i = 1,2,3 \text{ and } l = 1,2,3,4 \tag{B.47}$$

$$\text{DOF of } \lambda_n = \text{DOF of } \lambda_m = \begin{bmatrix} 5 & 6 & 11 \end{bmatrix} \text{ for } m = 1,2,3 \tag{B.48}$$

For three-dimensions (3D):

$$\text{DOF of } U_{jk} = \text{DOF of } U_{il} = \begin{bmatrix} 1 & 2 & 9 & 10 \\ 3 & 4 & 11 & 12 \\ 5 & 6 & 13 & 14 \end{bmatrix} \text{ for } i = 1,2,3 \text{ and } l = 1,2,3,4 \tag{B.49}$$

$$\text{DOF of } \lambda_n = \text{DOF of } \lambda_m = \begin{bmatrix} 7 & 8 & 15 \end{bmatrix} \text{ for } m = 1,2,3 \tag{B.50}$$

After re-numbering process is applied, the equation (B.46) can be re-written as [40, 58]:

$$\mathbf{F}^{(n)} - \mathbf{K}^{(n)}(\Delta \mathbf{y}) = 0 \tag{B.51}$$

$$\mathbf{y}^T = [U_{11}, U_{12}, U_{21}, U_{22}, U_{31}, U_{32}, \lambda_1, \lambda_2, U_{13}, U_{14}, U_{23}, U_{24}, U_{33}, U_{34}, \lambda_3] \tag{B.52}$$

$$\mathbf{F}^T = [R_{11}, R_{12}, R_{21}, R_{22}, R_{31}, R_{32}, -G_1, -G_2, R_{13}, R_{14}, R_{23}, R_{24}, R_{34}, R_{34}, -G_3] \tag{B.53}$$

Also, the force vector can be obtained from right hand side of equation (B.29) as below:

$$\mathbf{F}^{r} = \begin{bmatrix} -\bar{\lambda} r_i' + (EIr_i'')'\big|_{s=0,i=1} \\ -(EIr_i'')'_i \\ -\bar{\lambda} r_i' + (EIr_i'')'\big|_{s=0,i=2} \\ -(EIr_i'')'\big|_{s=0,i=2} \\ -\bar{\lambda} r_i' + (EIr_i'')'\big|_{s=0,i=3} \\ -(EIr_i'')'\big|_{s=0,i=3} \\ 0 \\ 0 \\ \bar{\lambda} r_i' - (EIr_i'')'\big|_{s=L,i=1} \\ (EIr_i'')'\big|_{s=L,i=1} \\ \bar{\lambda} r_i' - (EIr_i'')'\big|_{s=L,i=2} \\ (EIr_i'')'\big|_{s=L,i=2} \\ \bar{\lambda} r_i' - (EIr_i'')'\big|_{s=L,i=3} \\ (EIr_i'')'\big|_{s=L,i=3} \\ 0 \end{bmatrix} = \begin{bmatrix} -N^{[1]}{}_1 \\ -L^{[1]}{}_1 \\ -N^{[1]}{}_2 \\ -L^{[1]}{}_2 \\ -N^{[1]}{}_3 \\ -L^{[1]}{}_3 \\ 0 \\ 0 \\ N^{[2]}{}_1 \\ L^{[2]}{}_1 \\ N^{[2]}{}_2 \\ L^{[2]}{}_2 \\ N^{[2]}{}_3 \\ L^{[2]}{}_3 \\ 0 \end{bmatrix} \tag{B.54}$$

In the above equation, the subscript number one represents the first end of the element and number two means the second end (Ran, 2000; Kang, 2015). Also, the nodal resultant force can be expressed $\mathbf{N}=[N_1, N_2, N_3]^T$ and there is a relationship between $\mathbf{L}=[L_1, L_2, L_3]^T$ and $\mathbf{M}=\mathbf{L}\times\mathbf{r}'$ (the nodal resultant moment). From force vector $\mathbf{F}^r$, the resultant loads at the end element can be calculated after resolving using iterative approach [40, 58].

$$\mathbf{F}^r + \mathbf{F}^{(n+1)} = 0 \tag{B.55}$$

B.4 Formulation of Dynamic Problem – Time Domain Integration

It needs to be re-called here the equation of motion to resolve the dynamic response of the rod. These equations (B.35 and B.41) can be re-written as:

$$\begin{aligned}&(M_{ijlk} + M^{a}{}_{ijlk})\ddot{U}_{jk} + (K^{1}{}_{ijlk} + \lambda_n K^{2}{}_{nijlk})U_{jk} - F_{il} \\ &= (\hat{M}_{ijlk})\ddot{U}_{jk} + (K^{1}{}_{ijlk} + \lambda_n K^{2}{}_{nijlk})U_{jk} - F_{il} = 0\end{aligned} \tag{B.56}$$

$$\begin{aligned}&(\hat{M}_{ijlk})\ddot{U}_{jk} = -(K^{1}{}_{ijlk} + \lambda_n K^{2}{}_{nijlk})U_{jk} + F_{il} = 0 \\ &= -F^{1}{}_{il} - F^{2}{}_{il} + F_{il} = \hat{F}_{il}\end{aligned} \tag{B.57}$$

$$G_m = A_{mil}U_k U_{lk} = B_m + C_m\lambda_t \tag{B.58}$$

$$\hat{M}_{ijlk} = M_{ijlk} + M^{a}{}_{ijlk},\ \ F^{1}{}_{il} = K^{1}{}_{ijlk}U_{jk},\ \ F^{2}{}_{il} = \lambda_n K^{2}{}_{nijlk}U_{jk} \tag{B.59}$$

The equation (B.57) can be expressed to apply the integration scheme [40, 58].

$$\hat{M}_{ijlk}\dot{V}_{jk} = \hat{F}_{il} \tag{B.60}$$

$$\dot{U}_{jk} = V_{jk} \tag{B.61}$$

The above equations (first-order) can be integrated from $t^{(n)}$ to $t^{(n+1)}$:

$$\int_{t^{(n)}}^{t^{(n+1)}} \hat{M}_{ijlk}\dot{V}_{jk}\ dt = \int_{t^{(n)}}^{t^{(n+1)}} \hat{F}_{il}\ dt \tag{B.62}$$

$$\int_{t^{(n)}}^{t^{(n+1)}} \dot{U}_{jk}\ dt = \int_{t^{(n)}}^{t^{(n+1)}} V_{jk}\ dt \tag{B.63}$$

Due to the term $\hat{M}_{ijlk}$ can be varying with respect to the time, the term ($\int_{t^{(n)}}^{t^{(n+1)}} \hat{M}_{ijlk}\dot{V}_{jk}\ dt$) can be simplified up to second-order accuracy by approximating the time-varying term ($\hat{M}_{ijlk}$) in the time interval $\Delta t(= t^{(n+1} - t^{(n)})$ to be constant:

$$\int_{t^{(n)}}^{t^{(n+1)}} \hat{M}_{ijlk}\dot{V}_{jk}\ dt = \int_{t^{(n)}}^{t^{(n+1)}} \hat{F}_{il}\ dt$$
$$\hat{M}_{ijlk}{}^{(n+1/2)}V^{(n+1)}{}_{jk} - \hat{M}_{ijlk}{}^{(n+1/2)}V^{(n)}{}_{jk} = \int_{t^{(n)}}^{t^{(n+1)}} \hat{F}_{il}\ dt \tag{B.64}$$

Furthermore, the equation (B.63) can be re-arranged using the trapezoidal rule up to second order accuracy:

$$U^{(n+1)}{}_{jk} = U^{(n)}{}_{jk} + \frac{\Delta t}{2}[V^{(n+1)}{}_{jk} + V^{(n)}{}_{jk}] \tag{B.65}$$

By re-constructing above equation, the followings can be obtained:

$$V^{(n+1)}{}_{jk} = \frac{2}{\Delta t}[U^{(n+1)}{}_{jk} - U^{(n)}{}_{jk}] - V^{(n)}{}_{jk} = \frac{2}{\Delta t}(\Delta U_{jk}) \tag{B.66}$$

$$\frac{4}{\Delta t^2}\hat{M}_{ijlk}{}^{(n+1/2)}(\Delta U_{jk}) - \frac{4}{\Delta t^2}\hat{M}_{ijlk}{}^{(n+1/2)}(\Delta V_{jk}) - \frac{2}{\Delta t}\int_{t^{(n)}}^{t^{(n+1)}} \hat{F}_{il}\ dt = 0 \tag{B.67}$$

$$\Delta U_{jk} = U^{(n+1)}{}_{jk} - U^{(n)}{}_{jk}$$
$$\int_{t^{(n)}}^{t^{(n+1)}} \hat{F}_{il}\ dt = \int_{t^{(n)}}^{t^{(n+1)}} (-F^1{}_{il} - F^2{}_{il} + F_{il})dt = -(\int_{t^{(n)}}^{t^{(n+1)}} F^1{}_{il}\ dt + \int_{t^{(n)}}^{t^{(n+1)}} F^2{}_{il}\ dt) + \int_{t^{(n)}}^{t^{(n+1)}} F_{il}\ dt \tag{B.68}$$

By applying the trapezoidal rules to the above equations first terms:

$$\int_{t^{(n)}}^{t^{(n+1)}} F^1{}_{il}\ dt = \frac{\Delta t}{2}[K^1{}_{ijkl}(\Delta U_{jk} - 2U^{(n)}{}_{jk})] \tag{B.69}$$

$$\int_{t^{(n)}}^{t^{(n+1)}} F^2{}_{il}\ dt = \frac{\Delta t}{2}[2\lambda^{(n-1/2)}{}_n K^2{}_{nijlk}U^{(n)}{}_{jk} + 2(\Delta\lambda_n)K^2{}_{nijlk}U^{(n)}{}_{jk} + \lambda^{(n+1/2)}{}_n K^2{}_{nijlk}(\Delta U_{jk})] \tag{B.70}$$

$$\Delta\lambda_n = \lambda^{(n+1/2)}{}_n - \lambda^{(n-1/2)}{}_n \tag{B.71}$$

The terms ($\int_{t^{(n)}}^{t^{(n+1)}} F_{il}\ dt$) in (B.68) includes the applied force from hydrodynamic and gravity forces [40, 58]. To estimate the value, the *Adams-Bashforth* explicit scheme can be applied here.

$$\int_{t^{(n)}}^{t^{(n+1)}} F_{il}\ dt = \frac{\Delta t}{2}(3F^{(n)}{}_{il} - F^{(n-1)}{}_{il}) = \Delta t \cdot F^{(0)}{}_{il} \tag{B.72}$$

With combination of several equations (B.64, B.65, B.60, B.70 and B.72), the equation of motion for dynamic integration scheme can be expressed:

$$\begin{aligned}&[\frac{4}{\Delta t^2}\hat{M}_{ijlk}^{(n+1/2)} + K^1{}_{ijlk} + \lambda_n^{(n+1/2)} K^2{}_{ijlk}]\Delta U_{jk} + 2(\Delta\lambda_n)K^2{}_{nijlk}U^{(n)}{}_{jk} \\ &= \frac{4}{\Delta t}\hat{M}_{ijlk}^{(n+1/2)}V^{(n)}{}_{jk} - 2K^1{}_{ijlk}U^{(n)}{}_{jk} - \lambda_n^{(n-1/2)}K^2{}_{nijlk}U^{(n)}{}_{jk} + 3F^{(n)}{}_{il} - F^{(n-1)}{}_{il}\end{aligned} \tag{B.73}$$

Furthermore, the mass term ($\hat{M}_{ijlk}{}^{(n+1/2)}$) also can be approximated by the *Adams-Bashforth* explicit scheme:

$$\hat{M}_{ijlk}{}^{(n+1/2)} = \frac{1}{2}(3\hat{M}_{ijlk}{}^{(n)} - \hat{M}_{ijlk}{}^{(n-1)}) \tag{B.74}$$

However, in the equation (B.58) – the stretch condition, the term ($G^{(n+1)}{}_m$) can be approximated from previously time step ($G^{(n)}{}_m$) by applying *Taylor* expansion:

$$\begin{aligned}&G_m = A_{mil}U_kU_{lk} = B_m + C_m\lambda_t = 0 \\ &= 2G^{(n)}{}_m + 2K^2{}_{nijlk}U^{(n)}{}_{jk}\Delta U_{jk} + 2D^{t1(n)}{}_{mn}\Delta\lambda_n \\ &D^{t1(n)} = \frac{\partial G^{(n)}{}_m}{\partial\lambda_n}\end{aligned} \tag{B.75}$$

The above equations (B.73 and B.75) can be re-written for the time domain formula [40, 58]:

$$\begin{bmatrix} \hat{K}_{ijlk}^{t0(n)} & \hat{K}_{i\ln}^{t1(n)} \\ \hat{D}_{mjk}^{t0(n)} & \hat{D}_{mn}^{t1(n)} \end{bmatrix} \cdot \begin{bmatrix} \Delta U_{jk} \\ \Delta\lambda_n \end{bmatrix} = \begin{bmatrix} \hat{R}_{il}^{(n)} \\ -\hat{G}_m^{(n)} \end{bmatrix} \tag{B.76}$$

$$\hat{K}^{t0(n)} = \frac{2}{\Delta t^2}[3\hat{M}_{ijlk}^{(n)} - \hat{M}_{ijlk}^{(n-1)}] + K^1{}_{ijlk} + \lambda_n{}^{(n+1/2)} K^2{}_{nijlk} \tag{B.77}$$

$$\hat{K}_{i\ln}{}^{t0(n)} = 2K^2{}_{nijlk} U^{(n)}{}_{jk} \tag{B.78}$$

$$\hat{D}_{mjk}{}^{t0(n)} = 2K^2{}_{mijlk} U_{il}{}^{(n)} \tag{B.79}$$

$$\hat{D}_{mn}{}^{t1(n)} = 2D_{mn}{}^{t1(n)} \tag{B.80}$$

$$\hat{R}_{il}^{(n)} = \frac{2}{\Delta t}[3\hat{M}_{ijlk}^{(n)} - \hat{M}_{ijlk}^{(n-1)}] V_{jk}{}^{(n)} - 2K^1{}_{ijlk} U_{jk}{}^{(n)} - 2\lambda_n{}^{(n-1/2)} K^2{}_{nijlk} U_{jk}{}^{(n)} + 3F_{il}{}^{(n)} - F_{il}{}^{(n-1)} \tag{B.81}$$

$$\hat{G}_m^{(n)} = 2G_m{}^{(n)} \tag{B.82}$$

By changing the subscription (n) meaning (ex: n th time step in dynamic whereas n th iteration in static) and keeping the coefficients formulation, the final equation of motion of the rod can be obtained [40, 58]. After solving the combined equation of rod element motion for time step ($n+1$), the nodal resultant load can be obtained.

$$\hat{\mathbf{K}}^{(n)}(\Delta\mathbf{y}) - \hat{\mathbf{F}}^{(n)} = 0 \quad \text{at } n \text{ th time step} \tag{B.83}$$

$$\mathbf{F}^r + \mathbf{F}^{(n+1)} = 0 \tag{B.84}$$

APPENDIX C

COUPLING BETWEEN PLATFORMS AND MOORING LINES AND RISER

C.1 Spring Coupling Between the Floating Structure and Lines

The connection between the lines (mooring lines or riser) and the floating structure is modelled using springs such as translational (linear) and rotational. The translational motion can be defined using linear spring whereas the rotational spring is related to the rotation of the floater. Here, the nodal resultant forces and moments in the motion equation (right hand side of eqn. (B.29)) is re-expressed as below:

$$\begin{aligned}&\int_0^L [A_l(\rho \ddot{r}_i + C_A \ddot{r}_i^n) + EIA_l\,"\,r_i\,"+ \bar{\lambda} A_l\,'\,r_i\,' - A_l(\bar{w}_i + F_{d_i})]\,ds \\ &= EIr_i\,"\cdot A_l\,'\big|_0^L + [\bar{\lambda}_l r_i\,' - (EIr_i\,")\,']\cdot A_l\,'\big|_0^L\end{aligned} \tag{B.29}$$

Continually, its vector form is expressed in eqn. (B.54) where $\mathbf{N} = [N_1, N_2, N_3]^T$ is the nodal resultant force and $\mathbf{L} = [L_1, L_2, L_3]^T$ is the nodal resultant moment **M(=L×r')**. Furthermore, in the assembly equation, the resultant loads of the neighboring elements (intermediate nodes) are canceled out each other. However, the resultant forces and moment of the end element nodal point (connecting with the floating structure) are equivalent with the forces and moments from the spring. Thus, the forces exerted on the end node of the element caused from linear spring should be defined as below [40, 58].

$$\mathbf{N} = [\mathbf{K}^L]\cdot(\mathbf{X} + \mathbf{p} + \theta \times \mathbf{p} - \mathbf{r}) \tag{C.1}$$

where $[\mathbf{K}^L]$ represents 3 x 3 the linear spring stiffness matrix (diagonal), $\mathbf{X}$ is the translational motion of the floating structure, θ is the rotational motion of the structure, $\mathbf{p}$ is the position vector with respect to the body fixed coordinated system, $\mathbf{r}$ represents

the position of the end node of the last element which is connected to the floating structure using springs. Thus, the equations (3.33, 3.34) can be labeled newly as:

$$U_{13} = r_1(L,t),\ U_{23} = r_2(L,t),\ U_{33} = r_3(L,t) \tag{C.2}$$

With contribution from the linear spring connector between last element and the floating structure, the loads exerted on the floater:

$$\mathbf{F}^L + \mathbf{N} = 0 \tag{C.3}$$

$$\mathbf{M}^L + \mathbf{p} \times \mathbf{N} = 0 \tag{C.4}$$

However, since there is a proportional relationship between the moment applied the end node caused from rotational spring and the angle (between the tangent of the last element and the direction vector of the spring), it can be re-written with the assumption that small angular motion of the floater [40, 58].

$$\mathbf{L} = K^\theta[\mathbf{E} - \frac{\mathbf{r}'}{|\mathbf{r}'|}] = K^\theta[\mathbf{e} + \theta \times \mathbf{e} - \frac{\mathbf{r}'}{|\mathbf{r}'|}] \tag{C.5}$$

where $\mathbf{r}'$ represents the tangential vector of the line. To unity of the tangent, the term ($\frac{\mathbf{r}'}{|\mathbf{r}'|}$) can be used. Also, $\mathbf{E}$ denotes spring direction unit vector, $\mathbf{e}$ is equivalent with $\mathbf{E}$ in the body coordinate system and K^θ means the rotational spring constant.

Continually, with contribution from the rotational spring connector between last element and the floating structure, the loads exerted on the floater:

$$\mathbf{F}^\theta = 0 \tag{C.6}$$

$$\mathbf{M}^\theta = \mathbf{L} \times \mathbf{r}' \approx \mathbf{L} \times \mathbf{e} \tag{C.7}$$

The loads applied on the connector can be re-defined in subscript notation here as below:

$$N_i = K^L(X_i + p_i + \theta_j C_{ji} - r_i) \tag{C.8}$$

$$L_i = K^\theta[e_i + \theta_j D_{ji} - \frac{r_i'}{(r_k' r_k')^{1/2}}] \tag{C.9}$$

and the connector loads (forces and moments) on the floating structure are expressed:

$$F_i = -N_i = -K_i^L(X_i + p_i + \theta_j C_{ji} - r_i) \tag{C.10}$$

$$M_i = M^L + M^\theta = N_k C_{ki} + L_k D_{ki} \tag{C.11}$$

$$[C] = \begin{bmatrix} 0 & -p_3 & p_2 \\ p_3 & 0 & -p_1 \\ -p_2 & p_1 & 0 \end{bmatrix} \tag{C.12}$$

$$[D] = \begin{bmatrix} 0 & -e_3 & e_2 \\ e_3 & 0 & -e_1 \\ -e_2 & e_1 & 0 \end{bmatrix} \tag{C.13}$$

In the static analysis, the connector forces at the last node in n+1 iteration from iteration n (previous) can be defined as [40, 58]:

$$\begin{aligned} N_i^{(n+1)} &= N_i^{(n)} + \frac{\partial N_i}{\partial r_j}\Delta r_j + \frac{\partial N_i}{\partial X_j}\Delta X_j + \frac{\partial N_i}{\partial \theta_j}\Delta\theta_j + ... \\ &= N_i^{(n)} - K_{ij}^{rr}\Delta r_j - K_{ij}^{rX}\Delta X_j - K_{ij}^{r\theta}\Delta\theta_j + ... \end{aligned} \tag{C.14}$$

$$\begin{aligned} L_i^{(n+1)} &= L_i^{(n)} + \frac{\partial L_i}{\partial r_j}\Delta r_j' + \frac{\partial L_i}{\partial \theta_j}\Delta\theta_j + ... \\ &= L_i^{(n)} - K_{ij}^{r'r'}\Delta r_j' - K_{ij}^{r'\theta}\Delta\theta_j + ... \end{aligned} \tag{C.15}$$

where the tangential stiffness coefficient (K_{ij}^{AB}) for degree of freedom B_j in the equation A_i [40, 58].

$$K_{ij}^{rr} = -\frac{\partial N_i}{\partial r_j} = -\frac{\partial}{\partial r_j}[K_i^L(X_i + p_i + \theta_j C_{ji} - r_i)] = K_i^L \delta_{ij} \tag{C.16}$$

$$K_{ij}^{rX} = -\frac{\partial N_i}{\partial X_j} = -\frac{\partial}{\partial X_j}[K_i^L(X_i + p_i + \theta_j C_{ji} - r_i)] = -K_i^L \delta_{ij} \tag{C.17}$$

$$K_{ij}^{r\theta} = -\frac{\partial N_i}{\partial \theta_j} = -\frac{\partial}{\partial \theta_j}[K_i^L(X_i + p_i + \theta_j C_{ji} - r_i)] = -K_i^L \delta_{ij} \tag{C.18}$$

$$\begin{aligned} K_{ij}^{r'r'} &= -\frac{\partial L_i}{\partial r'_j} = -\frac{\partial}{\partial r'_j}[K_i^\theta(e_i + \theta_j D_{ji} - \frac{r_i'}{(r_k' r_k')^{1/2}})] \\ &= K^\theta[\frac{\delta_{ij}}{(r_m' r_m')^{1/2}} - \frac{r_i' r_j'}{(r_n' r_n')^{3/2}}] \end{aligned} \tag{C.19}$$

$$K_{ij}^{r'\theta} = -\frac{\partial L_i}{\partial \theta_j} = -\frac{\partial}{\partial \theta_j}[K_i^\theta(e_i + \theta_j D_{ji} - \frac{r_i'}{(r_k' r_k')^{1/2}})] = -K^\theta D_{ij} \tag{C.20}$$

In the static analysis, the connector forces at the platform in n+1 iteration from iteration n can be defined as [40, 58].

$$\begin{aligned} F_i^{(n+1)} &= F_i^{(n)} + \frac{\partial F_i}{\partial r_j}\Delta r_j + \frac{\partial F_i}{\partial X_j}\Delta X_j \frac{\partial F_i}{\partial \theta_j}\Delta\theta_j + ... \\ &= F_i^{(n)} - K_{ij}^{Xr}\Delta r_j - K_{ij}^{XX}\Delta X_j - K_{ij}^{X\theta}\Delta\theta_j + ... \end{aligned} \tag{C.21}$$

$$\begin{aligned} M_i^{(n+1)} &= M_i^{(n)} + \frac{\partial M_i}{\partial r_j}\Delta r_j + \frac{\partial M_i}{\partial r'_j}\Delta r'_j + \frac{\partial M_i}{\partial \theta_j}\Delta\theta_j + \frac{\partial M_i}{\partial X_j}\Delta X_j + ... \\ &= M_i^{(n)} - K_{ij}^{\theta r}\Delta r_j - K_{ij}^{\theta r'}\Delta r'_j - K_{ij}^{\theta\theta}\Delta\theta_j - K_{ij}^{\theta X}\Delta X_j + ... \end{aligned} \tag{C.22}$$

$$K_{ij}^{Xr} = -\frac{\partial F_i}{\partial r_j} = -\frac{\partial}{\partial r_j}[-K_i^L(X_i + p_i + \theta_j C_{ji} - r_i)] = -K_i^L \delta_{ij} \tag{C.23}$$

$$K_{ij}^{XX} = -\frac{\partial F_i}{\partial X_j} = -\frac{\partial}{\partial X_j}[-K_i^L(X_i + p_i + \theta_j C_{ji} - r_i)] = K_i^L \delta_{ij} \tag{C.24}$$

$$K_{ij}^{X\theta} = -\frac{\partial F_i}{\partial \theta_j} = -\frac{\partial}{\partial \theta_j}[-K_i^L(X_i + p_i + \theta_j C_{ji} - r_i)] = K_i^L C_{ij} \tag{C.25}$$

$$K_{ij}^{\theta r} = -\frac{\partial M_i}{\partial r_j} = -\frac{\partial}{\partial r_j}[N_k C_{ki} + L_k D_{ki}] = K_i^L C_{ij} \tag{C.26}$$

$$K_{ij}^{\theta r'} = -\frac{\partial M_i}{\partial r'_j} = -\frac{\partial}{\partial r'_j}[N_k C_{ki} + L_k D_{ki}] = K_i^{\theta} D_{ij} \tag{C.27}$$

During the iterative procedure, the rod stiffness coefficients (K_{ij}^{rr} and $K_{ij}^{r'r'}$) is included in the elemental equation, the rigid body coefficients (K_{ij}^{XX} , $K_{ij}^{X\theta}$ and $K_{ij}^{\theta\theta}$) is included in the floater motion equation and the coupling stiffness coefficients (K_{ij}^{rX} , K_{ij}^{Xr} , $K_{ij}^{r\theta}$, $K_{ij}^{r'\theta}$, $K_{ij}^{\theta r}$ and $K_{ij}^{\theta r'}$) is included to a coupling matrix. Furthermore, the forces vectors ($N_i^{(n)}$, $L_i^{(n)}$, $F_i^{(n)}$ and $M_i^{(n)}$) will be added the equation of the line element and the floater (B.68) and will be integrated from time $t^{(n)}$ to $t^{(n+1)}$: [40, 58].

$$\begin{aligned} &\Delta U_{jk} = U^{(n+1)}{}_{jk} - U^{(n)}{}_{jk} \\ &\int_{t^{(n)}}^{t^{(n+1)}} \hat{F}_{il}\, dt = \int_{t^{(n)}}^{t^{(n+1)}} (-F^1{}_{il} - F^2{}_{il} + F_{il})dt = -(\int_{t^{(n)}}^{t^{(n+1)}} F^1{}_{il}\, dt + \int_{t^{(n)}}^{t^{(n+1)}} F^2{}_{il}\, dt) + \int_{t^{(n)}}^{t^{(n+1)}} F_{il}\, dt \end{aligned} \tag{B.68}$$

Equations for r_i:

$$\begin{aligned} \int_{t^{(n)}}^{t^{(n+1)}} N_i\, dt &= \frac{\Delta t}{2}[N_i^{(n+1)} + N_i^{(n)}] \approx \frac{\Delta t}{2}[\frac{\partial N_i}{\partial r_j}\Delta r_j + \frac{\partial N_i}{\partial X_j}\Delta X_j + \frac{\partial N_i}{\partial \theta_j}\Delta \theta_j + 2N_i^{(n)}] \\ &= \frac{\Delta t}{2}[-K_{ij}^{rr}\Delta r_j - K_{ij}^{rX}\Delta X_j - K_{ij}^{r\theta}\Delta \theta_j + 2N_i^{(n)}] \end{aligned} \tag{C.28}$$

Equations for $r_i^{'}$:

$$\begin{aligned}\int_{t^{(n)}}^{t^{(n+1)}} L_i \, dt &= \frac{\Delta t}{2}[L_i^{(n+1)} + L_i^{(n)}] \approx \frac{\Delta t}{2}[\frac{\partial L_i}{\partial r_j}'\Delta r_j' + \frac{\partial L_i}{\partial \theta_j}\Delta\theta_j + 2L_i^{(n)}] \\ &= \frac{\Delta t}{2}[-K_{ij}^{r'r'}\Delta r_j' - K_{ij}^{r'\theta}\Delta\theta_j + 2L_i^{(n)}]\end{aligned} \tag{C.29}$$

and for connector loads on the floating structure.

Equations for X_i:

$$\begin{aligned}\int_{t^{(n)}}^{t^{(n+1)}} F_i \, dt &= \frac{\Delta t}{2}[F_i^{(n+1)} + F_i^{(n)}] \approx \frac{\Delta t}{2}[\frac{\partial F_i}{\partial r_j}\Delta r_j + \frac{\partial F_i}{\partial X_j}\Delta X_j + \frac{\partial F_i}{\partial \theta_j}\Delta\theta_j + 2F_i^{(n)}] \\ &= \frac{\Delta t}{2}[-K_{ij}^{Xr}\Delta r_j - K_{ij}^{XX}\Delta X_j - K_{ij}^{X\theta}\Delta\theta_j + 2F_i^{(n)}]\end{aligned} \tag{C.30}$$

Equations for θ_i:

$$\begin{aligned}\int_{t^{(n)}}^{t^{(n+1)}} M_i \, dt &= \frac{\Delta t}{2}[M_i^{(n+1)} + M_i^{(n)}] \approx \frac{\Delta t}{2}[\frac{\partial M_i}{\partial r_j}\Delta r_j + \frac{\partial M_i}{\partial X_j}\Delta r_j' + \frac{\partial M_i}{\partial \theta_j}\Delta\theta_j + 2M_i^{(n)}] \\ &= \frac{\Delta t}{2}[-K_{ij}^{\theta r}\Delta r_j - K_{ij}^{\theta r'}\Delta r_j' - K_{ij}^{\theta\theta}\Delta\theta_j + 2M_i^{(n)}]\end{aligned} \tag{C.31}$$

C.2 Damper Connection Modelling

In CHARM3D, linear damping force which is related to the relative translational velocity is applied. The damping force term (N_i^D) on the connection of the last line element is expressed:

$$N_i^D = D(\dot{X}_i + \dot{\theta}_j C_{ji} - \dot{r}_i) \tag{C.32}$$

where D is a linear damping coefficient, $\dot{r}$, $\dot{X}$ and $\dot{\theta}$ are the velocity of the node, translational / rotational velocity, and

$$C_{ij} \rightarrow [C] = \begin{bmatrix} 0 & -p_3 & p_2 \\ p_3 & 0 & -p_1 \\ -p_2 & p_1 & 0 \end{bmatrix} \tag{C.33}$$

In the time domain, the integration of the connecting force can be represented as below [40, 58]. Similar with previously explained, the damping coefficients are also added to the line and floater motion of equation (same way with stiffness case).

$$\begin{aligned} \int_{t^{(n)}}^{t^{(n+1)}} N_i^D \, dt &= \int_{t^{(n)}}^{t^{(n+1)}} D(\dot{X}_i + \theta_j C_{ji} - \dot{r}_i) \, dt = \int_{t^{(n)}}^{t^{(n+1)}} D \, dX_i + \int_{t^{(n)}}^{t^{(n+1)}} D \, C_{ji} d\theta_j - \int_{t^{(n)}}^{t^{(n+1)}} D \, dr_i \\ &= (D)\Delta X_i + (D\ )C_{ji}\Delta\theta_j - (D)\Delta r_i \end{aligned} \tag{C.34}$$

Equations for X_i:

$$\int_{t^{(n)}}^{t^{(n+1)}} F_i^D \, dt = -\int_{t^{(n)}}^{t^{(n+1)}} N_i^D \, dt = (-D)\Delta X_i + (D\ )C_{ji}\Delta\theta_j + (D)\Delta r_i \tag{C.35}$$

C.3 Force Vector of Hull, Mooring Lines and Riser Coupled Dynamics

After fully-coupled modelling between the floater and mooring lines and riser, assembled matrix has a $8\times(N+1)-1$ rows (N is the total element number) for legs. Also, a leg (mooring lines and risers) can be divided into N elements and its corresponding nodes (n = N+1) in CHARM3D. Due to coupling terms, the assembled matrix becomes sparse. At

every time step, the six degree of freedom motion of end nodes in each element can be defined by ΔU_{jk} and its corresponding tension also defined as $\Delta\lambda_n$. The fully-coupled global stiffness and forcing vector is presented in Figure 106.

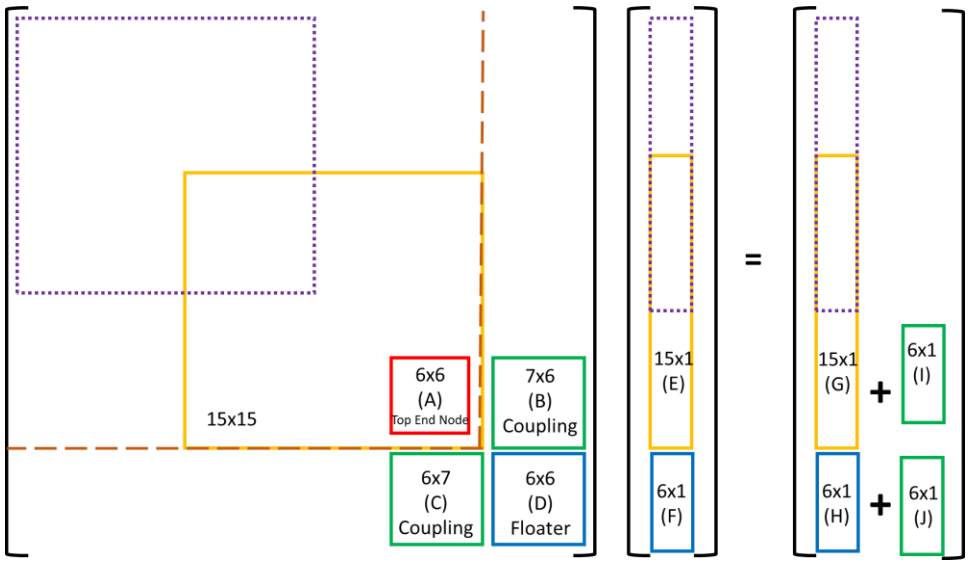

Figure 106 Coupled global stiffness and forcing vector matrix

$$(A)=\begin{bmatrix} K_{11}^{rr} & & & & \\ & K_{11}^{r'r'} & & 0 & \\ & & K_{22}^{rr} & & \\ & & & K_{22}^{r'r'} & \\ & 0 & & & K_{33}^{rr} \\ & & & & & K_{33}^{r'r'} \end{bmatrix}$$

$$(B)=\begin{bmatrix} K_{11}^{rX} & & & & K_{12}^{r\theta} & K_{13}^{r\theta} \\ & & & & K_{12}^{r'\theta} & K_{13}^{r'\theta} \\ & K_{22}^{rX} & & K_{21}^{r\theta} & & K_{23}^{r\theta} \\ & & & K_{21}^{r'\theta} & & K_{23}^{r'\theta} \\ & & K_{33}^{rX} & K_{31}^{r\theta} & K_{32}^{r\theta} & \\ & & & K_{31}^{r'\theta} & K_{32}^{r'\theta} & \\ & & & & & \end{bmatrix}_{7\times 6}$$, (C) *is the inverse matrix of* (B).

$$(D)=\begin{bmatrix} K_{11}^{XX} & & & & K_{15}^{X\theta} & K_{16}^{X\theta} \\ & K_{22}^{XX} & & & & K_{26}^{X\theta} \\ & & K_{33}^{XX} & K_{34}^{X\theta} & & \\ & K_{42}^{\theta X} & & K_{44}^{\theta\theta} & K_{45}^{\theta\theta} & K_{46}^{\theta\theta} \\ K_{51}^{\theta X} & & K_{53}^{\theta X} & K_{54}^{\theta\theta} & K_{55}^{\theta\theta} & K_{56}^{\theta\theta} \\ K_{61}^{\theta X} & K_{62}^{\theta X} & & K_{64}^{\theta\theta} & K_{65}^{\theta\theta} & K_{66}^{\theta\theta} \end{bmatrix}$$

(E) = the last line element, 15 x 1 matrix (ΔU_{jk}, $\Delta\lambda_n$)

(F) = the floater displacements, 6 x 1 matrix ($\Delta\zeta$)

(G) = the force vector of the line ,15 x 1 matrix ($\hat{R}_{il}^{(n)}$, $-\hat{G}_m^{(n))}$)

(H) = the force vector of the platform, 6 x 1 matrix=> represents right hand side of the equation (A.61)

(I) = the force vector of the connector on the end node of the line (N_i, L_i), 6 x 1 matrix=> represents right hand side of the equation (C.38)

(J) = the force vector of the connector on the end node of the line (F_i, M_i), 6 x 1 matrix=> represents right hand side of the equation (C.39)